MODELLING OF ULTRASONIC TRANSDUCTION AND MEASUREMENT USING FINITE ELEMENTS

SIMON A. FORSYTH

A thesis submitted in partial fulfilment of the
requirements of The Nottingham Trent University
for the degree of Doctor of Philosophy

February 2000

ACKNOWLEDGEMENTS

I would like to thank my supervisor Dr. Roger Hill for his guidance throughout this study. I would also like to give a special thanks to Patrick Macey and John King at PAFEC Ltd. (now SER Systems Ltd.) for their valuable time and effort spent in solving some of the coding problems.

I express appreciation for all the help and support of my family and friends, who have helped push me up to the finishing line.

ABSTRACT

The aim of this research was to investigate the behaviour of resonant transducers used for the detection of ultrasound, specifically acoustic emission (AE) in nondestructive evaluation (NDE) of materials. PAFEC-FE Vibroacoustics finite element (FE) software was employed on a computer workstation in order to gain an insight into the best methods of modelling ultrasonic transducers.

Two main methods of modelling were used. The first was a sinusoidal analysis, used to predict transducer frequency response and vibrational behaviour. The second was a transient analysis, in which the transducer response to a simulated AE event was predicted. Within these two broad categories, further variations upon the methods were investigated and evaluated.

Acoustic FE modelling was shown to provide the most realistic results for the sinusoidal analyses. Close agreement between FE predictions and experimental measurements were achieved for two different transducer designs. The software was then used to investigate transducer performance changes due to geometry and mounting conditions. It was also used to optimise the performance of a metal-ceramic composite design. Agreement with theory was also shown where appropriate.

Two methods of modelling an AE event were utilised in order to predict the response of a resonant transducer to a propagating wave in a plate. Both methods showed agreement and open up the possibility for modelling the transducer response to a variety of input sources. Similarities with experimental data showed that future work promises to be extremely useful in understanding the AE source and transducer response relationship. Improved agreement would stem from comparable bandpass filtering.

Resonant transducers appear to be capable of representing the deformation at the transducer surface before going into their resonant mode of vibration. Lamb wave modes which propagate in a plate are shown to influence the shape of the waveform, leading to information about the type and location of the source.

Further work to improve the realism of the modelling, associated with increased computing power, will allow the NDE engineer to obtain a much greater understanding of what the transducers are detecting. The transducer designer will also be able to tailor make transducers for specific applications with improved performance.

CONTENTS

CHAPTER TWO

FE MODELLING OF A PZT-5A DISC TRANSDUCER DESIGN

CHAPTER THREE
EXPONENTIAL HORN TRANSDUCER DESIGNS

Chapter One

Review of Measurement, Applications and Modelling using Ultrasonic Transducers

1.0 INTRODUCTION TO ULTRASOUND & ULTRASONIC TRANSDUCERS

Only since the late nineteenth century has acoustics been considered as a science rather than an art form. Whistles, gongs and sirens were used for controlling the generation of sound and the ears were the scientists' primary detection tool. Basic microphones consisted of a diaphragm connected to a mechanical stylus which recorded the wave shape, or a flame which varied in height according to the sound pressure. Work by scientists including Lamb, Helmholtz and Rayleigh, led to improved knowledge of acoustics, culminating in Lord Rayleigh's "Theory of Sound" volumes in the late 1870s. It was the start of the twentieth century before acoustics really became a science with the invention of the triode vacuum tube and developments in radio and telephony. With these new devices, sound that was previously undetectable could be generated and received effectively.

Ultrasound, generated above 20 kHz, is an extremely useful phenomenon for non-destructive inspection. It has found uses in engineering for nondestructive and power applications and also in the medical field. Areas of application have included; SONAR, metal and polymer forming, pulse echo materials inspection in numerous forms, resonant inspection, interrogation and monitoring.

High frequency sound waves are generated by rapidly vibrating the medium through which the sound wave will travel (solid, liquid or gas). This vibration can be achieved using piezoelectric materials, polymeric film or composite transducers. Piezoelectric materials are the most dominant, due to their relative simplicity and cost effectiveness.

Their use in nondestructive evaluation (NDE) of materials, is the primary area of application for the transducers studied here.

The behaviour of piezoelectric transducers is complicated and the need for improved designs, to aid better ultrasonic detection and generation, has required new methods to study and predict their performance. The use of computer modelling techniques for this purpose, is the topic of this thesis. Finite elements (FE) are used to discretise the transducer geometry and any other materials involved, into a mesh. FE computer software can then predict the performance of the transducer, used to either detect or generate ultrasound. The finite element software used was able to deal with fluid structure interactions, piezoelectric materials and transient simulations.

Recent developments in finite element techniques allow full three-dimensional and axisymmetric models to be created for piezoelectric and acoustic analyses, which are more accurate than one or two-dimensional models [**1**]. Because of its specialist features, PAFEC-FE Vibroacoustics software was chosen for the research. Later in the thesis, discussion is included on the philosophy of the modelling process and its application to real life piezoelectric transducer designs.

Several important engineering issues have been considered, including transducer design, mounting effects and response to transient acoustic emission (AE) sources. FE modelling has only been used as a design aid for some composite transducer designs. The work in this thesis has considered the issues of ultrasonic transducer design, using FE in more depth. Because of the materials and higher frequencies used by ultrasound systems, the modelling has explored the limits of FE modelling, when applied to ultrasound effects.

1.1 THE PIEZOELECTRIC EFFECT, MATERIALS & TRANSDUCERS

1.1.1 Piezoelectricity and Piezoelectric Materials

Discovered by Pierre and Jacques Curie in the 1880s, the piezoelectric effect is widely exploited. Piezoelectricity is "pressure electricity" and is a property of certain natural crystals such as quartz, Rochelle salt, tourmaline and barium titanate. Polycrystalline ceramic piezoelectrics can also be manufactured and these demonstrate a much wider range of properties.

A net electric charge is developed on the surface when pressure is applied to one of these piezoelectric materials, caused by the atomic dipoles being displaced asymmetrically. The reverse effect also occurs when the material expands or contracts in the presence of an electric field (fig. 1.1).

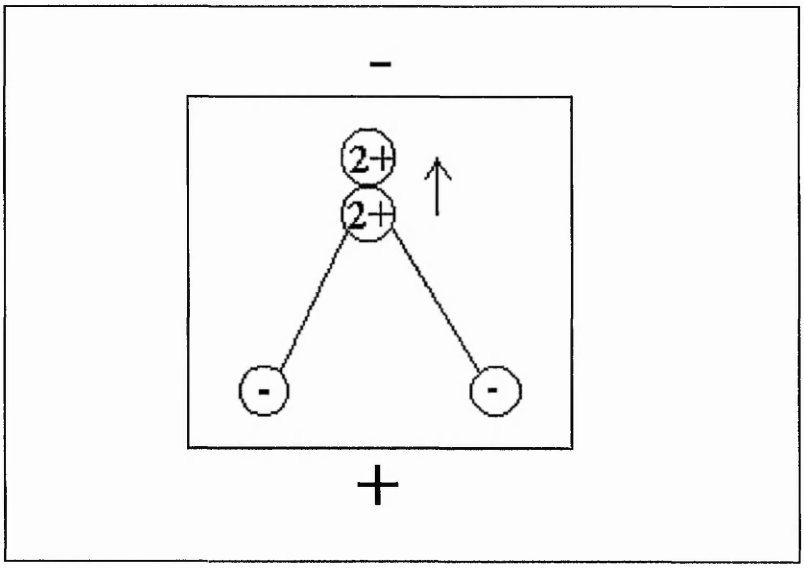

Fig. 1.1 Example of crystal expansion due to the presence of an electric field. In this case the 2^+ ion is displaced upwards.

The direct piezoelectric effect is used for measurement of sound, while the inverse piezoelectric effect is used for producing mechanical pressure deformations and oscillations. Fundamental research has shown that for the piezoelectric effect to occur, the crystals must lack a centre of symmetry. From the 32 classes of crystals, 21 have this

property. Of these, 20 crystal types show some piezoelectric properties, providing a wide range of different possible piezoelectric materials.

If an alternating field is applied across a piezoelectric material, an alternating displacement will be created at the same frequency. The displacement lags behind the applied field, but at a resonance frequency, the two are in phase.

Piezoelectric materials can be used as transmitters and receivers of acoustic power from very low frequencies, to high frequencies above 1 GHz. Their physical, chemical and piezoelectric characteristics can be adjusted to specific applications. For transducer applications they need to be chemically inert, immune to moisture and other atmospheric influences and mechanically robust.

The exact choice of piezoelectric material, whether natural or man made, will depend largely on the application. Quartz, for example, is popular in electronic timers, such as watches and also for frequency control in radios, due to its high 'Q' resonant frequencies. Barium titanate and lead zirconate titanate ceramics are preferred because of their large ultrasonic output. Relatively high conversion efficiencies enable ceramic piezoelectrics (piezoceramics) to receive small mechanical displacements and convert them to an effective electrical signal. This ability is used, for instance, in acoustic emission (AE) applications.

Piezoceramics are polycrystalline materials which show similar behaviour to natural crystals. Dating from the 1940s, piezoceramics first became popular in the lower frequency range and newer materials, developed in the 1960s, proved useful at higher frequencies. For extremely high MHz or GHz frequencies, thin films of piezoelectric material are used. The piezoceramics used in AE work and many other mid-range frequencies (from a few kHz to a few MHz), date from the mid to late 1950s.

The three main piezoceramics used [**2**] are barium titanate (BiTiO), lead zirconate titanate [$Pb(0.4Zr0.6Ti)O_3$ to $Pb(0.9Zr0.1Ti)O_3$] and modified lead metaniobate ($PbNb_2O_5$). These materials are low cost, hard and dense, can be manufactured in many

shapes and sizes and can have their properties tailored. They are made by compressing and sintering high purity oxide powders to form a polycrystalline, isotropic mass. Unbalanced, movable dipoles within their atomic microstructure give the piezoceramics ferroelectric properties. To make the ceramic anisotropic, the material is cooled in a DC electric field, which produces an alignment of dipoles or *poling* (fig. 1.2). The ceramic now has a polar axis and can demonstrate piezoelectric responses.

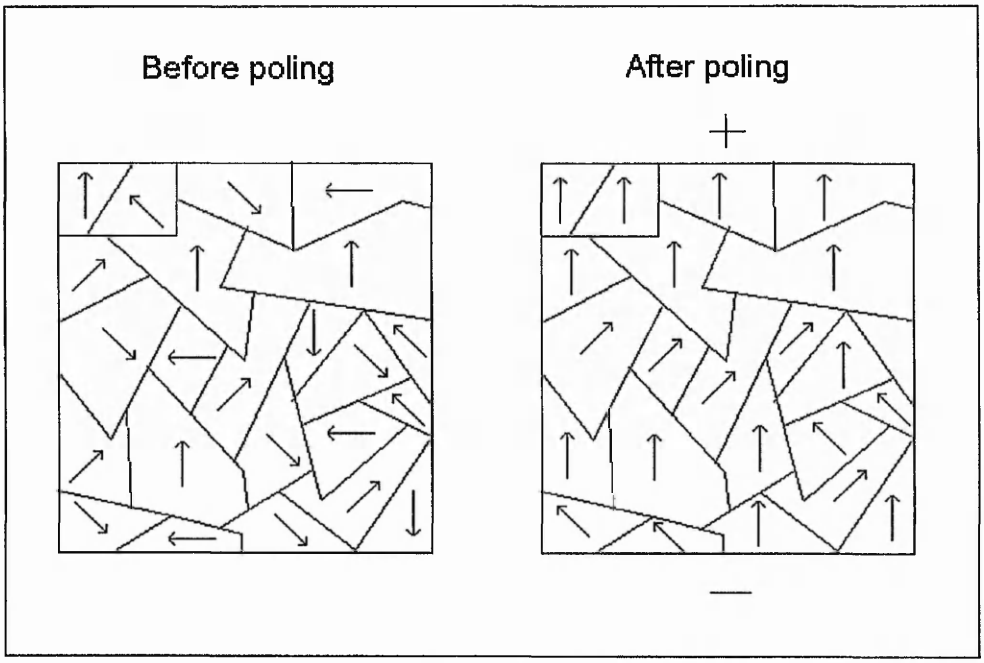

Fig. 1.2 Unpoled and poled piezoelectric material. The arrows indicate electric vectors within ferroelectric domains.

The mechanical and electrical axes of these ceramics can be accurately orientated in relation to the shape of the ceramic. This enables the appropriate vibrational properties to be chosen for the desired application. A simple plate can be made to vibrate [**3**] in three basic ways (fig. 1.3) i.e. thickness shear (1), face shear (2) and thickness expansion (3), just by applying the voltage to the electrodes with a different axis of polarisation. The first mode of vibration involves the two electrodes moving parallel to each other but in opposite directions, thus causing a shearing action. The second, face shear mode, occurs when the shear force is still acting parallel to the electrodes but this time causing a twisting motion about the normal to the electrode. The final basic mode of vibration involves the plate expanding or compressing in the thickness direction, normal to the electrode surfaces. By choosing the axes and electrodes carefully, the transducer can

detect displacements in specific directions, e.g. normal or tangential to its detection surface.

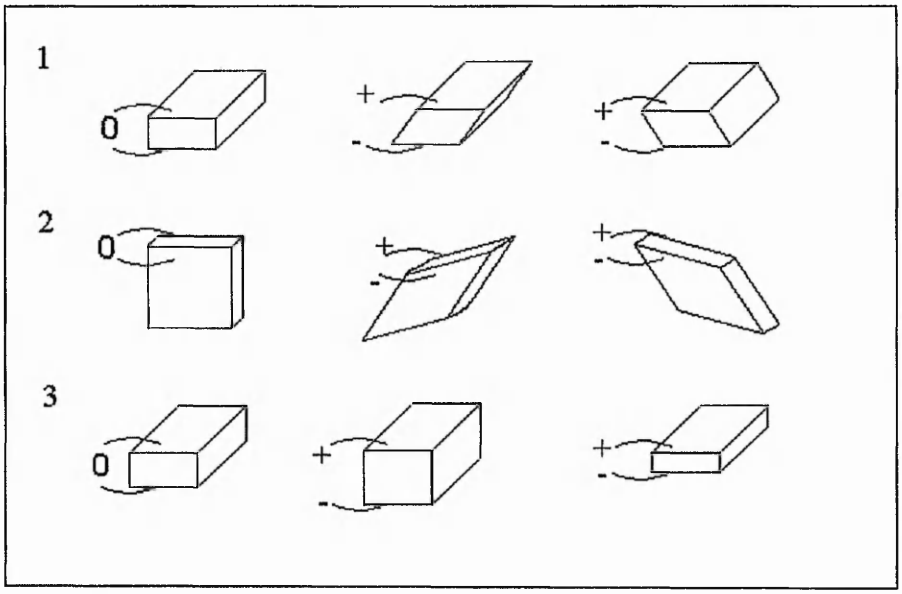

Fig. 1.3 Basic vibration modes of a piezoelectric plate i.e. thickness shear (1), face shear (2) and thickness expansion (3).

Much of the ceramic uses mixtures of lead zirconate and lead titanate to form PZT (lead zirconate titanate). The composition of ceramics is chosen to be close to the phase boundary, between the titanium-rich tetragonal phase and the zirconium-rich rhombohedral phase. This is done because maximum piezoelectric coupling, permittivity and compliance occur at or near to the phase boundary. Most lead zirconate titanate materials are on the tetragonal side of the phase boundary.

PZT-5A is the ceramic used for the transducers discussed in this thesis, due to its common use in NDT and for other ultrasonic devices. By using Nb^{5+} or La^{3+} to replace a proportion of either $(Ti, Zi)^{4+}$ or Pb^{2+} respectively, the PZT-5 series are created, characterised by high sensitivity due to increased piezoelectric coupling, permittivity, compliance, high time stability and resistivity at elevated temperatures [**4**]. This material can be used as the receiver or generator element in hydrophones, accelerometers and vibration pickups.

Piezoelectric ceramics have a maximum useful temperature determined by the Curie Point. If heated above this point they then lose their piezoelectric properties permanently, because the net polarisation is destroyed by thermal disorder effects. In practice, the ceramics must be used at a substantially lower temperature in order to maintain their original room temperature properties. For PZT-5A the Curie Point is 365°C and the approximate maximum operating temperature is 250°C.

1.1.2 Piezoelectric Constants

The electromechanical constants commonly employed are the coupling constant k, strain constant d and stress constant g. For each of these, the directions of field and stress or strain are indicated by two subscripts. The first subscript indicates the direction of electric field and the second subscript indicates the direction of stress or strain. Subscripts 4, 5, 6 denote shear stress or shear strain around the 1, 2 and 3 axes respectively.

1.1.2.1 Coupling Constant (k)

Constant k is the electro-mechanical coupling constant of a transducer, which quantifies the ability to convert electrical energy into mechanical energy and vice versa. Coupling constant squared is a measure of efficiency and equal to the transformed energy divided by the total energy input. The same constant is used when considering conversion from electrical to mechanical energy and from mechanical to electrical energy.

1.1.2.2 Piezoelectric (d) Constants

The d constants express the ratio of strain developed along or around a specific axis, to the field applied parallel to a specified axis, when all external stresses are constant. The d constants also express the ratio of short circuit charge per unit area of electrode between connected electrodes, which are perpendicular to a specified axis, to the stress applied along or around a specified axis, when all other external stresses are constant. An example is d_{31}, which denotes the ratio of strain in the 1 direction to the field applied

in the 3 direction, when the piezoelectric material is mechanically free in all directions. It also denotes the ratio of charge per unit area of electrode between electrodes which are perpendicular to the 3 axis and connected together, to the stress applied in the 1 direction, when the material is free of external stresses in all other directions.

1.1.2.3 Piezoelectric (g) constants

The g constants express the ratio of field developed along a specified axis to the stress applied along, or around, a specified axis when all other external stresses are constant. The g constants also express the ratio of strain developed along, or around, a specified axis to the electric charge per unit area of electrode applied to electrodes, which are perpendicular to a specified axis. Again, an example is g_{33}, which denotes the ratio of field developed in the 3 direction to stress applied in the 3 direction when all other external stresses are zero. It also denotes the ratio of strain developed in the 3 direction to the charge per unit area of electrode applied to electrodes on faces perpendicular to the 3 axis.

1.1.3 Piezoelectric Transducers & their Design

By definition a transducer is a device which transfers signals from one system to another by energy conversion. In the case of ultrasound, a signal is converted from either a pressure wave in a fluid, or a stress wave in a solid, into an electrical signal. Piezoelectric transducers are most commonly employed for this, due to the transduction efficiency of a piezoelectric material. Piezoelectric transducers are used both to detect and generate ultrasound, providing a combination of low cost, high sensitivity, ease of handling, selective frequency responses and rugged design.

If a piezoelectric transducer is placed on the surface of a material, the displacements caused by a stress (sound) wave can be detected in the form of an output voltage developed across the piezoelectric material. It is this voltage response which is one of the topics considered in this thesis. The sensor's ability to provide a reproducible signal

from a given source is important and transducer design affects the nature of this reproduction.

At resonant frequencies (f_r) a receiving transducer will produce a peak in output voltage. At these frequencies the transducer is most sensitive as a receiver, (or most powerful as a transmitter) because the conversion from mechanical to electrical energy, or vice versa, is most efficient. This frequency is governed by the geometry of the piezoelectric material and any other materials used in the transducer design. These are the frequencies at which a transducer will be most sensitive as a detector, because a small amplitude displacement of frequency f_r will produce a much larger voltage than the same displacement at a non-f_r frequency.

Frequency response of piezoelectric transducers is an issue of major importance in AE studies and all other ultrasonic applications. This is because of the above mentioned importance of the voltage-time signal produced by a given input waveform. The shape of the waveform can give valuable information about the source of the ultrasound. It is therefore important to know how a signal will be affected by the transducer response. Alternatively, if a specific frequency is of interest, then it is preferable that the transducer be resonant at this frequency to maximise the signal-to-noise ratio.

Transducer frequency response has been investigated for various transducer designs, sizes and mounting conditions. Finite element analysis is the primary analytical tool used in this research to achieve advanced mathematical computer modelling. FE has been chosen because it provides an accurate method to model different designs and test their performance, without having to construct large numbers of transducers. Experimental work is also used to validate some of the computer models.

1.2 REVIEW OF PIEZOELECTRIC TRANSDUCER DESIGNS & THEIR USES

Different piezoelectric materials can be used to generate and receive over the entire frequency range but ultrasound transducers operate at frequencies above 20 kHz and

often in the MHz range. For pulse-echo applications, general ultrasonic transducer design aims include generating high power, short pulses, with transducers having high sensitivity over a specific frequency range. High power output is desirable to ensure that the transducer can send out an ultrasonic wave and receive back a detectable reflection. Short pulses are desirable when generating ultrasound, so that timing of reflections, used in distance measurement, is accurate. Sensitivity is important for detecting ultrasound, because the material displacements involved are usually small. For example, displacements on a solid might be 10^{-12} metres for an acoustic emission waveform caused by crack growth. Capacitive transducers, with a sensitivity to displacements of 10^{-10} m, are considered insufficient [**5**].

The piezoelectric material alone acts as a transducer and is often formed into discs or cylinders of various geometries. Thin rectangular strips or sectioned rings are two other common ways of using a piezoelectric material. In most cases, however, the piezoelectric material is only part of the transducer. Plastics, rubbers and metals are often employed to form a more efficient and practical device. The shape and design of the transducer are crucial to its performance and the materials are chosen to take advantage of the design.

Ultrasonic transducers are defined using terms such as narrowband, multimode, or broadband. Narrowband, or resonant, transducers have a characteristic resonant frequency. Resonant transducers are popular, giving good sensitivity and appear to be used not just at their resonance, but over a range of frequencies. This would indicate that they are considered to have a reasonable bandwidth for detection as well. This type of sensor will be referred to as resonant rather than narrowband, in the main.

When designing resonant ultrasonic transducers, it is advantageous to be able to have a resonant frequency at, or close to, the frequency that is to be detected/generated because the conversion from electrical to mechanical energy, or vice versa, will be most efficient. Many piezoelectric transducers use simple disc designs because their resonant frequencies can be determined by theoretical calculations [**6**].

Ultrasound has many applications in a number of important fields. Medical diagnosis, underwater SONAR and NDE are probably the three most important and heavily used areas for ultrasonic transducers, although the range of applications within these fields is always increasing.

For underwater uses, ring transducer designs are most common [7]. These are often arranged in arrays, which involve several rings stacked together. By changing the phase of the voltage applied to each ring, the transducer can send or receive ultrasound in different directions. Another design involves a column stack of piezoelectric discs in the centre of an elliptical shell [**8**], which gives good directivity patterns and high power, important in underwater work due to the large distances the sound waves have to travel (fig 1.4).

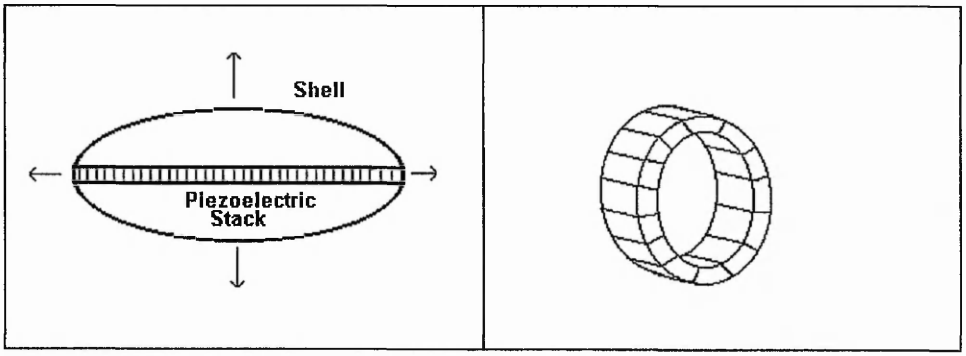

Fig. 1.4 Examples of elliptical and ring underwater transducer designs

Oil and rubber are used to couple the piezoelectric material to the water. Material such as foam is used to shield areas of the transducer from acoustic signals which may hinder the transducer performance.

Medical applications of ultrasound use similar technology. One design incorporates an array of concentric rings on the back of a composite disc [**9**]. This allows the transmitted pulse to be focused at various depths, therefore maintaining a clear focus for the signal, which is important for diagnosis. Body imaging is one such application. Treatment using ultrasound to heat tissues is commonly used to promote healing during physiotherapy. Frequencies involved are usually in the low MHz range.

An example of a simple disc design is an accelerometer, which measures vibratory acceleration. The design involves the piezoelectric disc being sandwiched by a base and a backing mass to adjust the resonant frequency, dampen the resonance effect and increase the bandwidth of the resonant frequency (fig 1.5). By using a cylindrical piezoelectric element, instead of a disc, an alternative accelerometer can be devised (fig 1.5).

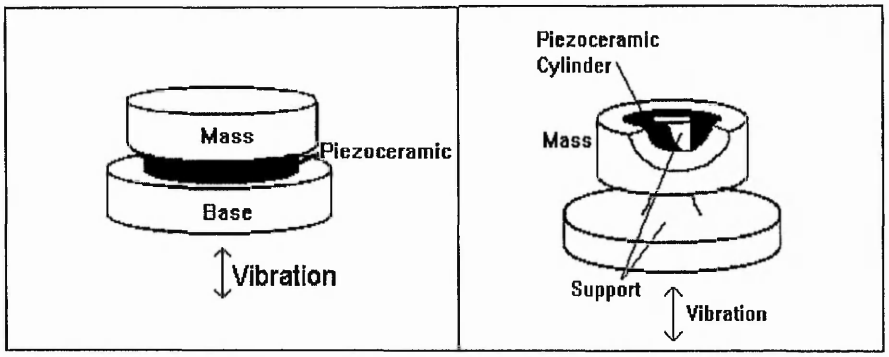

Fig. 1.5 Typical accelerometer designs for using normal compression (left) and shear stress (right) to excite the piezoelectric.

A simple airborne ultrasonic transducer design involves a piezoelectric disc laminated to an epoxy disc [**10**]. This type of design is aimed at non-contact distance measurement. By varying the epoxy disc thickness, the resonant frequencies can be altered.

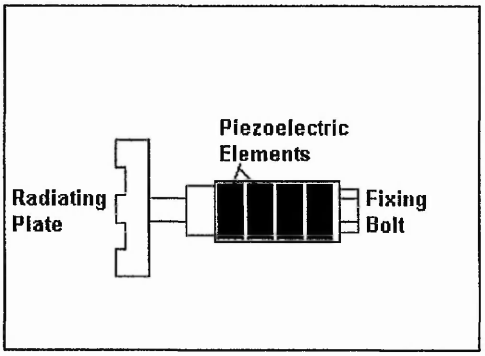

Fig. 1.6 High power transducer with stepped radiating plate.

High power applications use transducers with good impedance matching to the medium which they are driving and high amplitudes of vibration. Some designs incorporate a large radiating plate, usually with a shaped face, driven at the centre by a piezoelectrically activated vibrator [**8**]. The vibrator has a piezoelectric element in a

sandwich configuration and a solid horn to amplify the vibration. A stepped plate is often used as the driving plate (fig. 1.6).

A piezoelectric element, known as a bimorph, developed by Clevite Corporation, consists of two thin strips of piezoelectric which will bend or twist, depending on their axis of polarisation and mode of construction, when a voltage is applied [**11**]. This type of transducer is used in several designs, which include relays, microphones, linear actuators and electric bells (fig. 1.7). The mounting and driving conditions of such flexural elements greatly influence their performance. Ideally, the driving member would not interfere with the normal flexure of the element.

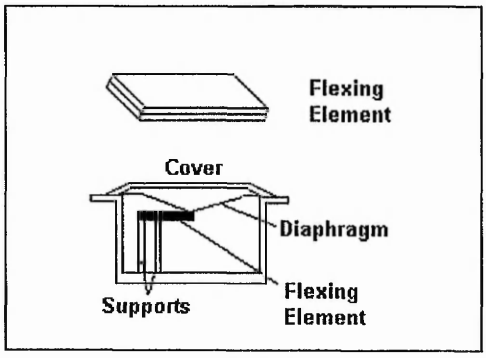

Fig. 1.7 Bimorph and application

However, mounting conditions and practical device application often influence the design. Varying the method of supporting the element is one way of controlling their response by introducing damping.

More recent advanced sensors have been developed using composite ceramic designs. Over the last decade, composite transducer designs have become of increasing interest, combining the positive aspects of two or more materials. Ceramic-polymer composites of 1-3 connectivity have been of particular interest. 1-3 means that the piezoelectric is only connected in one direction whereas the surrounding polymer is connected in all three directions. The piezoelectric is cut into rods (or pillars) and the gaps between rods are filled with a polymer (fig. 1.8). Investigation into their design has shown that they are very versatile and have higher sensitivity than pure ceramic transducers. The ceramic volume fraction can be adjusted to give either better receiving sensitivity (low volume

fraction), or better transmitting sensitivity (high volume fraction) [**12**]. Composite device performance is a complicated function of volume fraction, device geometry and electrical and mechanical loading. Optimum design is, therefore, application based. Finite element modelling is seen as the best tool for analysing such complex designs.

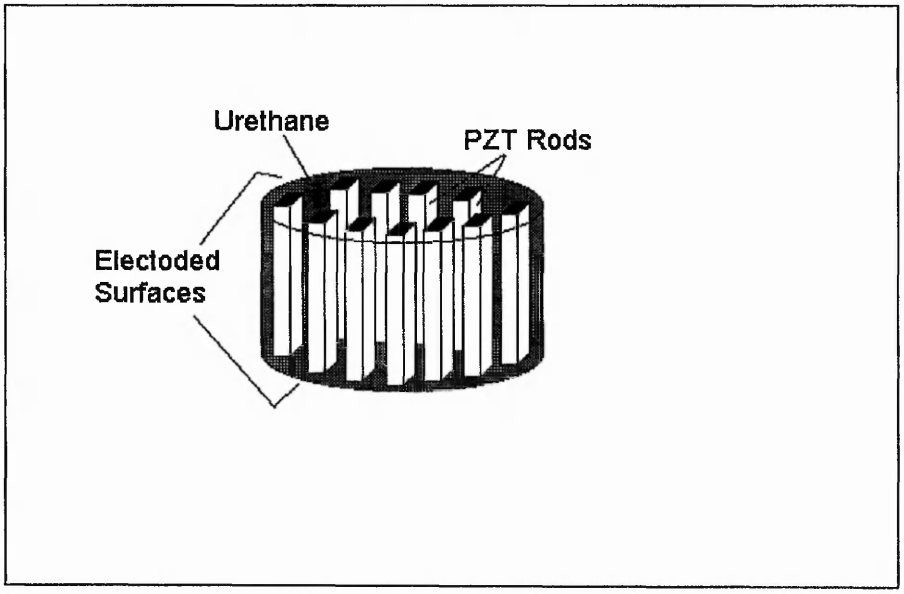

Fig. 1.8 Typical 1-3 composite transducer design

Further performance enhancements have been demonstrated by drilling holes into the polymer between the ceramic rods in a 1-3 composite [**13**]. This effectively creating a 1-3-1 connectivity, with the ceramic and air connected only in the thickness direction and the polymer connected in all three dimensions (fig. 1.9). This 1-3-1 design improves efficiency by lowering the Poisson's ratio, increasing sensitivity in both transmission and receiving modes by 10% to 30%.

For non-contact NDT applications (described in the next section), Hayward and Gachagan showed that air coupled transducers have benefited from use of the 1-3 connectivity [**12**]. Again, FEM has been shown to be very useful as a design tool and closely follows the performance trends seen in experimental work [**14**]. Variation of ceramic volume fraction is shown to change the performance. Backing layers have been modelled to show damping effects. These layers produce an increase in bandwidth, but with a decrease in sensitivity. Bandwidth is also said to improve if the first interpillar

mode is coupled to the main thickness mode of the transducer by tailoring the aspect ratio (width to height).

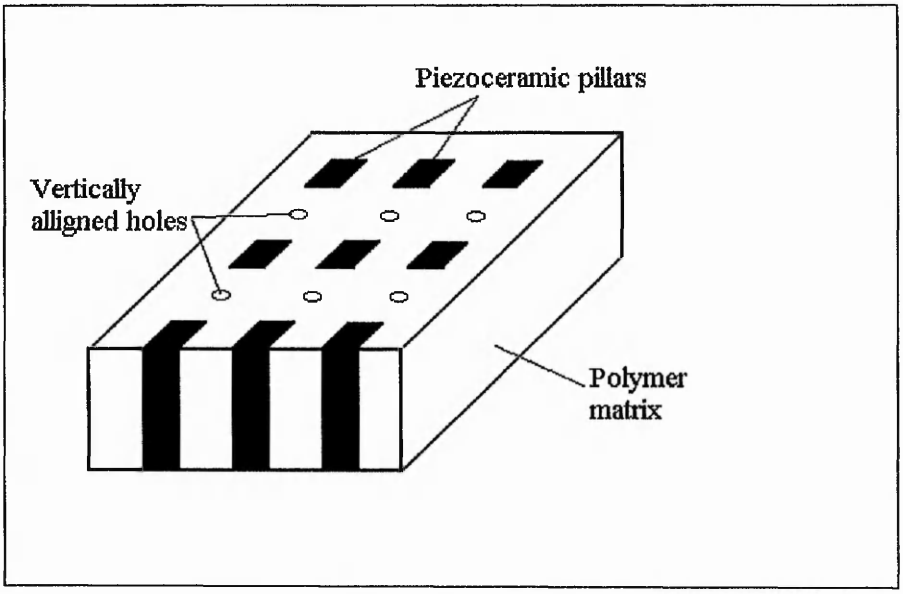

Fig. 1.9 A 1-3-1 composite transducer material.

Hayward [**15**] suggested 1-3 design improvements include shaped ceramic rods, loaded filling materials and improved manufacturing, allowing more complex designs. If the piezoceramic pillars (rods) are shaped from front to back, they can present an acoustic impedance gradient, giving a better match to air (transducer-air coupling has always been a major cause of inefficiency in air transducers). By using circular or triangular pillars, instead of square or rectangular based ones, the interpillar resonances can be reduced and a low impedance at the front face can be produced.

Shaping the piezoelectric element by using a taper has been used by Mitra et al. [**16**] to increase the understanding of transducer performance (fig. 1.10). Other workers had already shown that a linearly tapered piezoelectric disc could be used as a broadband transducer which didn't even need a backing layer. Small, unwanted tapers induced at manufacture, however, cause a variation in a transducer's performance which may be significant. Mitra et al. tested several taper gradients by measuring their normal displacement amplitudes near resonance and also, the acoustic output. The taper was shown to increase the spread of resonant peaks or cause a continuum in the vicinity of

resonance. Normal displacements increased at the thick end of the taper and were seen as a way of measuring tapers that had been added by accident.

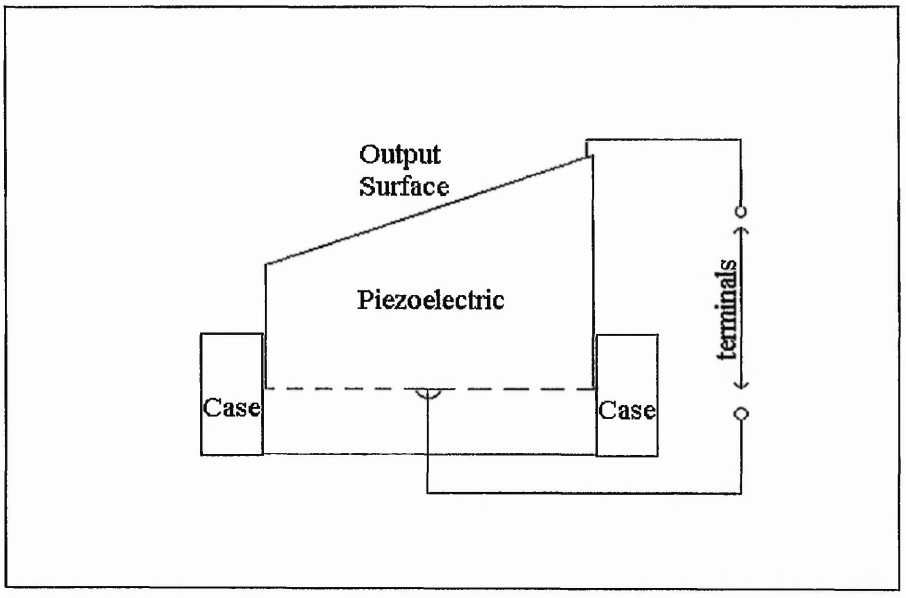

Fig. 1.10 Tapered piezoelectric used by Mitra et al. [**16**].

Alongside the work on ceramic-polymer composites, composites incorporating various other materials have been investigated. Metal-ceramic composite transducer designs, such as the 'Moonie', have been suggested by Dogan et al. [**17**]. This design investigation utilised FEM to model the effect of variations in dimensions and shape. The 'Moonie' design uses hollowed out metal end caps to lower the acoustic impedance of the ceramic to that of its surroundings.

Further improvements to the 'Moonie' design by the use of FEM have been presented very recently. The so called 'Cymbal' design, by Dogan et al. [**18**], has shaped metal end caps which give improved output displacements and forces and also, a more even behaviour across the transducer face. Both of these metal-ceramic composites have been suggested for use as actuators, accelerometers, hydrophones and air acoustic transducers. Advantages over polymer-ceramic composites include the ease of manufacture. The piezoelectric ceramic used in the metal composite transducers is a simple disc, all of the design advantages coming from shaping the metal. This can be

done using a simple press, whereas the 1-3 type composites have to be diced and filled, which is generally more complicated, costly and time consuming.

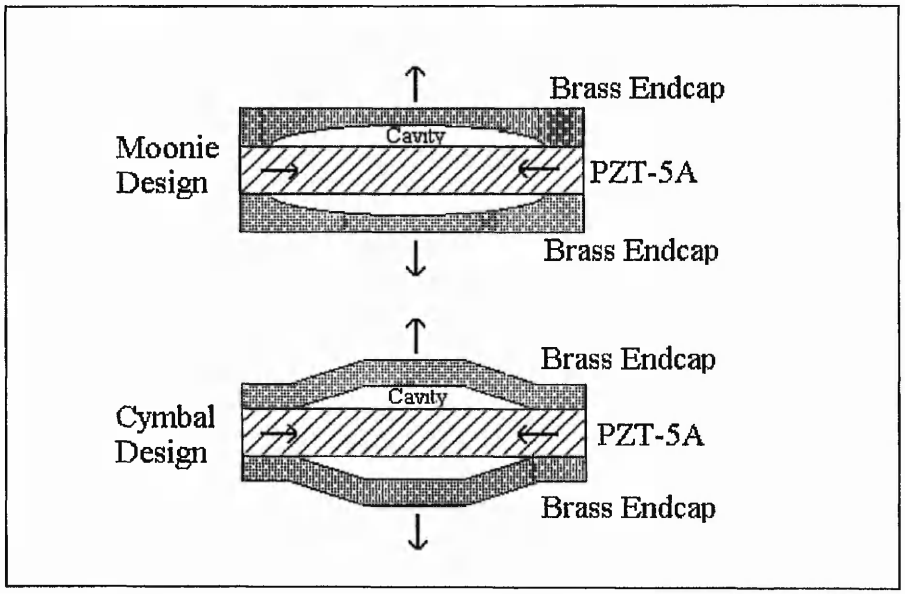

Fig. 1.11 The 'Moonie' and 'Cymbal' designs by Dogan et al. [**17,18**].

Other uses of metal-ceramic combinations occur in power ultrasonics, where ultrasound in used for machining and drilling. Horn designs are commonly used which provide a means of amplifying an input to produce a large displacement at the work end of the tool. Made of metals such as steel or brass, the horns are driven by piezoelectric elements at the resonant frequency of the horn. A detection transducer design based on these principles is considered in Chapter Three.

With rapidly increasing interest in more complicated composite transducer designs, especially for broadband applications, it is clear that finite element modelling is a useful tool for design.

1.3 DESIGN OF AE & PULSE-ECHO SENSORS USED IN NDE

A typical transducer would consist of a piezoelectric disc with an epoxy or ceramic on one face and a backing material, such as a tungsten-epoxy blend, on the other disc face [**19**]. The epoxy wear face protects the piezoelectric when in contact with the test

material. Backing materials are used to absorb the ultrasound and reduce reflections of incoming sound waves, which can affect the accuracy of the transducer when used in pulse-echo applications. Variations in the design of piezoelectric transducers allow measurement of parameters such as pressure, force and acceleration to be made, all of which will cause a displacement at the transducer face.

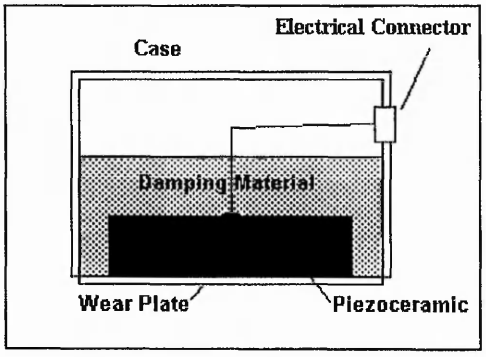

Fig. 1.12 A typical AE sensor taken from Stanley & Bray [**19**].

The basic AE disc design will be resonant in nature and the backing material is often used to suppress these resonances for a wider frequency response. Due to the complex nature of acoustic emission waveforms, a high fidelity broadband device is considered desirable for replicating the waveform for later analysis. The small displacements generally involved in AE work have meant that resonant devices are commonly employed for maximum sensitivity. This distorts the waveforms, but valuable data can still be gained to provide information about the material under test. Some general ultrasonic transducer designs could be employed for AE work but often these designs do not provide sufficient sensitivity, because they are intended for the generation or receiving of large wave particle displacements and are, therefore, less effective for AE work.

Broadband devices will be described in more detail because, generally, the resonant devices are very similar and simple in design. As mentioned in section 1.4, new 1-3 type and metal ceramic composite designs are showing that improvements in design can be achieved for resonant transducers.

Piezoelectric element thickness and diameter are the two characteristic dimensions of a typical circular acoustic emission transducer. Half wavelengths of thickness give primary

control over the resonant frequency sensitivity, with Poisson coupling leading to radial resonance at other frequencies. Damping with a backing mass will, of course, change the resonant frequency and broaden the bandwidth. If the diameter is large compared with the detected wavelength then, for AE detection, the sensor can average out the input for non-normal incidence. For the case where one or more wavelengths are detected, the average of the positive and negative components will tend to zero. This so called aperture effect has been investigated and it is recommended that as small a diameter as possible should be used to avoid this effect. Three millimetres is suitable for steel below 500 kHz [**5**], whilst one millimetre is deemed the ideal diameter in a review of advanced AE sensors by Lemon [**20**]. The aperture effect is most marked when trying to detect surface displacement components of acoustic emission. Most longitudinal waves travelling normal to the material surface will be largely unaffected, allowing sensitive detection.

Broadband (or wideband) is a term used to describe transducers that give a flat, high fidelity response over a wide frequency range, generally from 50 kHz to 1 MHz. Sensitivity is normally lower than for narrowband devices, but some high technology sensors claim to achieve good AE sensitivity with the use of built in electronics [**21**].

Broadband sensors are used in cases where good AE waveform definition is required, typically for source location accuracy and source characterisation. Traditionally, a broadband device was achieved by adding a large backing mass to a simple piezoelectric disc. This had the effect of suppressing the resonance, which caused a flat response over a wider frequency range. The mass of the backing mass will also determine to what degree the resonant frequency shifts from the non-backed piezoelectric disc. A backing mass may attenuate the wave energy by scattering and absorption if made of the correct material, e.g. tungsten loaded epoxy. Proportionally, the backing mass is often much larger in dimension than the piezoelectric element to reduce wave reflections back into the element, which will distort the input signal.

In the early eighties a novel broadband, high fidelity AE sensor was devised by Proctor, at the National Bureau of Standards (NBS) in the USA (now NIST, National Institute

for Standards and Technology). Sensitive to normal surface displacements, Proctor used a conical piezoelectric element asymmetrically attached to a backing material, at the cone's wide end [**22**]. The backing material was made of two materials, brass and tin (fig. 1.13). The diameter of the detecting face was only 1 mm to reduce the aperture effect. The piezoelectric element for this type of design may, however, become susceptible to damage. For more practical applications, this design was modified by Koberna [**23**] who mounted a larger conical element to a brass backing mass in a case, which could be attached to the object to be tested. A bronze foil was used as a wear plate and ground electrode and the transducer was spring-loaded. By changing the polarising direction of the conical element, a broadband sensor that could detect purely tangential displacements was achieved [**24**].

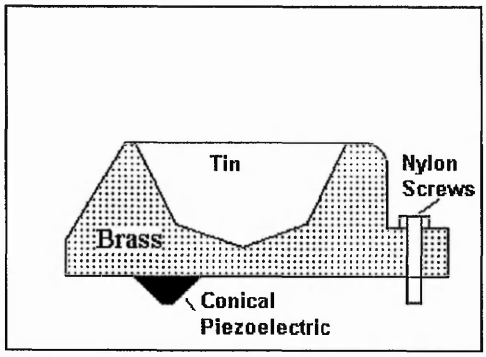

Fig. 1.13 Proctor wideband transducer using a conical piezoelectric element [**24**].

Work to compare the sensitivities of different types of NDE broadband transducer concluded that optical interferometers, air-coupled capacitive and electromagnetic acoustic transducer (EMAT) types, cannot meet the sensitivity requirements for broadband AE studies in metals [**21**]. Piezoelectric designs are much more suitable. Further refinement of the conical design, mentioned above, has produced a suitably sensitive broadband design for the 50 kHz-1.2 MHz frequency range. The new design is more sensitive and more suited to field applications due to more rugged design, optimised geometry and shielded electronics. It is deemed adequate for broadband AE detection in materials such as aluminium, steel and ceramics, which have a high modulus.

Alternative work by Ohara et al. [**25**] has suggested a new 1-3 composite transducer design for broadband use, giving increased sensitivity. This uses different length

piezoelectric rods (fig. 1.14) within a urethane rubber matrix, thus obtaining a range of resonances close together. Use of smaller aspect ratio pillars gave lower sensitivity, although overall, the transducer showed an increase in sensitivity over typical broadband devices, as well as providing increased bandwidth. It is designs such as this which may, eventually, replace the conical design that currently sets the standard for broadband piezoelectric detection devices.

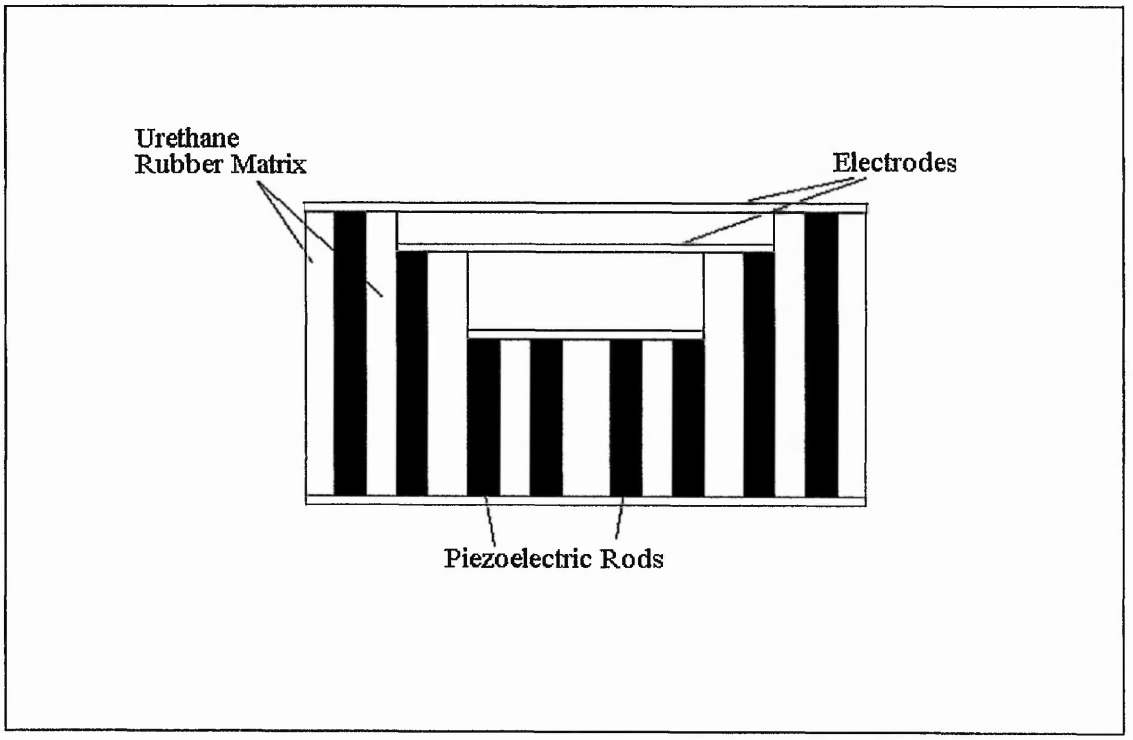

Fig. 1.14 1-3 broadband device by Ohara et al. [**25**].

Preferences for broadband designs have been expressed by Gorman due to their advantages in practical application [**26**]. Difficulties comparing laboratory work on small specimens to work on large, real life structures have encouraged the use of modal AE analysis. This modal AE approach is essentially based on recognising various information features of waveforms, such as Lamb wave modes and using them to infer something about the source. Broadband sensors coupled with appropriate preamplifiers were suggested to minimise frequency distortion. Their ability to reproduce transient waveforms is well established. Resonant transducers will change the appearance of a detected waveform, because the different frequency components of the signal will be

reproduced with different amplitude, i.e. frequency components equal to the resonant frequency will be much larger than non-resonant components.

Recent experimental studies by Surgeon and Wevers [**27**] and by Hamstad et al. [**28**] have also commented on the advantages of modal analysis and the use of broadband sensors respectively.

1.4 NDE APPLICATIONS OF ULTRASONIC TRANSDUCERS

Evaluating the quality of materials, commonly used in engineering, is the main area of application for the transducers discussed in this thesis. This field of study is commonly known as nondestructive testing (NDT) or non-destructive evaluation (NDE). As an example, when materials are loaded with a stress, the material may suffer damage at the microscopic level. This damage is often undetectable by any kind of visual inspection. Ultrasound is employed to listen to the noise made by this propagating damage. This noise is called acoustic emission (AE).

When reviewing the literature on the subject of acoustic emission it is obvious that the technique is becoming increasingly useful. The list of practical applications of AE is extensive, including such diverse areas as evaluation of damage in materials, pressure vessel monitoring, monitoring of bridges and tunnels, dams, mining outburst prediction, machining, thermal loading and slip plane monitoring in soils. Theoretical modelling techniques are struggling to keep up with the practical uses, but advances are helping to understand material behaviour.

NDE uses many different transducer designs to 'listen' to materials and check for flaws such as cracks in metals, poor quality welds and delaminations in composite laminates. Structures may be examined after manufacture as a quality check and NDE methods can also be used as an ongoing test method. Detection of acoustic emission, caused by growth of material defects, has led to a huge range of applications.

To make ultrasonic NDE a viable method of scanning a material after manufacture, it has to be done rapidly so as not to delay the production process. Careful manufacture should avoid problems, but with, for instance, composite laminates being used increasingly in areas where safety is paramount, quality and reliability have to be guaranteed. Traditional C-scan ultrasound techniques are relatively time consuming and expensive. Thermography, shearography and scanning laser ultrasonics are suggested alternatives by Cawley [**29**].

Thermography uses thermal imaging to monitor the heat pulse sent through a material when a surface is rapidly heated. Flaws in the material are highlighted by a change in the thermal impedance causing 'hotspots'. Laser and shearography are optical techniques. Laser techniques are good because they can be used on complex geometry, but are very expensive and have low signal levels. Shearography involves the comparison of speckle patterns produced by the material when loaded and unloaded. New ESPI (Electronic speckle pattern interferometry) has also been proposed as a rapid inspection technique.

Lamb wave modes combined with acousto-ultrasonic methods, in particular detecting the s_0 and a_0 modes, provide an effective method for inspecting a large area plate-like structure for defects. Improvements to the piezoelectric transducers are necessary for suitable field applications. When using pulse-echo ultrasound to generate Lamb waves the transducer has to be angled to the test piece to generate the desired Lamb mode, both transducers being held at the desired angle.

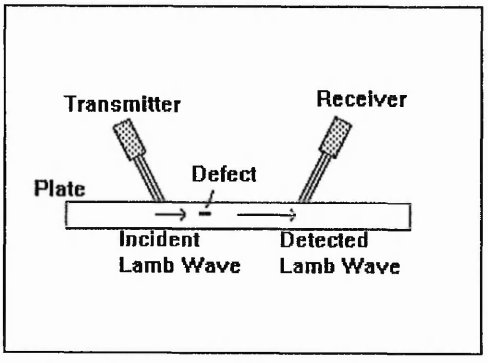

Fig. 1.15 An air coupled Lamb wave inspection arrangement [**30**].

Non-contact methods of NDE are desirable for rapid inspection. However, the naturally poor acoustic coupling between air and solids has been the deterrent. Normal incidence pulse-echo techniques are therefore ruled out, but the possibility of using Lamb waves exists. Using the Snell-Descartes law, the angle of incidence for the transducer can be chosen which will generate the s_0 mode.

Developments in the 1-3 composite type transducer have led to improved air coupling [**12**]. These devices are described as narrowband and are, therefore, resonant sensors. The advantage of a resonant device for non-contact work is that they give a long duration pulse and the short bandwidth will only excite the desired Lamb wave mode. Improved signal-to-noise ratio is also an advantage of the 1-3 type design.

Advantages of non-contact inspection include increased convenience for inspection, an ability to inspect complicated shaped components and higher speed for inspecting large objects (bridges, aircraft, marine vessels). Transmitting and receiving transducers were used which had to be angled to the normal (fig. 1.15), so as to generate the desired mode of Lamb wave (typically the a_0 or s_0 modes). The work by Cawley [**30**] shows successful use of the 1-3 design, although the angles required to generate the Lamb waves have to be chosen and set up accurately to avoid a large loss in wave amplitude ($\pm 0.6^{\circ}$ orientation can reduce amplitude in a_0 and s_0 modes by 50%).

In practice, this angular sensitivity could cause problems. The fact that this is a long range technique for single sided inspection means that sensors will only have to be arranged a few times to scan a large structure. The best configuration was one in which the receiver detects waves, which are reflected back towards the transmitter by defects.

Recent interest has seen the use of a single transducer to detect and locate an acoustic emission source [**31**]. This is done by the detection of Lamb wave modes which, due to their dispersive nature, make it possible to locate the source based on the arrival of different frequency components. Again, the purpose of using these type of waves is the fact that they can be used for inspection of large areas with a single transducer. Normally it takes several transducers to locate an AE source. A resonant transducer was

suggested by Maji et al. [**31**] to be advantageous over a broadband device. The source is located by comparing the arrival times of the different frequency components of a waveform. The frequencies chosen are preferably the resonances of the sensor. This method is used with the transducer in contact with the test structure and has been used successfully on bridges and could be applied to other large structures, such as storage tanks and aircraft body structures.

The components of the waveform are used to identify the wave mode and therefore, provide information about the source from dispersion information. Wave dispersion occurs due to different modes having different group velocities. The wave mode pattern changes shape as the wave propagates in a structure and so the wave shape is a function of position and time. Using this information, source location can be achieved.

Smart materials provide the capability for in-situ NDE and are capable of detecting defects occurring during material use. Having small piezoelectric discs embedded into a composite plate, for instance, is one way of producing a smart material. These discs are capable of generating Lamb wave modes, including the s_0 mode commonly used in flaw detection [**32**]. FEM was used to model embedded piezoelectrics, with the piezoelectric resonance modes and their appropriate Lamb modes identified. Selective choice of piezoelectric mode will produce the desired Lamb mode. It was found that the disc's radial mode coupled best to provide efficient s_0 Lamb waves, which are arguably the best for large scale flaw detection.

More recently, transient FE analysis has been used to model the wave propagation in plates. Moser et al. [**33, 34**] have shown the method to be accurate and have established suitable criteria for spatial and temporal sampling. Hamstad et al. [**35, 36**] have also used and developed the FE method to model acoustic emission events and investigate problems associated with acoustic boundaries, such as reflections. Transient analysis is clearly an area of increasing interest and is studied in Chapter Four.

Looking at the literature on the many applications of ultrasonic transducers for acoustic emission work, the use of resonant devices is still seen to be advantageous in many

applications. Therefore, investigation of advanced resonant and multimode devices will be considered in this study. Effective broadband devices are now available and ways to improve sensitivity are not obvious. FEM would, however, provide the most effective way of achieving any improvements.

Although many signal processing and waveform analysis methods have been developed, it seems that many users still use off-the-shelf transducers. Sensitivity is still a major priority to ensure detection.

From the review of literature, a number of priorities are clear, when considering ultrasound transducers. These apply particularly to AE sensors, which are of most interest in this thesis.

1. Sensitivity is paramount in most systems.
2. Sensitivity over a range of ultrasonic frequencies is desirable.
3. For systems where waveform characterisation is important, a flat response is preferred.
4. Resonant devices were preferred for some source location and Lamb wave applications.
5. Transient analysis is an area in which understanding of acoustic emission and wave propagation can be developed.

Resonant devices are effective for satisfying the first two criteria and could probably conform to the third requirement using suitable electronics. The use of FEM to design transducers for specific applications appears to be a tool with increasing potential.

1.5 COMPUTATIONAL METHODS & COMPUTER MODELLING USING FINITE ELEMENT METHODS

Since their advent, electronic computers have been employed to solve mathematical equations, which are too tedious or impossible to solve by manual numerical methods. As the computers became more powerful, they became more useful as engineering tools and software has been developed to take advantage of this. Modern computers and

software can be used to model the behaviour of complex systems in many areas of engineering and physics, modelling responses in terms of stress, strain, heat flow, fluid flow and modelling magnetic and acoustic fields. With computer and software developments, faster methods of solving the mathematical equations have been devised. This means that computational methods are becoming increasingly popular in all types of applications.

One such computational method is the finite element method. The theory on which the method is based was developed by mathematicians, including Ritz and Galerkin, at the start of the twentieth century. Modern finite element (FE) theory can be traced back to the early 1940s, but it was in the next decade (with the advent of the computer) that engineers first applied finite elements to structural problems. Since then, rigorous mathematical analysis has led to finite elements being applied to a diverse range of engineering applications.

Currently, FE modelling (FEM) is a widely used tool in the design stage of many engineering projects. It can also be used to evaluate performance and monitor effects of environmental changes on components after they have entered service, which might be a change of operating temperature, or an increase in loading. In this thesis, FEM is used to evaluate performance of current transducer designs, to model the effects of changes to these designs and, to predict transducer response as a receiver, particularly to acoustic emission sources.

Closed form solutions to mathematical problems were the only method for predicting real life situations prior to finite element modelling. The trouble with the closed form solutions is that they are limited to simple problems involving simple geometry, material properties and boundary conditions. Piezoelectricity is an area where the complexity of the equations does not lead to closed form solutions, except in the simplest cases.

If a structure to be modelled is treated as the sum of lots of very small elements then the geometry of each element can be simple, even for geometrically complicated structures. The shapes of the elements are simple beams for one dimensional problems.

Quadrilateral or triangular elements are used for two dimensional problems and brick (cubic) or prism elements for three dimensional problems. The four sided elements are more accurate generally, but the triangular shaped elements are useful for describing complex geometry (fig. 1.16).

Elements are non-overlapping and have nodes at each corner. Some elements have additional nodes along each side, to provide more accuracy. The nodes are close together due to the small size of the elements with respect to the overall structure. This means that the change of any parameter (such as displacement) between each node will be small and accurately predicted by a linear or quadratic interpolation function. The solutions for each element are then patched together to give the overall solution for the whole structure. Equations are put into matrix form, because these can be handled in arrays within a computer programming language, such as FORTRAN, the language used for the PAFEC-FE software.

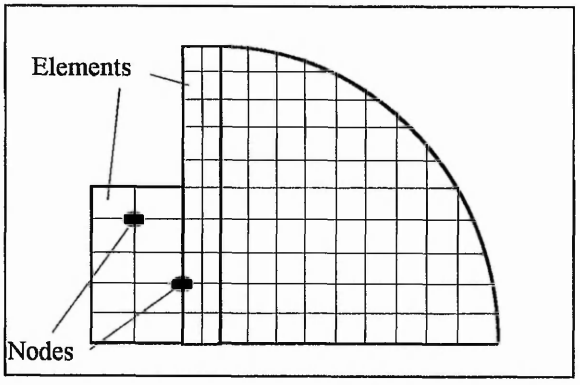

Fig. 1.16 An FE mesh used for an acoustic analysis of a simple axisymmetric transducer. The piezoelectric material is on the left, the acoustic medium is on the right.

The data input to achieve an accurate model depends on the problem, but would include parameters such as dimensional and geometrical details, material properties and boundary conditions such as applied forces. The software takes this data and uses it to solve the partial differential equations which are appropriate for describing the system behaviour. These equations cannot be solved directly by a computer unless they are replaced by a set of algebraic equations.

There are several methods of solving the partial differential equations including finite element, finite difference and finite volume. The methods are based on sub-dividing the desired domain into small enough areas, or volumes, so that the variation of any parameter is simple within each division. For the finite element (FE) method this is achieved by defining the domain geometry with nodes (points).

An interpolation function is used to approximate the change of the dependant variables within the element based on the value of the variable at the adjacent nodes. The function is defined relative to the values of the dependant variable at the associated nodes and is usually linear or quadratic in form, providing a simple variation within each element.

This spatial information is combined with the other data given by the user. An equivalent integral statement is used to replace the original partial differential equations. The interpolation functions are then substituted into the integral statement, integrated and then combined with the results from all of the other elements. This yields the algebraic equations to be solved for the dependant variable at each node; i.e. the variable which is changing due to an applied force or other boundary condition.

The computers use iterative techniques, such as the Newton-Raphson method, to solve the algebraic equations, which are in matrix form. Complex problems require huge numbers of equations to be solved, which takes a large amount of computer processing time.

The finite element method has several advantages over other techniques:

- Arbitrary mesh grading allows detailed analysis of important areas and a more coarse grid representation in less important ones. Other finite methods have to employ various mathematical tricks to achieve this.
- Boundary conditions are easily represented. Special boundary elements are employed in the PAFEC-FE software used to increase accuracy.
- The standard FE formulation can handle inhomogeneous problems i.e. composite materials such as laminates. (In a homogeneous medium the physical properties are constant from point to point).

For the purpose of piezoelectric transducer modelling, PAFEC-FE Vibroacoustics software was selected due to its specialist acoustic features [**37**]. The software uses standard methods of FE modelling as well as utilising specialist elements for dealing with piezoelectrics, fluid-structure interaction and boundary elements (BE), for modelling infinite acoustic fluid media [**38**].

FEM is superior to other methods for working with piezoelectrics because it can cope with any geometry. The one-dimensional methods of mathematical solution, used originally, are only relevant for certain geometries and cannot predict the more complex modes of vibration observed with FEM [**1**]. This led to the development of three-dimensional and axisymmetric FE methods [**38-42**].

Piezoelectric materials have both electrical and mechanical properties and, therefore, it is necessary to solve the elastic and electrostatic equations simultaneously. A full understanding of the methods is not required to use the software. A short overview of some of the equations and methods employed follows.

Several methods of formulating finite element equations can be used and their choice depends on several factors including the type and size of problem being solved and what computer hardware is being employed. Generally, all of the techniques involve describing the system behaviour with a mathematical equation. This must be put into a form that describes the behaviour in each element in relation to nodal values before each element's contribution is patched together.

Most of the techniques begin by assuming the variation of the unknown variable (displacement for vibration problems) to be solved can be described by a linear or quadratic function. This *interpolation* function is not of a higher order because, otherwise, spurious oscillations can occur. Instead, accuracy is achieved by having many small elements. Next the interpolation function is substituted into the equation describing the system behaviour, such as $M\frac{\partial^2 u}{\partial t^2} + Su = F$ etc., to give a residual error. An integral statement is then produced involving the integral of this residual error and

some other function, such as a weighting function. This integral is set equal to zero to solve for the exact solution of the original equation. In the popular Galerkin method, the weighting function is taken to be the interpolation functions. Other methods of weighting include collocation points and subdomain methods. Whichever method is chosen, the results should ultimately be the same.

Finite elements achieve good overall accuracy because they consider the integral of the error produced by the initial trial solution and then minimise this error until the desired solution accuracy is achieved. This is generally more accurate than considering point by point agreement.

Due to the complexity of modelling piezoelectric and acoustic problems, PAFEC-FE software incorporates several advanced mathematical techniques **[37, 38, 43 & 44]**. The main interest is in the piezoelectric effect and so the method relating to that will be considered in most detail. The finite element method for piezoelectric vibration is based on variational principles which became popular after their development by Euler in the eighteenth century. This approach involves setting an integral equation equal to a stationary value, usually the minimum and is a generalisation of the calculus of minima and maxima. Usually, the integrand is a function of the nodal co-ordinates, field amplitudes and their derivatives.

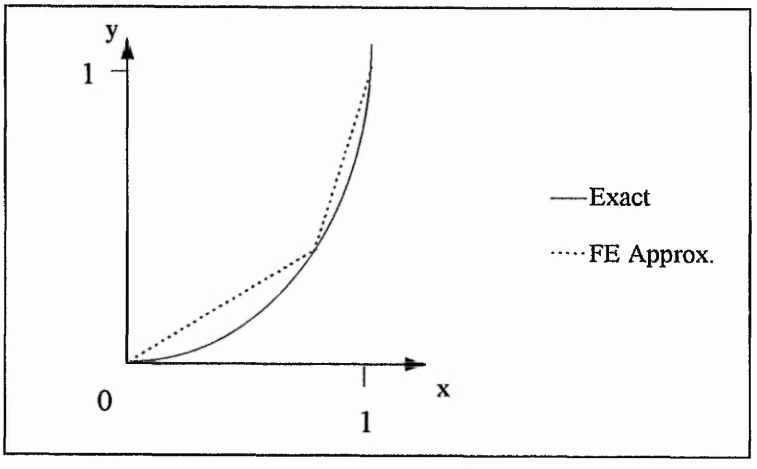

Fig. 1.17 Comparison of a two element linear approximation with an exact solution.

Piezoelectric vibration involves mechanical and electrical behaviour which is described by two fundamental equations shown below in equation 2. The variational principle is based on the principle of minimum potential energy from elasticity, with the addition of electrical quantities. Displacements and potentials are found which give the minimum total potential energy within the system.

The general finite element method for piezoelectricity was developed by Allik et al. [**41**] and begins with the equation for virtual work density

$$W = \{u\}^T \{F\} - \phi q \tag{1}$$

where u is the displacement, F is the force, ϕ is the potential and q the charge density. The fundamental piezoelectric equations are:

$$\begin{aligned} \sigma &= S\varepsilon - eE \\ D &= e^T \varepsilon + \xi E \end{aligned} \tag{2}$$

where σ is the stress, S the elastic stiffness tensor, ε is the strain, e is the piezoelectric tensor, E is the electric field, D the flux density and ξ the dielectric 'stiffness' tensor. The finite element equations can then be derived after applying the principle of virtual work.

As mentioned before, an integral statement is used to describe the system behaviour. Over the piezoelectric volume V, the integral statement is as follows;

$$\begin{aligned} \iiint_V \Big(&\{\delta\varepsilon\}^T [S]\{\varepsilon\} - \{\delta\varepsilon\}^T [e]\{E\} - \{\delta E\}^T [e]^T \{\varepsilon\} - \{\delta E\}^T [\xi]\{E\} - \{\delta u\}^T \{\overline{F}\} \\ &+ \rho \{\delta u\}^T \{\ddot{u}\} + \delta\phi\overline{q}\Big) dV - \iint_{S_1} \{\delta u\}^T \{\overline{T}\} ds + \iint_{S_2} \delta\phi\overline{q'} ds - \{\delta u\}\{P\} + \delta\phi Q = 0 \end{aligned} \tag{3}$$

where the symbols have their meanings as mentioned earlier. In addition, $\{\overline{F}\}$ is the body force, $\{\overline{T}\}$ is the surface traction, $\{P\}$ is the point force, $\overline{q}$ is the body charge, $\overline{q'}$ is

the surface charge and **Q** the point charge. V denotes the volume of the body, S_1 the boundary where traction is prescribed and S_2 is the boundary where charge is prescribed. The piezoelectric material density is ρ.

This integral statement represents a continuous system and must be modified to express the terms with respect to i nodal values via interpolation functions f_u and f_ϕ for displacement and potential respectively, i.e.

$$\begin{aligned} \{u\} &= [f_u]\{u_i\} \\ \phi &= [f_\phi]\{\phi_i\} \end{aligned} \tag{4}$$

Their derivatives provide the equations for strain and electric field thus

$$\begin{aligned} \{\varepsilon\} &= [B_u]\{u_i\} \\ \{E\} &= -[B_\phi]\{\phi_i\} \end{aligned} \tag{5}$$

Other terms are also expressed with relation to nodal values

$$\begin{aligned} \{\overline{F}\} &= [f_{\overline{F}}]\{\overline{F_i}\} \\ \{\overline{T}\} &= [f_{\overline{T}}]\{\overline{T_i}\} \\ \overline{q} &= [f_q]\{\overline{q_i}\} \\ \overline{q'} &= [f_{\overline{q'}}]\{\overline{q_i'}\} \end{aligned} \tag{6}$$

Substitution of these equations into the original integral statement leads to the force and charge expressions. In matrix form these are as follows;

$$[M_{uu}]\{\ddot{u}\} + [S_{uu}]\{u\} + [S_{u\phi}]\{\phi\} = \{F\} \tag{7}$$

$$[S_{\phi u}]\{u\} + [S_{\phi\phi}]\{\phi\} = -Q \tag{8}$$

Which can be combined to give

$$\begin{bmatrix} [M_{uu}] & [0] \\ [0] & [0] \end{bmatrix} \begin{Bmatrix} \{\ddot{u}\} \\ \{\ddot{\phi}\} \end{Bmatrix} + \begin{bmatrix} [S_{uu}] & [S_{u\phi}] \\ [S_{\phi u}] & [S_{\phi\phi}] \end{bmatrix} \begin{Bmatrix} \{u\} \\ \{\phi\} \end{Bmatrix} = \begin{Bmatrix} \{F\} \\ -\{Q\} \end{Bmatrix} \tag{9}$$

{U} is a vector of displacements and {ϕ} is a vector of electric potentials. A table of analogues between mechanical and electrical quantities is shown in table 1.1.

An electrode on the piezoelectric material can be modelled by giving all of the points on the equipotential surface repeated freedoms by collapsing the rows and columns in the stiffness and mass matrices and the force vector. For an earthed electrode, the electric potential freedom is set to zero, removing the appropriate row and column in the stiffness ([S]) and mass ([M]) matrices and the force vector ({F}).

MECHANICAL	ELECTRICAL
Force F	Charge Q
Displacement u	Electric potential ϕ
Stress σ	Flux density D
Strain ε	Electric Field E

Table 1.1 Mechanical and Electrical Analogues.

Using static condensation, the electric freedoms can be eliminated by being replaced by an equivalent term. Considering the components of the matrix in (9), it follows that;

$$[M_{uu}]\{\ddot{u}\} + [S_{uu}]\{u\} + [S_{u\phi}]\{\phi\} = \{F\} \tag{7}$$

$$[S_{\phi u}]\{u\} + [S_{\phi\phi}]\{\phi\} = -Q \tag{8}$$

Rearranging 8 gives the potential as;

$$\phi = \left[S_{\phi\phi}\right]^{-1}\left(-Q - \left[S_{\phi u}\right]\{u\}\right) \tag{10}$$

substituting into 7 gives;

$$\left[M_{uu}\right]\{\ddot{u}\} + \left[S_{uu}\right]\{u\} + \left[S_{u\phi}\right]\left[S_{\phi\phi}\right]^{-1}\left(-Q - \left[S_{\phi u}\right]\{u\}\right) = \{F\} \tag{11}$$

$$\left[M_{uu}\right]\{\ddot{u}\} + \left(\left[S_{uu}\right] - \left[S_{u\phi}\right]\left[S_{\phi\phi}\right]^{-1}\left[S_{\phi u}\right]\right)\{u\} = \{F\} + \left[S_{u\phi}\right]\left[S_{\phi\phi}\right]^{-1}\{Q\} \tag{12}$$

The following equation is left;

$$\left[M^*\right]\{\ddot{u}\} + \left[S^*\right]\{u\} = \{F^*\} \tag{13}$$

where;

$$\begin{aligned} \left[M^*\right] &= \left[M_{uu}\right] \\ \left[S^*\right] &= \left[S_{uu}\right] - \left[S_{u\phi}\right]\left[S_{\phi\phi}\right]^{-1}\left[S_{\phi u}\right] \\ \left[F^*\right] &= [F] + \left[S_{u\phi}\right]\left[S_{\phi\phi}\right]^{-1}\{Q\} \end{aligned} \tag{14}$$

Some electrical restraint must be applied to ensure that $[S_{\phi\phi}]$ is not singular in order to perform the above operation. If $[S_{\phi\phi}]$ is singular that means its determinant is zero and therefore, its inverse cannot be found and the equations cannot be solved correctly. This problem is avoided by earthing nodes on an electrode surface. For harmonic vibrations at frequency ω the equation becomes

$$\left(\left[S^*\right] - \omega^2\left[M^*\right]\right)\{u\} = \{F^*\} \tag{15}$$

where F^* is set to zero in order to solve the eigenvalue problem for natural frequencies and mode shapes. The frequencies to be analysed are specified and the finite element software then solves the equation to give the nodal displacements. These values are exact and are approximate at other points within the elements.

The method developed by Allik et al. is the method on which the PAFEC-FE software is based [7] and is similar to methods seen in other work on the subject [**39**].

More complex equations can be used to incorporate damping within a system and other boundary conditions. Additional damping terms would involve a damping factor and the first derivative of displacement i.e. the velocity.

1.5.1 Advantages of Computer Modelling

Modelling using FE methods is more accurate than using theoretical methods with inappropriate approximations and boundary conditions and has advantages in that a product design can be tested before a prototype is built. This is especially useful if expensive materials and high quality manufacturing techniques are being used.

Acoustic emission and ultrasonic transducers are inherently complex in their vibrational behaviour and therefore, computer modelling will help to give a better understanding of performance, indicating what effects any changes in size, design, or materials, will have on performance.

1.5.2 Types of Analysis Used

The main method of finite element analysis used to model the transducers, in this work, involves the use of specialist acoustic finite and boundary elements employed by the PAFEC-FE Vibroacoustics software. Transducers were modelled with piezoelectric and solid elements. A finite fluid region was then created at the transducer face, attached to which were boundary elements that simulate an infinite acoustic fluid region. From a point within this fluid medium, on the central axis, normal to the transducer face, a harmonic acoustic source emits a continuous pressure wave at a specified frequency. The software then calculates the response of the transducer due to this excitation.

Two other types of harmonic analysis were employed: forced sinusoidal and enforced harmonic motion. The first method involves forcing specified degrees of freedom on

nodes. These were either nodes on the transducer face or electrodes on the piezoelectric. The degrees of freedom excited were either the displacement in the x direction i.e. normal to the transducer face, or the electrical output on the piezoelectric electrode.

The second harmonic method, enforced harmonic analysis, involved moving specified nodes with a harmonically varying displacement.

Transient analysis was also employed for later work (Chapter Four), which involved the input of a time history of displacements at different nodes on the transducer face, or simulating acoustic emission events by means of a step force input, or step displacement input to specified nodes. The software manufacturers had to modify the software used in this work to deal with this more complicated type of analysis.

1.5.3 Constructing an FE Model

Generally, a finite element analysis using PAFEC-FE software consists of a few key stages. The first stage involves defining the transducer geometry by one of two methods. Either the co-ordinates of the nodes can be typed in manually [**45**], or the PAFEC Interactive Graphics System (PIGS) [**46**] could be used. This is an interactive graphics screen which can be used to construct finite element models. This can also be used to display results and other post processing functions.

Once the co-ordinates of the nodes are defined, the nodes are joined together to form elements. Again, the element topology can be defined manually or in PIGS. Large elements could be used initially, which could be subdivided into smaller elements later. Following this, a PAFEC data file called (NAME).DAT was created and further data was added to the nodal co-ordinates and element topology. The data included material properties, nodal restraints and repeated freedoms.

Finally, the type of analysis had to be specified. Data such as the frequencies of interest were input. Additional modules may be added to specify any output of results required [**45**].

When performing an FE analysis, the aim is to keep the number of nodes and elements to a minimum whilst achieving the desired accuracy of result. This is because the time of the analysis rises dramatically with the number of degrees of freedom, i.e. the number of variables at each node. For example, a typical piezoelectric element has four degrees of freedom per node. These are displacement in the x, y and z directions and the voltage. The "cpu" time is the time it takes the computer's processor to perform a given task. It is approximately proportional to the product of the number of degrees of freedom and the front size squared. The front size is the number of degrees of freedom being solved at any one time and is dependent on the number of nodes and the geometry of the mesh. In order to achieve a small mesh, axisymmetric models were often employed. These involved modelling an area of revolution and applying certain boundary conditions. An example of the axisymmetric model of a simple bi-laminar disc design is shown in fig. 1.18.

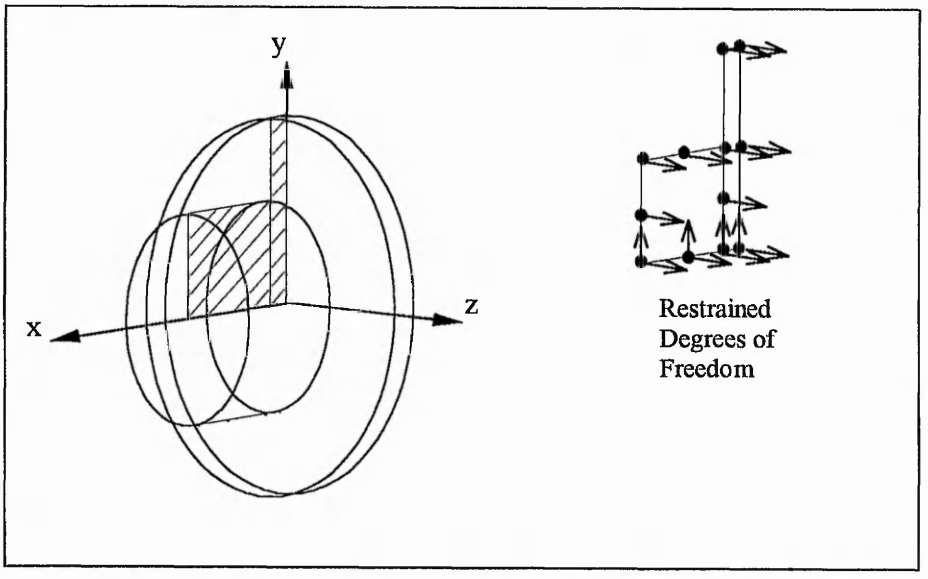

Fig. 1.18 A plane of revolution used in an axisymmetric model and its applied restraints. The z-axis is normal to the modelled shaded region, which is in the x-y plane.

The shaded region is the area of revolution i.e. the area which, if rotated about the x-axis by 360 degrees, would form the three dimensional volume. Arrows indicate freedoms which were restrained to simulate the three dimensional effects. The x-axis was restrained from movement in the y and z directions because this movement would be uniform in all directions if it were a solid and would therefore cancel out. For the same reasons all nodes were restricted from movement in the z direction. Displacements in the x, y and z directions were represented by the degrees of freedom u_1, u_2 and u_3 respectively. The electrical degree of freedom for the piezoelectric elements was u_4, which is usually a rotational freedom about the x-axis for other elements. These u_4 freedoms were restrained where there was an earthed electrode. Allowing degrees of freedom to be repeated freedoms meant that all of the specified nodes would have the same displacement in the specified direction. To simulate an electrode on the piezoelectric, the u_4 freedoms were repeated on the relevant nodes.

The time for analysis is also largely dependent on the type of analysis used. As explained previously, the finite element software is solving various matrix equations. Many of the methods of formulating the finite element equations result in symmetrical matrices. This means that only half of the information has to be stored as the calculations proceed, naturally speeding up the whole process. Some methods result in unsymmetric matrix equations which take longer to evaluate. Also, some problems simply involve the use of more equations when determining the unknown quantities.

The acoustic analysis method commonly employed in this study is one of the more lengthy types of analysis. Even small jobs, in terms of the numbers of elements, could take many hours to complete when exploring the transducer response over a wide range of frequencies. Careful preparation of each model was therefore important. The results of acoustic analyses also gave large amounts of data and took up several megabytes of disc space for each model.

The forced sinusoidal and enforced harmonic analyses methods were much faster to run for the same number of elements. These jobs could often be completed in minutes rather than hours, even for a wide range of frequencies.

Transient modelling of acoustic emission events also proved very demanding on the hardware resources. Due to the small time increments used (i.e. microseconds), the meshes had to be very dense which resulted in many thousands of elements per model. These generated lengthy calculations taking several days to run and using many megabytes of disc space to store results.

1.5.3.1 Summary of Model Construction using PIGS

The model was constructed in PIGS (PAFEC Interactive Graphics System) which allows the user to define the dimensions and other data necessary for calculation. The model was constructed by the following method **[46]**:

- Nodes (points) were plotted to define the dimensions using a co-ordinate system.
- Elements to be created were given a type number and property number.
- Elements were created by joining the nodes together in either quadrilaterals or triangles.
- Large elements were divided up so that there were at least three elements per wavelength of sound in each material.
- A data file was created listing all the nodal co-ordinates and the elements' topology, type number and property number.
- The datafile was edited to include details such as material properties, type of analysis, range of frequencies for analysis and other essential data.

The acoustic models consisted of the following elements:

axisymmetric piezoelectric elements	(type 35425)
axisymmetric solid Fourier elements	(type 36610)
axisymmetric fluid Fourier elements	(type 29210)
axisymmetric boundary elements	(type 23610)
thin shell of revolution elements	(type 42130)

Details about the elements are given in the PAFEC-FE Data Preparation manuals [**46**]. However, here a brief explanation is provided of why each type is used. All elements are specifically designed for use in axisymmetric problems.

PIEZOELECTRIC ELEMENTS

These elements can be used to model the piezoelectric ceramic because they have an electrical degree of freedom as well as displacements in the x, y and z directions.

SOLID FOURIER ELEMENTS

These elements can be used to model solids attached to the piezoelectric material. Fourier elements can also deal with non-symmetric loading if required.

FLUID FOURIER ELEMENTS

These can be used to model a finite region of fluid close to the transducer.

FLUID BOUNDARY ELEMENTS

Boundary elements can be used to model an infinite region of fluid and they imply certain mathematical assumptions and save computational time.

THIN SHELL OF REVOLUTION ELEMENTS

The axisymmetric model was first created on an older version of the software that required a very thin flexible membrane to be incorporated into the boundary of the fluid region, to couple the finite and boundary elements. This is no longer required, although its inclusion does not affect the results.

DATA FILE MODULES

The details of each module are given in the Data Preparation Manuals [**45**]. The 'Materials' and 'Laminates' modules are used to define the properties of each material used. The 'Restraints' and 'Repeated Freedom' modules are included to define the electrodes of the piezoelectric and axes of symmetry for the axisymmetric problem.

For an acoustic analysis other modules have to be included to specify the types of method to be used in calculation at the boundary elements [37]. Also, a 'Sources' module is included to define a point wave source in the fluid. In the 'Control' module of the data file the 'Frontal Sinusoidal Solution' command is used, which tells the program to use a direct solution of the sinusoidal equations for the whole structure. This makes the calculation faster.

The 'CHIEF' method of solution was used for modelling the fluid-structure interaction and this is based on the Helmholtz equations. The results obtained give nodal displacements in the solids, piezoelectric voltages and fluid pressures.

The 'Frequencies For Analysis' module was used to define the range of frequencies for the input signal. For the PZT-5A disc being modelled, the transducer response was calculated in a typical working range from 50 kHz to 1 MHz. The resolution used was 0.5 kHz to give an accurate representation of the transducer response without taking excessive computer time (each frequency taking about 10 minutes processing time). This range was broken down into smaller intervals for ease of data management.

For a forced sinusoidal analysis, the acoustic modules are not required. A 'Sine Loading' module is used to assign the input force or charge on the electrode. This is replaced by the 'Enforced Harmonic Motion' module for the relevant analysis.

1.6 SOME UNDERLYING FACTORS AFFECTING THE MODELLING TECHNIQUES EMPLOYED

Before results are considered, it is important to consider the output being presented. Much of the data analysed is in graphical form, showing the output voltage of the transducer at various frequencies of interest for a specific input type. The finite element software calculates the amplitude of solutions in relative units, which in this case are metres for displacement, volts for the electrical response of the piezoelectric and Hertz for the frequency.

In harmonic response calculations with no damping, the solutions to the eigenvalue problem for forced excitation will be infinite at natural frequencies. For this to occur in the computer model the FE calculation would have to predict the frequency accurate to several decimal places. However, this helps to explain why the resonant peaks are extremely large for some cases. When the frequency range of investigation has been specified, a typical resolution of 0.5 kHz has been used. This was deemed adequate for predicting the transducer response over large frequency ranges, whilst avoiding excessively long computations.

Sometimes the FE models predict one resonant frequency having a greater amplitude peak than another. This may be because the exact resonant frequency occurs very close to the 0.5 kHz interval specified and therefore, in practice, the mode might not actually be larger in amplitude. This is why the vibration modes are also analysed and care is taken when comparing different transducers. Only in models that employ damping will the output amplitudes have a real meaning. This is the case for the acoustic FE models in which an infinite fluid region provides natural radiation damping. Applying other forms of damping, such as mass or stiffness proportional damping, was considered in the initial stages of the research, but with the acoustic FE models proving suitable, other methods were left for further investigations.

By keeping the acoustic source strength constant for all of the acoustic FE models, the output voltage amplitudes give an indication as to the transducers' relative sensitivities. Because the piezoelectric properties were kept constant for this study, the only variables are the transducer geometry and other materials used in the transducers. Although the output amplitude may be different with other forms of damping, the acoustic FE models at least provide a relative scale to work with. If one design is predicted to be more sensitive than another, then this should translate to a real life improvement.

In real life, the relative output amplitudes may not be as predicted by the model, but an FE prediction of improvement should provide some real life improvements, however small. Other factors, such as the Q value of the resonances, will also vary in real life. The undamped models produce very high Q peaks, while in the acoustic FE models they

are often lower due to the fluid damping effects. Naturally, model estimates of Q are only accurate within the 0.5 kHz of resolution used. Again, because all of the models use the same frequency resolution, the relative differences in Q value should give information that translates into real life information.

Several types of analysis have been used during the course of the research and their various merits have been assessed. The aim of the modelling was to compare the relative merits of different transducer designs. FEM provides a suitable method for doing this if the boundary conditions for each model are the same. If the input forces or acoustic wave pressures are kept constant, then the output of the models is directly comparable where the transducers have the same input conditions at their face (i.e. same boundary conditions and dimensions). Agreement with experiment and theory has been demonstrated, where appropriate, to confirm the accuracy of FEM frequency predictions. However, attempts to accurately quantify model output amplitude data against practical data have not been made for the reasons above.

Chapter Two

FE Modelling of a PZT-5A Disc Transducer Design

2.0 INTRODUCTION

Chapter One considered a review of the literature concerned with ultrasonic transducer design and, discussed the use of finite element analysis in modelling ultrasonic transducer performance. Chapter Two will consider FE modelling of a simple piezoelectric transducer consisting of a simple disc piezoelectric element, providing a resonant design suitable for detection of acoustic emission.

Although the design is geometrically simple, the fact that the disc is able to vibrate in a complex way introduces associated complexity in predicting its performance and, demonstrates the importance of FE modelling even in such a simple system.

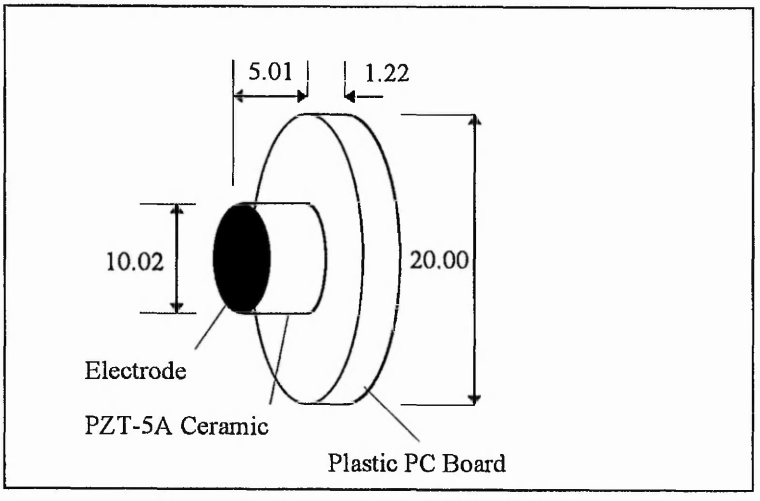

Fig. 2.1 Resonant transducer design consisting of a piezoelectric disc and a larger plastic facing disc. Dimensions are in millimetres.

A piezoelectric disc was mounted on a slightly larger, thinner, plastic facing disc (fig. 2.1). The presence of the protective plastic facing disc meant that the vibrational modes and, therefore, the performance of the transducer would be different from a freely vibrating piezoelectric disc.

The performance of an experimental transducer was compared with the modelling data. In this case, the plastic disc was attached to the piezoelectric disc using Araldite epoxy resin adhesive. The piezoelectric material was a lead zirconate titanate ceramic (PZT-5A).

The aims of modelling the transducer response were;

1. To predict its resonant frequencies and compare modelling, experimental and theoretical data.
2. To examine the vibrational modes of the transducer, to classify them and to consider the effect of varying the piezoelectric disc geometry and its effect on the transducer's frequency response and sensitivity.
3. To investigate what happens to the transducer performance when it is mounted on a large metal plate, as in a practical application.

The results from this model were to be used to validate and develop the modelling techniques, as well as providing a design aid for more complex transducers.

2.0.1 FE Methods used to Model the PZT-5A Disc

Due to the circular symmetry of the disc, an axisymmetric model was used. An axisymmetric model involves establishing a plane of revolution for the transducer about an axis of symmetry, and applying boundary conditions to simulate the effect of a three dimensional model. The plane of revolution used for the bi-laminar disc transducer was shown in fig. 1.18 and is shown in more detail, with the addition of a fluid region, in fig. 2.2. This axisymmetric procedure saved on computer processor time because the number of elements was greatly reduced. The fluid region was included in an acoustic FE model, described in section 2.2.3.

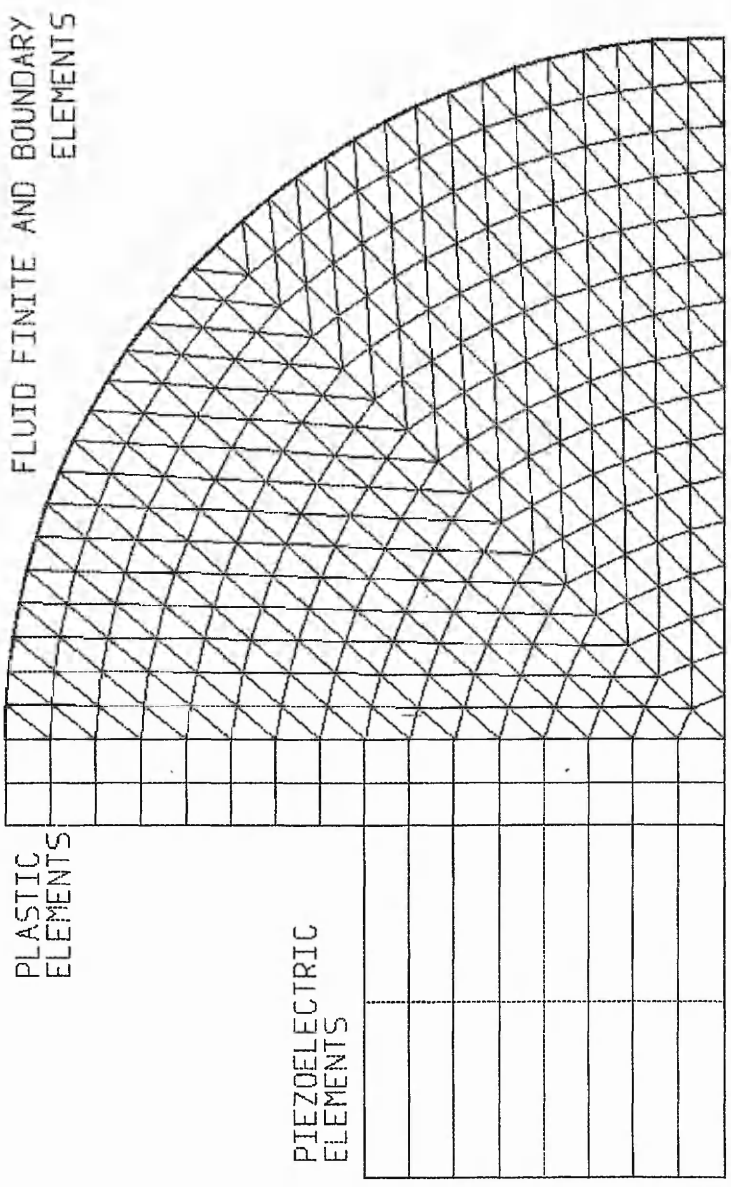

Fig. 2.2 FE mesh of piezoelectric elements (bottom), solid elements (middle), and fluid finite and boundary elements (top circular area), used for an acoustic analysis model of the bi-laminar disc transducer. The model is axisymmetric about the right hand vertical axis.

Different types of analysis were performed using the FE software, in order to investigate their various merits. Models considered were all forced sinusoidal vibration analyses, some involving a free boundary condition or repeated freedoms on specific nodes. Others used fluid loading on the transducer face with an acoustic analysis method (fig. 2.2).

Fig. 2.2 includes the fluid finite elements and boundary elements required for an acoustic FE analysis, which is described in section 2.2.3. For the model, an acoustic point source is situated 0.1 m from the transducer face, on the axis of symmetry.

Different boundary conditions were used for the unloaded (non-acoustic) models to investigate their effects on the transducer's frequency response. One approach involved applying a sinusoidal input to the electrodes of the piezoelectric element. The other approach involved the nodes on the transducer face being given repeated freedoms (they moved with the same displacement). The models that showed the closest agreement with experimental data were used for a more thorough study later.

2.1 FREQUENCY RESPONSE AND VIBRATIONAL MODES OF THE TRANSDUCER'S PIEZOELECTRIC DISC

A resonant transducer will give the maximum output when excited by the frequency components of a waveform corresponding to its resonant frequencies. The nature of this vibration varies depending on the frequency of the resonance and is known as the "mode shape". Simple mode shapes will occur at the lowest resonance, with more complex vibration occurring at higher frequencies.

The first piezoelectric disc vibrational modes depend on the diameter to thickness ratio (D/t). The piezoelectric disc in the bi-laminar disc transducer modelled has a D/t ratio of 2. Several modes have been classified by Ono [1] for piezoelectric discs with single figure D/t ratios. These are classified in fig. 2.3 as "concave-extension" vibration, seen in D/t ratios less than 1.8, "circular-bending", seen in intermediate D/t ratios (>2.5), "radial-compression" type, also seen in intermediate D/t ratio discs, and "convex-

compression", seen at higher modes for D/t ratios between 0.75 and 1.0. These are the first few modes to be observed, the order and number of which depend on the exact geometry.

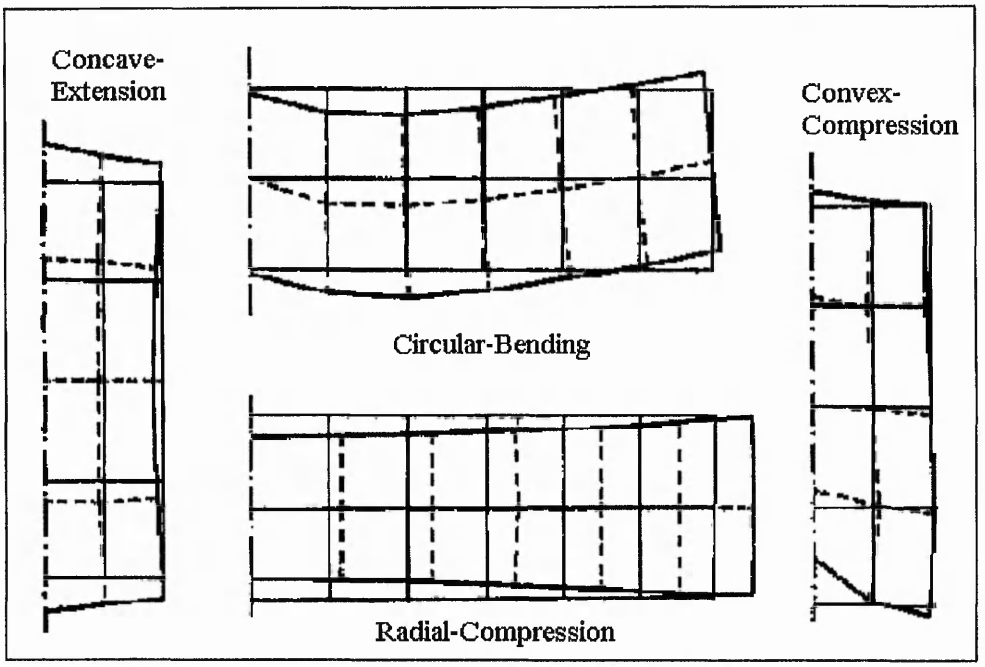

Fig. 2.3 Mode shapes of piezoelectric discs and cylinders described by Ono [1]. The discs are axisymmetric about the left hand vertical axes. Dashed lines indicate the deformed structure during vibration.

More complex modes also exist which are harder to classify as one specific type. For discs with larger D/t ratios of 10 and 20, five common mode shapes have been identified by Cawley [**39**], [**40**]. These are the radial mode, edge mode, thickness shear mode, thickness extensional mode, and high frequency radial mode (fig. 2.4). They appear in order of increasing frequency. Pure thickness modes appear in thin plates, where the lateral dimensions exceed the thickness by more than an order of magnitude. For discs with smaller D/t ratios, the modes of vibration can couple.

In an attempt to categorise the descriptions by Ono in a more quantitative way, the number of quarter wavelengths of deformation in the thickness and radial directions have been used. A particular mode is thus designated $M_{i,j}$, where i is the number in the thickness direction and j is the number in the radial direction. The descriptions are quantified in table 2.1. The aim was to provide a unique identification of each mode

rather than specific i, j values used to predict the resonant frequency. The number of wavelengths in the radial direction (j) must be doubled to provide the number across the disc diameter, because of the symmetry of the models.

Ono description	**$M_{i,j}$ value**
Concave-Extension	M_{21}
Circular-Bending	M_{03}
Radial-Compression	M_{01}
Convex-Compression	M_{41}

Table 2.1 Mode shape descriptions by Ono [**1**] quantified in terms of quarter wavelengths in the thickness (i) and radial (j) directions as $M_{i,j}$.

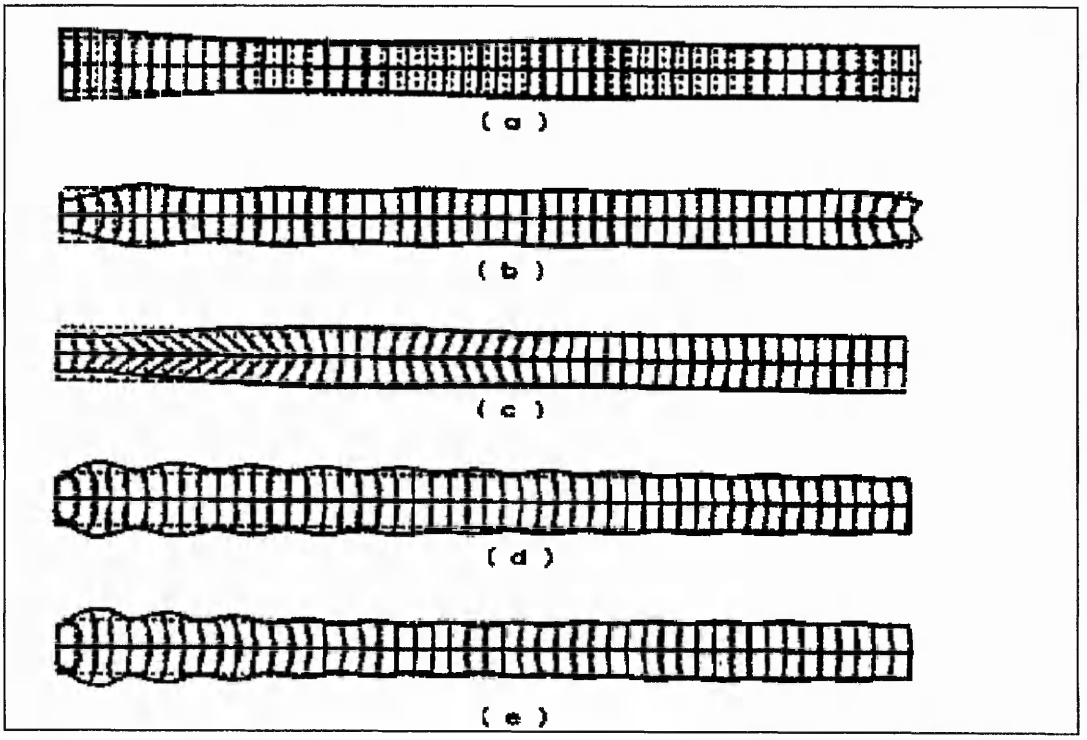

Fig. 2.4 Five vibrational modes of thin discs [**39**]. Radial mode (a), edge mode (b), thickness shear mode (c), thickness extensional (d) and high frequency radial mode (e). Discs are axisymmetric about the left hand vertical axis.

The mode shapes of the piezoelectric disc, used in the bi-laminar disc transducer in fig. 2.1, were predicted by applying a sinusoidal voltage to the positive electrode, in a PAFEC-FE model. This modelling was carried out for comparison with the mode shapes predicted by other authors [**1, 39**]. The piezoelectric disc model consists of the

piezoelectric elements shown in fig. 2.2. The calculated vibrational modes were later compared to the modes of the bi-laminar disc transducer model to determine the effect of the thin plastic facing disc. There were no loads or repeated freedoms on the disc, simulating the free vibration condition. The 'Sine Loading' module was used to apply the voltage in the PAFEC data file.

Considering the FE modelling of the electrically excited disc, the first mode of vibration occurred at 137 kHz and fig. 2.5 shows a simple flexing of the disc about the centre, in the thickness direction (the disc centre is the baseline in the fig.). This could be given an M_{01} mode description because there is no deformation about the thickness axis and a quarter wavelength of deformation about the radial axis. At 180 kHz, the M_{21} mode showed the concave-extension described by Ono, in which the disc, seen in fig. 2.6, is expanding and contracting in both the thickness and radial directions. At 258.5 kHz was an M_{22} mode that produced a lot of displacement at the centre (fig. 2.7), like the convex-compression mode in fig. 2.3. Many of the higher order modes show similar but more complex vibration characteristics.

Mode 4 (not shown) was at 260 kHz and is similar to the 180 kHz mode with an M_{21} shape. Mode 5 in fig. 2.8 has shape M_{43} at 317 kHz, and is a higher order version of the M_{21} mode. At 340 kHz in fig. 2.9, the disc's sixth mode is M_{44}. Finally, as an example, fig. 2.10 shows resonance at 718 kHz, which is highly complex and has been assigned a possible modal notation of M_{98}. This type of complex deformation highlights the advantages of using FEM for complex vibrational analysis. It appears that the mesh density may be losing its resolution at this higher frequency.

When comparing these disc vibration predictions to other work [**1**], similar mode shapes are observed (e.g. the M_{21} mode and the concave-extension mode). Other workers' classifications are not so obvious, because their studies have involved much larger diameter/thickness ratios, such as 10 or 20 [**39**]. However, there are still similarities near to the disc centre and disc edge (fig. 2.4) which can be identified, and so the reliability of the model is strengthened by these comparisons.

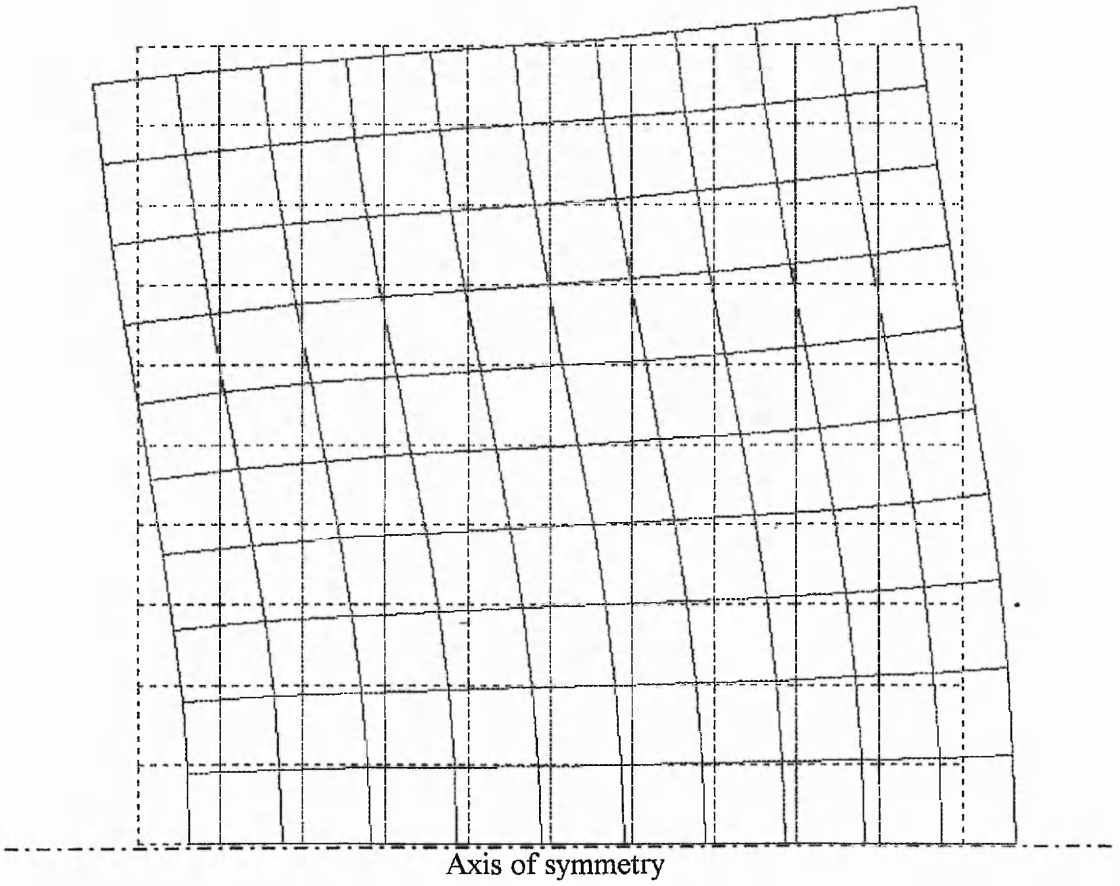

Fig. 2.5 Mode 1 at 137 kHz, shape M_{01}. The stationary disc position is represented by the dashed lines. The model is axisymmetric about the base line.

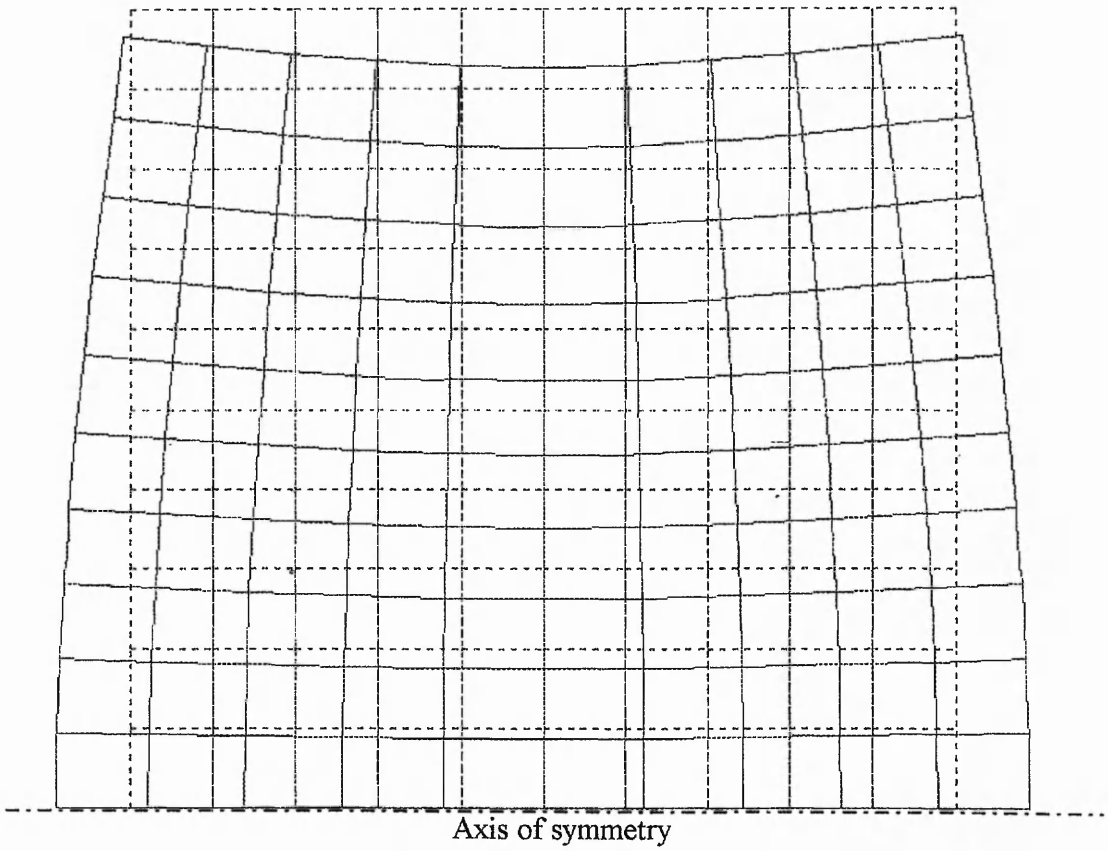

Fig. 2.6 Mode 2 at 180 kHz, shape M_{21}. The stationary disc position is represented by the dashed lines. The model is axisymmetric about the base line.

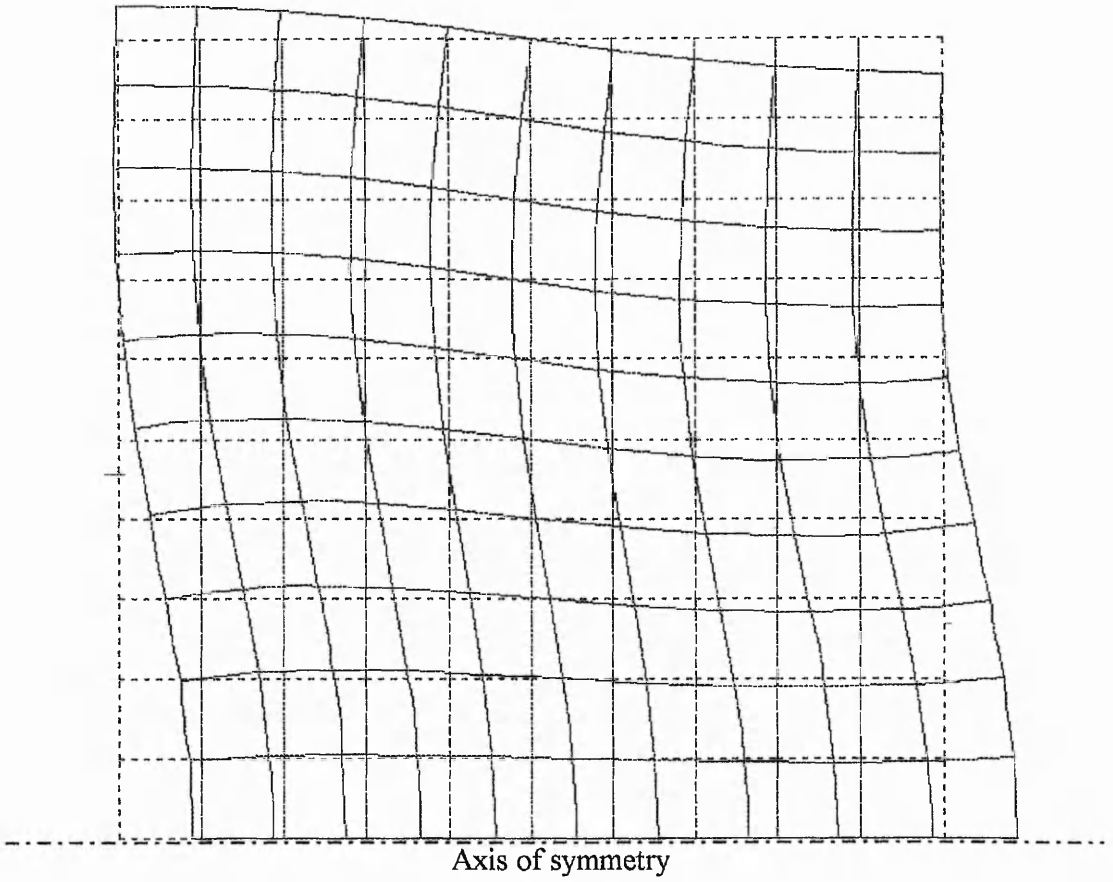

Fig. 2.7 Mode 3 at 258.5 kHz, shape M_{22}. The stationary disc position is represented by the dashed lines. The model is axisymmetric about the base line.

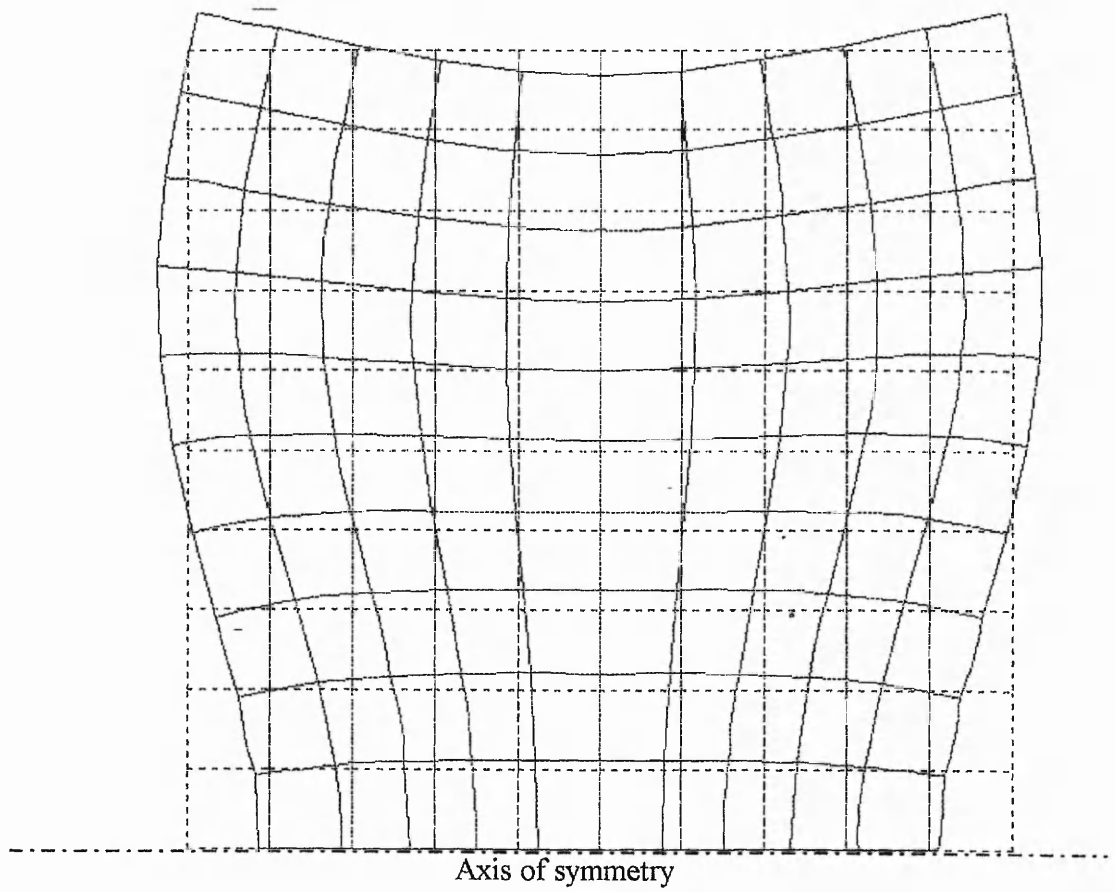

Fig. 2.8 Mode 5 at 317 kHz, shape M_{43}. The stationary disc position is represented by the dashed lines. The model is axisymmetric about the base line.

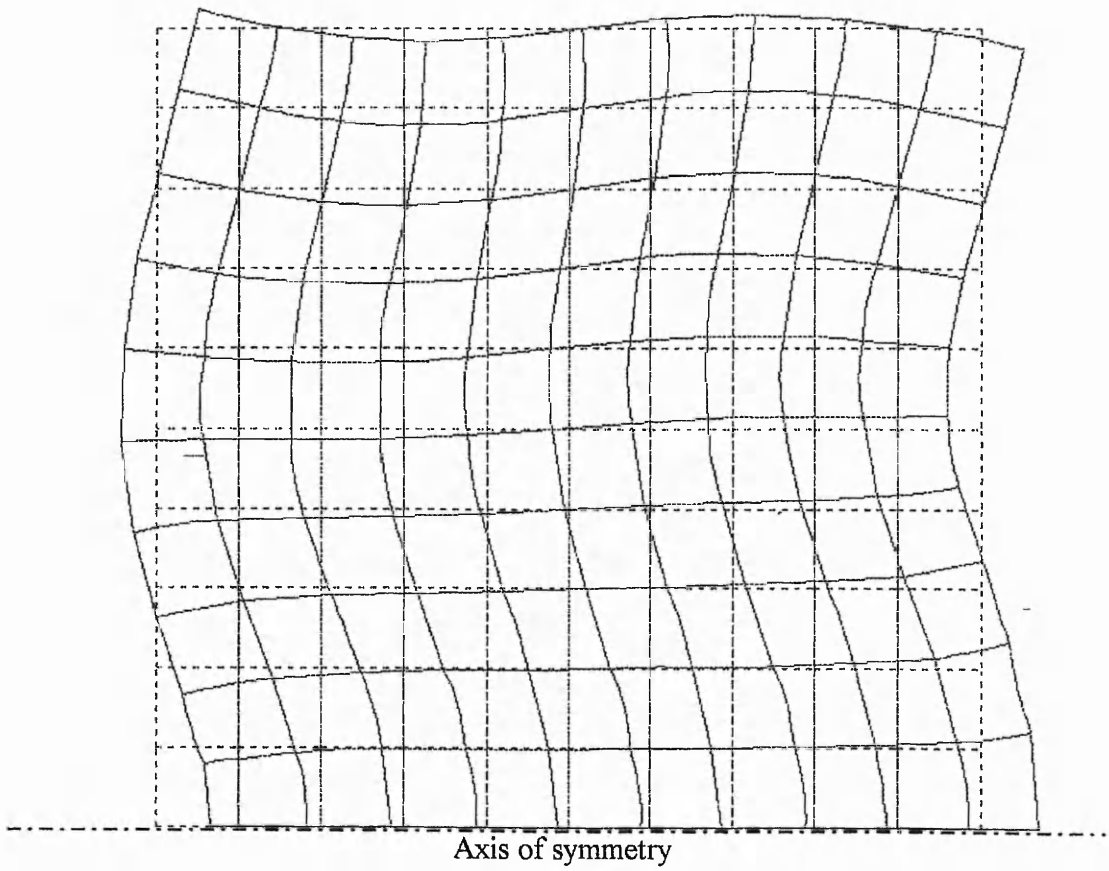

Fig. 2.9 Mode 6 at 340 kHz, shape M_{44}. The stationary disc position is represented by the dashed lines. The model is axisymmetric about the base line.

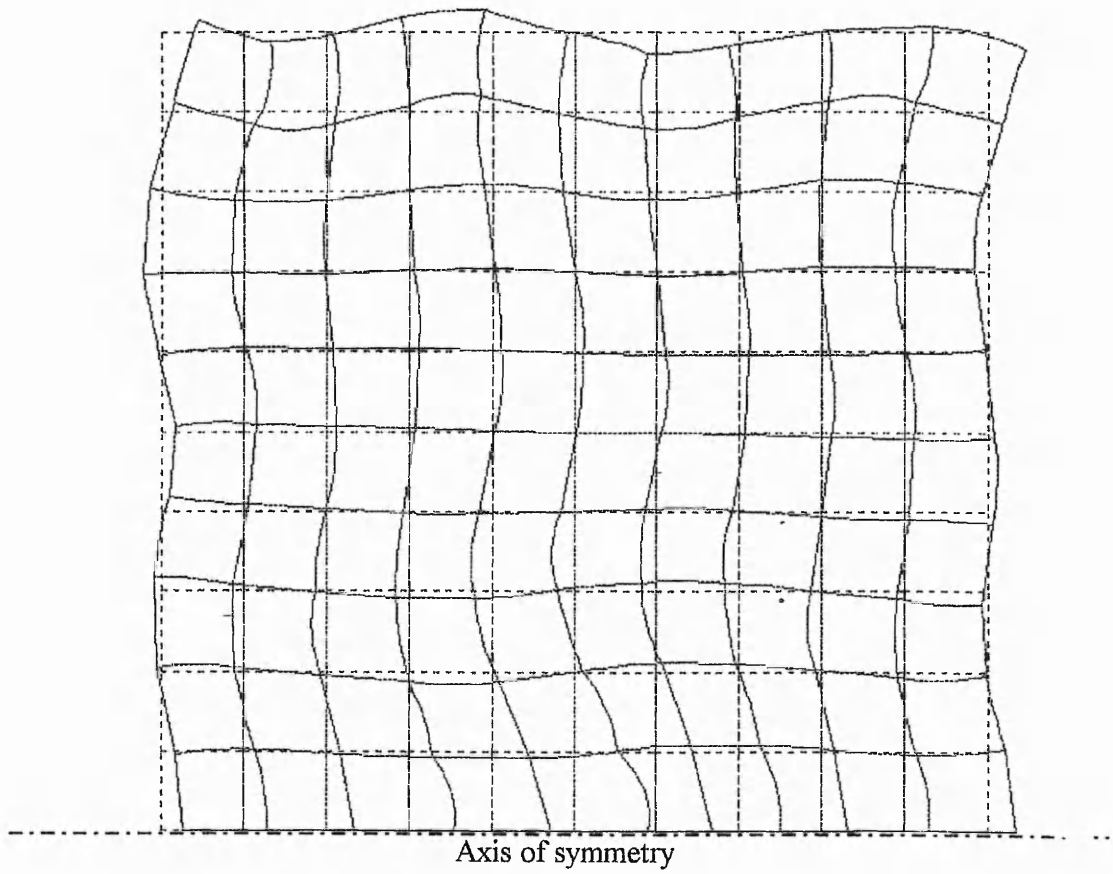

Fig. 2.10 Mode 20 at 718 kHz, shape M_{98}. The stationary disc position is represented by the dashed lines. The model is axisymmetric about the base line.

2.2 FREQUENCY RESPONSE AND VIBRATIONAL MODES OF THE TRANSDUCER

2.2.1 Modelling a Sinusoidal Voltage Applied to the Electrodes

Now that the mode shapes of the piezoelectric disc alone have been studied and compared to other work, the mode shapes of a more practical transducer design will be investigated. The practical transducer might involve the piezoelectric element being mounted to a plastic face plate, and this section explores how this might affect the resonant behaviour of the piezoelectric system.

So that a direct comparison with the mode shapes of the piezoelectric disc could be achieved, the bi-laminar transducer model was excited electrically with a sinusoidal voltage between the piezoelectric electrodes, and allowed to vibrate freely. This would give an indication of the effect of the plastic facing on the frequency and mode of resonance.

The first mode shape M_{00} occurred at only 19 kHz. This involved a simple flexing of the plastic about the edge of the piezoelectric disc (fig. 2.11). This mode would not occur in practice since the edge of the face plate would be constrained by the transducer case and mounting conditions.

The second mode in fig. 2.12 at 94.5 kHz, was comparable to the 137 kHz M_{01} mode of the free disc in fig. 2.5. The piezoelectric is moving in the thickness direction along the centre of symmetry. Beyond the edge of the piezoelectric, the plastic was curving in the opposite direction to the direction of motion of the PZT. This motion of the plastic disc was again seen at the third mode, M_{11} at 125 kHz (fig. 2.13). The piezoelectric mode is similar to the M_{01} shape, but with the plastic causing motion in the thickness direction leading to the M_{11} shape in the piezoelectric.

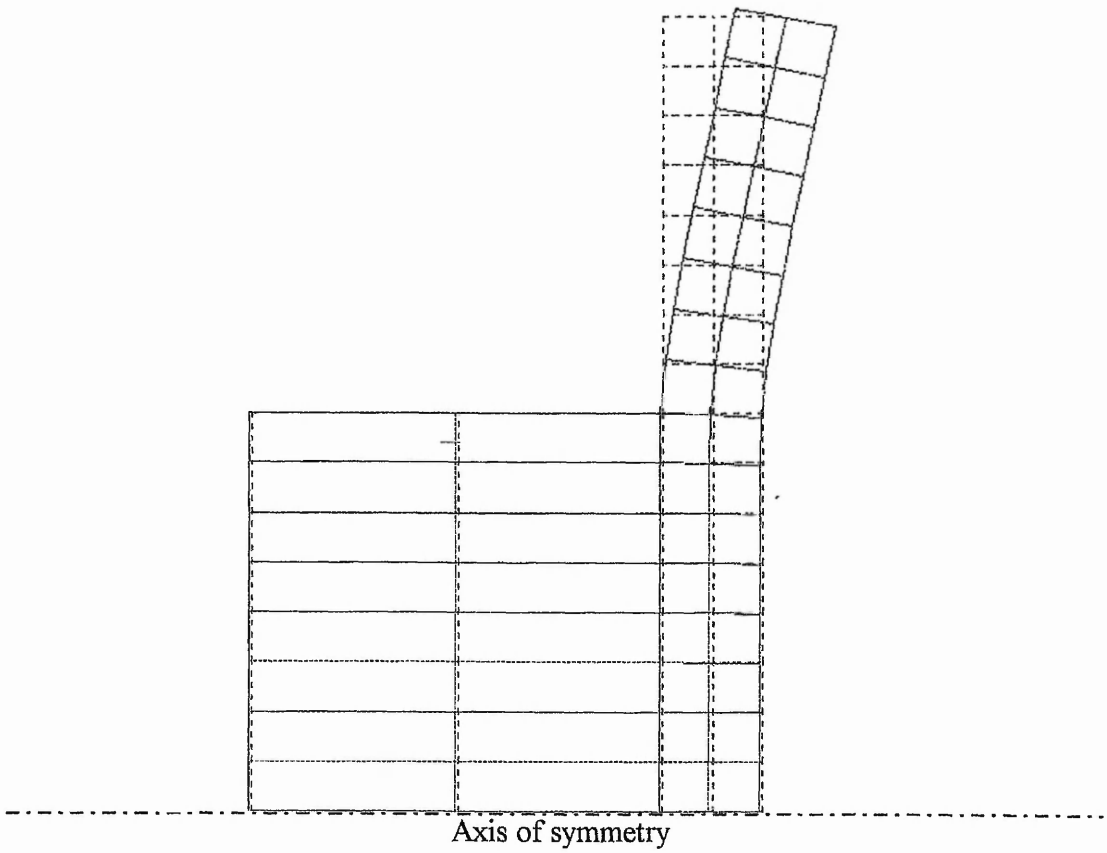

Fig. 2.11 Mode 1 at 19 kHz, shape M_{00}. The stationary transducer position is represented by the dashed lines. The model is axisymmetric about the base line.

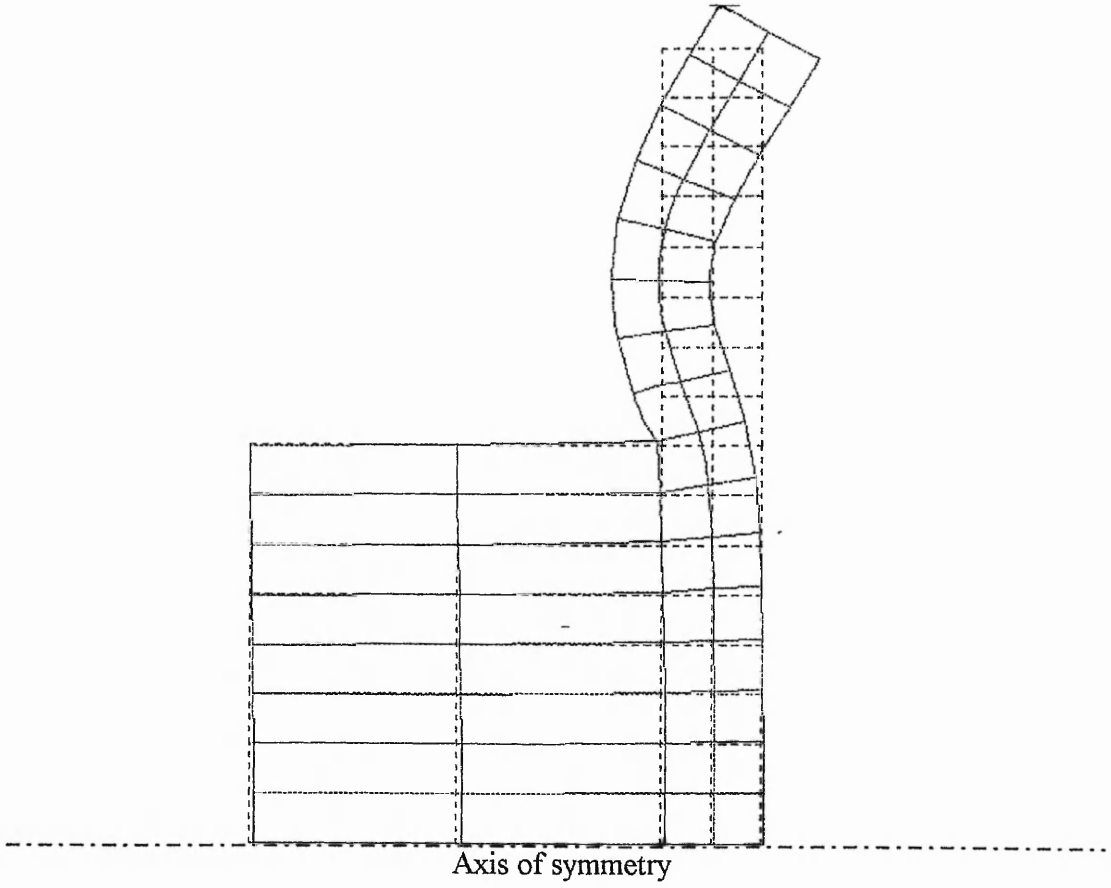

Fig. 2.12 Mode 2 at 94.5 kHz, shape M_{01}. The stationary transducer position is represented by the dashed lines. The model is axisymmetric about the base line.

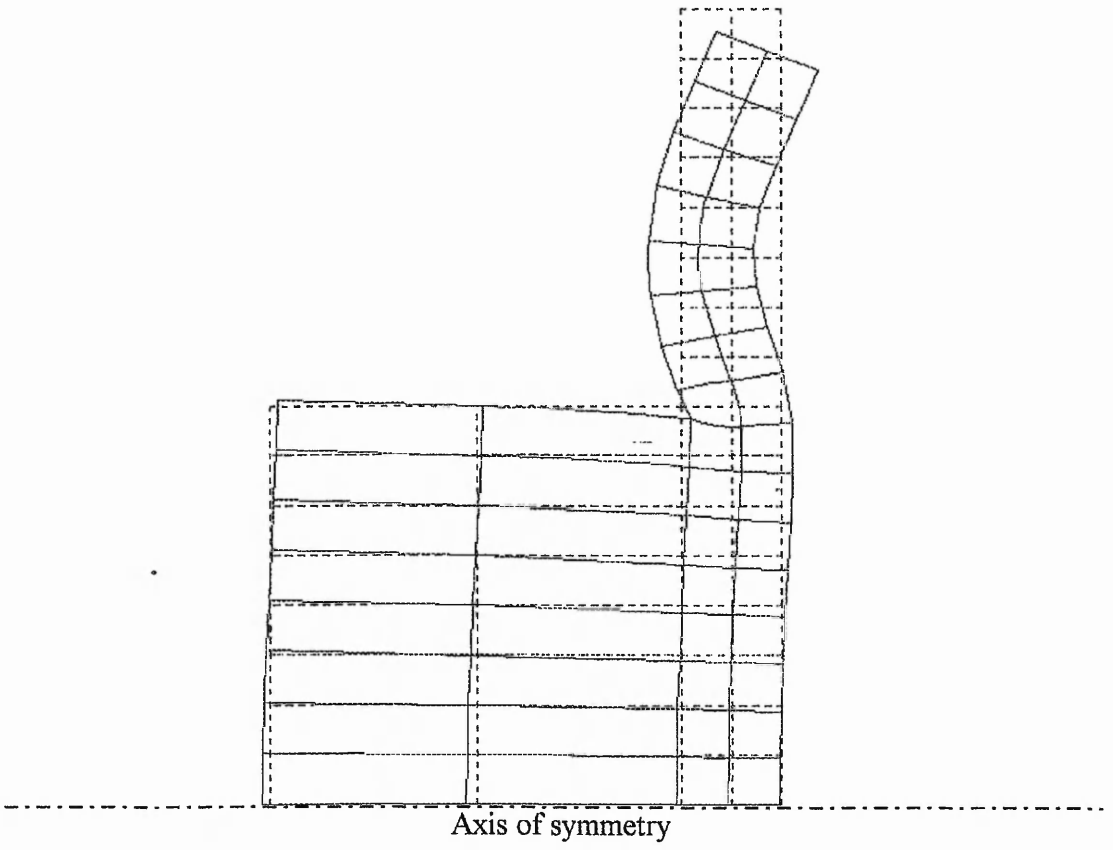

Fig. 2.13 Mode 3 at 125 kHz, shape M_{11}. The stationary transducer position is represented by the dashed lines. The model is axisymmetric about the base line.

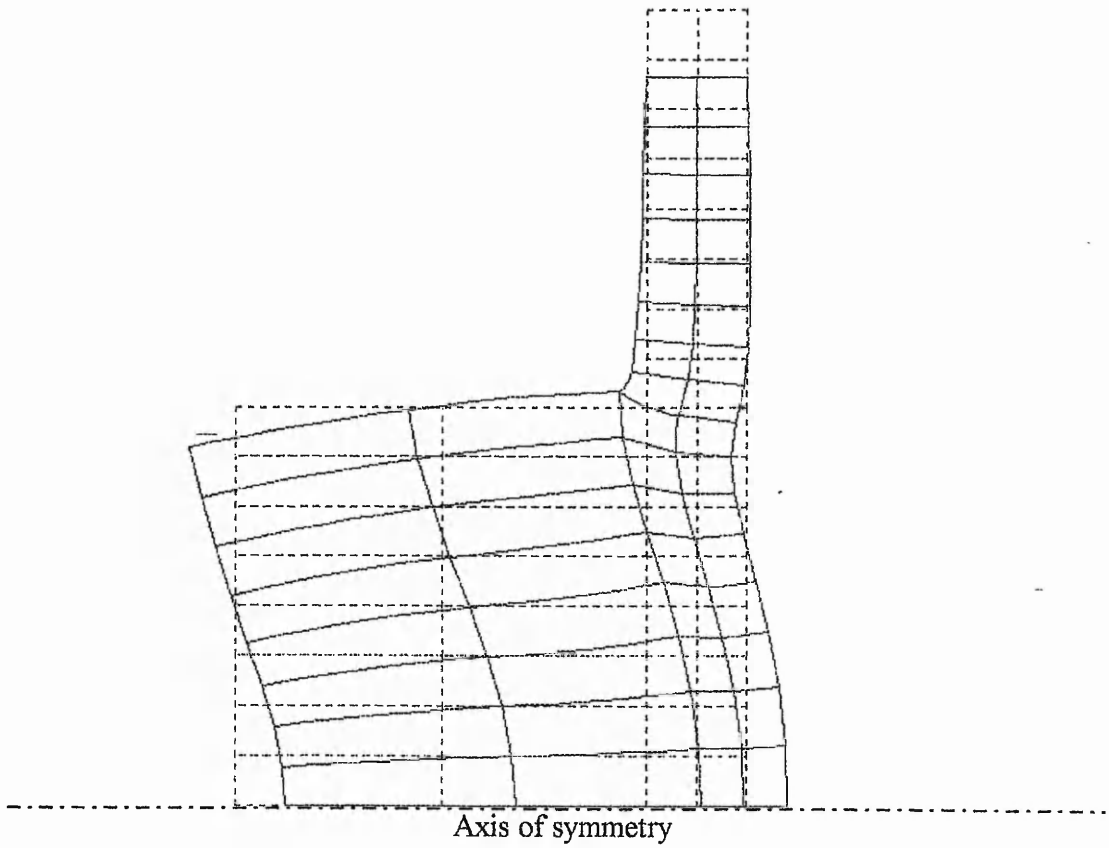

Fig. 2.14 Mode 4 at 149 kHz, shape M_{11}. The stationary transducer position is represented by the dashed lines. The model is axisymmetric about the base line.

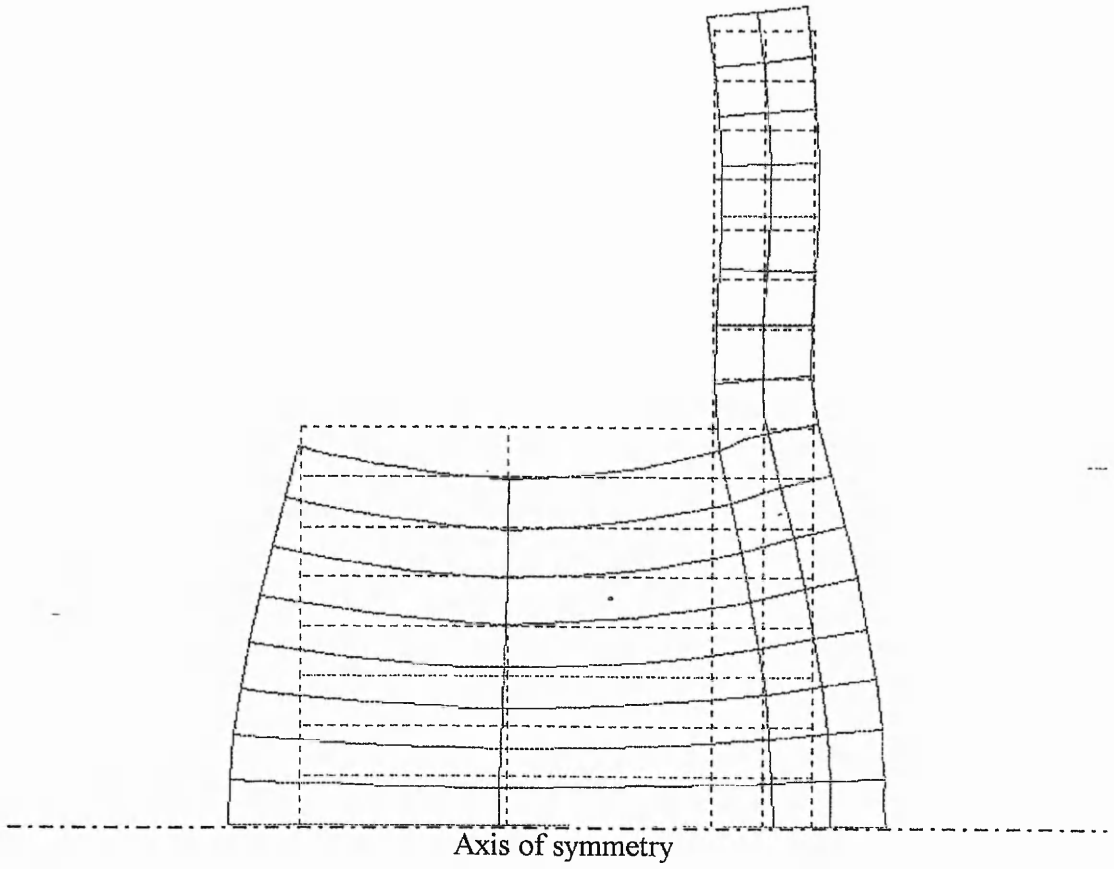

Fig. 2.15 Mode 5 at 178 kHz, shape M_{21}. The stationary transducer position is represented by the dashed lines. The model is axisymmetric about the base line. The disc deformation is similar to that seen in fig. 2.6.

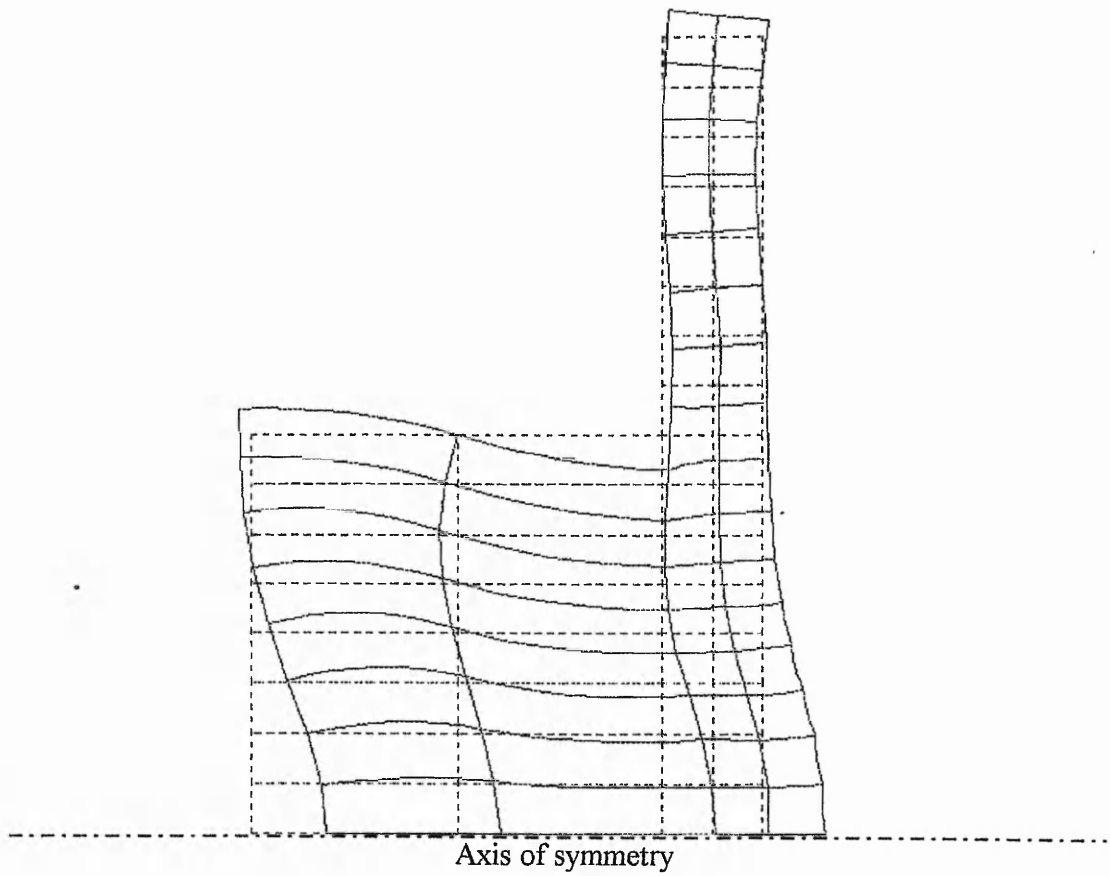

Fig. 2.16 Mode 6 at 259 kHz, shape M_{22}. The stationary transducer position is represented by the dashed lines. The model is axisymmetric about the base line.

At 149 kHz the M_{11} mode showed that the plastic was expanding radially, in fig. 2.14. The piezoelectric deformation bore resemblance to the circular-bending motion in fig. 2.3. Mode 5 (fig. 2.15) at 178 kHz was the M_{21} mode, seen at 180 kHz in the PZT disc alone (fig. 2.6). The constraining effect of the plastic disc caused this motion to be slightly skewed towards the plastic. Beyond the piezoelectric edge, the largest plastic displacement was in a radial direction, with smaller motion in the thickness direction. Fig. 2.16 suggests an M_{22} mode shape at 259 kHz. This mode of the piezoelectric was seen in the free disc at 258.5 kHz in fig. 2.7. Further modes were not examined formally as the similarities between the piezoelectric disc modes for the transducer and free disc were clear, as was the constraining effect of the plastic disc.

The addition of the protective plastic disc to the piezoelectric disc produced extra modes of vibration, compared with the piezoelectric disc alone i.e. the M_{00} and M_{11} modes. Where the modes were directly comparable to the plain piezoelectric disc modes, the effect of the plastic was to lower the frequency of the mode (e.g. M_{01} shifted from 137 to 94.5 kHz and M_{21} shifted from 180 to 178 kHz). This suggests the plastic is changing the effective diameter to thickness (D/t) ratio of the piezoelectric disc. The comparisons between the plain disc and bi-laminar transducer are seen later in table 2.2, section 2.2.2.

2.2.2 Forcing the Transducer Face using Repeated Freedoms

Forcing the face of the plastic sinusoidally was another method of analysing the modes of the transducer. All of the nodes on the transducer face were given repeated freedoms i.e. they all moved in phase and with the same x displacement (i.e. in the thickness direction, normal to the transducer face). This caused a straight edge on the displaced shape which, compared to modes seen in the previous analysis (section 2.2.1), is not realistic. An alternative is to just force the centre node, which will allow the structure to move freely but does not provide a realistic method of modelling a real situation. In practice, the whole transducer face is excited by the passing acoustic wave. By giving the nodes on the transducer face repeated freedoms in the x-direction, this analysis is assuming a uniform excitation across the face, which may not be a representation of a practical situation.

Because the motion of the transducer face was restricted by the repeated freedoms, the flexing mode of the plastic at 19 kHz, seen in fig. 2.11, was not observed. The first mode (fig. 2.17) was at 121.5 kHz, in which the PZT bent away from the plastic about the centre, in an M_{11} mode. There was some deformation about the thickness axis, giving the appearance of an M_{21} mode. Beyond the edge of the piezoelectric, the plastic moved in a radial motion.

Mode 2 at 152 kHz shows the plastic in a radial mode, with the PZT in an M_{11} mode (fig. 2.18). A familiar M_{21} mode was seen in fig. 2.19 at 173 kHz, which was a radial mode of the PZT. Again, the plastic caused the PZT to skew slightly towards it. The plastic moved inwards radially beyond the PZT, but was prevented from doing so where it was attached to the piezoelectric. The frequency of this mode has dropped further from the comparable M_{21} mode of the plain disc (180 kHz) and of the electrically driven transducer (178 kHz).

The M_{22} mode of the piezoelectric disc occurs at 222 kHz (fig. 2.20). Where the plastic is free, it again compresses radially whilst expanding slightly in the thickness direction. This M_{22} mode of vibration is seen in the free disc at 258.5 kHz, and in the electrically excited model of the whole transducer at 259 kHz. Where the PZT disc is constrained by the plastic, it gives the appearance of an M_{21} mode shape. Mode 5 at 269 kHz (fig. 2.21) involves expansion at the centre in the thickness direction, while the piezoelectric disc curves in the radial direction, giving an M_{23} mode shape. The free part of the plastic has relatively small displacement.

Mode 6 at 292 kHz (fig. 2.22) suggests an M_{42} mode, which resembles the edge mode in fig. 2.4(b), as described by Cawley [**39**], in which the edge of the disc is displaced most at the top and bottom surfaces and the centre is compressed in the thickness direction. The plastic moves like a piston, with some radial displacement caused by the PZT.

These results are compared with the previous sections' results in table 2.2.

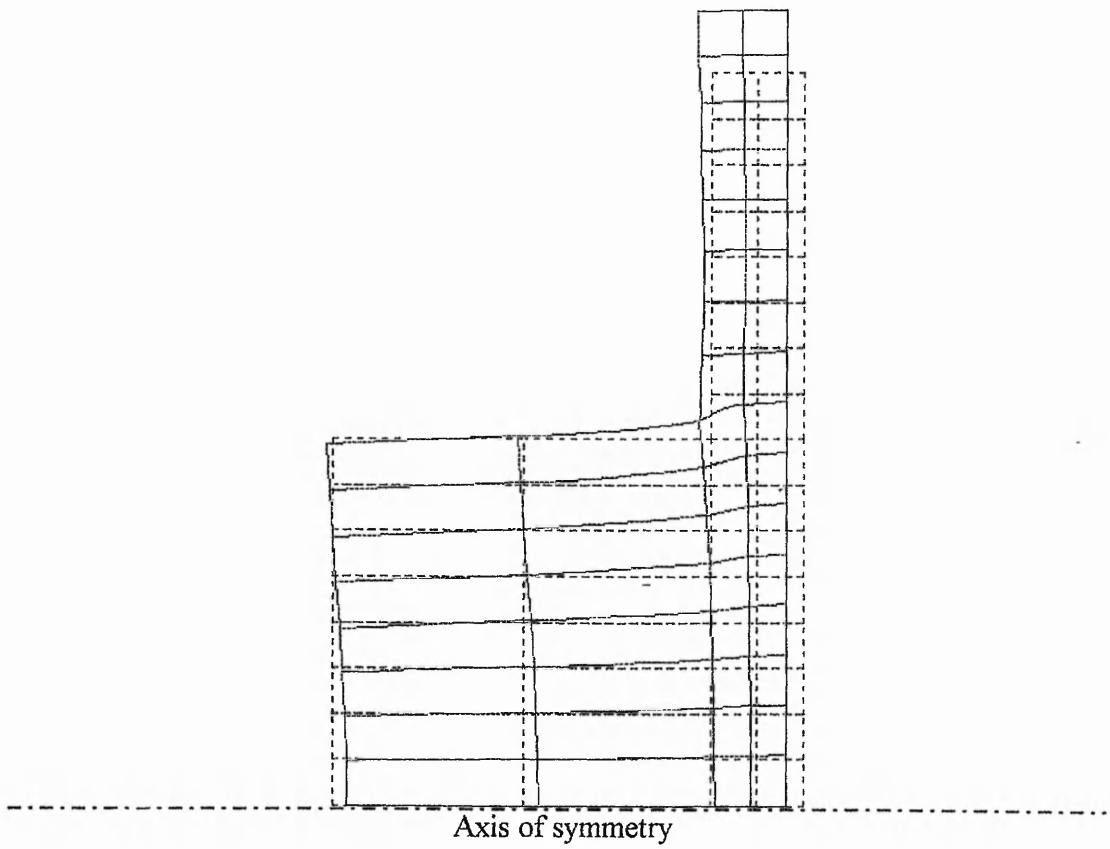

Fig. 2.17 Mode 1 at 121.5 kHz, shape M_{11}. The stationary transducer position is represented by the dashed lines. The model is axisymmetric about the base line. The transducer face (vertical right axis) has repeated freedoms on all nodes.

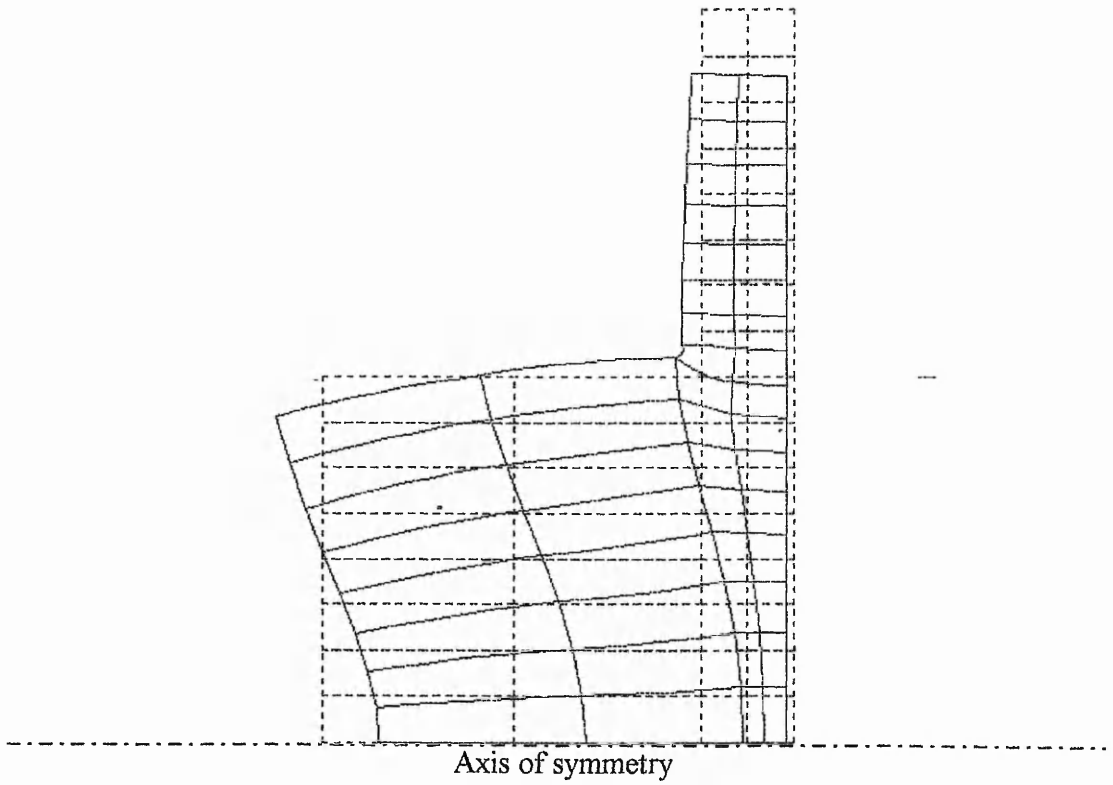

Fig. 2.18 Mode 2 at 152 kHz, shape M_{11}. The stationary transducer position is represented by the dashed lines. The model is axisymmetric about the base line. The transducer face (vertical right axis) has repeated freedoms on all nodes.

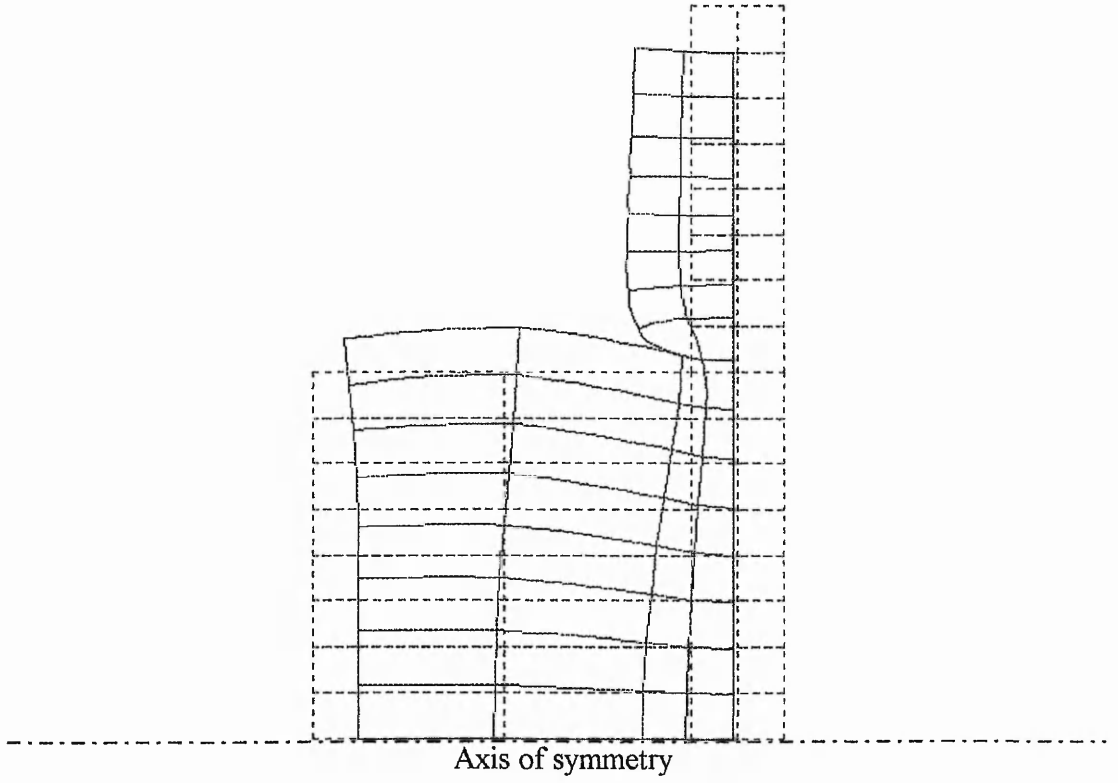

Fig. 2.19 Mode 3 at 173 kHz, shape M_{21}. The stationary transducer position is represented by the dashed lines. The model is axisymmetric about the base line. The transducer face (vertical right axis) has repeated freedoms on all nodes.

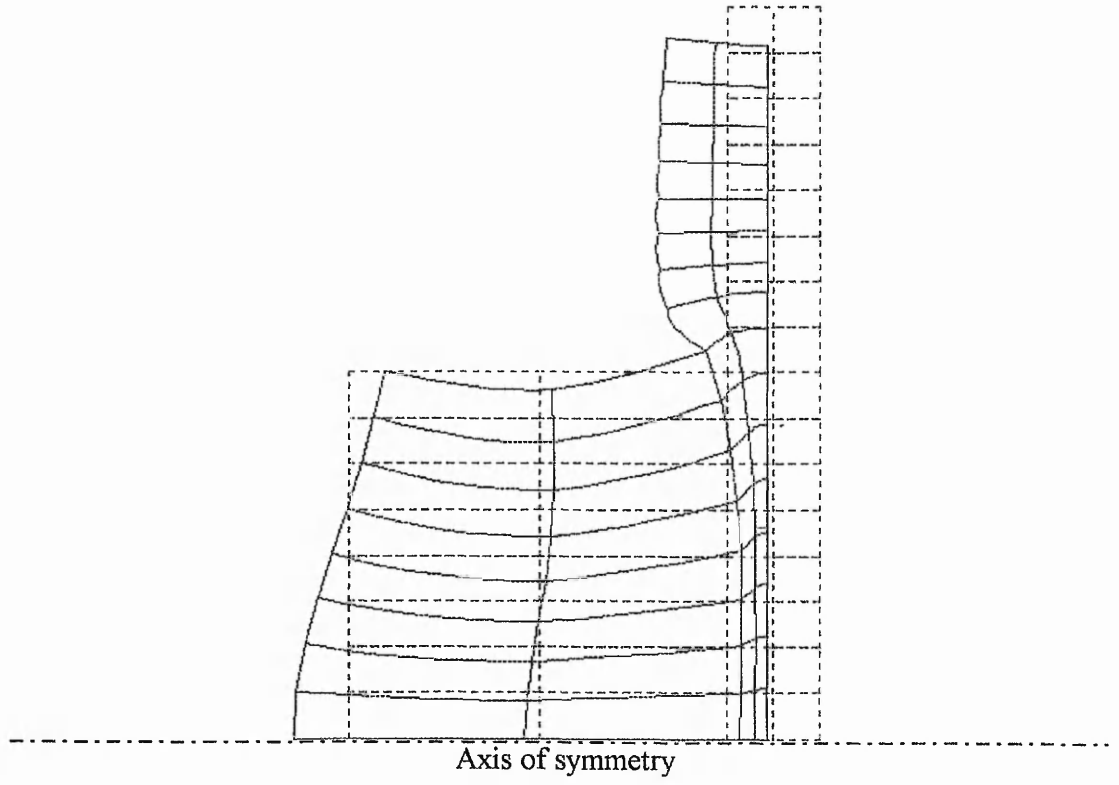

Fig. 2.20 Mode 4 at 222 kHz, shape M_{22}. The stationary transducer position is represented by the dashed lines. The model is axisymmetric about the base line. The transducer face (vertical right axis) has repeated freedoms on all nodes.

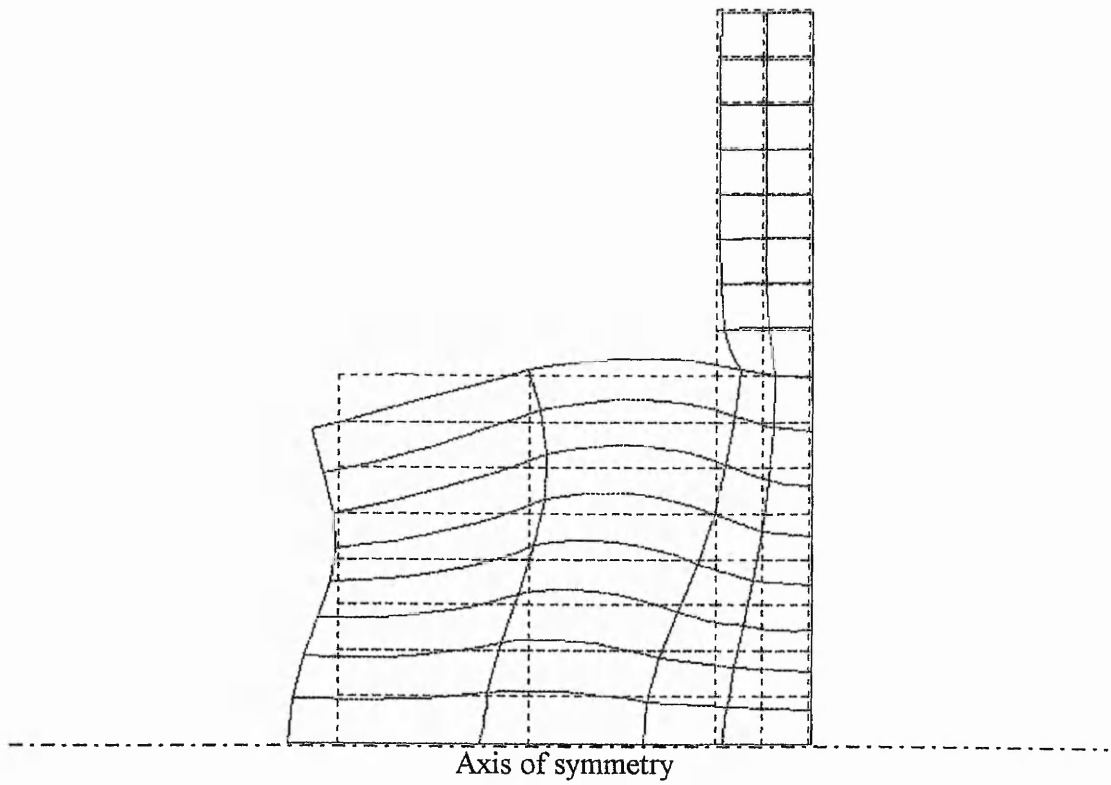

Fig. 2.21 Mode 5 at 269 kHz, shape M_{23}. The stationary transducer position is represented by the dashed lines. The model is axisymmetric about the base line. The transducer face (vertical right axis) has repeated freedoms on all nodes.

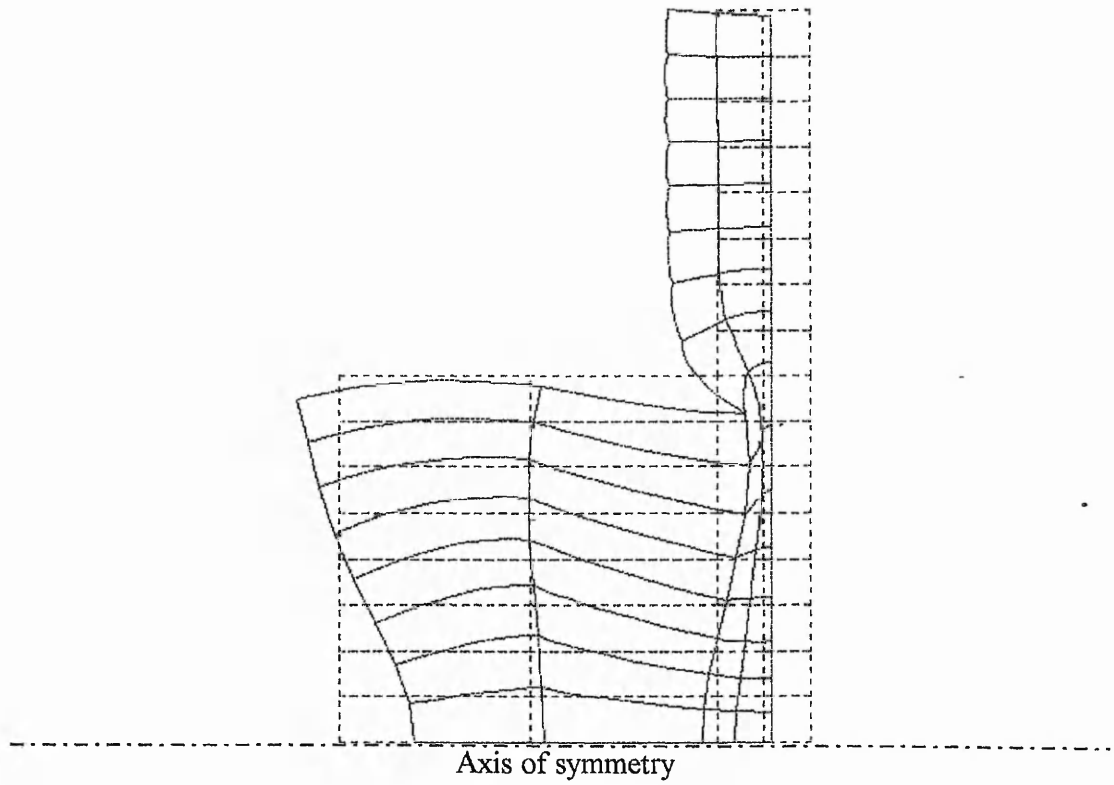

Fig. 2.22 Mode 6 at 292 kHz, shape M_{42}. The stationary transducer position is represented by the dashed lines. The model is axisymmetric about the base line. The transducer face (vertical right axis) has repeated freedoms on all nodes.

The change of the boundary conditions and excitation method has shown a shift in the modal frequencies. Some of the modes (M_{00}, M_{01}) seen in the free bi-laminar transducer are gone, indicating they are due to the plastic vibration.

Modal Notation	Electrically Excited Disc	Electrically Excited Transducer	Transducer Face Forced with Repeated Freedoms	Acoustically Excited Transducer
M_{01}	137	94.5	-	61.5
M_{10}	-	-	-	108
M_{11}	-	125, 149	121.5, 152	119, 149
M_{21}	180	178	173	176.5
M_{22}	258.5	234, 259	222	-
M_{33}	-	-	-	249
M_{42}	-	-	292	-
M_{43}	317	-	-	-
M_{44}	340	-	-	-
M_{98}	718	-	-	-

Table 2.2 Summary of resonant frequencies [kHz] and piezoelectric mode notation [$M_{i,j}$] for the plain disc and bi-laminar disc transducer models. The modelling method is indicated at the top of each column.

The M_{21} and M_{22} modes have seen a frequency drop from their plain disc equivalents (180 to 173 kHz and 258.5 to 222 kHz respectively). Other modes, such as M_{11} at 152 kHz, have increased slightly from their free boundary condition equivalent i.e. M_{11} at 149 kHz in fig. 2.14.

Traditionally, the free vibration condition is assumed and for many applications this provides an adequate prediction. The practitioner would be aware that attaching the piezoelectric disc to a plastic wear plate would cause a slight change to the resonant frequency in such a simple design. However, more complex boundary conditions or a complex transducer design may require more detailed predictions. Predicting this more complex behaviour of varied boundary conditions and loading is where FEM comes into its own as a tool.

2.2.2.1 FE Prediction of the Transducer Resonance Spectrum

In section 2.2.2, the resonances have been considered in terms of the modal shapes of vibration. Using FE analysis, a corresponding resonance spectrum can be produced. The data in fig. 2.23 corresponds to the modal shapes seen in fig. 2.17 to 2.22, predicted using the forced sinusoidal excitation, using repeated freedoms on the transducer face. The output voltage against frequency response in the 50-250 kHz range shows the most powerful mode at 173 kHz. This is the third mode, which is the M21 concave-extension type mode. The spectrum indicates very high Q peaks because of the absence of damping. The frequency sampling interval of 0.5 kHz means that only the resonant frequencies nearest to an interval value will have large amplitude peaks, while others may be poorly represented on the same scale (e.g. the 152 kHz mode). It must be borne in mind that these output ratios would change with the application of damping.

Simple disc vibration theory suggests that radial modes are important in the vibration of piezoelectric ceramics for materials evaluation [6]. Radial modes are strong modes of vibration and are naturally free from unwanted (spurious) responses, unlike some more complex, high frequency modes. This means that the transducer will behave predictably and consistently to the same input, which is an important feature for most applications. It is the radial mode that is responsible for the main resonant frequency in most designs of transducer used for AE detection, which dominates the response of such a device.

2.2.3 Acoustic FE Analysis

Now that the conventional FE methods of modelling vibration problems had been used, an acoustic analysis was performed to investigate transducer response further. As discussed in Chapter One, this type of FE analysis utilises the fluid finite and boundary elements of the PAFEC Vibroacoustics software. A point source in the fluid region emits a sinusoidal acoustic wave at a specified frequency. This travels through the fluid, in this case water, until it strikes the transducer surface. The pressure wave then becomes an internal wave in the solid, displacing the plastic and piezoelectric nodes.

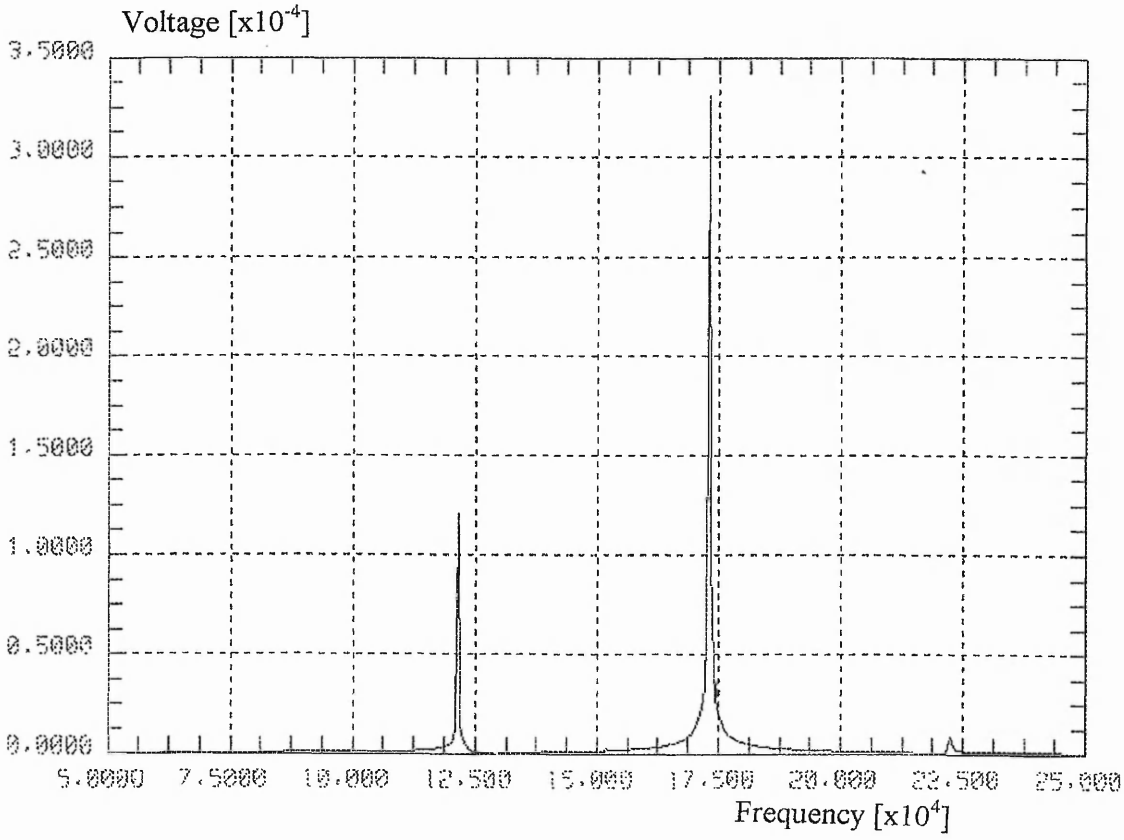

Fig. 2.23 Resonance spectrum for the bi-laminar disc transducer, predicted by a forced sinusoidal excitation, using repeated freedoms on the face nodes in the x-direction (i.e. normal to the transducer face). The graph shows output voltage from the transducer against frequency, in the range 50-250 kHz.

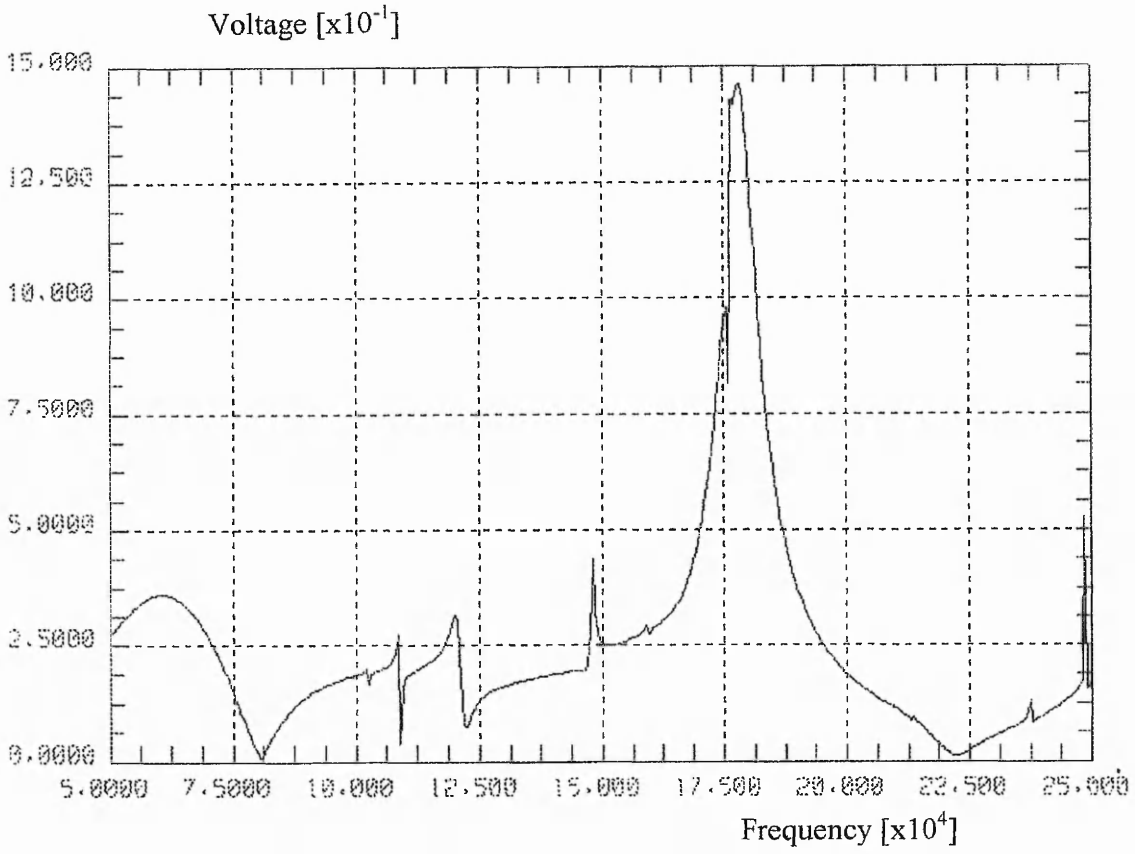

Fig. 2.24 Acoustic FE prediction of the bi-laminar disc transducer resonance spectrum. The graph shows output voltage from the transducer against frequency, in the range 50-250 kHz.

The acoustic FE modelling provides a suitable method for determining the transducer response in a more realistic manner. The advantage over the forced sinusoidal approach is that all of the nodes on the transducer face can be individually excited without using repeated freedoms. This allows the mode shapes of the transducer to be more realistic and free in their movement. The second advantage over the purely electrical excitation is that more modes seem to be observed. The fluid also provides a natural form of radiation damping to the transducer whilst avoiding the problems associated with an acoustic point source in a solid and, the associated complex propagation in this solid. Some other workers have found that simulating a fluid region, by means of an acoustic impedance, provided successful results [**42**].

The frequency spectrum in fig. 2.24 was predicted by an acoustic FE model for the bi-laminar disc transducer seen in fig. 2.1, and shows a main resonant frequency of 176.5 kHz.

As seen in fig. 2.24, the transducer responds well between 50 and 250 kHz and the output is relatively small above 250 kHz (not shown). No other peaks are predicted which have an amplitude above fifty percent of the main resonant output voltage. This main peak output voltage is just under 1.4 volts for the input source strength used. The fluid provides natural damping and therefore, the amplitudes of the output voltage have relative meaning. The obvious difference in the shape of the acoustic FE model spectrum, in fig. 2.24 and that of the forced sinusoidal FE model, in fig. 2.23, is due to the damping effect of the fluid. Its effect is to lower the Q of the resonant peaks whilst reducing the difference between their amplitudes.

The fact that the amplitude of the main resonance is larger than the other resonant peaks, in this frequency range, indicates that this is a strong mode of excitation (which was also suggested by the forced sinusoidal model).

The modal shapes concentrated in the 50-250 kHz frequency range are shown in fig. 2.25 to 2.30. At 61.5 kHz, the M_{01} mode of vibration involves an almost piston-like motion of the piezoelectric in the thickness direction (fig. 2.25).

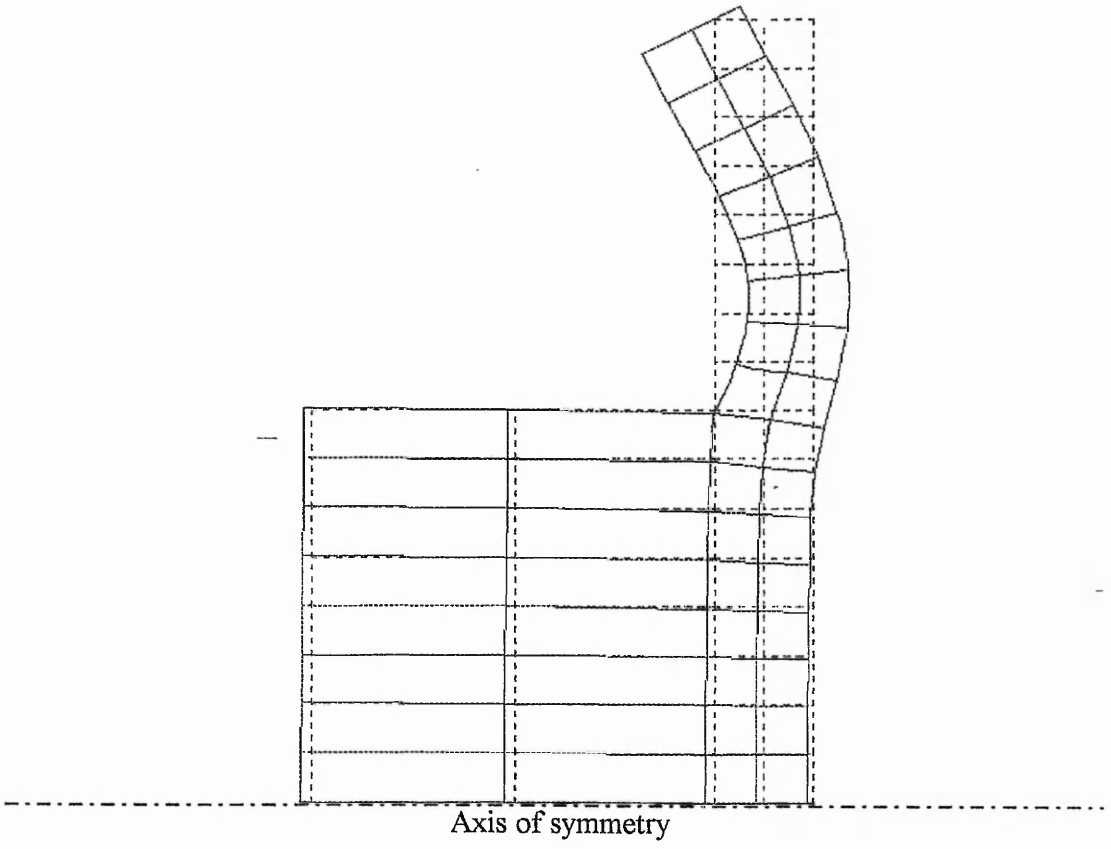

Fig. 2.25 Mode 1 at 61.5 kHz, shape M_{01}. The stationary transducer position is represented by the dashed lines. The model is axisymmetric about the base line. The fluid is to the right of the transducer face and is not shown.

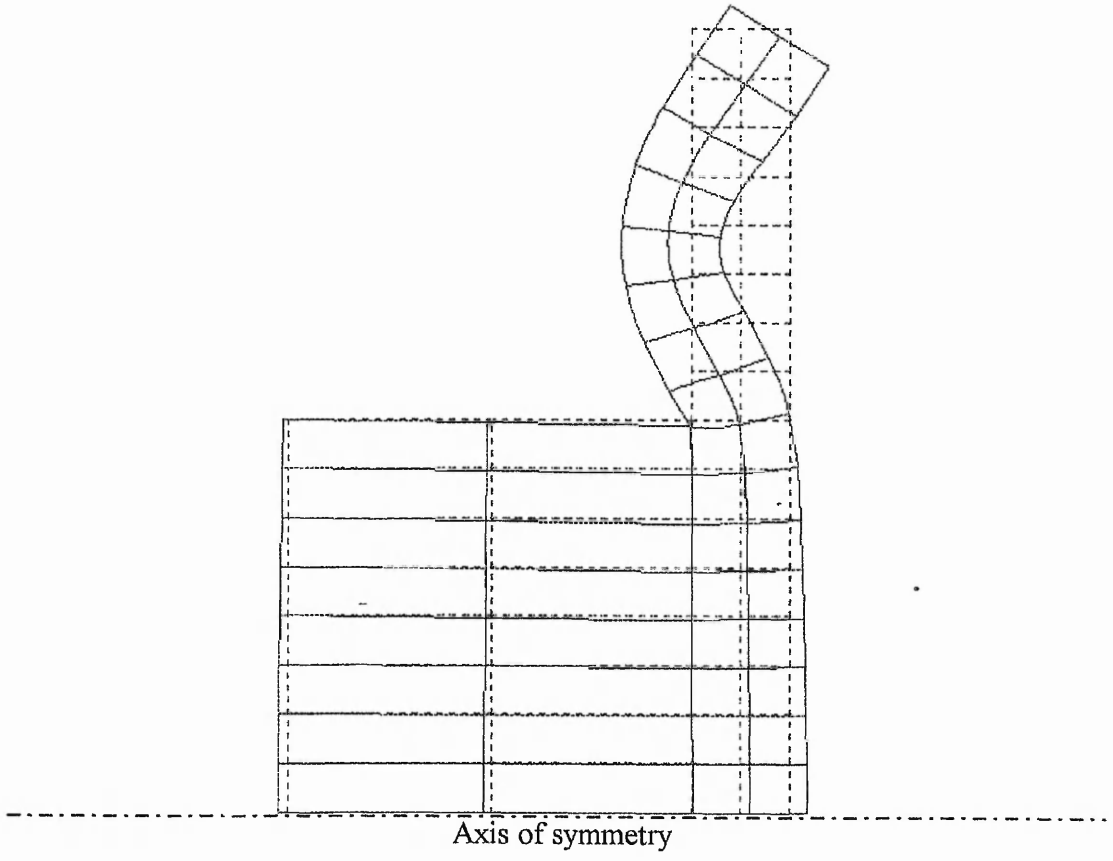

Fig. 2.26 Mode 2 at 108 kHz, shape M_{10}. The stationary transducer position is represented by the dashed lines. The model is axisymmetric about the base line. The fluid is to the right of the transducer face and is not shown.

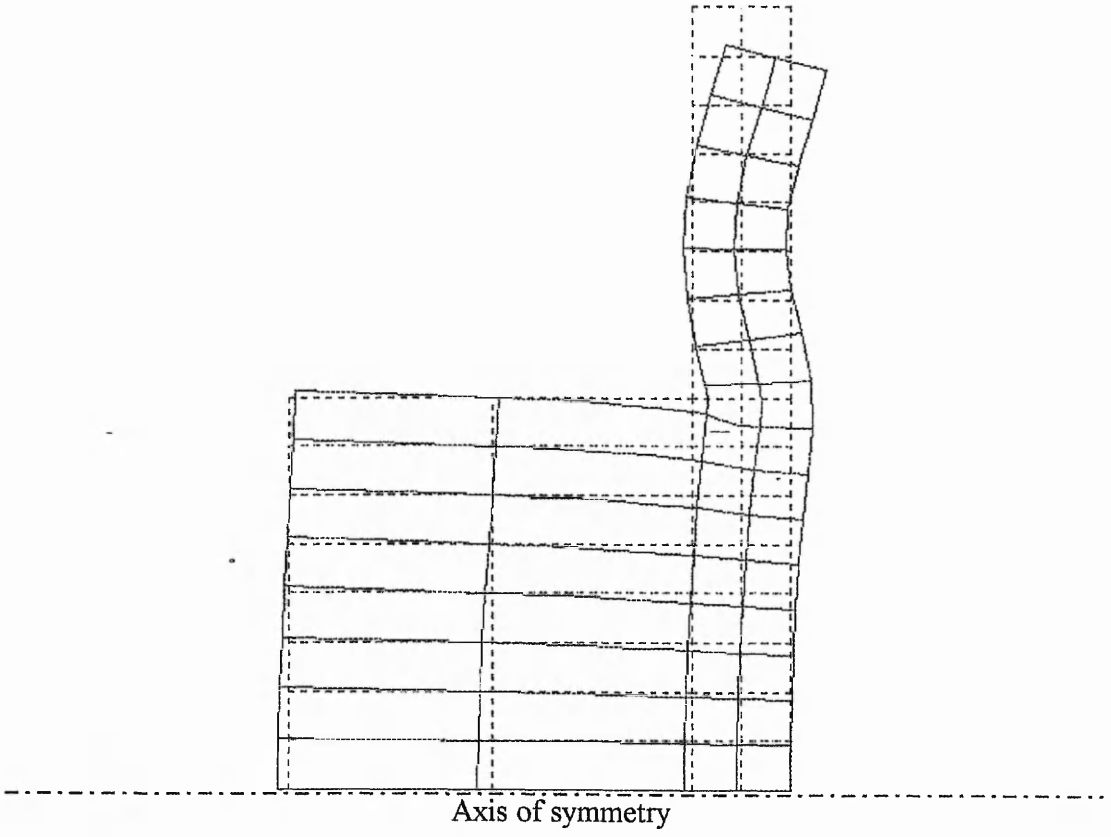

Fig. 2.27 Mode 3 at 119 kHz, shape M_{11}. The stationary transducer position is represented by the dashed lines. The model is axisymmetric about the base line. The fluid is to the right of the transducer face and is not shown.

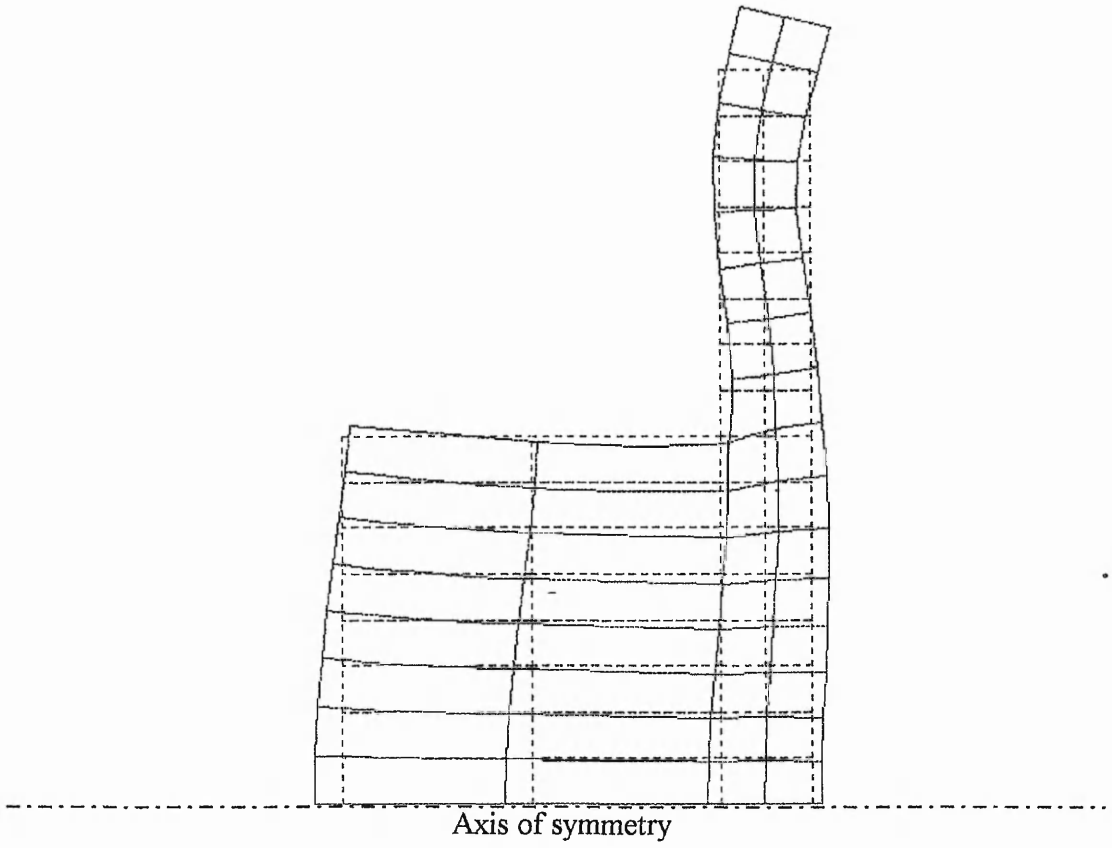

Fig. 2.28 Mode 4 at 149 kHz, shape M_{11}. The stationary transducer position is represented by the dashed lines. The model is axisymmetric about the base line. The fluid is to the right of the transducer face and is not shown.

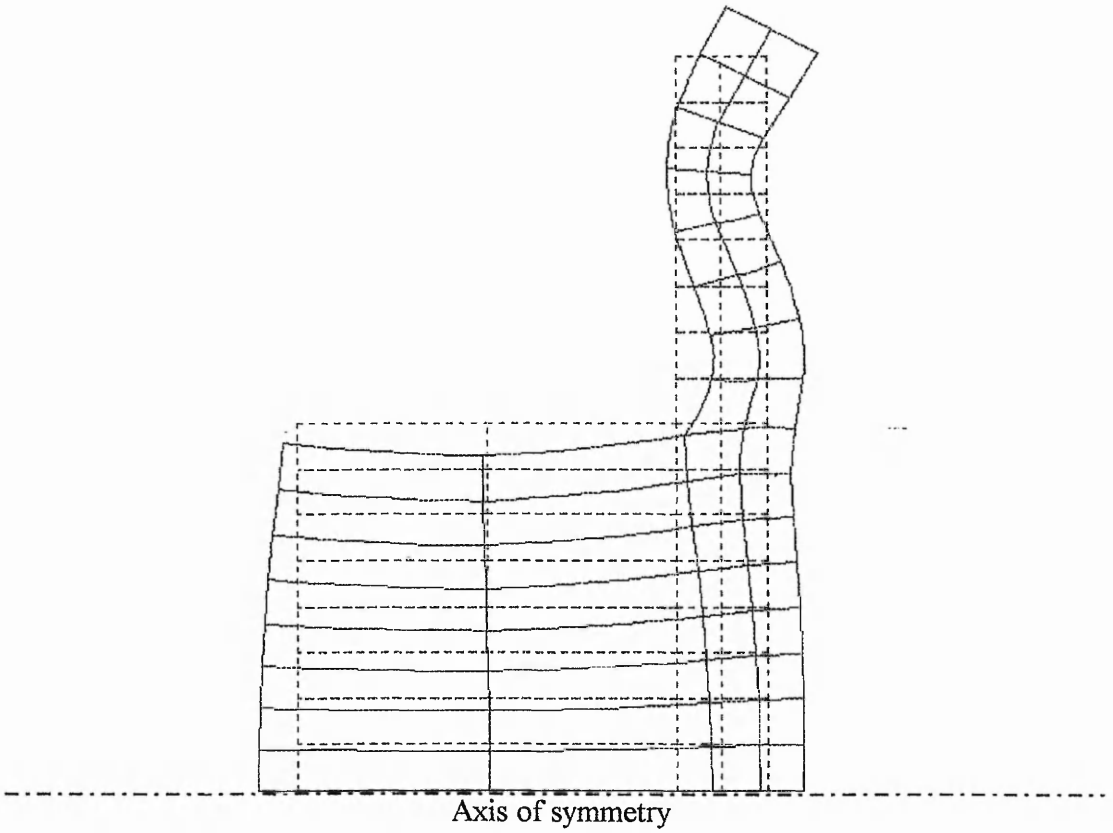

Fig. 2.29 Mode 5 at 176.5 kHz, shape M_{21}. The stationary transducer position is represented by the dashed lines. The model is axisymmetric about the base line. The fluid is to the right of the transducer face and is not shown.

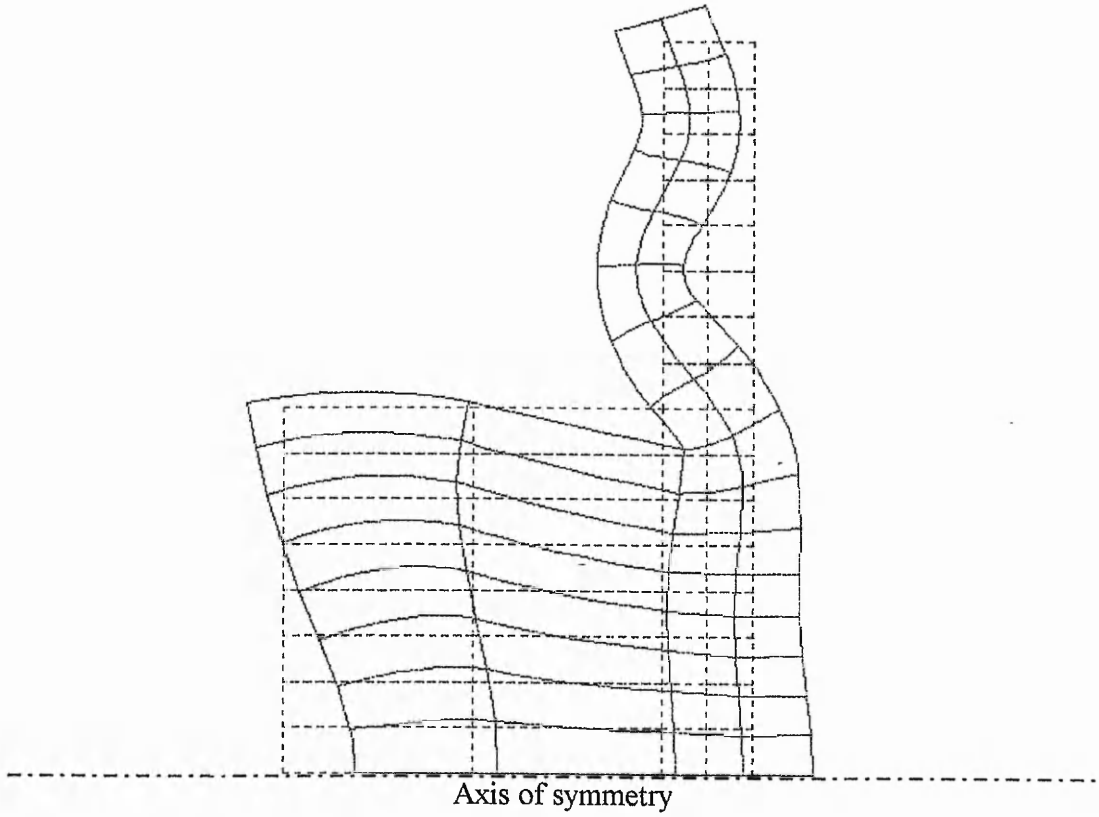

Fig. 2.30 Mode 6 at 249 kHz, shape M_{33}. The stationary transducer position is represented by the dashed lines. The model is axisymmetric about the base line. The fluid is to the right of the transducer face and is not shown.

Beyond the PZT, the plastic was displaced in a circular-bending mode in the same direction as the piezoelectric.

Similar motion is observed in fig. 2.26 at 108 kHz with an M_{10} mode, except that the plastic is bending in the opposite phase to that seen in fig. 2.25. At 119 kHz, more radial vibration is observed in the plastic (fig. 2.27). The piezoelectric M_{11} mode has most movement in the thickness direction at the centre. In the M_{11} mode at 149 kHz, larger motion is seen in the thickness direction, and is most pronounced at the centre (fig. 2.28). Radial and bending motion is seen in the plastic.

Mode 5 at 176.5 kHz produces the highest amplitude voltage response to the acoustic wave. The M_{21} mode shape in fig. 2.29 involves radial-compression while the centre thickness expands. It is this large displacement at the centre, in the direction of polarisation, which causes the large voltage. This mode shape shows half a wavelength of deformation in the thickness direction and a quarter wavelength in the radial direction. This equates to a half wavelength across the disc diameter. Plastic disc motion is complicated beyond the PZT edge, showing circular-bending in one direction and then the other direction, as the radius increases.

At 249 kHz there is thickness compression at the centre, with a shearing type radial motion that suggests an M_{33} mode (fig. 2.30). The plastic is again bending in both directions beyond the PZT edge.

Confidence in the predicted modes is high, due to similarities between these results and those of other workers [1, 39]. A bi-laminar disc transducer for airborne work also showed similarities [10], which again increases the confidence in the FEM (fig. 2.31).

Table 2.2 in section 2.2.2 has a summary of all of the predicted resonant frequencies from the various FE methods, along with their modal notation. The modal notation integers are assumed to follow the convention in which the magnitude (n) of the integers increases proportionally to the resonant frequency, i.e. f_r is proportional to $n = \sqrt{i^2 + j^2}$.

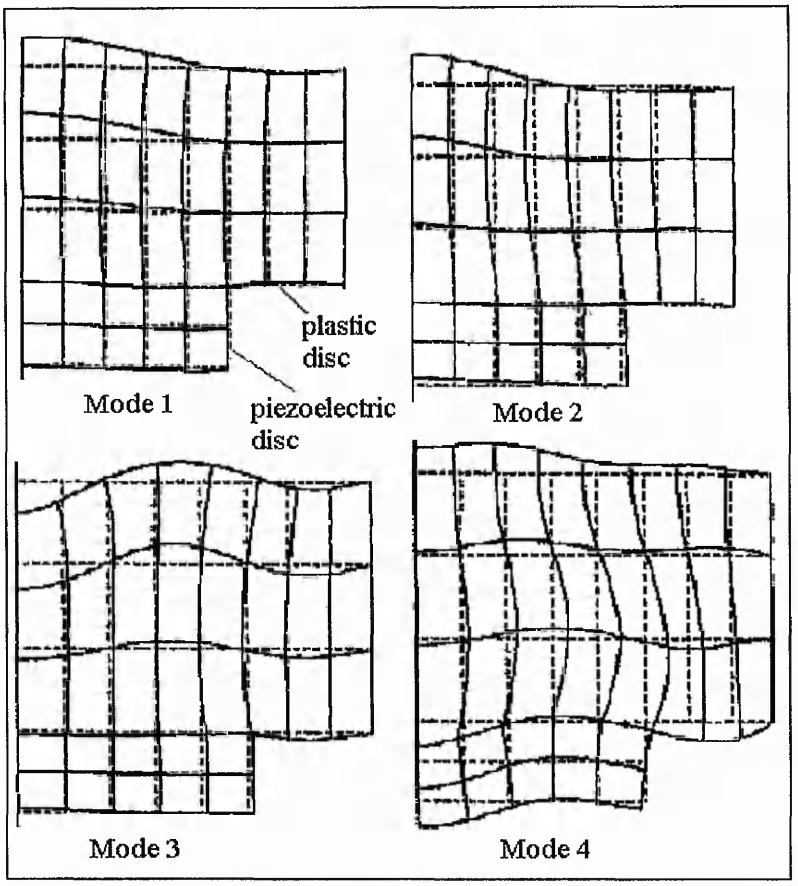

Fig. 2.31 Mode shapes 1-4 modelled by Durris et al. [**10**]. The stationary transducer position is represented by the dashed lines. The model is axisymmetric about the left hand edge. (Note the piezoelectric is the thin disc).

This means that low frequencies should produce low order modes (such as M_{01}), while high frequencies should produce high order modes (such as M_{44}). Because the mode shapes seen in fig. 2.5 to fig. 2.30 were often difficult to classify exactly, this rule was used to check that appropriate notation was being used. The modal notation in table 2.2 (section 2.2.2) adheres to this rule and is considered a suitable method of describing the piezoelectric mode shapes.

2.2.4 Experimental Method used for Comparison with FEM

Three distinct methods of FEM have been used to predict the resonant frequencies of the bi-laminar transducer. In order to choose the most suitable method, there is a need to compare the predicted data with data obtained by experimental measurement.

The experimental method used is described fully in the standard IEEE 177 [**48**]. It is based on an electrical π network shown in fig. 2.32, in which the piezoelectric transducer is driven by a sinusoidal voltage over a range of frequencies and the output voltage response is measured. Suitable values for the components R_T, C_L (this was optional) and L_0 in fig. 2.32 were found to be 1kΩ, 0F and 0.1H respectively.

The sinusoidal signal was supplied by a HP 33120A arbitrary waveform generator, controlled by a PC QBasic computer program via the RS-232 port. A data acquisition processor (DAP) board was used to record the voltage response of the transducer to the given input signal [Appendix II]. The frequency of the input signal was swept through a wide range of frequencies in order to locate the resonant frequency of the transducer.

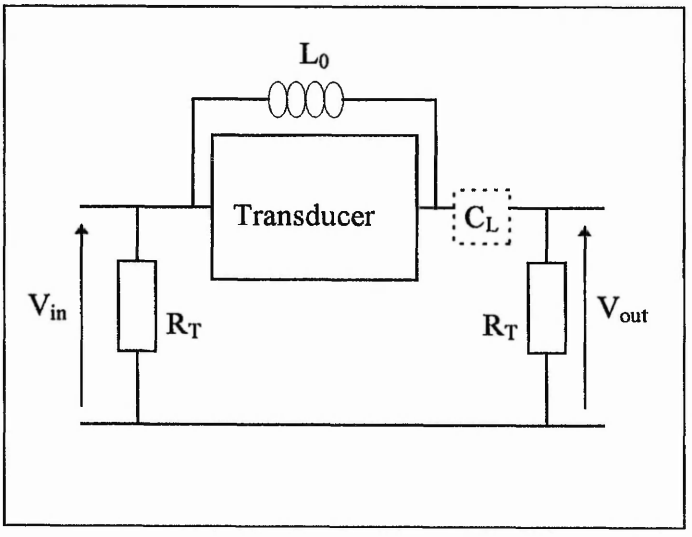

Fig. 2.32 π Network used in IEEE 177 testing standard.

The frequency at which the peak output voltage occurs is the motional resonance frequency f_s, or series resonance, and occurs when the electrical impedance of the transducer is at a minimum. The experiment was repeated several times to obtain an average result and a typical transducer output is seen in fig. 2.33.

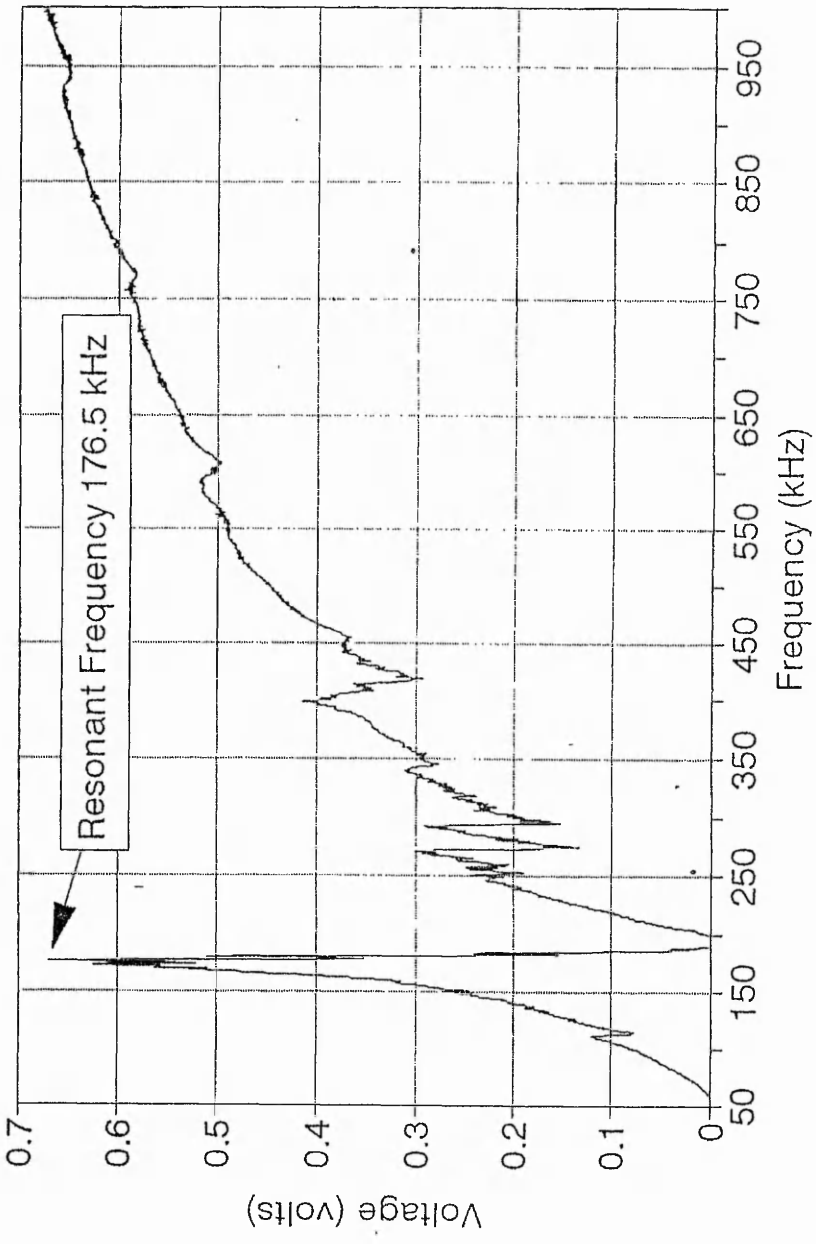

Fig. 2.33 Output voltage against frequency measured by an experimental π network, for the bi-laminar disc transducer.

2.2.5 Comparison of FE Model Predictions and Experimental Results

Using the method described in section 2.2.4, the main transducer resonant frequency was found to be at 176.2 kHz, by taking the mean of several values. The closest FE predicted resonance to this was 176.5 kHz, seen in the acoustic FE model. The next closest was 178 kHz, predicted by the electrically excited model of the free transducer.

Due to the close match between the acoustic FE prediction and the experimental value for the resonant frequency and, the fact that the acoustic model provides individual nodal excitation at the transducer face, as well as partial loading to the transducer with the fluid region, it was chosen as the primary modelling method. The undamped sinusoidal analysis could be used as a comparison for other investigations as it also provides a reasonably accurate and faster method of resonant frequency prediction.

2.3 INVESTIGATION OF PIEZOELECTRIC DISC GEOMETRY ON PERFORMANCE

2.3.1 Resonant Frequency variation with Disc Diameter to Thickness Ratio

With the acoustic wave input established as a suitable FE modelling technique, a basic investigation into the variation of resonant frequency with transducer geometry was carried out. For the case of a PZT-5A disc mounted on a thin plastic protective facing, the acoustic FE model was run with **various thicknesses** of piezoelectric disc with a **constant diameter**, thus varying the diameter/thickness ratio (D/t ratio). The dimensions of the plastic facing disc were left constant.

Another study involved using the conventional FE method of sinusoidally varying the voltage across the electrodes. Various D/t ratios for a piezoelectric disc were modelled by varying the **diameter** for a constant disc thickness of 5.01 mm. There was **no** plastic facing disc for this model and so the resonant frequency predictions could be compared with other work. These could also be compared to the transducer, modelled using acoustic excitation.

The frequency thickness product (MHz mm) is plotted against the D/t ratio for several modes of the electrically excited plain disc in fig. 2.34, and follows the patterns seen by other workers for plain PZT-5A discs [**1**]. Taking a D/t ratio of 2, the modes and frequencies correspond to those seen in table 2.2 for the plain disc i.e. mode 2 in fig. 2.34 is the M_{21} mode, at 180 kHz and mode 3 is the M_{22} mode, at 258.5 kHz.

The main resonant frequency of the bi-laminar disc transducer is also plotted as a frequency thickness product against D/t ratio in fig. 2.34. In this case, the piezoelectric disc **thickness** was varied while the diameter remained constant. The plastic disc dimensions remained constant. An acoustic FE analysis was used, as described in section 2.2.3.

Referring to fig. 2.34, the curve for the variation of the main resonant frequency for the bi-laminar disc transducer (labelled "transducer") is a different shape to that of the plain disc. This curve indicates how the transducer's main mode of vibration changes, as the piezoelectric disc thickness changes. The main resonant frequencies caused by disc thickness variation are shown in table 2.3.

For the bi-laminar disc transducer, with a D/t ratio of 2 and a resonant frequency of 176.5 kHz, the nearest plain disc mode is mode 2 at 180 kHz. This mode is the M_{21} mode, which is similar to the M_{21} mode seen for the transducer's piezoelectric disc alone. For a plain disc to have a resonant frequency of 176.5 kHz for mode 2, it would require a larger D/t ratio.

This suggests that the plastic effectively increases the D/t ratio of the piezoelectric to which it is attached. This explains why the M_{21} mode seen in the transducer is at 176.5 kHz and not at 180 kHz, as seen in the electrically excited plain disc, with a D/t ratio of 2. A D/t ratio of 2.1 corresponds to a piezoelectric diameter of 10.52 mm with a 5.01 mm thickness, or a 4.77 mm thickness with a 10.02 mm diameter. The effective increase in D/t ratio of the piezoelectric caused by the plastic, lowers the resonant frequency of other modes, such as the M_{01} mode. From table 2.2 it is difficult to compare other modes because their shapes differ slightly.

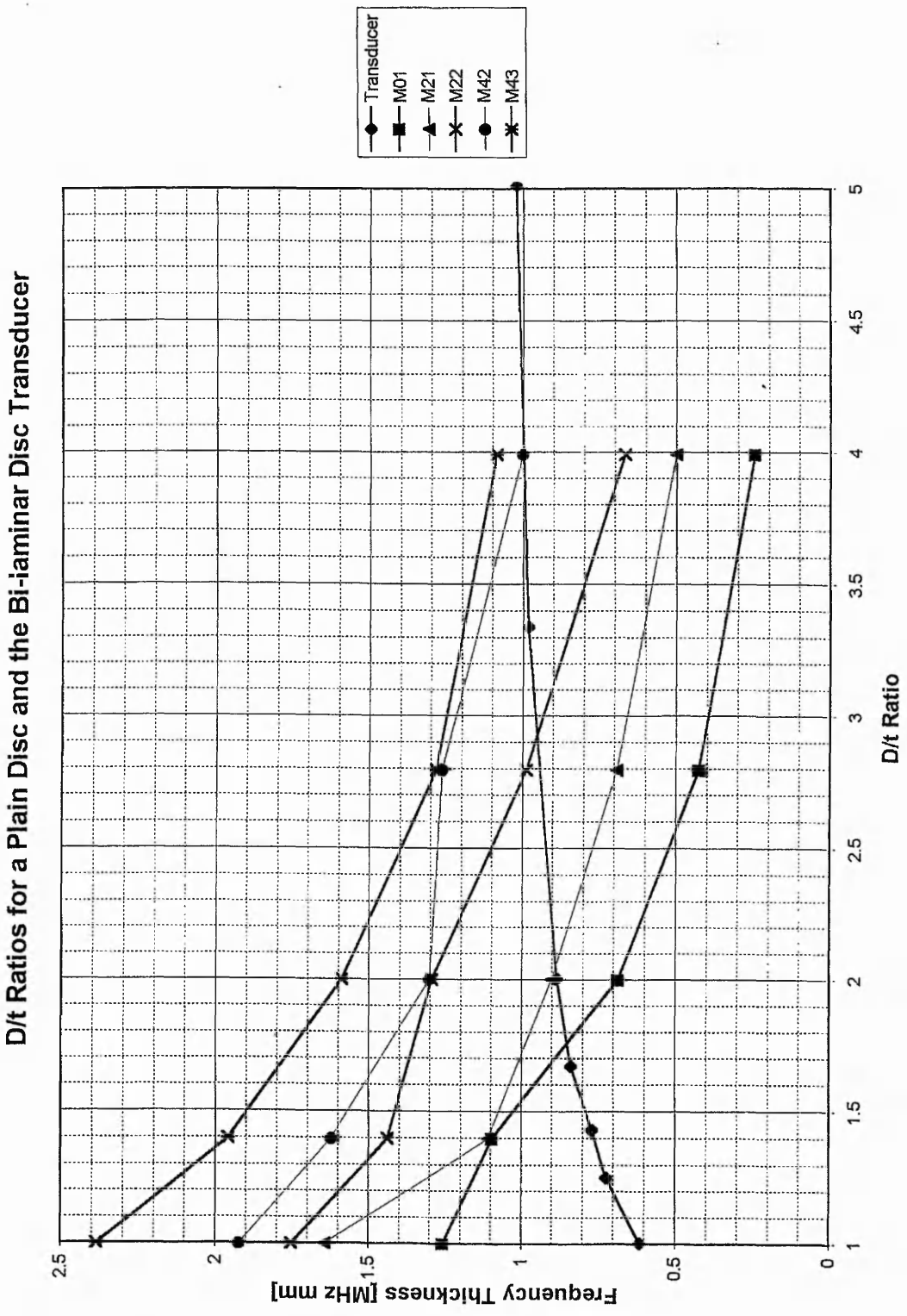

Fig. 2.34 Frequency thickness product against D/t ratio for five modes of a plain piezoelectric disc and for the main resonant frequencies of the bi-laminar disc transducer.

Because all of the FE transducer models predict lower frequencies of several piezoelectric modes than for the free disc, suggests that the constraining effect of the plastic is to increase the D/t ratio of the piezoelectric disc.

Fig. 2.34 provides an approximate method of predicting the resonant frequency of a given transducer design, using different piezoelectric disc dimensions.

2.3.2 Effect of Piezoelectric Disc Thickness on Transducer Sensitivity

As will be seen later, there are various definitions of sensitivity for transducers. FE has been used to model the effect of varying the piezoelectric disc thickness, with the transducer responding to a point source excitation in the fluid. The magnitude of the source is the same for all of the models and, therefore, the voltage developed by the piezoelectric will give a direct indication of the relative sensitivities.

Disc Thickness [mm]	Resonant Frequency [kHz]	Output Voltage [volts]
10	123	2.9
7	153.5	1.7
5	176.5	1.4
3	196	0.7
2	204	0.7
1	216	0.5

Table 2.3 Summary of acoustic FE model predictions of the main resonant frequency for the bi-laminar disc transducer with a constant diameter (10.02 mm) piezoelectric disc.

Considering the voltage developed by the various disc thicknesses (table 2.3), it can be seen that there is an increase in output voltage for an increase in disc thickness, with the diameter kept constant. A thickness increase in the disc is accompanied by a shift in the resonant frequency, which must be considered when optimising any transducer design. The data in table 2.3 gives an indication of how to increase, or decrease, the transducer sensitivity and can be used in conjunction with the frequency thickness product against D/t ratio data in fig. 2.34 to help in design considerations.

2.3.3 Transducer Sensitivity Issues

The issue of transducer sensitivity, important as it is, continues to raise the question of how to define sensitivity suitably. For detection of ultrasound using piezoelectric transducers, one definition of sensitivity that might be used is the output voltage per unit input at the transducer face. Some initial investigations used the displacement normal to the transducer face as the input i.e. along the axis of polarisation.

The problem with using displacement at the transducer face to define the transducer sensitivity is that the displacement often varies from point to point, due to the complex vibration modes of resonant devices and the type of source exciting the transducer. The electrodes average the transducer's electrical output to a single value and so the output voltage per unit input displacement at the transducer face will effectively vary from point to point. Therefore, if the transducer sensitivity were defined as the output voltage per unit displacement at the transducer face (V/m) then, strictly speaking, the exact position at which this sensitivity is obtained should be specified. The user of a transducer may find that the sensitivity of the device varies depending upon the specific application and the stated sensitivity may not be attainable.

With computer modelling using finite elements, exact definitions of sensitivity could be obtained for a variety of situations. The sensitivity in volts per metre (V/m) could be stated at exact positions on the transducer face, or for the case of all points on the face moving uniformly. This would allow the user to decide which value was most appropriate for a given application and, allow selection of the most suitable transducer. Another definition for sensitivity might be the output voltage per unit input force. This type of definition is suitable if the transducer face is excited uniformly, as in the FE model using repeated freedoms (section 2.2.2). However, in practice this may not be the case, due to the complex nature of the transducer vibration. Again, more specific definitions could be employed with the use of FE modelling.

With the FE modelling considered thus far, the input to each type of model has been constant in magnitude. For the forced sinusoidal analysis, the input force was constant

and so the variation of output voltage is a direct measure of the transducer's sensitivity to different frequency components. For the acoustic FE analysis, the strength of the acoustic point source is constant and the output voltage again provides a direct measure of the transducer's sensitivity. With the source being away from the transducer face, the acoustic FE model is likely to give a more universal definition of sensitivity because the transducer face is excited fully, whilst being free in its response.

2.4 FE ANALYSIS OF TRANSDUCER MOUNTING CONDITIONS

When used in materials evaluation, the piezoelectric transducers are often mounted onto, typically, a composite or metallic structure under test. The FE model was now used to see what effect mounting the transducer would have on transducer response. Clearly this might be an issue when undertaking transducer design for a specific application.

2.4.1 Enforced Harmonic Motion Analysis

Propagation of acoustic waves through an infinite solid (as opposed to a fluid) are not taken into account by the acoustic FE analysis. Later, attempts to model such effects will be considered in Chapter Four. At this stage, a study of the effect of transducer mounting will be considered.

To simulate a transducer attached to a large object that has a much larger mass and geometry, an enforced harmonic displacement analysis was used, which involves the application of a harmonic displacement to prescribed points on the FE model. In this case, a displacement was applied to the outer surface of a steel plate to which the transducer was attached. When computing the response over a large range of frequencies this type of FE analysis is very fast. Analysis was also carried out on the transducer alone, to compare the results in the unmounted state with those already found by the other models. The transducer face was given repeated freedoms so that it behaved in a piston-like manner. A large steel plate will vibrate in flexural modes and therefore, the surface under the transducer will be displaced normal to the transducer face and, over a small area, give a piston-like excitation to the transducer face.

Fig. 2.35 shows the piezoelectric transducer resonance spectrum. The results for this unmounted transducer differ from those predicted by the acoustic analysis and for the forced sinusoidal analysis. Four peaks occur at 117, 140, 212 and 225 kHz. However, there is no peak in the 175 kHz range found by both the acoustic FE model and experimental measurement. Comparable frequencies are the 117 kHz and 225 kHz, which are close to frequencies seen in the forced sinusoidal and electrical analyses. All models, including the acoustic one, show a mode in the 120 kHz region. This suggests that it is an easy mode of vibration to excite by all excitation methods, due to the fact that most transducer displacement is in the thickness direction and not the radial one. Variations in the frequency of this mode are caused by the presence of the plastic and, therefore, depend on how the plastic face is modelled i.e. whether the nodes are free, or whether the face nodes are given repeated freedoms.

The spectrum when mounting the transducer on a 50 mm diameter, 25 mm thick, steel plate, still shows a large peak at 140 kHz (fig. 2.36). The other large peaks have disappeared, but there are small peaks at 160 and 186 kHz.

Varying the thickness of the steel plate creates variations in the resonance between 130 and 140 kHz, with responses summarised in table 2.4.

Plate thicknesses of 25, 15, 10 and 5 mm were used. As the plate thickness decreased, the amplitude of the resonant peaks varied and more peaks were observed. The largest amplitude voltages in the 130-140 kHz range were achieved with a 10 mm thick plate (table 2.4). The smallest amplitudes being achieved with a 5 mm plate (table 2.4 & fig. 2.37).

Enforced harmonic analysis predicts a main resonant frequency for the system of transducer and plate of 140 kHz, with other resonance peaks present as indicated in table 2.4. These resonances occur at different frequencies or with different amplitudes, depending on the thickness of the mounting plate used.

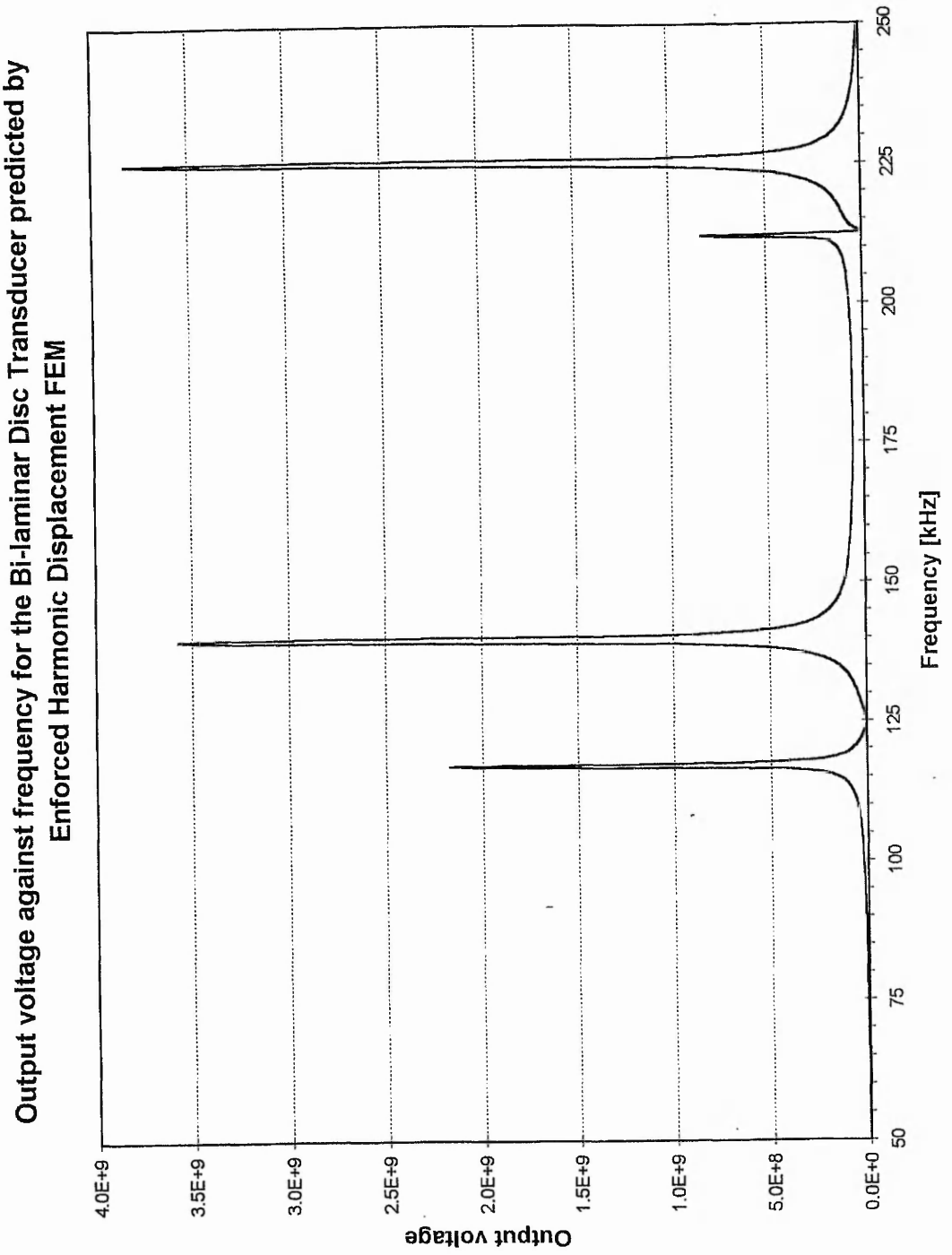

Fig. 2.35 Output voltage against frequency for the unmounted bi-laminar disc transducer, predicted by an enforced harmonic motion FE analysis.

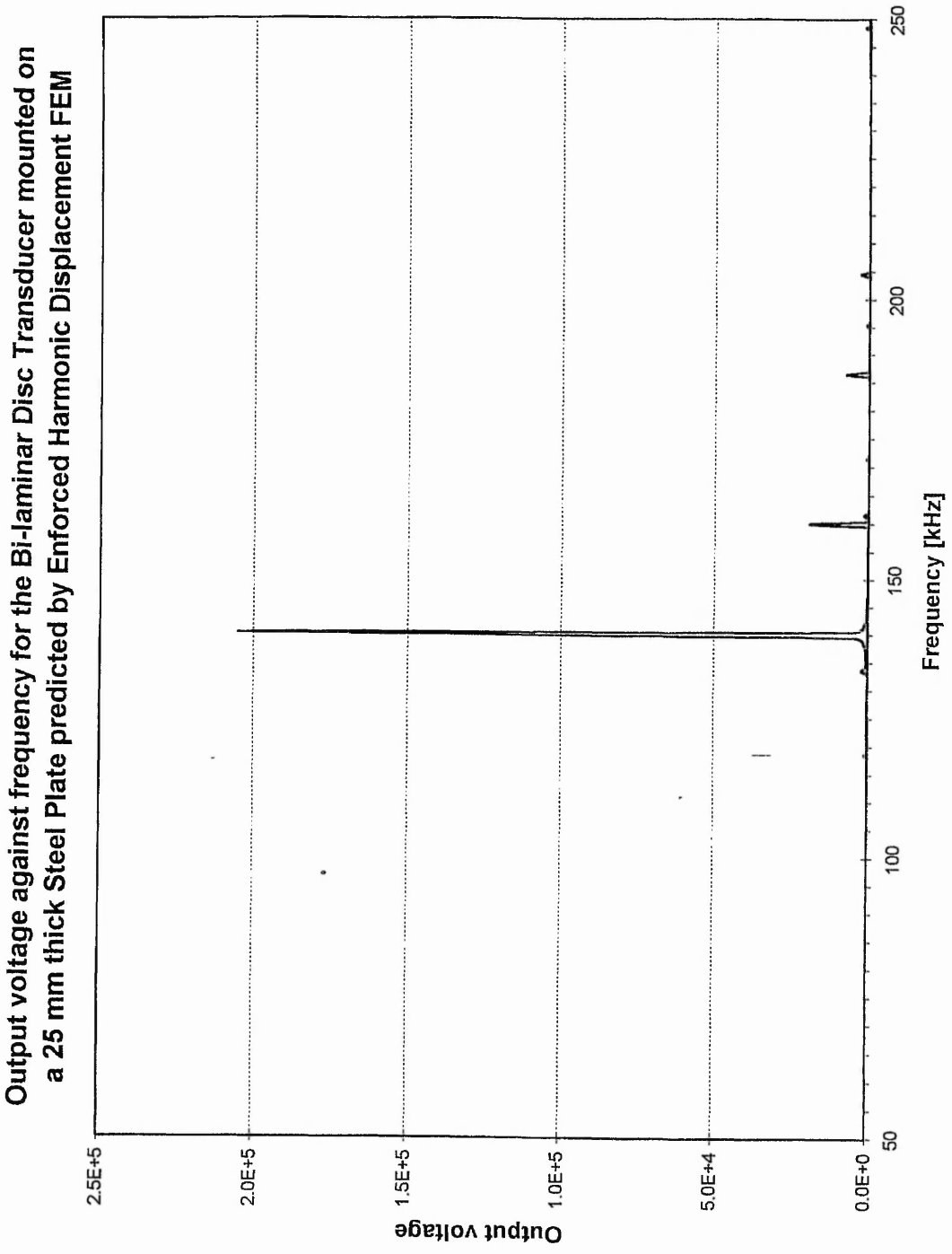

Fig. 2.36 Output voltage against frequency predicted for the bi-laminar disc transducer, mounted on a 25 mm thick steel plate, using an enforced harmonic motion FE analysis.

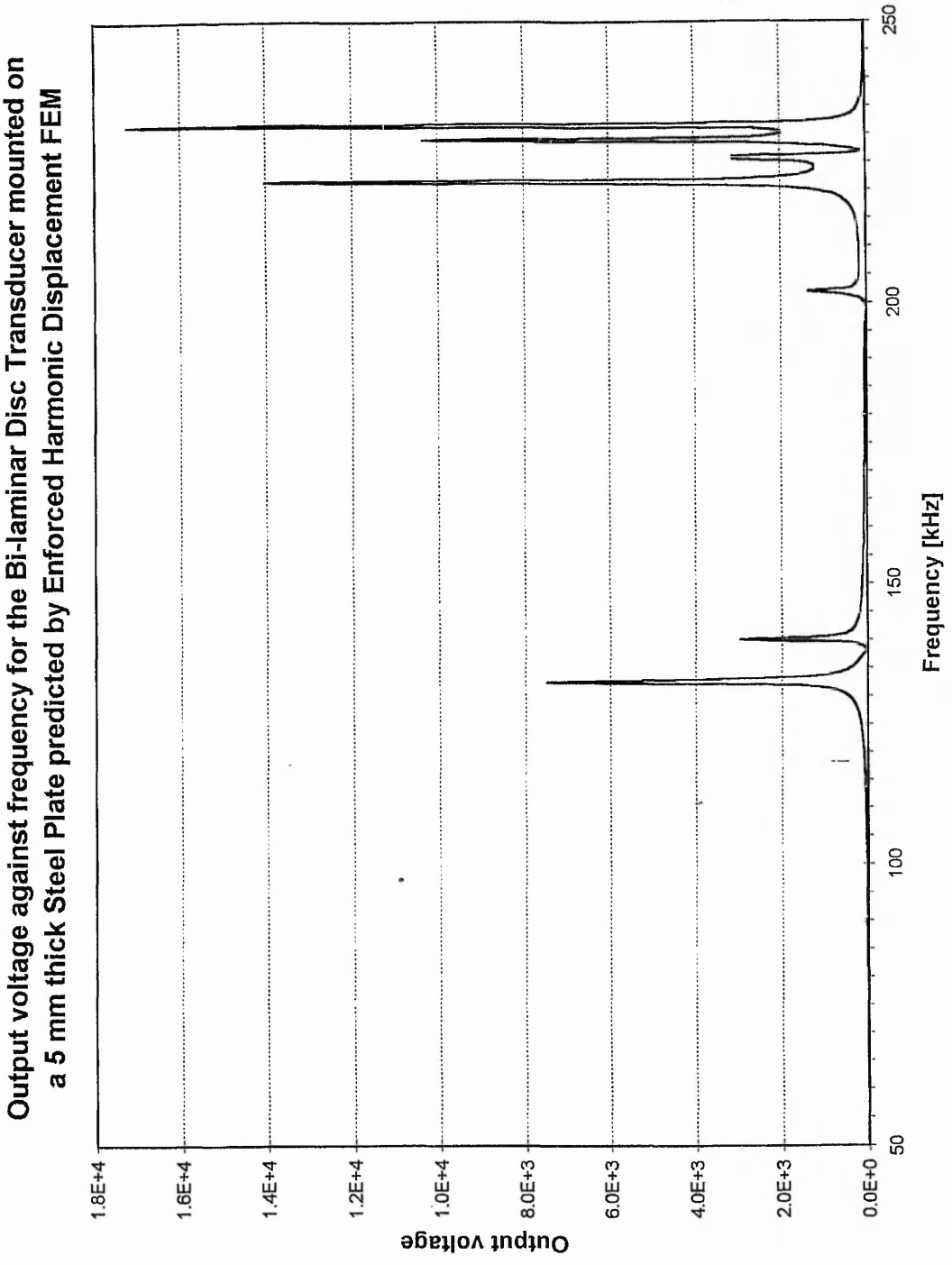

Fig. 2.37 Output voltage against frequency predicted for the bi-laminar disc transducer, mounted on a 5 mm thick steel plate, using an enforced harmonic motion FE analysis.

The aim of this study was to consider the effect of mounting the transducer on an infinite plate structure, but the constraints of the modelling require the use of a finite plate. A 50 mm diameter, 25 mm thick steel plate was used in the model and such a system would produce mechanical resonances outside the frequency range of study. However, some resonances will occur in the 50-250 kHz frequency range and therefore, influence the transducer response. When resonant frequencies of the plate occur close to, or at resonant frequencies of the transducer then mode coupling will produce the largest output amplitudes.

Plate Thickness [mm]	f_r	Output	f_r	Output	f_r	Output	f_r	Output	f_r	Output
	[kHz]	[volts]	[kHz]	[volts]	[kHz]	[volts]	[kHz]	[volts]	[kHz]	[volts]
25	133	0.02E5	**140**	2.05E5	160	0.20E5	186	0.08E5	204	0.03E5
15	98.5	0.27E4	117	0.18E4	**135.5**	4.46E4	240	0.18E4	246.5	0.70E4
10	134	2.97E5	**137**	3.35E5	148	0.48E5	158	0.09E5	137	0.13E5
5	133	0.75E4	140	0.30E4	221	1.4E4	229	1.04E4	**231**	1.72E4
no plate	117	2.19E9	140	3.59E9	212	0.83E9	**225**	3.83E9	-	-

Table 2.4 Summary of resonant frequencies and output voltage amplitudes predicted using the enforced harmonic displacement (EHD) FE for the bi-laminar disc transducer mounted to a steel plate. The main resonance is shown in bold type.

When carrying out experimental comparisons, the transducer was bonded to a 23 mm thick steel plate. Fig. 2.38 shows that the main unmounted resonance of 176.5 kHz (measured as electrical impedance variation) had only shifted to 184 kHz, with a satellite peak at 187.5 kHz. The EHD FE model does show a peak at 186 kHz and so the method of modelling shows some validity. However, the main model resonance is at 140 kHz for a 25 mm thick plate, and so the method is not very realistic.

Consideration is now given to traditional, theoretical approaches, which might be used to explain the frequency shift from the unmounted transducer state. The first is to consider the acoustic radiation loading of the transducer by the steel plate.

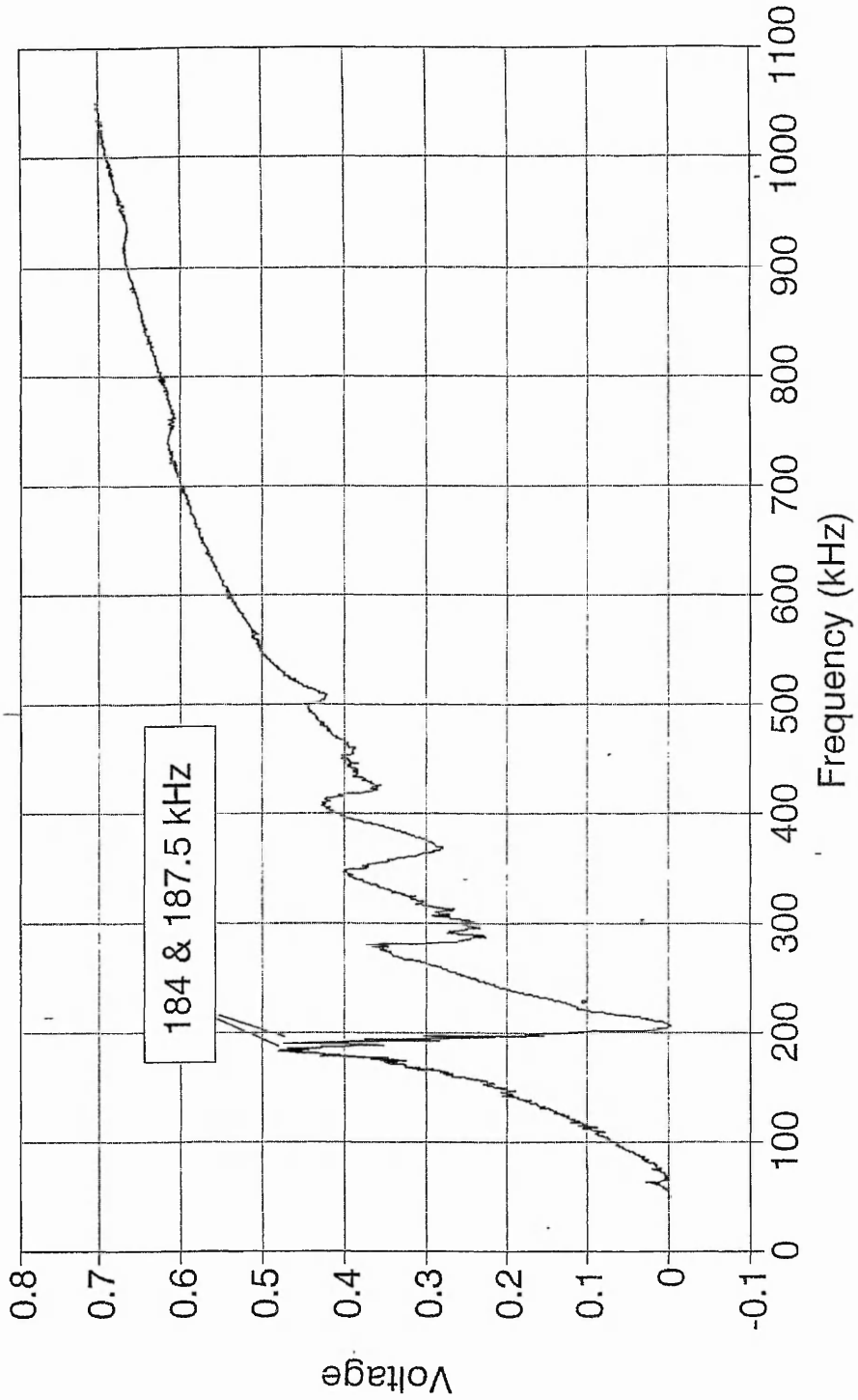

Fig. 2.38 Output voltage against frequency for the bi-laminar disc transducer, mounted on a 23 mm thick steel plate, measured experimentally using the π network in fig. 2.32.

2.4.1.1 Acoustic Radiation Loading of a Piston source

This classical theory, quoted in text by Kinsler and Frey [**49**] is based on a piston radiating into an infinite half space. The principle of reciprocity allows the effect of the medium on the acoustic output to be studied. When a piston is radiating into a medium, then the medium produces a radiation impedance (Z_r) consisting of a radiation resistance (R_r) and a radiation reactance (X_r). The radiation reactance is always positive and therefore, has the effect of adding a mass to the piston (transducer). This mass loading will reduce the resonant frequency of the transducer.

The additional mass m_r varies with frequency and is given by;

$$m_r = \frac{X_r}{\omega} = \pi a^2 \rho_0 \frac{X_1(2ka)}{k} \tag{1}$$

where $X_1(2ka)$ is a Bessel function defined by :

$$X_1(x) = \frac{4}{3}\left(\frac{x}{3} - \frac{x^3}{3^2 \cdot 5} + \frac{x^5}{3^2 \cdot 5^2 \cdot 7} - \ldots\right) \tag{2}$$

The radius of the piston (a) is taken as the radius of the piezoelectric disc and $k = \frac{2\pi f}{c}$.

Taking the transducer resonant frequency as 176.5 kHz, the value of added mass for steel is approximately 2.2×10^{-3} kg. This will reduce the transducer resonant frequency by approximately 42 kHz. The frequency was calculated using equation (3), in which s is the stiffness of the transducer, calculated using the same formula with zero added mass (m_r) and a frequency of 176.5 kHz.

$$\omega^2 = \frac{s}{(m + m_r)} \tag{3}$$

The added mass reduces the transducer resonant frequency from 176.5 kHz to 134.5 kHz, a frequency that is close to those predicted for all plate thicknesses by the enforced harmonic displacement FE analysis.

It is clear that by applying a uniform displacement to the face of the transducer then the transducer is subjected to piston-like input. Table 2.5 shows close agreement between the calculated frequency (134.5 kHz) and the nearest resonance predicted by the enforced harmonic displacement FE (EHD), demonstrating the accuracy of the FEM.

Plate thickness [mm]	Theoretical frequency [kHz]	EHD FE nearest resonance [kHz]	EHD FE main resonance [kHz]
25	134.5	134	140
15	134.5	135.5	135.5
10	134.5	134	137
5	134.5	133	233

Table 2.5 Comparison between the theoretical transducer resonant frequency and the enforced harmonic displacement (EHD) FE predictions for the bi-laminar disc transducer mounted to a steel plate.

The FE model also appears to take into account the thickness of the plate while the theory [**49**] assumes an infinite medium. This is suggested by the fact that the theory predicts one shift while the main resonant frequency in the FE models varies with plate thickness. However, for the experimental case of the transducer mounted to a steel plate, the transducer is clearly not behaving as an ideal piston because the main experimental resonant frequency is quite different to that of the EHD FE model (184 kHz compared to 140 kHz). Therefore, the transducer mounted on a steel plate must be modelled in a more suitable way.

2.4.2 Acoustic Analysis

Section 2.2.3 showed good agreement between the acoustic FE model and experimental measurement, suggesting the validity of using acoustic excitation as part of the FE modelling process. Due to this success, acoustic FE modelling will now be used to

model the transducer mounted to a steel plate, a problem already considered in section 2.4.1. Section 2.4.1.1 confirmed the EHD FE method simulated the radiation loading of the steel plate accurately. However, section 2.4.1 showed that there was considerable difference (approximately 45 kHz) between the main resonance of the EHD model and the experimental measurement. The aim of using acoustic FEM is to simulate the loading effect whilst allowing more natural vibration of the system.

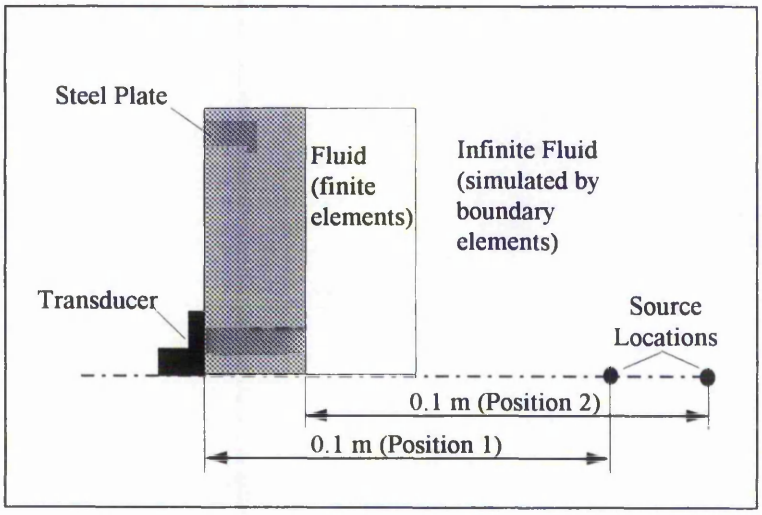

Fig. 2.39 The acoustic FE model used to investigate the effect of mounting the bi-laminar disc transducer to a steel plate. The thickness of the steel plate was varied between 10 and 25 mm and had a 50 mm diameter.

The FE model consists of the transducer bonded to a steel plate with water on the opposite side (fig. 2.39). The point source was again positioned in the fluid, along the axis of symmetry. Two source positions were simulated, one at a fixed distance (0.1 m) from the face of the transducer (position 1) and one at a fixed distance (0.1 m) from the edge of the metal plate (position 2).

Because the nodes on the transducer face can be individually excited, this should allow more realistic excitation of the transducer modes. Now that a suitable finite element model had been developed, the effect on transducer response of varying the plate thickness and material could be investigated, with the point source in both positions. Plate thicknesses of 25, 20, 15 and 10 mm were modelled.

2.4.3 Effect of Varying the Thickness of the Steel Plate

With the steel plate in position 1, the output voltages obtained on the piezoelectric were greatly increased compared to the unmounted transducer. This is because there is less fluid between the source and the transducer (0.075 m compared to 0.1 m for the unmounted transducer). This causes a pressure increase at the steel/fluid interface, close to the axis of symmetry. The result is a greater displacement of the solid at the interface which then propagates through to the piezoelectric.

Fig. 2.40 shows that the main resonant frequency at 187 kHz is much closer to the experimental result of 184 and 187.5 kHz, seen in fig. 2.38. From the close match, it is assumed that the acoustic FE model is giving acceptable results. The acoustic analysis has been reliable and will, therefore, be used to further analyse the mounting effects. There are three other peaks in voltage at 191.5, 197 and 200 kHz.

The result for the source in position 2, at 0.1 metres from the steel plate/fluid interface, gives peaks at the same frequencies (table 2.6), but their amplitudes differ. With the source in this second position, the main resonance is shown at 200 kHz with a second peak at 187 kHz (fig. 2.41). The amplitude of the output voltage at 187 kHz is less than with the source in position 1 (108 compared to 256 volts), but this is because the source is further away from the transducer. Also, the acoustic wave front may apply a more uniform pressure to the steel, which could vary the transducer excitation slightly.

The higher frequency peaks do not appear to lose any amplitude. In fact, with the 200 kHz peak on the 25 mm steel plate model, the amplitude appears to have increased from 110 volts to 148 volts (table 2.6). This indicates that one of the plate modes is coupling with a transducer resonance.

It was not possible to analyse the vibration modes in the transducer, because the displacement was very small compared to the size of the overall model. If possible, this would have helped provide further understanding of the effect of mounting the transducer.

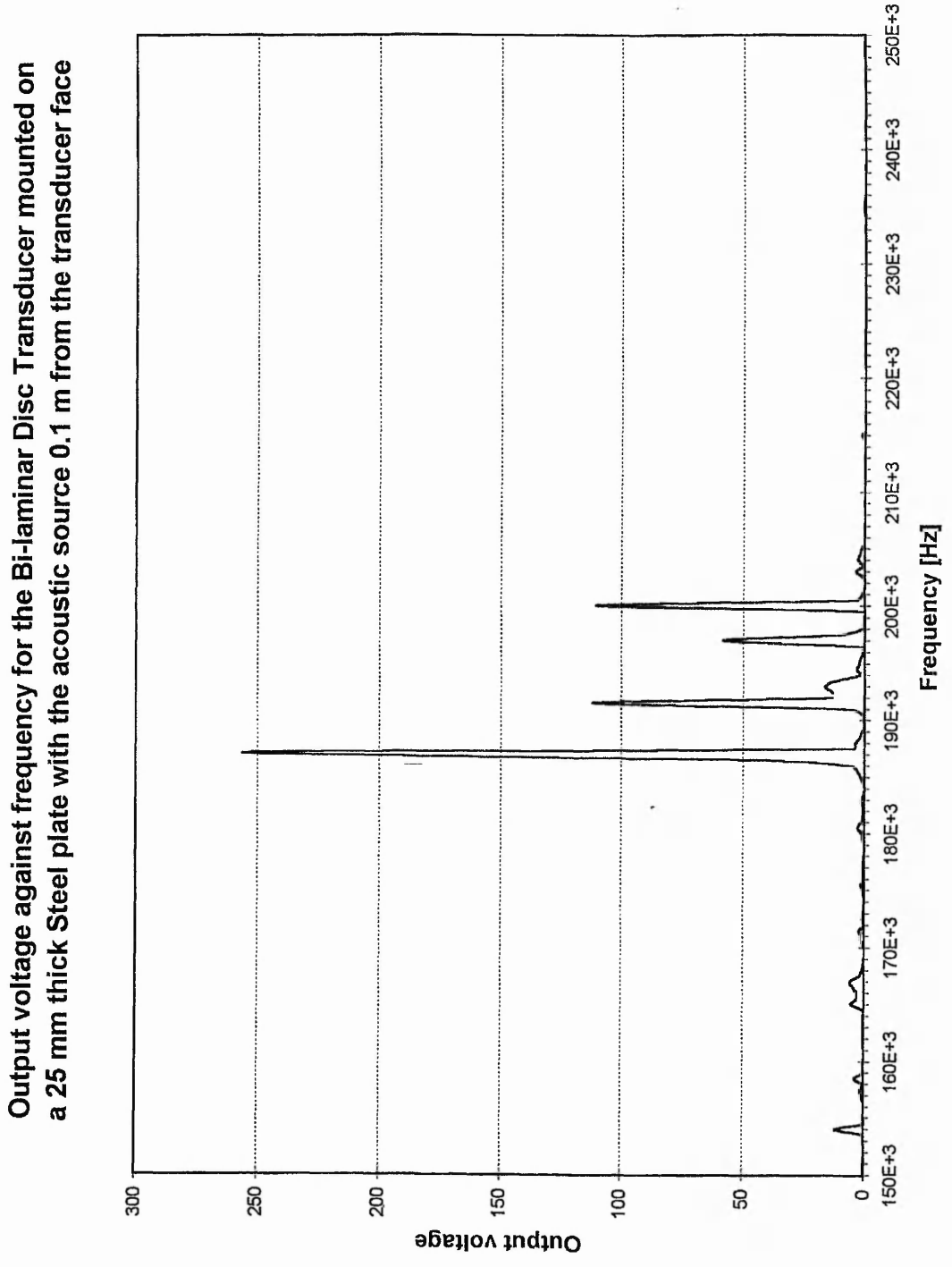

Fig. 2.40 Output voltage against frequency predicted for the bi-laminar disc transducer, mounted on a 25 mm thick steel plate, using an acoustic FE analysis.

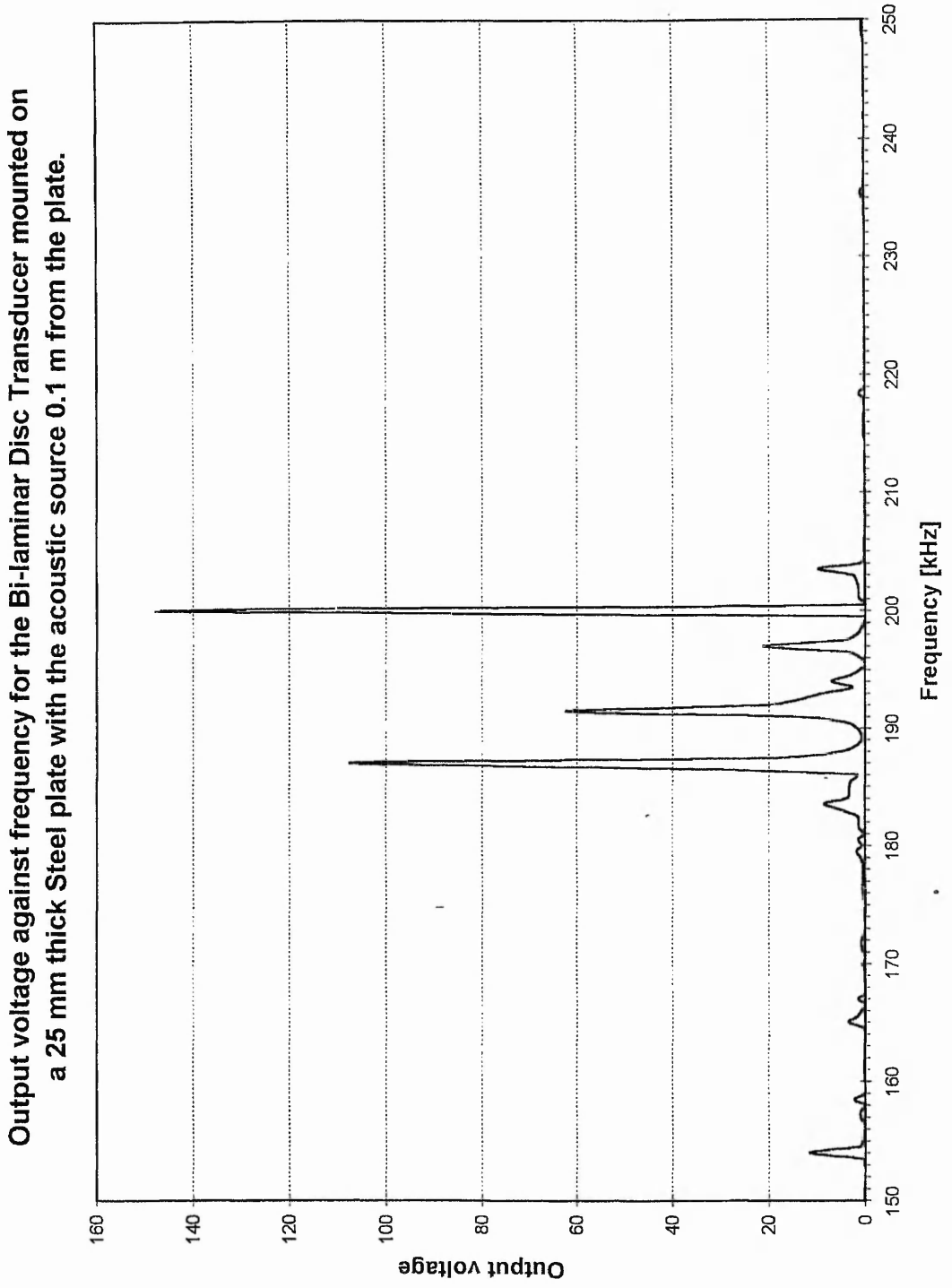

Fig. 2.41 Output voltage against frequency predicted for the bi-laminar disc transducer, mounted on a 25 mm thick steel plate, using an acoustic FE analysis with the source 0.1 m from the steel.

Plate Thickness [mm]	f_r	Output	f_r	Output	f_r	Output	f_r	Output	f_r	Output
Position 1	[kHz]	[volts]	[kHz]	[volts]	[kHz]	[volts]	[kHz]	[volts]	[kHz]	[volts]
25	155	11	**187**	256	191.5	112	197	57	200	110
20	**158**	42	173	32	187	36	191.5	6	197	9
15	158	33	183.5	13	191.5	31	**197**	59	-	-
10	158	20	187	140	**191.5**	160	197	34	-	-
Position 2										
25	155	12	187	108	191.5	62	197	22	**200**	148
20	154	8	158.5	35	173	6	**187**	49	-	7
15	**158**	30	183.5	8	188.5	8	191.5	12	197	34
10	158.5	18	185	39	**187**	287	191.5	78	200	8

Table 2.6 Predicted resonant frequencies and their respective output voltage amplitudes for the bi-laminar disc transducer mounted onto a steel plate. The main resonance is shown in bold type.

Experimentally, two peaks occurred very close together (fig. 2.38) but they are not well resolved, due to higher damping in the real transducer. This is caused by natural conditions involving complex vibration, damping, and mode coupling, causing multimode response. It is likely that, in practice, the four close resonances seen between 187 and 200 kHz would produce one large peak, with the highest amplitude possibly occurring at the main resonant frequency seen in the undamped models.

2.4.4 Theoretical Calculations involving a Multilayer Transduction System

Theory concerning some of the variables associated with AE transducers has been presented by Hill and El-Dardiry [**50**]. This work considered the transducer-specimen system as consisting of multiple layers, which were infinite in the plane parallel to the transducer face. Transmission of acoustic signals through the system can then be considered in terms of the thickness of each layer and the physical properties of each layer.

Fig. 2.42 portrays the layers for a bi-laminar disc transducer, mounted to a metal plate, receiving an acoustic plane wave through water. The transducer piezoelectric was assumed to be backed by air. The theory was used to calculate the output pressure amplitude relative to the input amplitude of an incident plane wave. The equations used

are given in appendix III. The multilayer theory is not ideal because the layers are infinite in their area and will not take into account the complex vibration modes of the real finite transducer. However, the aim in modelling the multilayer transmission system is to provide an alternative method of comparison to account for the material loading on the transducer.

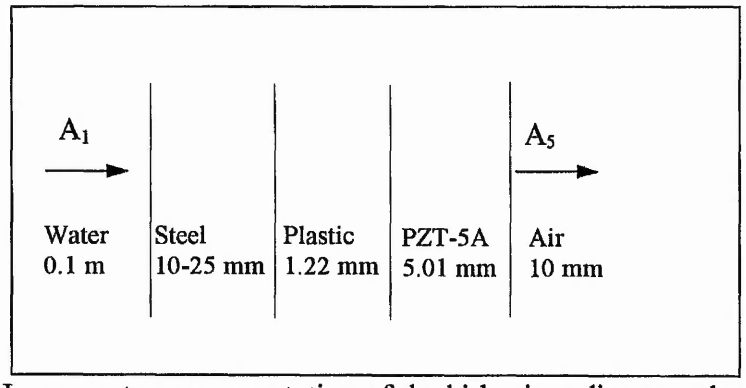

Fig. 2.42 Layer system representation of the bi-laminar disc transducer, mounted to a steel plate, receiving an acoustic plane wave through water. A_1 is the input wave amplitude and A_5 is the amplitude of the wave transmitted into layer 5 (air).

The equations in appendix III calculate the output to input ratio $\left(\frac{A_5}{A_1}\right)$ of the acoustic plane wave acoustic pressure amplitude. The input was assumed to be one, giving output per unit input plotted against frequency, for four thicknesses of steel plate which is plotted in fig. 2.43.

From fig. 2.43 it is clear that there are several resonant frequencies from this theory that occur in the 50-250 kHz range of interest. Table 2.8 shows the resonant frequency values in the 0-300 kHz range, predicted using the multilayer theory, with their closest FEM agreements. The acoustic FE data is for the source in position 2 i.e. 0.1 m from the steel/fluid interface, the distance used in the theoretical calculations.

Table 2.8 shows close agreement between some of the theoretical resonant frequencies and the resonant frequencies predicted by acoustic FEM, for plate thicknesses of 25, 20 and 15 mm. For a 10 mm plate there is only one resonance in the 50-250 kHz range and the agreement is poor.

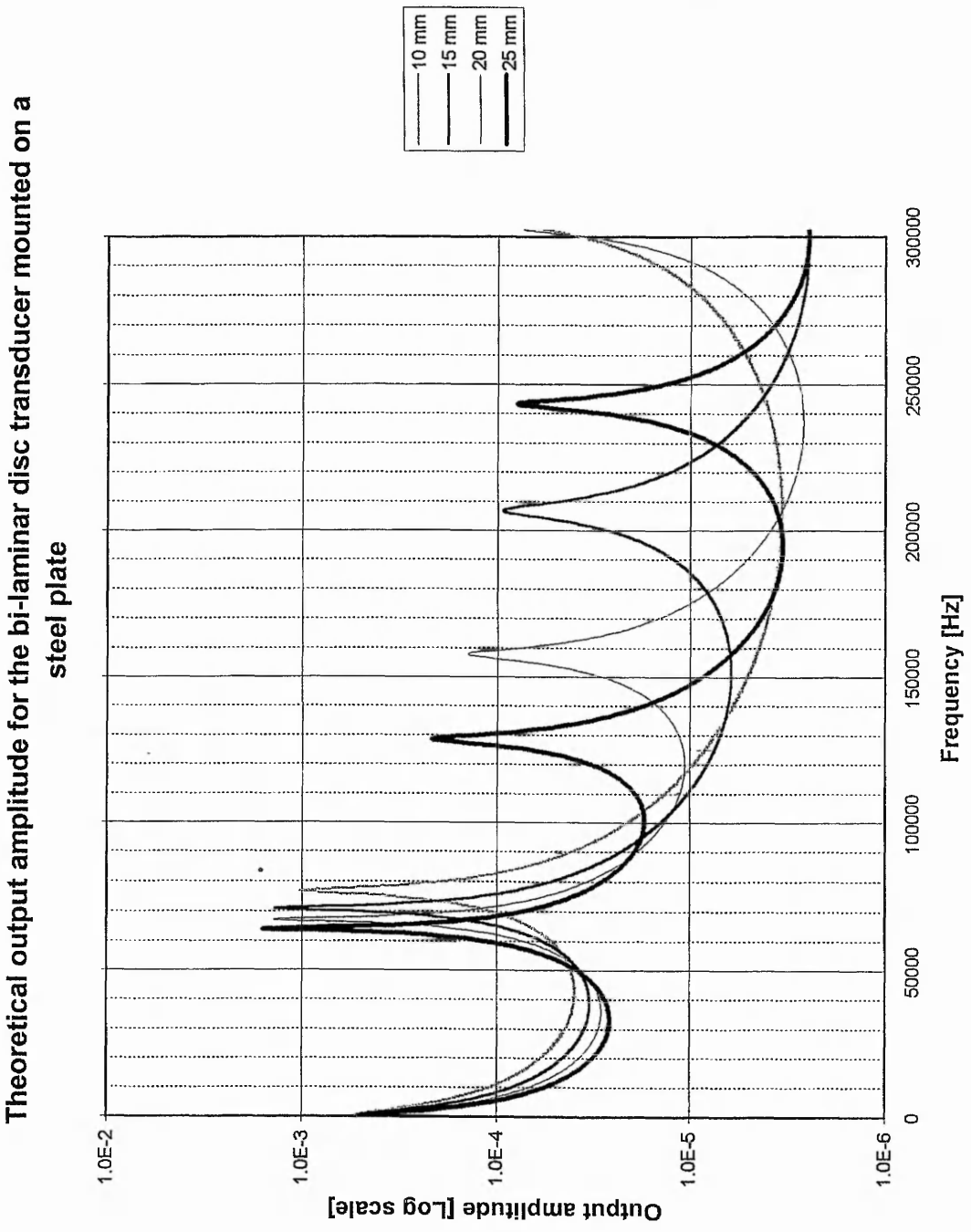

Fig. 2.43 Transducer output amplitude against frequency for four plate thicknesses, calculated using the theory presented by Hill and El-Dardiry [**50**] for a multiple layer transducer system.

Frequencies from the enforced harmonic displacement (EHD) FE model, in section 2.4.1, which are close to the multilayer resonant frequencies are also shown in table 2.8.

Plate Thickness [mm]	Multilayer Theory [kHz]	Acoustic FE [kHz]	EHD FE [kHz]
25	128.5, 244	155, 249	134
20	67, 159	158	-
15	71, 207	209	202
10	77	154	115

Table 2.8 Comparison of multilayer theoretical resonant frequencies with their nearest FEM agreements for the bi-laminar disc transducer mounted on a steel plate. The acoustic FE data is for the source in position 2. EHD is the Enforced Harmonic Displacement described in section 2.4.1.

Their agreement with this theory is clearly not as good as the closest acoustic FE frequency predictions, although for 25 and 15 mm plate the agreement is reasonable (<10 kHz difference).

Where there is agreement between the multilayer theory and the acoustic FEM allows this theory to be used to explain the system behaviour at these frequencies. The theory does not predict a frequency around 187 kHz, which is predicted by both acoustic FEM and experimental measurement. This suggests that the assumptions of infinite layer dimensions used in the theory are still not realistic enough, although it is valid for some modes (where there is close agreement with the acoustic FEM). Because the transducer modes are complex and, radial modes dominate the transducer response in the 50-250 kHz range, the infinite 'radial' dimension in the theory is inappropriate.

The system of the transducer mounted to a steel plate has been considered using a variety of methods. Acoustic FEM has again proved its validity by showing close agreement with experimental measurement. This type of modelling also showed close agreement with multilayer transmission theory **[50]** at some frequencies, giving added confidence in the FE method. Another FE method of modelling the mounted transducer system involved applying a sinusoidal displacement to the face of the transducer. This

method gave close agreement to theory for a piston radiating into a infinite half space [**49**]. The agreement was encouraging in that it was proof that the FE model was accurately modelling piston-like behaviour. The EHD FE method was inappropriate, however, for modelling the mounted transducer.

Mounting the transducer to a large steel plate raised important issues of the transducer behaviour and modelling using FE. While theories exist that explain transducer behaviour with specific boundary conditions, they were shown to be inadequate for accurately predicting the output of a finite size system. Finite element modelling was shown to be capable of predicting the transducer response using theoretical boundary conditions and, for real life situations.

Section 2.4.1 showed that care must be taken when applying boundary conditions to an FE model. When the FE model gives poor results, more traditional mathematical analysis may be useful for understanding what is being modelled and providing insights into how the FE modelling is working.

The acoustic FEM has again been shown to be a valid and realistic method of predicting ultrasonic transducer response in real life situations.

Chapter Three

Exponential Horn Transducer Designs

3.0 INTRODUCTION TO HORN DESIGNS

Chapter Two considered a simple resonant transducer design. Chapter Three will now consider a more complicated resonant design, involving the use of an exponential horn. The advantages of such a design will be investigated, along with the effects of changing various transducer dimensions. The aim is to produce a convenient method of improving the transducer performance.

Composite 1-3 transducer designs offer improved performance over basic designs. However, they are expensive and complicated to manufacture. An alternative is to design a transducer having a combined metal-ceramic structure, as discussed in section 1.2. The exponential horn studied here was intended for use as a detector for geotechnical AE applications. Desirable resonances for geotechnical work might be in the 30 to 50 kHz range.

The transducer to be modelled had a horn shaped brass receiver, with a rectangular piezoelectric bimorph bender mounted on a brass disc, at the narrow end of the horn (fig. 3.1). The shape of the horn follows an exponential curve, which is intended to magnify the particle displacements it receives from the structure being monitored. The bimorph bender was made from PZT-5A piezoelectric ceramic. Bimorph is the name for a flexing, two part, piezoelectric element.

In using the horn as an ultrasonic receiver, the mouth (wide end) would be in contact with the test specimen, and the acoustic emission would be amplified and detected by a transducer at the throat (narrow end).

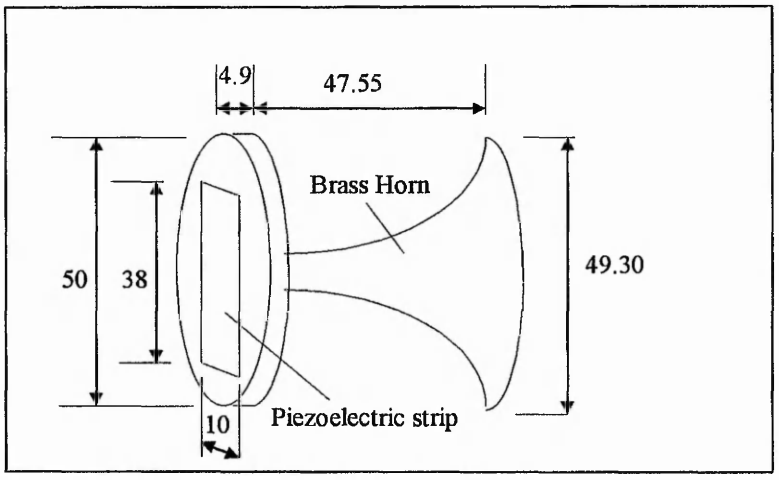

Fig. 3.1 Brass Exponential Horn Transducer. Dimensions are in mm. The piezoelectric strip is 0.5 mm thick.

Finite element modelling is the ideal tool for designing and testing more complex transducers. FEM was used to analyse and optimise this design. From this model an understanding of the design principles would hopefully be gained, which could then be used to design transducers to operate at any desired frequency.

The aims of the work in this chapter are:

1. To model the exponential horn transducer using acoustic FEM and verify the model with experimental data and some theoretical calculations where possible.
2. To optimise the design to give maximum sensitivity at the design frequency.
3. To gain understanding of design features that may further improve the transducer performance.

3.1 HORN DESIGN AND PHILOSOPHY

A solid horn acts as a particle velocity transformer for ultrasound, in which the particle velocity at the small end v_t (throat) is larger than at the large end v_m (mouth). The velocities are related to the cross sectional areas by the following relationship [**51**]

$$\frac{v_t}{v_m} = -\left(\frac{A_m}{A_t}\right)^{0.5}$$

The ability of a solid horn to increase the particle velocity, from the large end to the small end, has been utilised for many years [**52**]. These amplitude transformers are commonly used in high amplitude applications, such as ultrasonic machining. In such a case, the mouth of the horn is driven by a resonating transducer giving magnified particle velocity at the throat.

Nicholson et al. recently studied horns to couple waveguides to transducers used in medical ultrasonics [**51**]. This is because horns provide an efficient means of acoustic energy transfer, using acoustic impedance matching. The authors tested several horn shapes, including conical, exponential, Gaussian, hyperbolic and elliptical (fig. 3.2). Different materials were also investigated. The conclusion was that horns provide a suitable mechanical means of connecting the wire waveguide to a larger diameter transducer. This experimental study highlights the advantages and need for FE analysis of this problem.

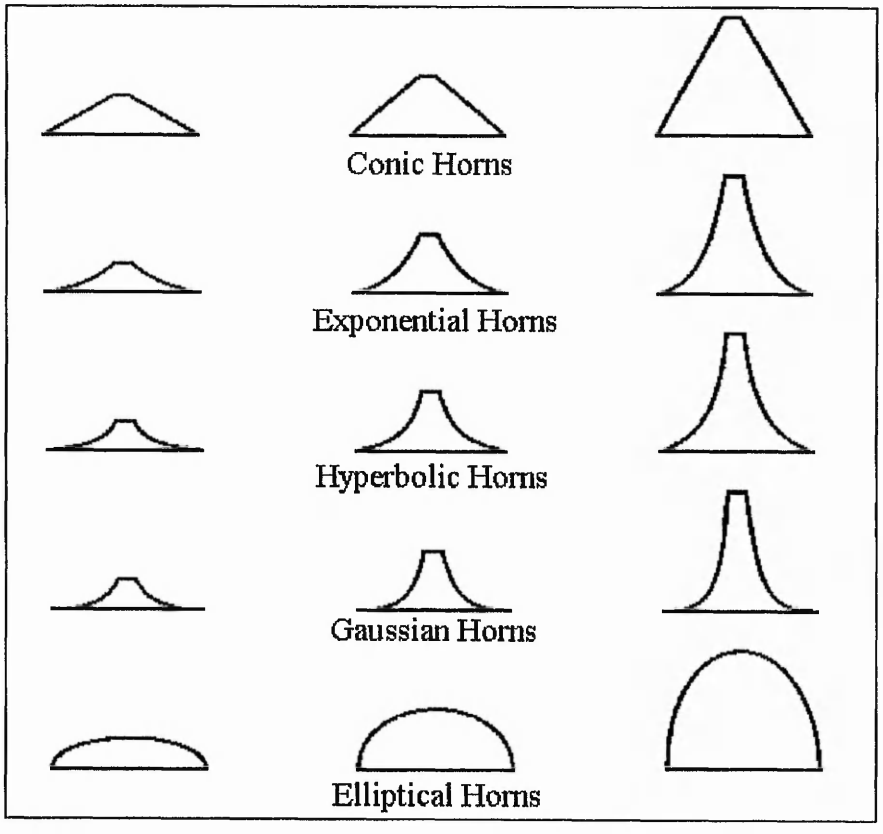

Fig. 3.2 Examples of different horn shapes used to couple a waveguide to a transducer in a study by Nicholson et al. [**51**].

Current use of exponential horns for ultrasonic machining shows that improvements to performance can be obtained by coupling two modes of vibration [**53, 54**]. These two modes are the longitudinal and the torsional modes. Resonance at the same frequency is achieved by changing the flare constant of the cross sectional area. The result is very large amplitude displacements, useful for ultrasonic machining, drilling, and in fatigue testing machines. Exponential horns are, of course, good acoustic receivers and have been shown to enhance the hearing sensitivity of certain animals over a broad frequency range [**55**].

3.1.1 Longitudinal Vibration in an Exponential Horn

The cross-sectional radius of an exponential horn is described by

$$R(x) = R_t \exp(\beta x) \tag{1}$$

where β is known as the flare constant.

The sound velocity in the exponential horn C_l' is related to the sound velocity in an untapered thin rod by the following relationship

$$C_l' = \frac{C_l}{\sqrt{1-(\beta C_l / \omega)^2}} \tag{2}$$

in which $C_l=(E/\rho)^{1/2}$. When considering free vibration of the horn, the resonant frequency of the horn is related to the horn length l by

$l = n\lambda_1' / 2, (n = 1,2,3,\ldots)$ and $\lambda_1' = C_l' / f$ where f is the resonant frequency.

3.2 MODELLING THE EXPONENTIAL HORN TRANSDUCER

An exponential horn was manufactured from brass, with a flare constant β of 47.5 m^{-1}. Using equation (1), the co-ordinates of the horn were used to create an FE mesh in

PIGS. A three dimensional model was needed if a non-axisymmetric (rectangular) piezoelectric element was being modelled. The consequence was that the model would take longer to execute.

The manufactured transducer was modelled to predict the resonant frequency, and the results were compared to experimental data. Once the accuracy of the FE model was confirmed, it could be used alone to investigate the effect of design parameter changes.

The elements used in the modelling are as follows:

three dimensional piezoelectric brick element	(type 35115)
three dimensional brick and triangular prism elements	(type 37110 and 37210)
three dimensional pressure based fluid elements	(type 29620 and 29610)
acoustic boundary elements	(type 24640 and 24630)

Here is a brief explanation of why each type is used in the model.

THREE DIMENSIONAL PIEZOELECTRIC BRICK ELEMENT

This is the only 3D piezoelectric element, which allows definition of x, y and z displacements and electric potential.

THREE DIMENSIONAL BRICK AND PRISM ELEMENTS

These are standard 3D elements used for stress analysis. They are used to model the brass horn.

PRESSURE BASED FLUID ELEMENTS

These are the acoustic finite elements and are used to model a small finite region of water in contact with the mouth of the horn.

ACOUSTIC BOUNDARY ELEMENTS

These are constant pressure patches, which model an infinite exterior region of fluid.

The 3D brass horn transducer model is constructed in PIGS in the following way:

- Nodes (points) are plotted to define a two dimensional profile of the brass horn.
- Two dimensional elements are created and sub-divided appropriately.
- Boundary lines are drawn to outline the small finite region of fluid.
- Automeshing is used to construct elements within this boundary. The elements couple exactly to the brass elements for accuracy.
- One dimension beam elements are used to define the infinite fluid boundary.
- The 2D model is then rotated about the x-axis to create the 3D model.
- Nodes to outline the 3D piezoelectric element are created.
- The piezoelectric element is then created and subdivided.
- A data file is created listing all the nodal co-ordinates and the elements' topology, type number and property number.
- The data file is edited to include details such as material properties, type of analysis, range of frequencies for analysis, and other essential data.

The data modules used are the same as for the axisymmetric model except that no planes of symmetry are defined. The acoustic point source was of the same magnitude as that used in Chapter Two and is again situated 0.1 m from the transducer face, on the horn's axis of symmetry. Modelled excitation frequencies were between 1 kHz and 100 kHz. A resolution of 0.5 kHz was used.

In the 'Control' module some important commands were added to get the model to run smoothly. In PHASE 4 of the job, the routine R25544 was required, to get correct coupling between the piezoelectric elements and the brass elements. The memory allocation for this phase was also extended manually in the Control module.

Material	E [Nm^{-2}]	ν Poisson's ratio	ρ [kgm^{-3}]
Brass	$104x10^9$	0.37	8500

Table 3.1 Material properties for brass used in the FE models.

In PHASE 7 the routine S50100 was used, to get the model to run correctly on the UNIX system. Again, an increase in the standard memory allocation for this phase is required for this large calculation.

The PAFEC data file for this 3D model is shown in appendix IV.

3.2.1 Number of Elements in the Mesh

For accuracy the number of elements should be more than three elements per wavelength [**37**]. As the wavelength varies in each material, so does the number of elements required.

The sound velocities of brass and water are given below.

Brass $c = 4652\ ms^{-1}$

Water $c = 1482\ ms^{-1}$

It is not necessary to check the grid size of the piezoelectric as it is very thin (<1 mm) and has a similar sound velocity to the brass ($4350\ ms^{-1}$). Therefore, the $\lambda/3$ requirement is easily satisfied. The desired frequency of the transducer was selected to be 40 kHz. The wavelengths at 40 kHz are, therefore,

Brass $\lambda = 0.116$ m

Water $\lambda = 0.037$ m

In order to satisfy the accuracy requirements there should be an element every $\lambda/3$ metres in the model. This was easily achieved as the transducer was only 0.05 m long, with much finer FE mesh superimposed. A mesh finer than the theoretical density was used so as to accurately define the shape of the horn and to permit higher frequency analysis.

3.3 TRANSDUCER CHARACTERISTICS AND VIBRATION MODES

3.3.1 Resonant Frequency Comparison Between Model & Experimental Methods

The transducer's frequency response was measured experimentally using the measurement system described in section 2.2.4. Audible resonances were heard at 5.2 kHz and 16.9 kHz. Although higher frequency resonances were found, they were smaller in output voltage amplitude compared to these first two. The first two resonances can be seen as voltage fluctuations on the curve in fig. 3.3.

The 3D acoustic FE model was run between 1 kHz and 100 kHz at 0.5 kHz intervals. In this range the first resonant frequency was found at 5.5 kHz (fig. 3.4). A second peak in voltage amplitude was at 17 kHz, indicating another resonant frequency.

Higher frequency resonances were predicted by the FE model at 41 kHz, 64 kHz and 86 kHz. A few smaller amplitude peaks also occurred in the frequency range modelled.

The first two frequencies show good agreement with the experimental values. The amplitude of the first peak is greater than the second peak, with further amplitude drops at higher frequencies. This was the case for the experimental data as well.

3.3.2 Axisymmetric Model of the Horn Transducer

With the three dimensional model showing good agreement with experimental data, an axisymmetric model was attempted in order to reduce the running times for each model. In order to be axisymmetric, the piezoelectric element would now be a disc and not a rectangular strip. A 1 mm thick disc with a 38 mm diameter, equal to the piezoelectric strip length, was used in the axisymmetric model. The resonant frequencies from the axisymmetric model agreed well with those from the 3D model (fig. 3.5), allowing axisymmetric modelling to be used further. The results from these models will, therefore, be directly comparable to the original data.

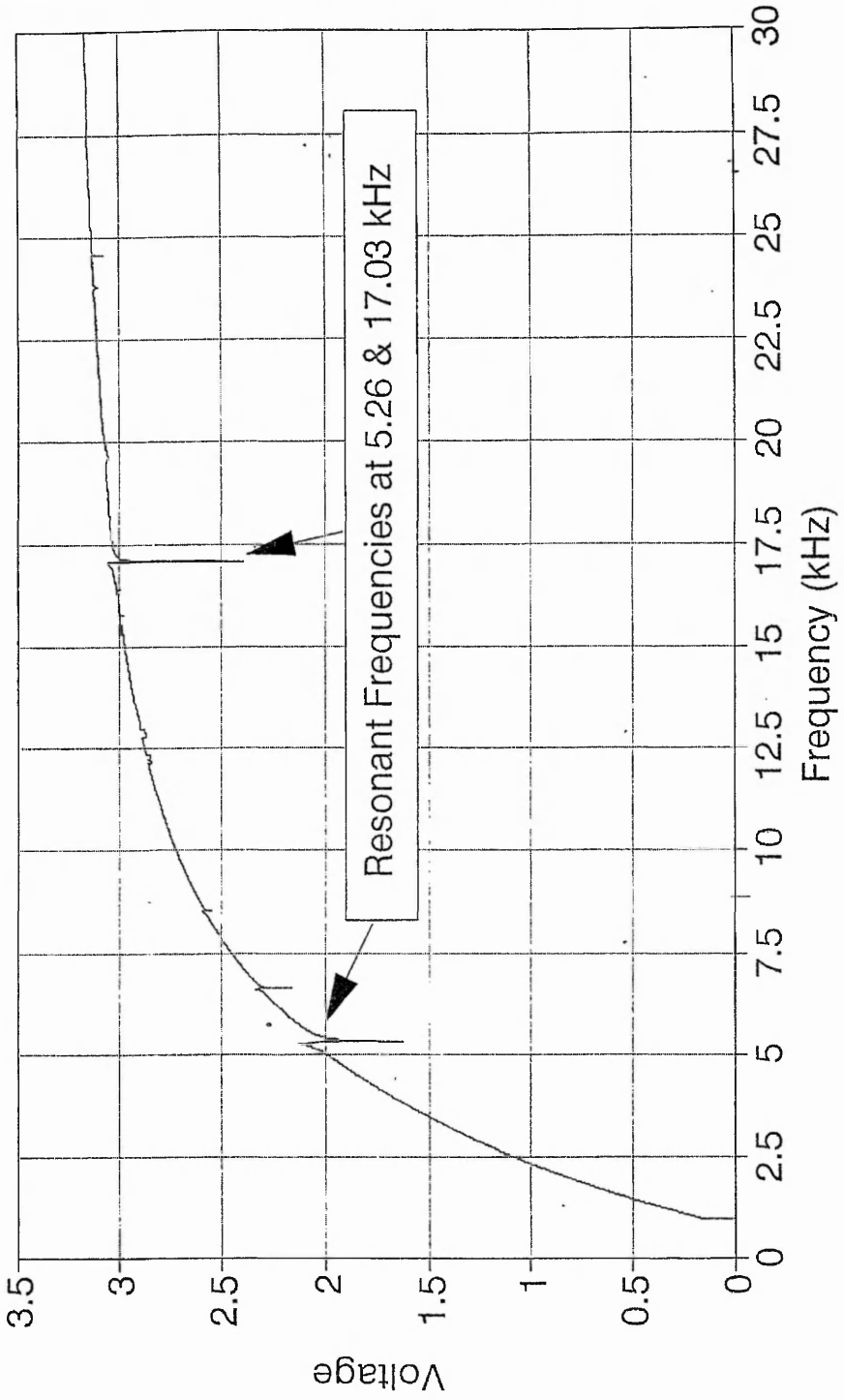

Fig. 3.3 Output voltage against frequency graph for a brass exponential horn transducer, measured using the experimental π network in section 2.2.4.

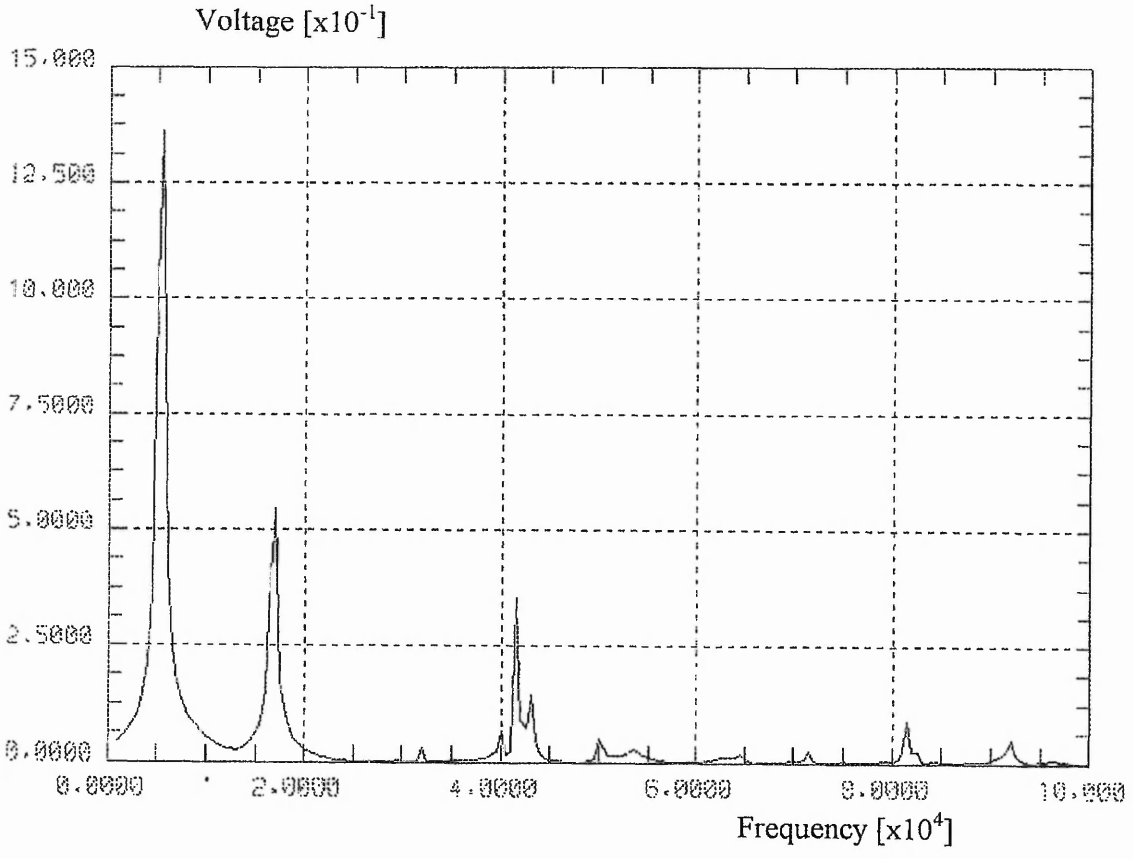

Fig. 3.4 Output voltage against frequency graph for a brass exponential horn transducer, predicted by a 3D acoustic FE model.

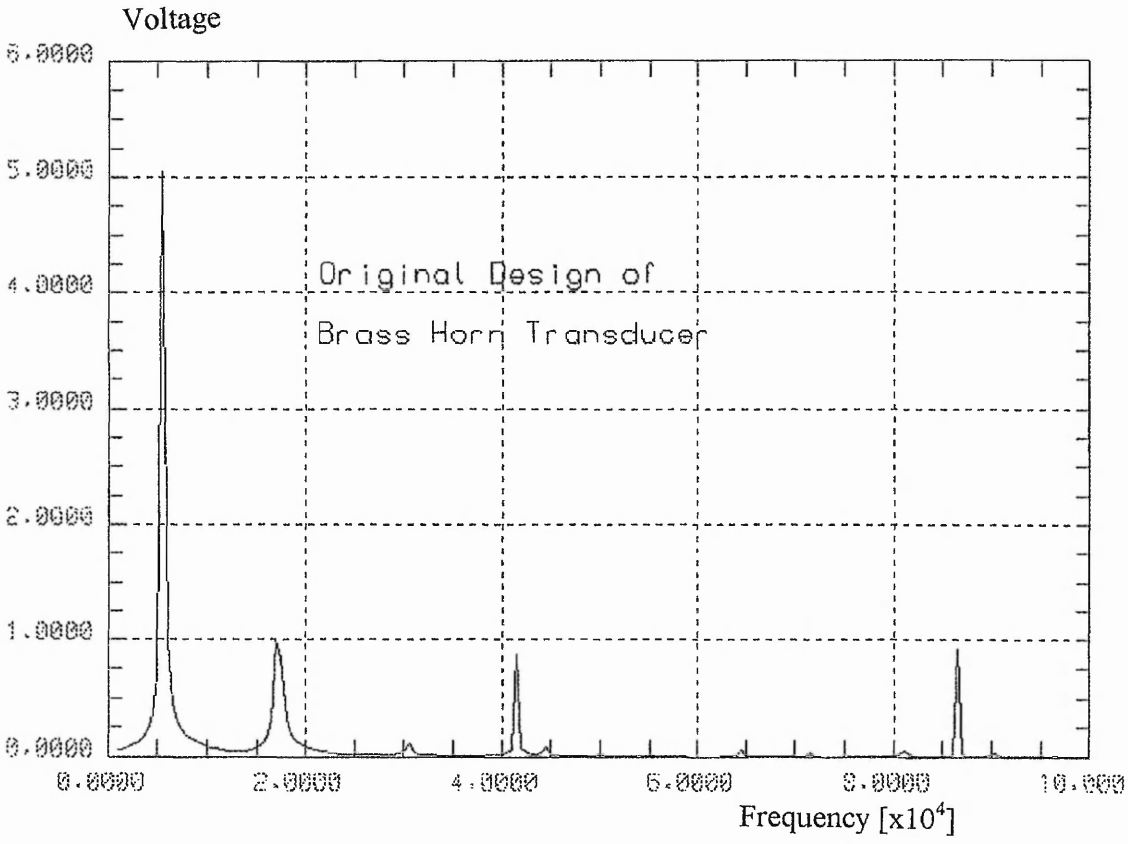

Fig. 3.5 Output voltage against frequency for the axisymmetric model of the original exponential horn design, described in section 3.3.2.

One difference between the axisymmetric and 3D models is the output voltage amplitude. In the axisymmetric model, the output voltage amplitude is larger (5.05 compared with 1.38 volts) even though the same amplitude of source was used, due to the different modelling methods. The output voltage from other axisymmetric models used in future will be comparable in amplitude to fig. 3.5. The drop in amplitude in the 3D case is a final design consideration, but is not of direct interest in this study.

3.3.3 Vibration Modes of the Horn Transducer

As a secondary check that the axisymmetric and 3D models were giving the same results, the vibration modes at the resonant frequencies were compared.

When analysed in PIGS, the modes of vibration were the same in both models, confirming they were predicting the same resonances. The mode shapes, predicted by the axisymmetric model, of the 5, 17 and 41 kHz modes are shown in fig. 3.6, 3.7 and 3.8 respectively.

At 5.5 kHz the horn section was vibrating in a longitudinal mode (fig. 3.6), with the displacement occurring along the length of the horn. The back plate to which the piezoelectric element is attached, bent about its centre, with maximum displacement occurring at the plate circumference.

The vibration at 17 kHz was similar (fig. 3.7). In the 3D model, this mode was asymmetric about the centre and so the back plate looked like an s in profile. This cannot be appreciated in the axisymmetric model.

In the horn section, the transducer face (mouth of horn) was not displaced evenly, as at the lower frequency resonance. Instead, the outside edge was displaced more than the face centre.

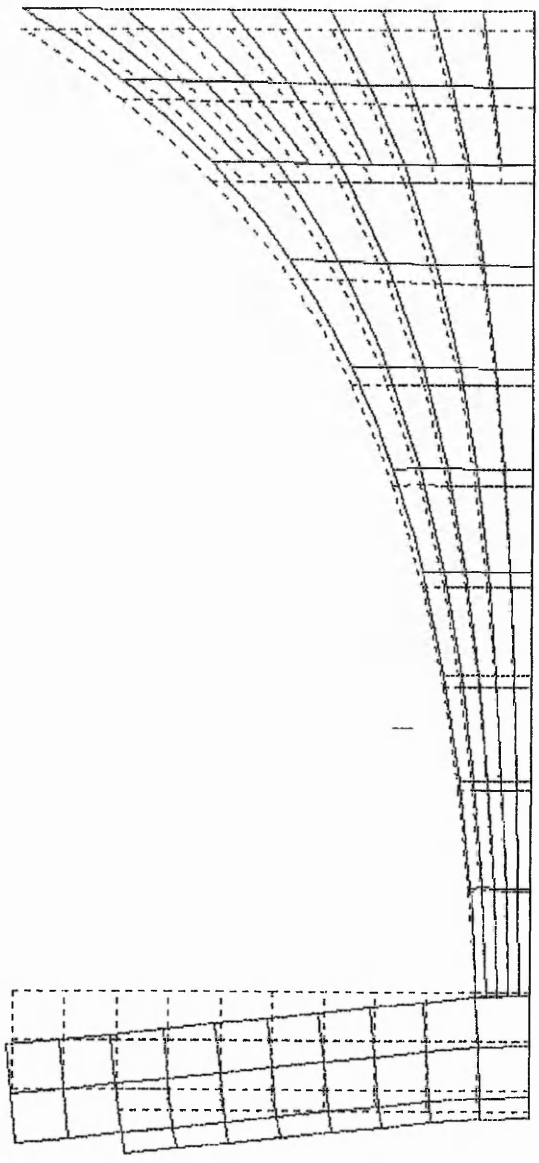

Fig. 3.6 Mode 1 at 5.5 kHz of the brass exponential horn transducer, predicted by an axisymmetric FE model. Model is axisymmetric about the right hand vertical axis.

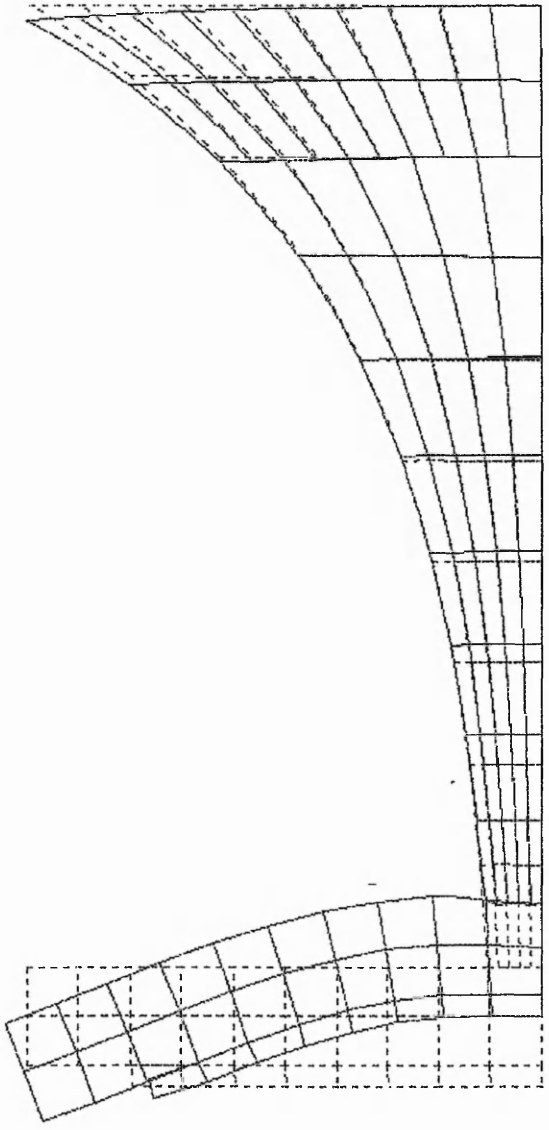

Fig. 3.7 Mode 2 at 17 kHz of the brass exponential horn transducer, predicted by an axisymmetric FE model. Model is axisymmetric about the right hand vertical axis.

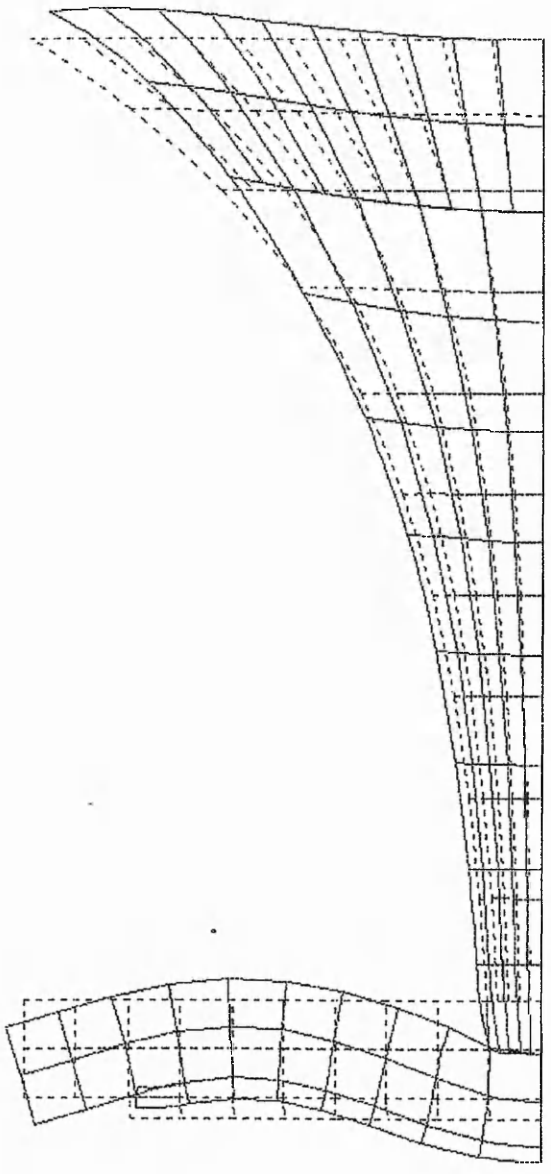

Fig. 3.8 Mode 3 at 41 kHz of the brass exponential horn transducer, predicted by an axisymmetric FE model. Model is axisymmetric about the right hand vertical axis.

Mode 3 at 41 kHz (fig. 3.8) was more complicated, with the back plate showing displacement in different directions. At the centre there is large axial displacement (along the length of the transducer). Beyond the throat of the horn, back plate vibration looks like the M_{03} circular-bending mode, seen in fig. 2.3 in the piezoelectric discs in Chapter Two. Higher modes showed increasingly complicated motion in both the back plate, and horn sections.

3.3.4 Circular plate theory

Due to the contribution that the back plate makes to the transducer's vibration modes, a comparison of the resonant frequencies and mode shapes was made with those calculated from circular plate theory. Although the model has been shown to be accurate when compared to experimental measurement, a further theoretical comparison would be advantageous.

Classical plate theory can be found as far back as the middle of the 1800s, developed by mathematicians such as Kirchhoff. Timoshenko **[56]** has also produced work on the topic along with many others. From this theory the resonant frequency of a circular plate is given by the formula;

$$\omega = \frac{\alpha}{a^2}\sqrt{\frac{D}{\rho h}} \tag{3}$$

Where a is the plate radius, α is a constant, ρ is the mass density, h is the plate thickness and D is the flexural rigidity, defined as;

$$D = \frac{Eh^3}{12(1-\nu^2)} \tag{4}$$

E is the Young's modulus and ν is the Poisson's ratio. α varies depending on the modes and boundary conditions. Unfortunately, the exact boundary conditions for the transducer back plate are not easy to determine. Texts only cover specific boundary

conditions, such as the cases of a clamped circumference, free vibration or a fixed centre. The last two were deemed most appropriate for comparison with the transducer's back plate behaviour. Table 3.2 and 3.3 show α values for free vibration and the case of a plate with a fixed centre respectively.

Equation (3) was used to calculate the resonant frequency of the back plate using the various α values. A 25 mm radius corresponds to the back plate diameter and the calculated frequencies are shown in table 3.4.

M	n=0	1	2	3
0	-	-	5.251	12.23
1	9.076	20.52	35.24	52.91
2	38.52	59.86	-	-

Table 3.2 α values for a circular plate with a free boundary condition and n nodal diameters and s nodal circles [**57**].

s	0	1	2	3
α	3.75	20.91	60.68	119.7

Table 3.3 α values for a circular plate with a fixed centre boundary condition and s nodal circles [**57**].

From table 3.4 it is clear that the first mode predicted by the FE model shows agreement with the frequency calculated using an α value of 3.75. This is the first mode with a fixed centre boundary condition. The second mode predicted by FEM was at 17 kHz and this corresponds to a calculated frequency with an α value of 12.23, which is for a plate with a free boundary condition, shown in table 3.2.

Several other frequencies of peaks in fig. 3.5 correspond to circular plate modes in table 3.4. Most frequencies are those predicted by α values for a free vibration boundary condition and not the fixed centre condition. It is interesting, however, that the largest amplitude peak, predicted by the model, is the first peak, which corresponds to an α value for a plate with a fixed centre.

Modes in which the back plate vibration is dominant, such as the first two modes, show good agreement with the theory and these agreements confirm that the FE modelling is giving a good prediction of the resonant frequencies of the transducer.

The predicted mode shapes for circular plates also show suitable agreement with typical examples in texts [**58**], adding to the confidence in the FE modelling process.

α value	Theoretical frequency [kHz]	FE predicted frequency of horn transducer [kHz]
3.75 (F)	5.086	5.5
5.251	7.121	-
9.076	12.309	-
12.23	16.586	17.0
20.52	27.829	-
20.91 (F)	28.358	31.0
35.24	47.792	49.0
38.52	52.240	51.0
52.91	71.756	72.0
59.86	81.181	82.0
60.86 (F)	82.294	86.0

Table 3.4 Resonant frequencies for a 25 mm radius brass plate with h=4.9 mm compared with their nearest FE resonances (taken from fig. 3.5) in the brass exponential horn transducer for all α values. F denotes α values for the fixed centre boundary condition.

More detailed comparison between theory and FEM is inappropriate due to the obvious differences in the boundary conditions employed and the constraining effect that the piezoelectric will have on the back plate vibration. However, the confidence in the FEM accuracy is high, encouraging further investigation into the transducer performance.

3.4 EFFECT OF TRANSDUCER COMPONENTS ON PERFORMANCE

The exponential horn transducer modelled can be considered as three sections. These are the piezoelectric element, the back plate, and the horn section. The back plate refers to the brass disc to which the piezoelectric element is attached and this is at the throat end of the horn (fig. 3.1). Each of these components contributes to the overall transducer performance. In order to gain an understanding of how the transducer behaviour was affected by each component, changes in the dimensions of the components were investigated systematically, to identify design guidelines.

Again, axisymmetric FE meshes were used to run acoustic models. Each transducer received an acoustic signal from a point source in water, at a distance of 0.1 metres from the transducer face. The frequency of the acoustic signal was varied between 1 kHz and 100 kHz, and the output voltage produced across the piezoelectric element was predicted.

3.4.1 Modelling the Effect of Varying the Piezoelectric Diameter

The first transducer component to be varied was the piezoelectric element. A 5 mm thick piezoelectric disc was modelled instead of the thinner one used for the analysis seen in section 3.3.3. This is because the thicker disc had been shown to give more transducer sensitivity, than a thin disc of the same diameter (Chapter Two section 2.3.2). The only parameter that was varied was the piezoelectric diameter. Diameters were systematically increased from 2.5 to 50 mm, which correspond to piezoelectric diameter to back plate diameter ratios (D_p/D_{bp}) of 0.1 to 1 respectively. The back plate was held at a constant diameter of 50 mm in the model. Output voltage from the piezoelectric was plotted against the D_p/D_{bp} ratio for several resonant frequencies.

For all piezoelectric diameters, resonance occurred at several frequencies within the modelled frequency range. Although the exact values varied slightly, the resonant frequencies are in the proximity of 5, 20, 41, 64 and 86 kHz.

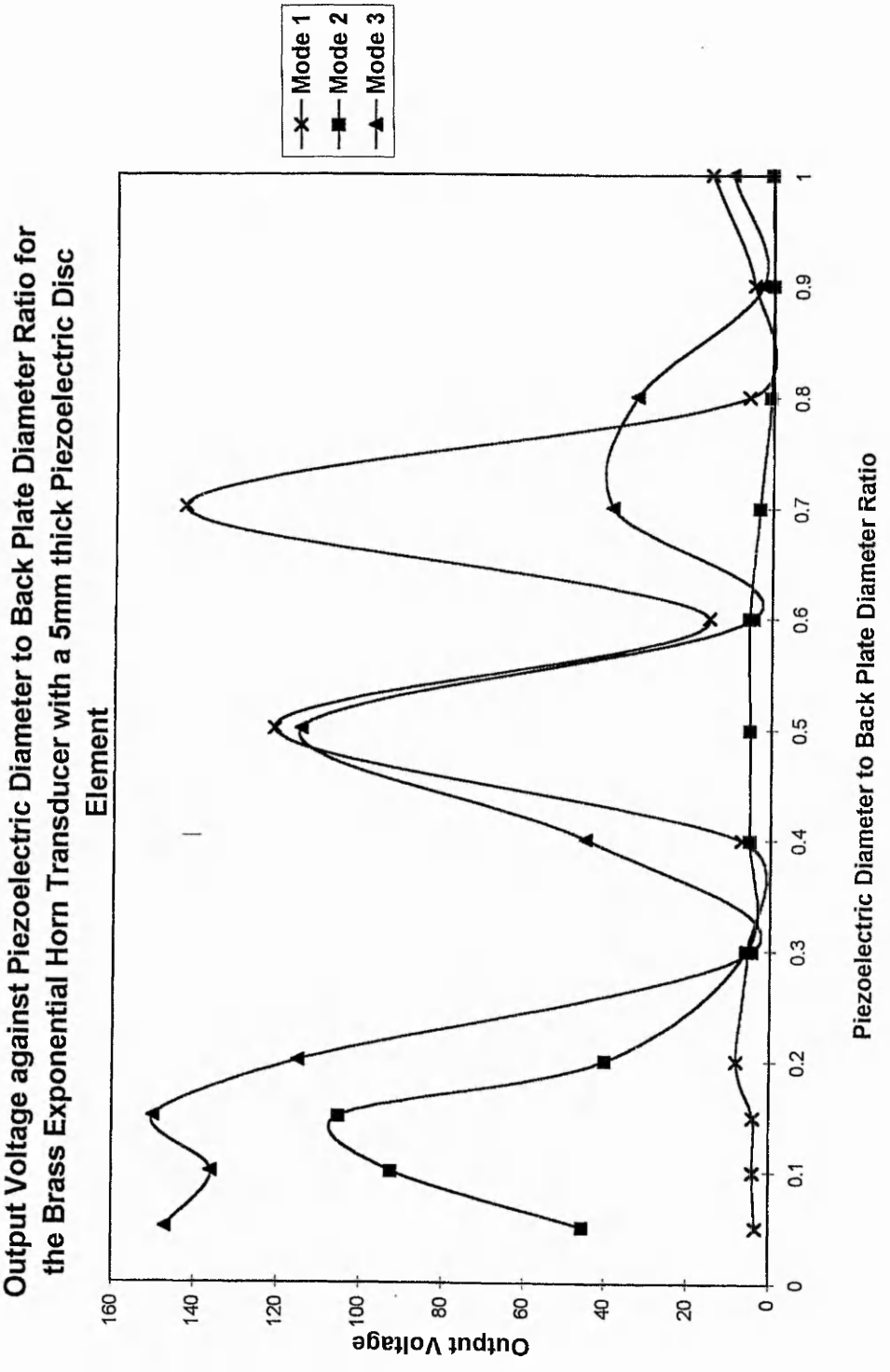

Fig. 3.9 Output voltage against piezoelectric diameter to back plate diameter ratio. Each graph represents one of the transducer resonances.

The frequencies with the largest amplitude responses, were used to plot output voltage against the D_p/D_{bp} ratio (fig. 3.9). These were 5 kHz, 41 kHz and 86 kHz frequencies, and are referred to as mode 1, mode 2, and mode 3 respectively, in fig. 3.9. From fig. 3.9 it can be seen that the output voltage from mode 1 is constantly low, except for ratios of 0.5 and 0.7, when the output voltage peaks.

In contrast, mode 2 at 41 kHz has a high output voltage up to a D_p/D_{bp} ratio of 0.2 and then gives a constant, low output. The mode 3 resonance goes through three maxima at D_p/D_{bp} ratios of 0.15, 0.5, and 0.7.

It is clear from fig. 3.9 that the piezoelectric diameter will greatly effect the output voltage of the transducer at each resonant frequency. This is because the voltage produced is proportional to the overall displacement of the piezoelectric. The first mode of vibration is a bending mode of the back plate and, therefore, when the piezoelectric disc has a small diameter, the net displacement is small. As the diameter increases, the net displacement of the piezoelectric is greater, thus increasing the output voltage.

At 41 kHz the bending of the back plate is more complicated and, therefore, the displacement depends on the diameter of the piezoelectric. Once the piezoelectric becomes larger, and the D_p/D_{bp} ratio is greater than 0.2, the overall displacement of the piezoelectric is less than at small diameters because the positive and negative bending cancel each other out and, therefore, a lower output voltage is produced.

For the intended geotechnical use of the transducer, the mode of interest would be the 40 kHz mode. High output for this mode is restricted to small diameter discs, typically just less than 0.2 times the back plate diameter. This small D_p/D_{bp} is also desirable to reduce the audio frequency resonance at mode 1.

3.4.2 Modelling the Effect of Varying the Back Plate Diameter

To model the effect of varying the back plate diameter, a small diameter piezoelectric disc (2.5 mm diameter and 5 mm thick) was used in the model. With a small diameter

disc, its influence on the back plate vibration would thus be minimised. Secondly, section 3.4.1 has shown that a smaller diameter piezoelectric disc would be desirable since it would lower the amplitude of the audio frequency resonance mode (around 5 kHz), and increase the amplitude of the 41 kHz mode.

Output voltages are shown in fig. 3.10, when varying the back plate diameter to throat diameter ratio (D_{bp}/D_t). The diameter of the back plate was increased from a diameter equal to that of the horn throat (5.15 mm), up to 50 mm. This time, the reason for the variation of the transducer output was more obvious.

Fig. 3.10 shows that for a given throat diameter, the transducer was most effective at one size of back plate i.e. when the back plate is about five times the throat diameter. At all diameters the first mode occurred between a frequency of 5 to 10 kHz, producing a low output voltage. This is because the first back plate mode is a bending mode, in which the outer most edge of the back plate undergoes the largest displacement. The small diameter piezoelectric element was, therefore, largely unaffected by the back plate displacement.

The variation in output for the second mode at 41 kHz, shown in fig. 3.10, gave a reasonable output for ratios up to 3, and then dropped before peaking at a back plate diameter of around 25 mm.

For the variation in amplitude of the 86 kHz peak, the output voltage follows almost the same pattern as the 41 kHz output, except it is consistently 3 to 4 times greater in magnitude.

The more complicated vibration in the transducer at 86 kHz, must produce greater net displacement of the piezoelectric element, than at 41 kHz, in order to produce consistently higher voltages. The ideal D_{bp}/D_t ratio is 4.85 to give maximum output voltage at the 41 kHz mode.

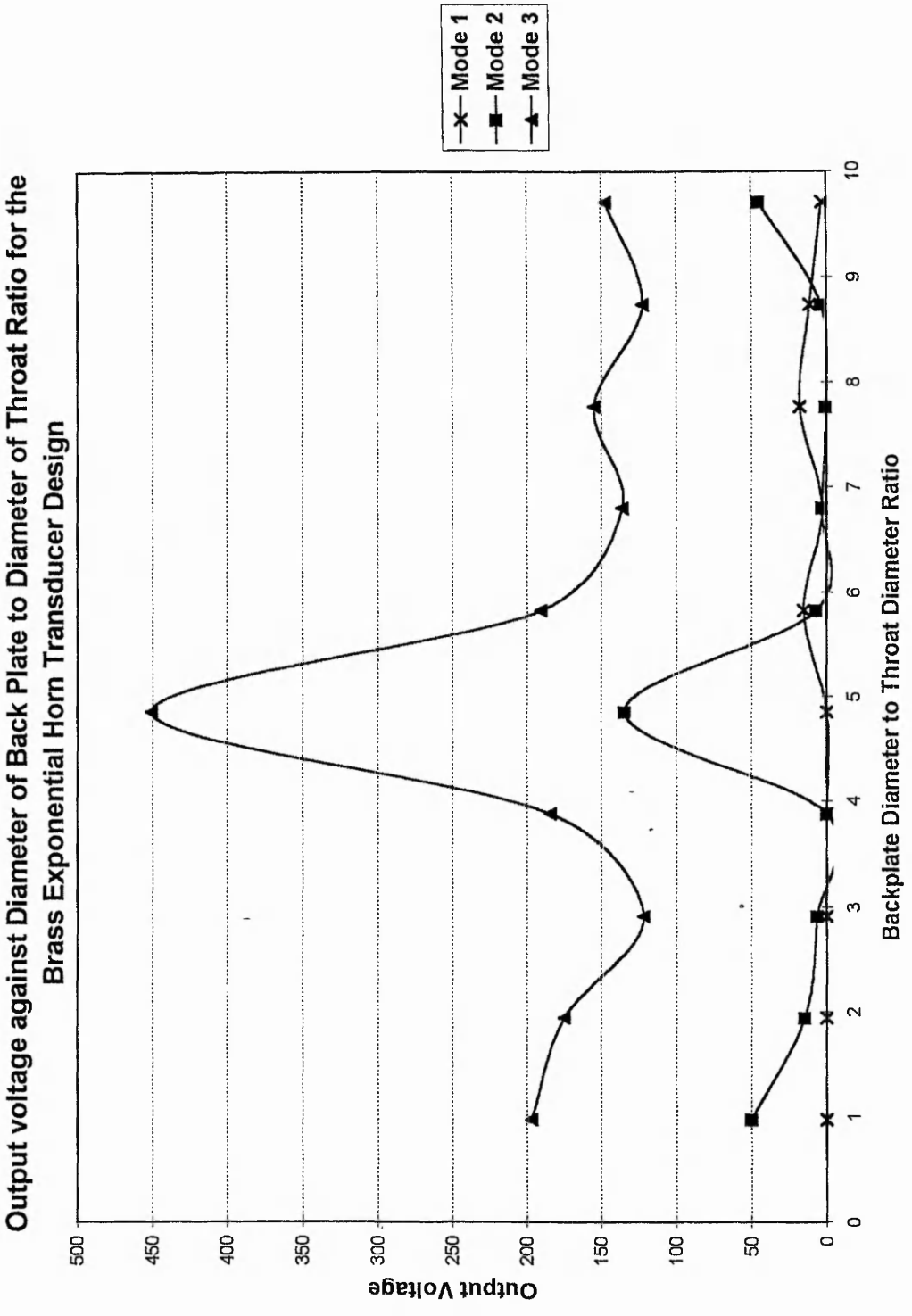

Fig. 3.10 Output voltage against back plate diameter to horn throat diameter ratio. Each graph represents one of the transducer resonances and the throat diameter is 5.15 mm.

The theory for circular plate vibration, studied in section 3.3.4, should give an indication as to which back plate diameters will have a 40 kHz resonance. Theory and modelling show close agreement (table 3.4) at a back plate radius of 25 mm, the original back plate dimension. Taking a frequency of 40 kHz, the theory indicates that back plate radii of 9, 10.5, 13.9, 16 and 21 mm will produce a back plate resonance. The FE model indicates that a radius of 12.5 mm (4.85 x $D_t/2$ = 4.85 x 5.15 mm/2) will give a maximum amplitude.

Circular plate theory has been applied to a brass disc with a thickness of 4.9 mm, as in the transducer. In the transducer there is a piezoelectric disc attached to the brass back plate. When the back plate is large with respect to the piezoelectric disc then the theory and FEM show close agreement, because the back plate is dominating the vibration. When the piezoelectric is large, due to either the back plate becoming smaller or the piezoelectric becoming larger, then the theory looses its validity and cannot predict the resonances of the more complex system. This highlights the way theoretical closed form solutions quickly become redundant for predicting complex system behaviour. FEM has shown it is both effective (when comparison with theory is possible) and, is able to deal with more complex systems.

3.4.3 Modelling the Effect of Varying the Horn Length

Variation of the exponential horn section was the last component to be modelled. Horn length was the parameter chosen to be systematically varied. Removing or adding material from either end could vary the horn length. It was decided to keep the horn mouth radius constant and remove length from the throat end. This meant that the throat radius increased as the horn length decreased, because the shape of the horn remained unchanged.

This also meant the transducer face area was constant, giving a consistent acoustic input condition. The original back plate (25 mm radius, 4.9 mm thick) and thin piezoelectric disc (19 mm radius, 1 mm thick) were used, to allow comparison with the first axisymmetric model of section 3.3.2.

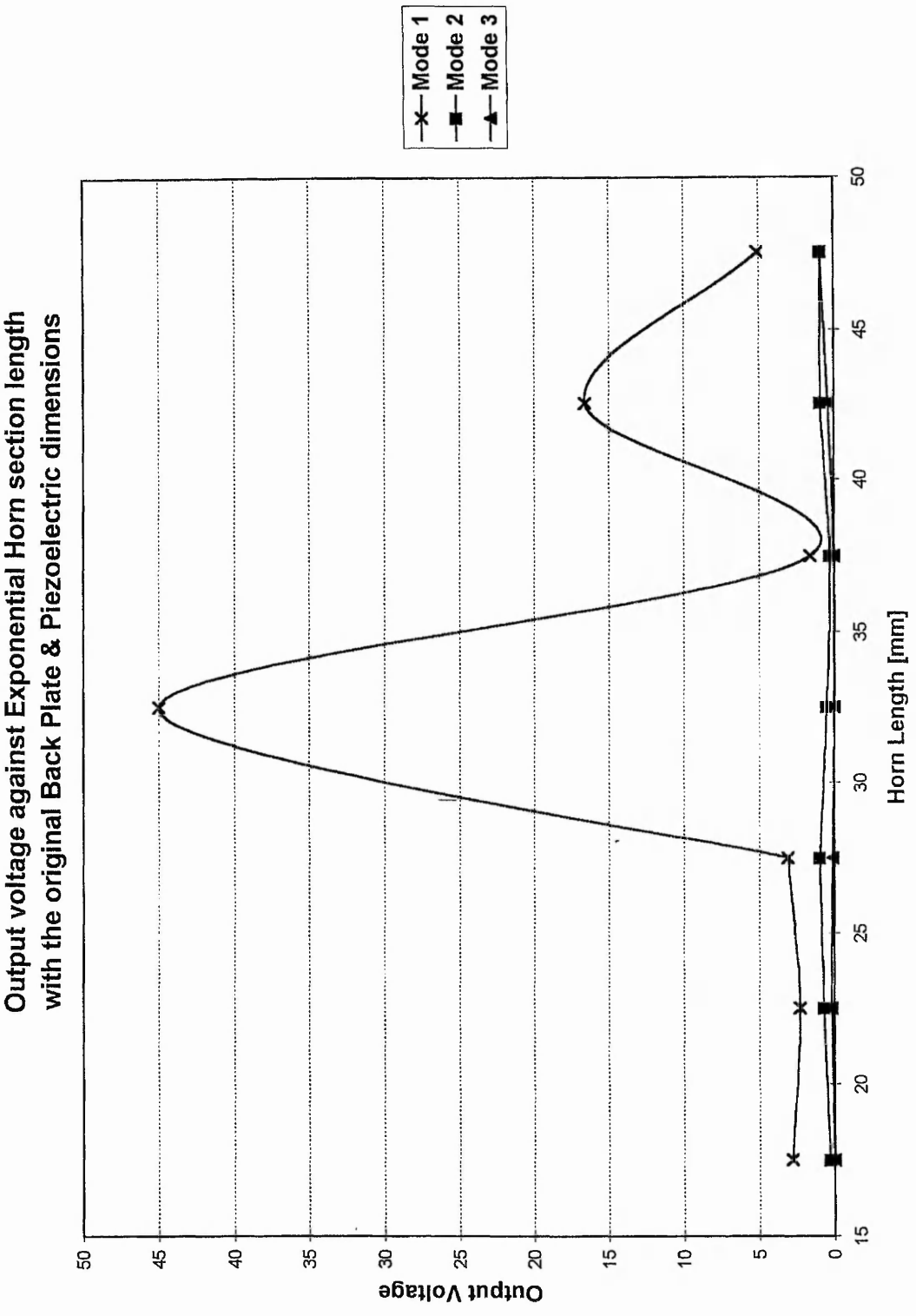

Fig. 3.11 Output voltage against exponential horn length. Each graph represents one of the transducer resonances. The transducer has the original back plate and piezoelectric element used in the first axisymmetric model.

The horn length was modelled at 2.5 mm intervals between 17.5 and 47.55 mm (the original length). Output voltage against horn length was plotted at the three main resonances in the 5, 41 and 86 kHz regions, modes 1, 2, and 3 respectively (fig. 3.11). Modes 2 and 3 both gave a relatively low output voltage at all horn lengths in the frequency range modelled. At 32 mm, mode 1 produced a maximum output voltage, with a second peak occurring at 42.5 mm. Mode 1 is the undesirable audio frequency that involves the back plate bending about the horn throat (fig. 3.6). Suitable horn lengths for minimising the audio frequency mode, from fig. 3.9, appear to be less than 25 mm, or 37.5 mm. The original length of 47.55 mm is still much better than lengths of 32.5 or 42.5 mm.

3.4.4 Modelling the Effect of Varying the Horn Length, No Back Plate

To further the understanding of the effect of the horn length on the transducer performance, the horn length was again varied in the FE model, but this time without a back plate.

Instead a small (2.5 mm diameter, 5 mm thick) piezoelectric attached directly to the horn throat. This would eliminate the back plate contribution altogether. Horn lengths of 27.5 to 47.55 mm were modelled at 2.5 mm intervals. Since transducer output voltages were reducing, for horn lengths below 27.5 mm, horns with lengths below this value were not modelled in detail. The variation of output voltage with horn length is shown in fig. 3.12.

No first mode transducer resonance in the 5-10 kHz range was observed, due to the lack of the back plate. The frequencies used to plot output voltage against horn length were 41, 64 and 86 kHz, labelled modes 2, 2a, and 3 in fig. 3.12 .

Mode 2 at 41 kHz showed a rapid increase in output voltage after a length of 40 mm. For all the lengths investigated, this mode produced higher amplitude voltages than with other, previously modelled, designs. This mode also produced the highest amplitude voltage for this investigation.

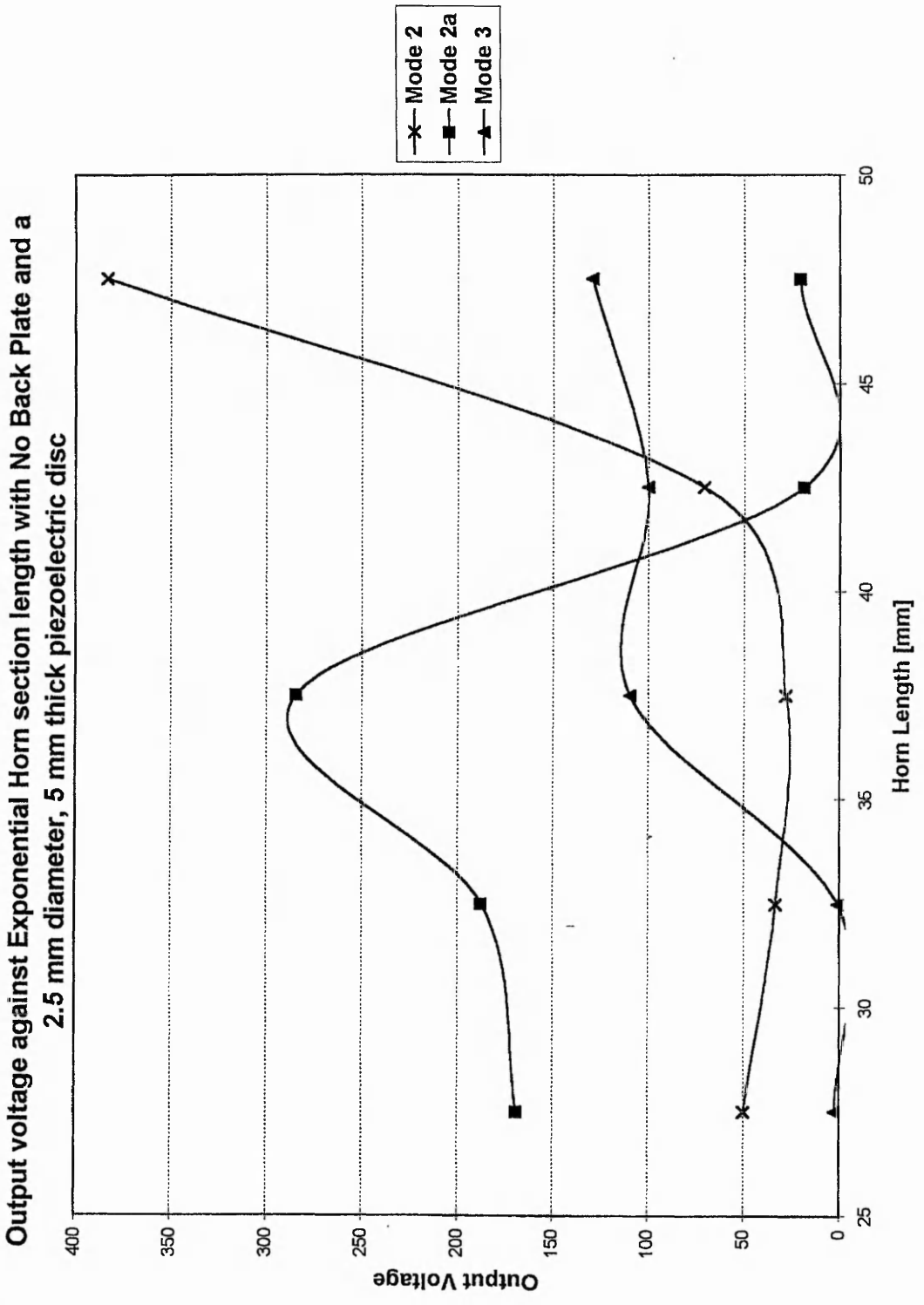

Fig. 3.12 Output voltage against exponential horn length. Each graph represents one of the transducer resonances. The transducer has no back plate and the piezoelectric element used is 2.5 mm diameter and 5 mm thick.

At 64 kHz and for horn lengths below 35 mm, the output voltage was highest when compared to the other modes, with a maximum output at 37.5 mm. Beyond this maximum, the output dropped (fig. 3.12). The higher frequency output (mode 3) slowly increases in amplitude, as the horn length increased, for the lengths of horn up to 47.55 mm.

3.5 OPTIMISING THE BRASS EXPONENTIAL HORN TRANSDUCER DESIGN

The aim was to optimise the exponential horn design to produce a transducer for geotechnical work, with a resonant frequency of 40 kHz, high sensitivity, and narrow bandwidth.

The original horn section had been designed to have a resonance at 40 kHz. The back plate design was used as a suitable method for attaching a piezoelectric element to the narrow throat end. This, however, introduced larger resonances in the audible frequency range, as shown in section 3.3.1. With appropriate electronic filtering these would be removed.

A forced sinusoidal analysis of the horn section alone was carried out, with no piezoelectric element present. This showed a resonant frequency of 40 kHz, which is the desired frequency. The horn length investigation, without a back plate (section 3.4.4), also showed the main resonance, in the 1-100 kHz range modelled, to be at 41 kHz. By optimising the original design, a large amplitude resonant peak at 40 kHz should be possible, with no lower frequencies arising from the transducer.

Using the information gained from the systematic modelling of the transducer components, the ideal back plate and piezoelectric diameter were chosen. The original horn length of 47.55 mm was used, as data in fig. 3.12 has shown this to be best. The optimal diameter for the back plate was 25 mm and for the piezoelectric disc was 3.75 mm, which are seen in fig. 3.13. These were chosen using the graphs of output voltage against D_p/D_{bp} ratio, and output voltage against D_{bp}/D_t ratio, shown in fig. 3.9 and 3.10.

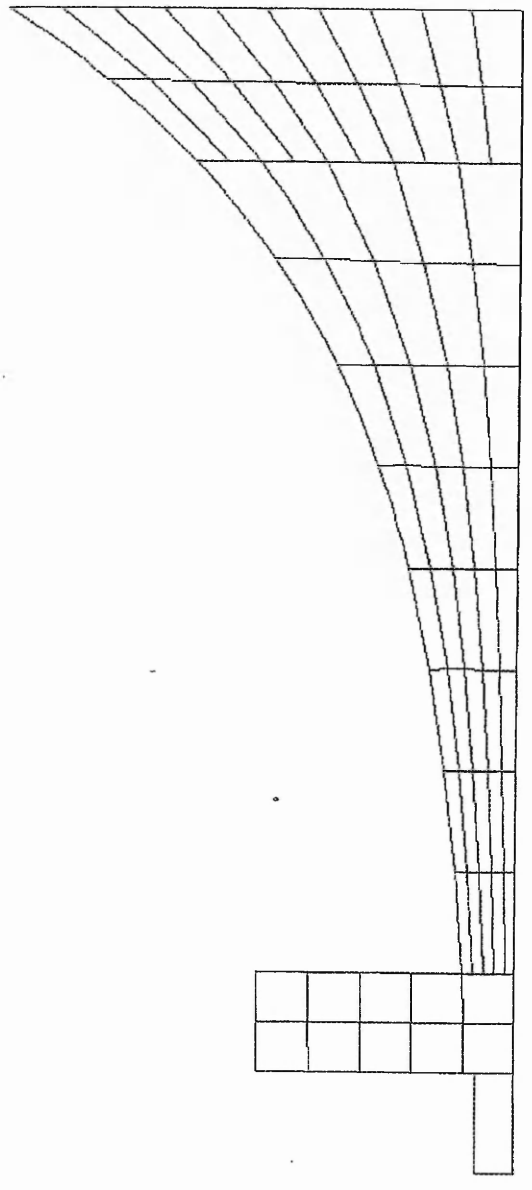

Fig. 3.13 FE mesh of the **optimised** exponential horn transducer design. Model is axisymmetric about the right hand vertical axis.

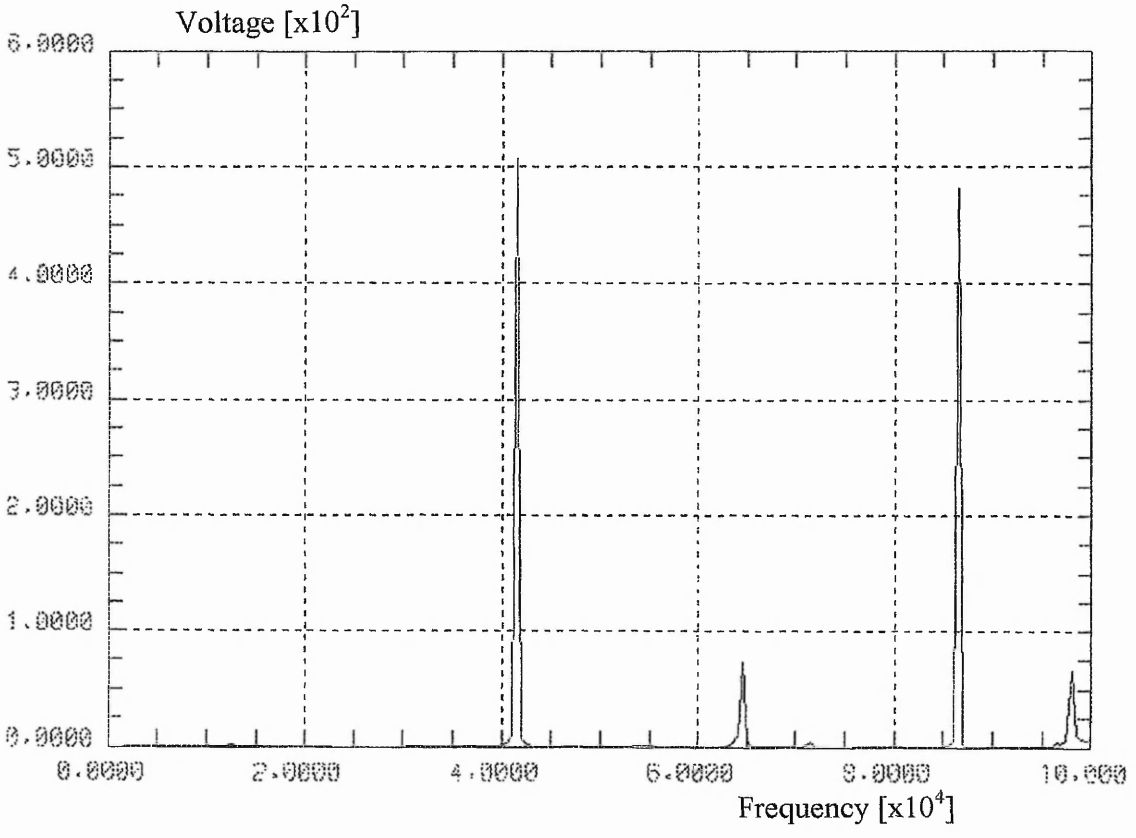

Fig. 3.14 Output voltage against frequency for the **optimised** exponential horn transducer design.

The mode of interest was the second mode at 41 kHz. The aim was to choose dimensions that gave a high output voltage for mode 2 while giving a low output voltage for mode 1 and, if possible, mode 3 as well.

Acoustic finite element modelling of the ideal design showed a marked improvement in the transducer's output voltage (fig. 3.14). As expected, the output at the 40 kHz mode (actually 41.5 kHz) was greatly improved, increasing by over 500 times. The lowest resonance in the audible range appears to have disappeared, on this scale, although there is a tiny peak around 12 kHz (<3 volts). High output voltage was also observed at 86 kHz (481 volts).

The amplitude of the output voltage at 41.5 kHz was even greater than when the original horn length was modelled, without a back plate and with a small piezoelectric attached directly to the horn throat (506 compared to 380 volts), seen in section 3.4.4.

The model of the horn with no back plate, in section 3.4.4, had previously given the largest amplitude voltage seen in any of the variations of the brass exponential horn design modelled, until the design was optimised. The fact that the 40 kHz mode output voltage is even greater in amplitude (506 compared to 380 volts), with a carefully designed back plate and piezoelectric than with no back plate, shows that popular transducer designs, such as horns used for ultrasound applications, can have their performance enhanced by adding other components. These added components will only provide improvements, however, if designed accurately. While the exponential horn transducer has been optimised to receive ultrasound at a particular frequency, the optimisation process is equally important for transducers involved in the generation of ultrasound.

The brass exponential horn investigation has demonstrated several important issues with regard to designing a transducer.

1. Classical mathematical theory can only be used to evaluate the simplest designs.
2. Any additions to the original simple design will affect performance, possibly in a complex way, which is difficult to predict.

3. FEM can be used to investigate the effect of these changes and provides a valuable design tool, without the need for a lengthy build and test programme.

3.6 USE OF DIFFERENT MATERIALS TO IMPROVE TRANSDUCER PERFORMANCE

In order to gain some understanding of the best material choice, the original exponential horn transducer design was modelled with the transducer made of aluminium and steel, instead of brass. Combinations of these materials were also tried, but in practice this would probably cause more problems associated with joining and acoustic impedance mismatches.

Aluminium and mild steel were the two materials chosen as alternatives to brass. The reason for these choices was that aluminium offered a lighter, low stiffness metal. Steel, on the other hand, provided a stiffer material than brass. The material properties are compared to brass in table 3.5.

Modelling using aluminium provided a trebling of the first mode output voltage (fig. 3.15), with an increase in the resonant frequency by about 1.5 kHz. The reason the first mode amplitude increases is because the back plate can flex more, due to the lower stiffness of the aluminium. The flexural rigidity (D) of the aluminium back plate is 0.64 times that of the same dimension brass back plate. D is given by equation 4 in section 3.3.4. For aluminium, small resonance peaks also occurred at 23 kHz and 41 kHz. Other strong resonances were not apparent. If the first mode resonance could be tuned to the correct frequency then aluminium appears to be a good material for a resonant transducer, because the amplitude of this mode is much greater than any other in the 1-100 kHz frequency range.

The theory for circular plate vibration, described in section 3.3.4, should accurately predict the first back plate resonance, as well as some of the other transducer output voltage peaks. As with the original brass transducer, the theory for a circular plate with a fixed centre provides a close agreement with the FE model prediction for the first mode frequency, for a 25 mm radius back plate.

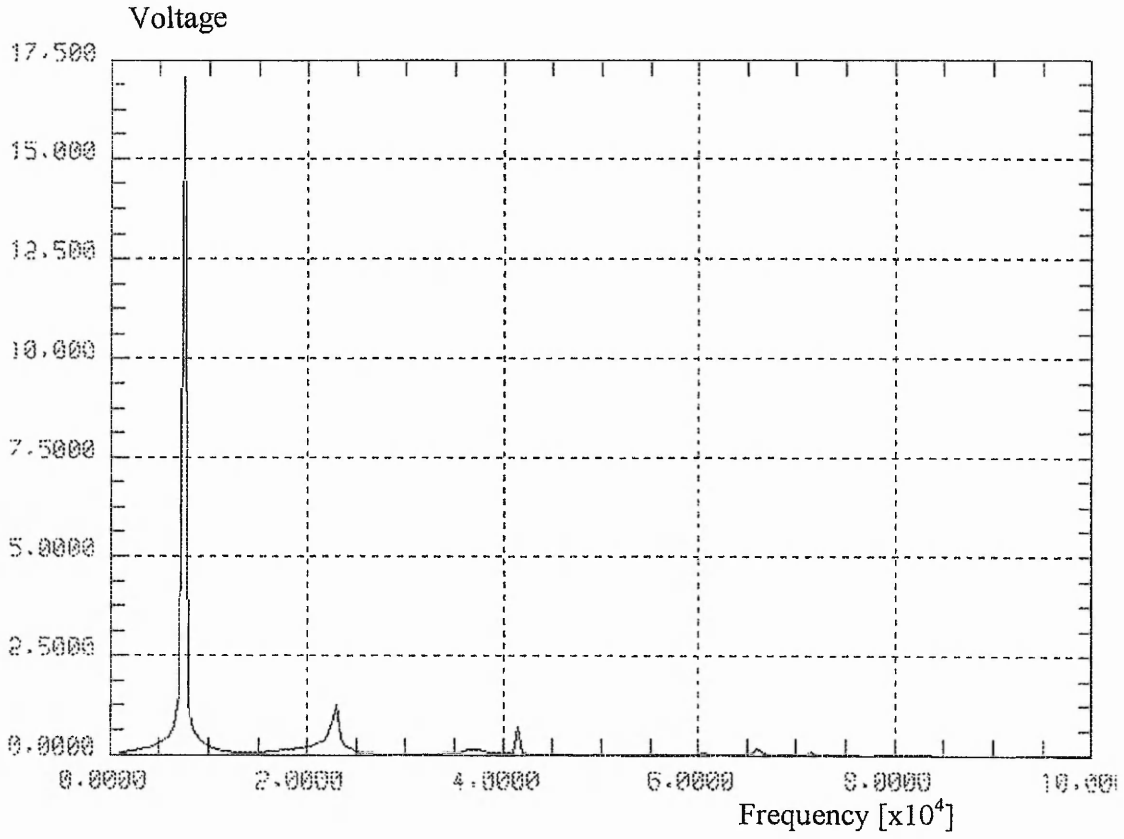

Fig. 3.15 Output voltage against frequency for an aluminium exponential horn transducer of the original design.

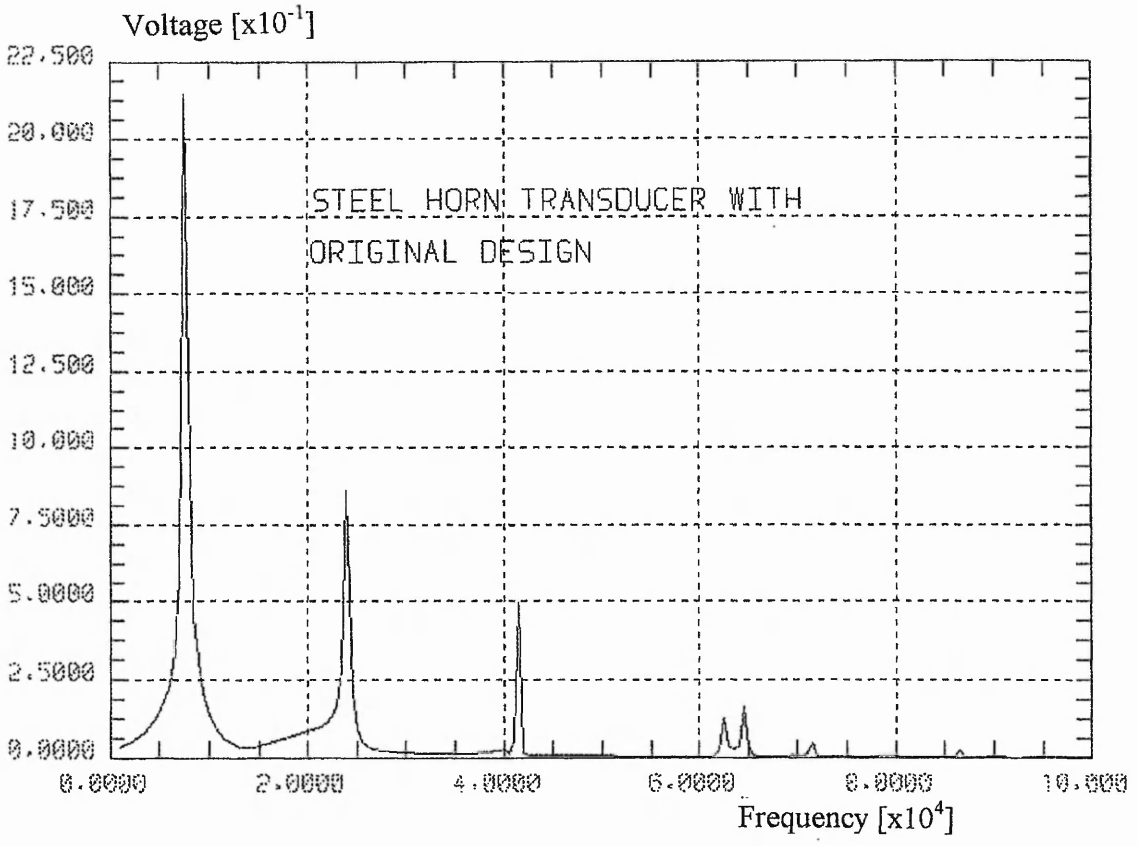

Fig. 3.16 Output voltage against frequency for a steel exponential horn transducer of the original design.

The theoretical resonant frequency for an aluminium back plate increases from that of the same dimension brass back plate to 7 kHz. The FE model agrees with this.

A steel transducer was also used to compare to the brass and aluminium ones already modelled. Theory and FE both predict an increase for the 5.5 kHz mode of the brass transducer to 7 kHz for the steel transducer. The steel back plate has a flexural rigidity of 2.25×10^3 Nm compared with 1.18×10^3 Nm for brass (table 3.5). This prevents large displacement of the flexural modes and hence, a lower output voltage is achieved across the piezoelectric element (table 3.6). The 17 kHz mode of the brass transducer was now at 24 kHz, a frequency also predicted by the theory. This time, although still at 41 kHz, the third resonant peak (fig. 3.16) was half the amplitude of the same peak in the brass or aluminium transducers. This is a horn section resonance and the drop in amplitude indicates that, for steel, this length of horn is no longer ideal for producing a resonant mode of vibration.

Property	Brass	Aluminium	Steel
E [Nm^{-2}]	1.04×10^{11}	6.85×10^{10}	2.09×10^{11}
ρ [kgm^{-3}]	8500	2695	7800
ν	0.37	0.33	0.3
c [ms^{-1}]	4652	6137	6006
Z [$kgm^{-2}s^{-1}$]	3.95×10^7	1.65×10^7	4.68×10^7
D [Nm]	1.18×10^3	7.54×10^2	2.25×10^3
G [Nm^{-2}]	3.80×10^{10}	2.58×10^{10}	8.04×10^{10}

Table 3.5 Material properties used in the FE models. E is the Young's modulus, ρ is the density, ν the Poisson's ratio, c the sound velocity, Z the acoustic impedance, D the flexural rigidity and G the shear modulus.

The fact that the frequency of the 5.5 and 17 kHz modes has shifted, while the 41 and 64 kHz modes have not, suggests that the horn is a robust design and would be resilient to slight variations to its dimensions in practice. These variations may occur at the manufacturing stage.

Table 3.5 shows the properties for brass, steel and aluminium. The acoustic transmission coefficient T is dependent on the relative acoustic impedances between the different materials and it indicates the ratio of incident acoustic pressure transmitted through the material boundary. This may help to further explain the relative amplitudes because T

for steel to PZT-5A is lower than for brass to PZT-5A, while T for aluminium to PZT-5A indicates a pressure amplification and, therefore, an increase in the output voltage. T is calculated by the formula $T = \frac{2Z_2}{Z_1 + Z_2}$, where Z_1 and Z_2 are the impedances of the two materials e.g. brass and PZT-5A.

When a combination of the brass horn with an aluminium back plate was tried, the output was similar in magnitude and shape to that obtained when using an all steel transducer (fig. 3.17). The impedance difference between brass and aluminium means that there is a poor transmission coefficient T of 0.59. The first resonant peak is at 7 kHz, as in the all aluminium transducer, confirming that this mode is dominated by the back plate.

The output voltage for a steel horn section and aluminium back plate is shown in fig. 3.18. The first mode is at 7 kHz and has the same amplitude as the original brass transducer (table 3.6). The 41 kHz mode also has the same output voltage amplitude as for the brass transducer. However, the 84 kHz peak has an amplitude of nearly 400 times that achieved at 86 kHz in the all brass transducer (table 3.6). If this frequency could be tuned then this material combination would provide a very large sensitivity for a resonant transducer.

Brass		Aluminium		Steel		Brass/Alum		Steel/Alum	
[kHz]	[volts]	[kHz]	[volts]	[kHz]	[volts]	[kHz]	[volts]	[kHz]	[volts]
5.5	5.0	7	17	7	2.2	7	2	7	5
17	1.0	22	1.8	24	0.8	23	0.9	-	-
41	0.9	41	1	41	0.5	41	0.8	41	1
64	0.1	66	0.2	64	0.2	66	0.2	-	-
86	0.9	86	0	86	0	86	0.1	84	400

Table 3.6 Resonant frequencies and output voltages for the exponential horn transducer modelled with different material combinations.

The predicted success of this combination lies in the material properties mentioned above. The flexible aluminium back plate will vibrate with a larger amplitude for a given input force at the throat. Being stiffer, the steel transmits more of the incoming sound energy directly in the longitudinal mode, and energy is not dissipated by modal coupling and radial flexure.

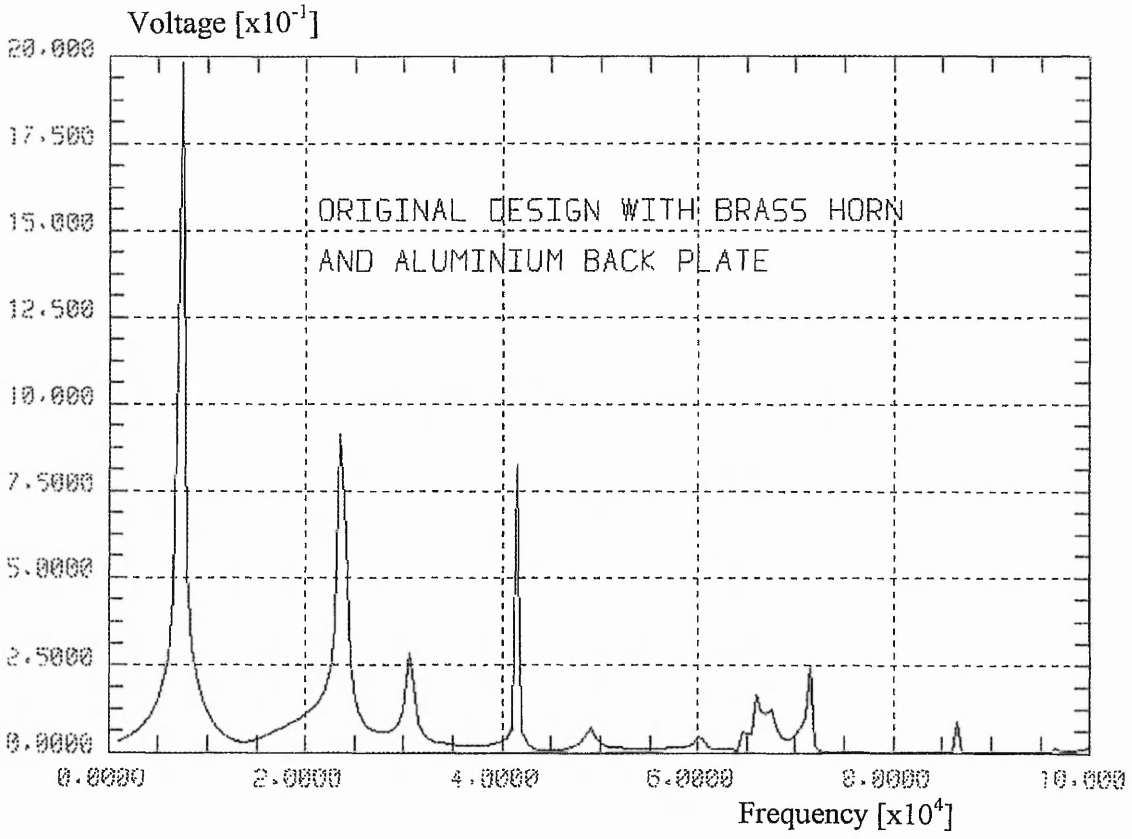

Fig. 3.17 Output voltage against frequency for an exponential horn transducer of the original design, with a brass horn section and an aluminium back plate.

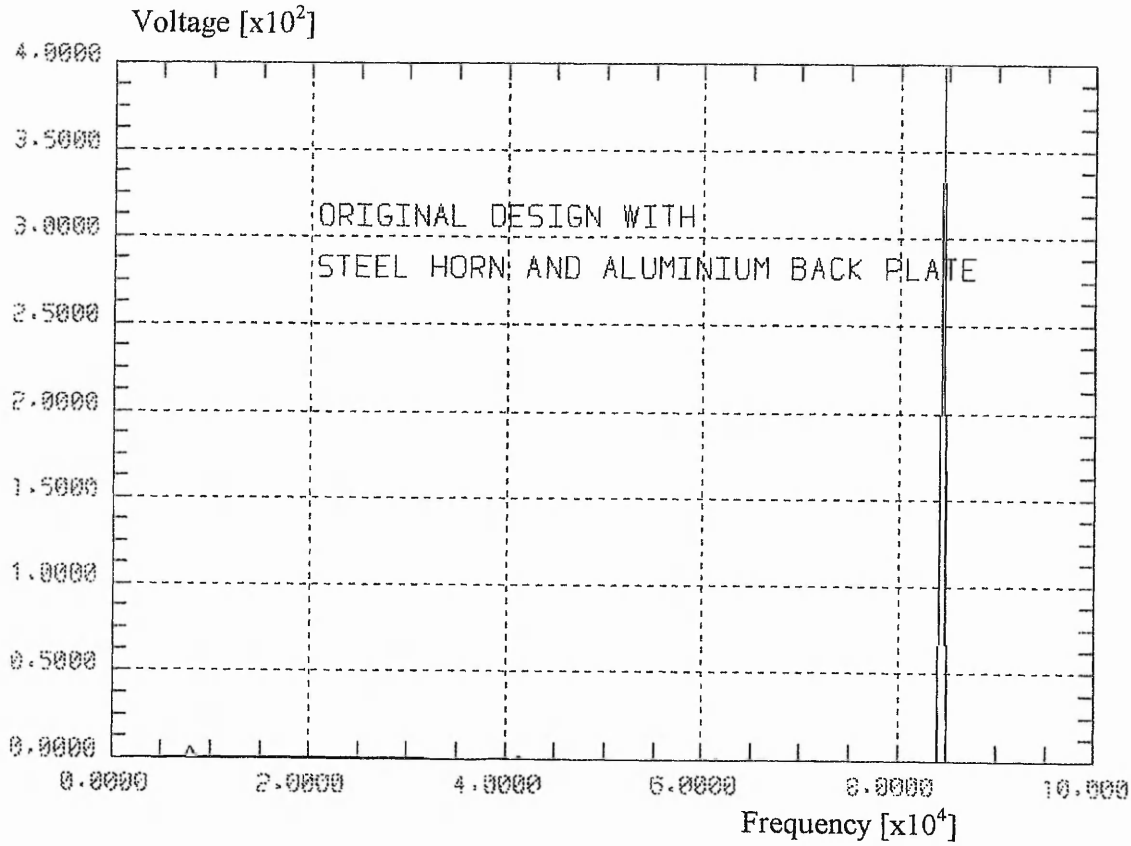

Fig. 3.18 Output voltage against frequency for an exponential horn transducer of the original design, with a steel horn section and an aluminium back plate.

The fact that the FE models predict the slight shift in the resonant frequencies of the 5 kHz mode and the 17 kHz mode, calculated using the circular plate theory in section 3.3.4, suggests that the modelling is good at frequency predictions. Changes in the output amplitudes of these modes, predicted by FEM, can mainly be explained by the changes to the material properties e.g. increased back plate flexural rigidity. However, the extremely large increase in amplitude at 84 kHz in the steel and aluminium combination, is hard to explain fully. Such dramatic predictions of output amplitude indicate that further damping to the model, other than that provided by the fluid, should be employed to make the models more realistic. In this case, it is likely that the exact resonant frequency occurs at 84 kHz and on one of the modelling values, therefore causing an extremely large output voltage prediction. This suggests that a higher frequency resolution than 0.5 kHz would be required if more accurate amplitude predictions are to be achieved.

3.7 EFFECT OF BACK PLATE SHAPE ON RESONANT FREQUENCY

3.7.1 Using a Tapered Back Plate

So far, methods of increasing the transducer sensitivity have been considered. This section considers ways to increase the transducer bandwidth. It is known that tapering of the back plate might increase the bandwidth. The aim was not to create a broadband transducer response, but a broader resonant peak. An experimental study by Mitra et al. **[16]** demonstrated this effect by tapering a piezoelectric element. Mitra et al. found that by changing the angle of taper, multiple resonant peaks would occur or a continuum in the vicinity of resonance. Also, the amplitude of higher harmonics was reduced.

A tapered design was chosen for this study, in which the thickness of the back plate varied with its diameter. A convenient angle of 10° was used for this investigation. The model considered a back plate, with an angle of taper of 10°, thinning with increasing diameter (fig. 3.19). The second model considered the back plate becoming thicker as the diameter increased, again with an angle of taper of 10° (fig. 3.20). For both models the top of the back plate was kept flat, because it carried the piezoelectric disc.

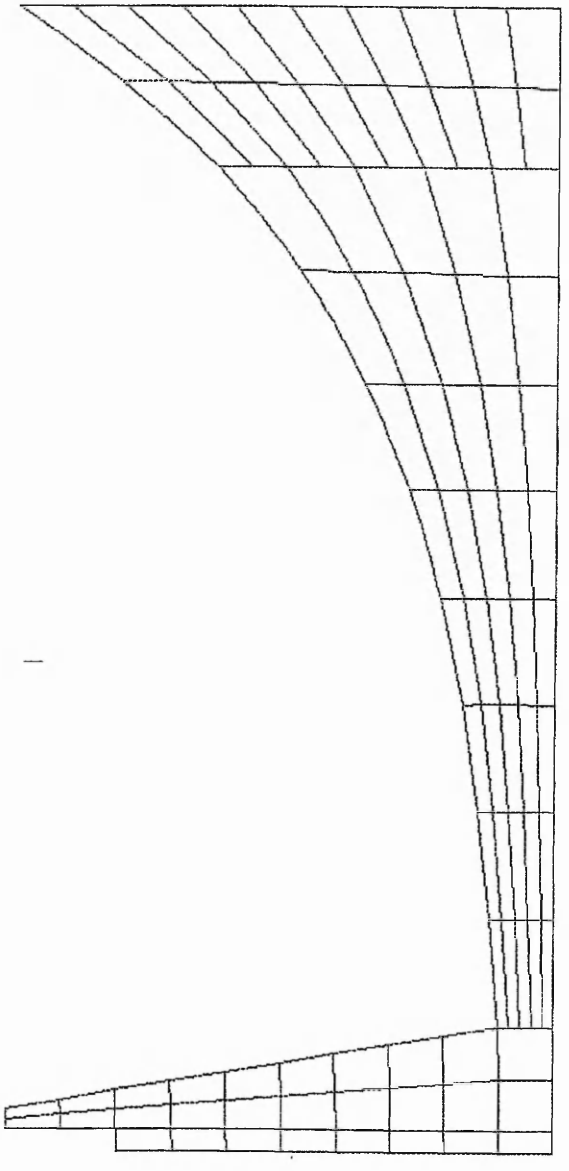

Fig. 3.19 FE mesh of an exponential horn transducer with a tapered back plate. The model is axisymmetric about the right hand vertical axis. The taper angle is 10° below the horizontal - **Taper 1**.

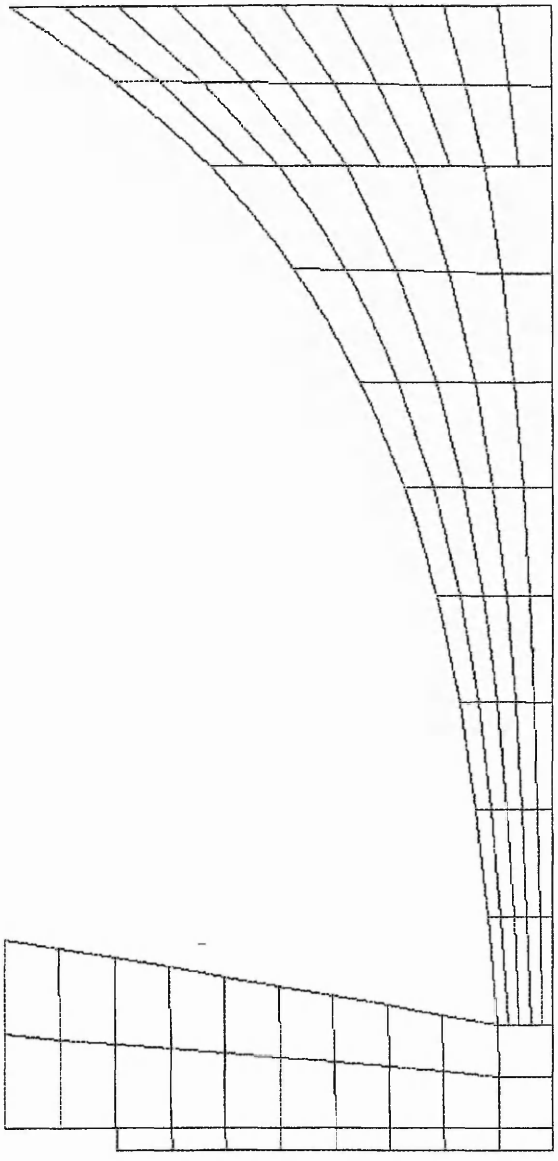

Fig. 3.20 FE mesh of an exponential horn transducer with a tapered back plate. The model is axisymmetric about the right hand vertical axis. The taper angle is 10° above the horizontal - **Taper 2**.

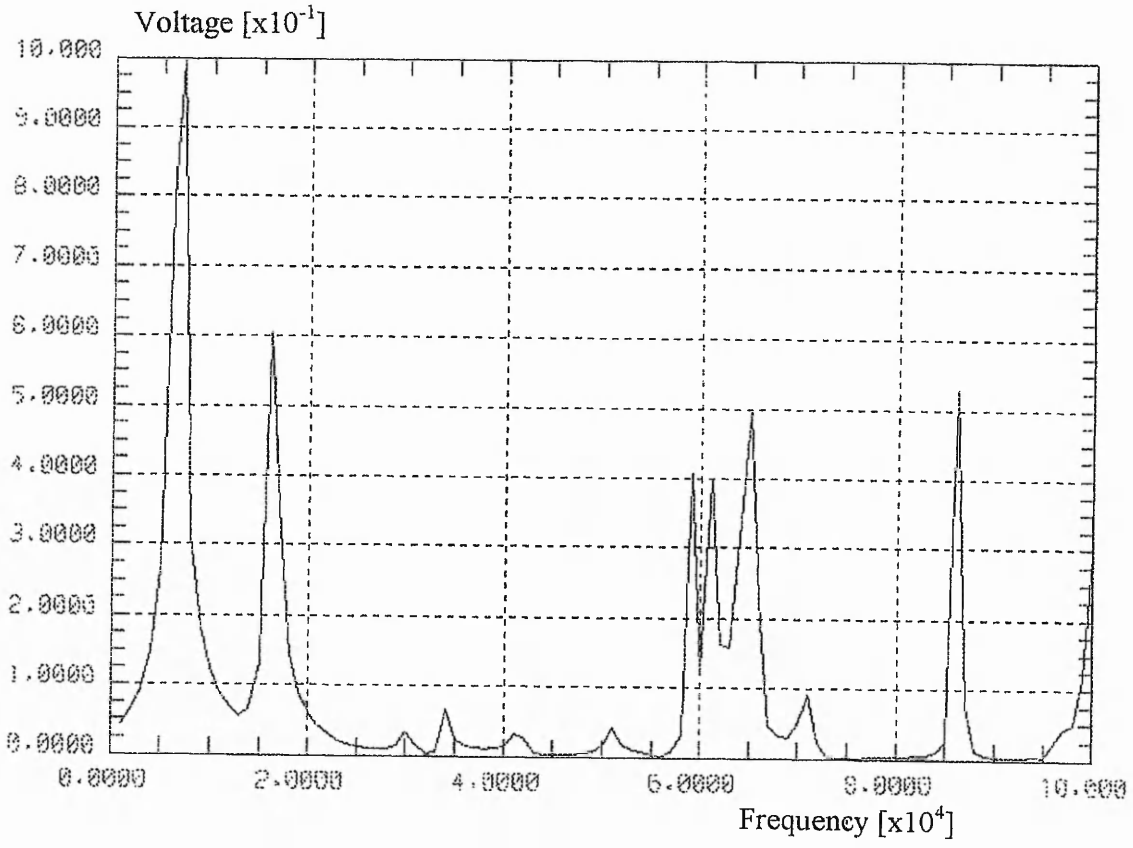

Fig. 3.21 Output voltage against frequency for the original size exponential horn transducer with a tapered back plate. The angle of the taper is 10° below the horizontal - **Taper 1**.

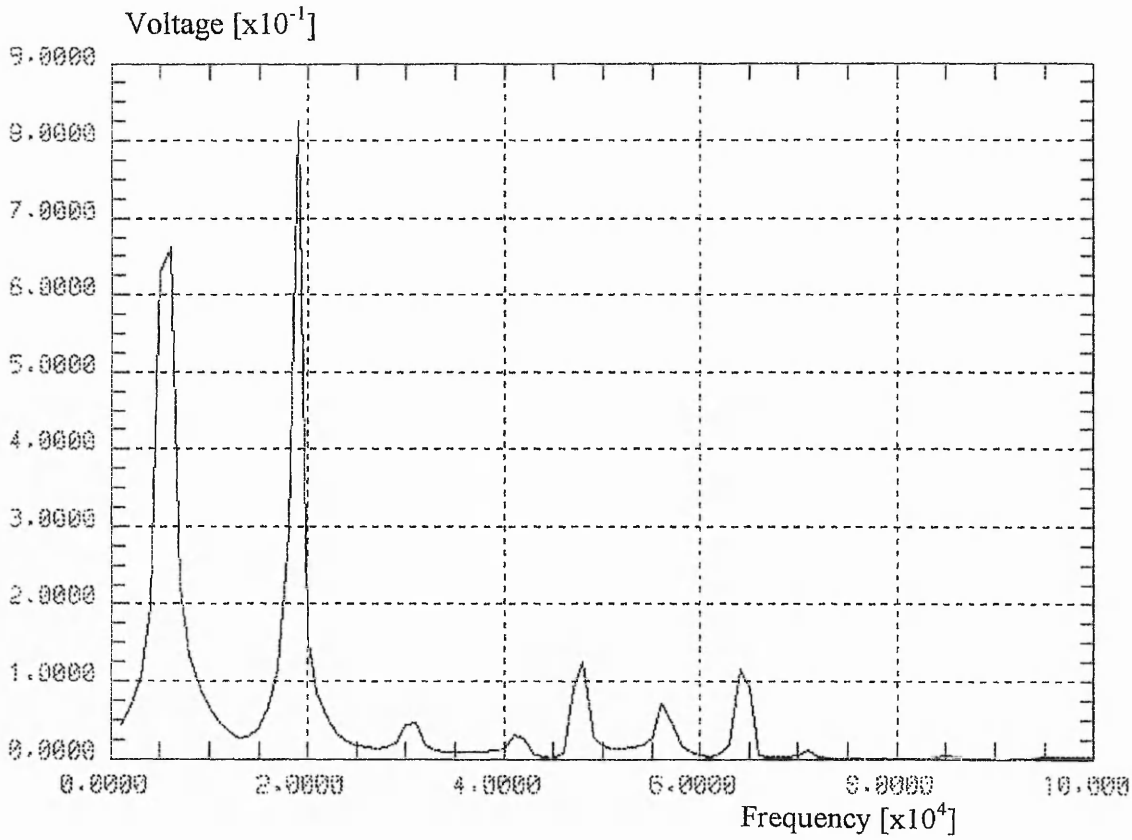

Fig. 3.22 Output voltage against frequency for the original size exponential horn transducer with a tapered back plate. The angle of the taper is 10° above the horizontal - **Taper 2**.

Taking the case of the thinning back plate (taper 1), the output voltage amplitudes (fig. 3.21) are less than those seen in the original design, as table 3.7 shows. This is most obvious for the first mode, around 7 kHz, for which there is an 80% reduction in amplitude. The 86 kHz mode suffers less of a loss in amplitude, but does show a broader peak (fig. 3.21). The most interesting region is the 60-70 kHz frequency range that showed very little response originally. Now, a broad peak topped by three spikes is seen, with a fourth spike skewed to the right. This highlights the fact that by careful control of transducer geometry, increased bandwidth is possible.

From the circular plate theory in table 3.4, no modes in the 60-70 kHz region are predicted, for a 25 mm radius back plate. Reduction of the plate thickness will lower the frequency of a given mode (α value) at a fixed radius. At shorter radii there are several modes in the 60-70 kHz range. The taper can be viewed as giving a combination of large radius, thin discs and short radius, thick discs providing a range of modes at a given frequency. If the taper caused the back plate to act as a smaller diameter disc of the original thickness (4.9 mm) then the lowest mode (α=3.75) would increase in frequency. A frequency increase (5.5 to 7 kHz) is predicted by the FE model and seen in table 3.7. The amplitude of the mode at 7 kHz is reduced from that of the 5.5 kHz original value, which is also an indication of the back plate's changing behaviour. For the α value of 3.75 to produce resonances in the 60-70 kHz range the 4.9 mm thick disc would have an effective radius of about 7 mm. Due to the increase in amplitude in this frequency range, it is likely that this mode is active.

When the back plate becomes thicker with diameter (taper 2, fig. 3.22), the predicted output voltage amplitude of the transducer is again lowered from that of the original design (table 3.7). Up to 45 kHz, the response of the transducer is almost the same as with taper 1 (fig. 3.21 & 3.22). The 19 kHz peak is a higher frequency than the 17 kHz peak for the original back plate, which indicates the back plate is behaving as a thicker disc (increasing the disc thickness increases the resonant frequency of a circular plate).

A broadband region is seen between 45 and 60 kHz, again with three peaks and a smaller fourth peak to the right. However, comparing the output voltage amplitudes in table 3.7,

they are about a fifth of the taper 1 amplitudes and there is only a tiny output voltage peak at 86 kHz.

Original Design		Taper 1		Taper 2	
[kHz]	[volts]	[kHz]	[volts]	[kHz]	[volts]
5.5	5	7	1	6	0.6
17	1	16	0.6	19	0.8
41	0.9	41	<0.1	41	<0.1
-	-	59	0.4	-	-
-	-	61	0.4	-	-
64	<0.1	65	0.5	64	0.1
-	-	71	<0.1	-	-
86	0.9	86	0.5	85	<0.1

Table 3.7 Comparison of transducer resonant frequencies and their respective output voltage amplitudes, for the tapered and original transducer designs.

Detailed comparison with any theory was not possible as Meirovich [57] has indicated that no closed form solutions exist for tapered plates. Circular plate theory allows some understanding of what is happening to be gained. Taking a frequency of 64 kHz, several modes of vibration can occur at different disc radii for one disc thickness. A change in the disc thickness shifts the frequency of the resonances at each disc radius. If the thinning tapered back plate (taper 1) is considered as many thin discs, with increasing radii, joined together, then it is possible to see that the same frequency could be caused by a number of different α values for a variety of disc radii. The taper 1 design showed that the effect of spreading the frequency of resonant peaks, observed in piezoelectric discs by Mitra, can also be achieved by tapering the back plate.

The tapered back plate is reducing the Q values of all of the modes from the values seen for the original transducer. This effect is a result of a drop in the maximum amplitude of the peaks and/or a broadening of the resonant peak. Much of the reduction in Q value appears to stem from the reduction in the output amplitudes.

Further investigation was not carried out as the aim to induce broader resonant peaks has been demonstrated. The drop in output voltage amplitude indicates a decrease in the transducer sensitivity, which is clearly undesirable. In order to benefit from the multiple

resonance idea, it is recommended that the tapered back plate would have to be combined with some of the output optimisation principles, already considered.

3.7.2 Using a Grooved Back Plate

By complicating the shape of the transducer back plate further it was hoped that an alternative approach to resonance broadening could be achieved. Section 3.7.1 considered a shaped back plate and showed that it had potential for lowering the Q value of the existing disc back plate resonant peaks. Additional peaks were created because the shaped back plate appeared to excite a number of different modes in a small frequency range, indicating the shape was encouraging the back plate to behave as a series of different sized discs joined together.

This section will consider a back plate with concentric circular grooves, also with the aim of causing the disc to act as if it consisted of different geometry components added together. Stepped plates are combined with horns in some high power designs (fig. 1.6), usually when generating ultrasound into air, in order to produce a uniform pressure wave at a distance from the transducer. Considering the case of the transducer in the receiving mode of operation, perhaps the stepped plate could offer further performance improvements in terms of resonance broadening or sensitivity by adjusting back plate flexural rigidity.

An axisymmetric model was used. Grooves were cut into the top of the original brass back plate (fig. 3.23), with the 1 mm thick, 38 mm diameter piezoelectric disc, laid over the grooves.

Of course the grooves could be put on the underside of the back plate, but it was felt that having the gaps under the piezoelectric disc might increase the stress transferred to the disc by providing non-uniform loading from point-to-point on the disc surface.

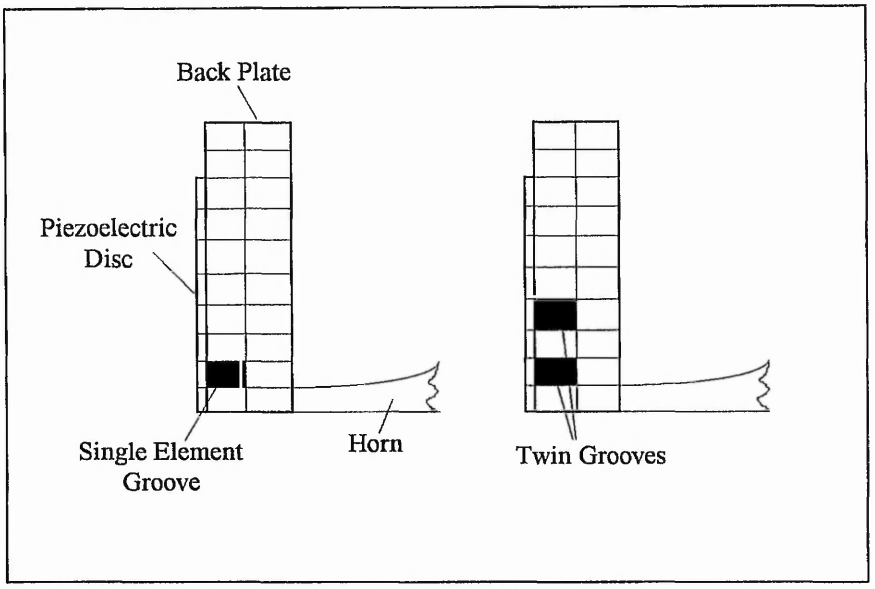

Fig. 3.23 Example of the grooved back plate designs with one and two elements removed. The models are axisymmetric about the baseline and therefore, one removed element represents a concentric hollow.

By removing material from the back plate, the disc modes will be affected and may show increased amplitudes because of the reduction to the back plate's flexural rigidity.

Models were run with a groove at increasing distances from the back plate centre. The first model had a hole in the centre rather than a groove. The grooves were one finite element in width and depth so that on the FE model this simply involved removing an element. The depth of the cuts was half of the back plate thickness (2.45 mm), and the width was 2.5 mm.

Transducer response spectra are plotted for each groove distance (fig. 3.24-3.31) and the data compared in table 3.8 with that of the original axisymmetric model (fig. 3.5). With the hole in the centre (fig. 3.24), the output voltage amplitude for the first mode has dropped to less than twenty percent of the original value, while the second mode is the same. Other peaks in the 1-100 kHz range are very small in comparison to the original output. Circular plate theory (fig. 3.9) for a plate with a fixed centre showed closest agreement with the first back plate mode, at 5.5 kHz, using an α value of 3.75. The large amplitude decrease for this mode indicates that the hole has greatly affected this first mode of excitation, by interfering with the back plate vibration. The longitudinal

vibration in the horn section appears to move in and out of the hole, thus lowering the energy transferred directly into the back plate and piezoelectric.

As the first groove is modelled (fig. 3.25), the output voltages of the first two peaks are of equal amplitude, this amplitude being greater than when the groove (hole) was central. Again, between 20 and 100 kHz there are no large resonances, but there are two small peaks around 50 kHz.

As the groove is moved further away to 5 mm from the centre, the output voltage amplitude of the second mode decreases (table. 3.8) to less than the original value. This time, the mode at 41 kHz is producing a larger peak than the previous designs, but it is still not as large as the original design (table 3.8). There are several smaller peaks forming up to 65 kHz.

The next groove location (at 7.5 mm) gives a significant increase to the 41 kHz output voltage amplitude, but it is still less than with the original back plate (table 3.8). Output voltage amplitudes for the first two resonant frequencies are slightly lower than those for the previous groove location. Above 45 kHz, the resonant peaks are very small.

With the groove at 10 mm from the back plate centre, the output voltage from the 41 kHz mode becomes the largest amplitude (fig. 3.26) in the 1-100 kHz range. It is greater than in the original model (fig. 3.5). The second resonance is almost the same size in amplitude, while the first mode has decreased. Referring back to fig. 3.8, the groove at 10 mm to 12.5 mm is in a position where maximum plate bending and compression occurs (the fifth element from the r.h.s. in the fig.). The removal of this element allows increased bending of the back plate and piezoelectric, which results in the higher output voltage.

The next groove location has a similar amplitude output voltage peak for the 41 kHz mode (table 3.8), again due to the fact that the groove is at the point of maximum bending. The second resonance is much larger than before and is now the dominant mode.

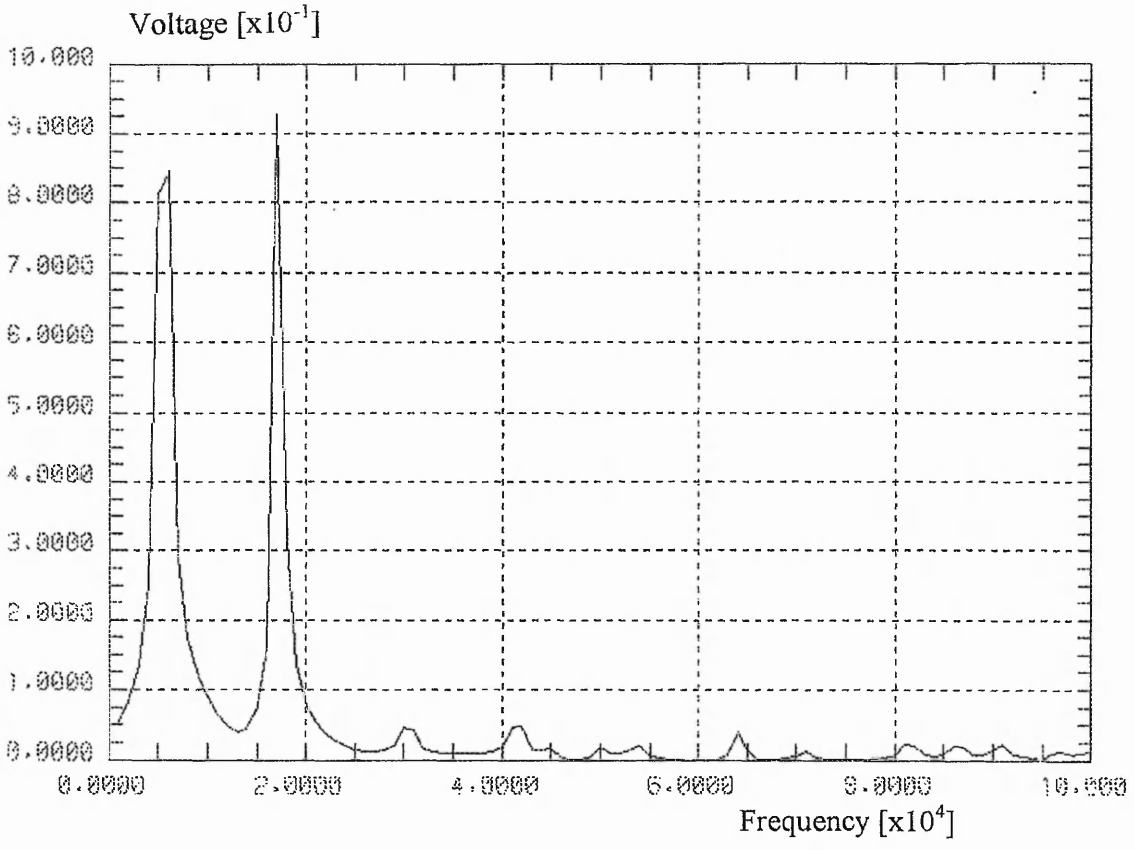

Fig. 3.24 Output voltage against frequency for the exponential horn design, with a hole in the centre of the back plate.

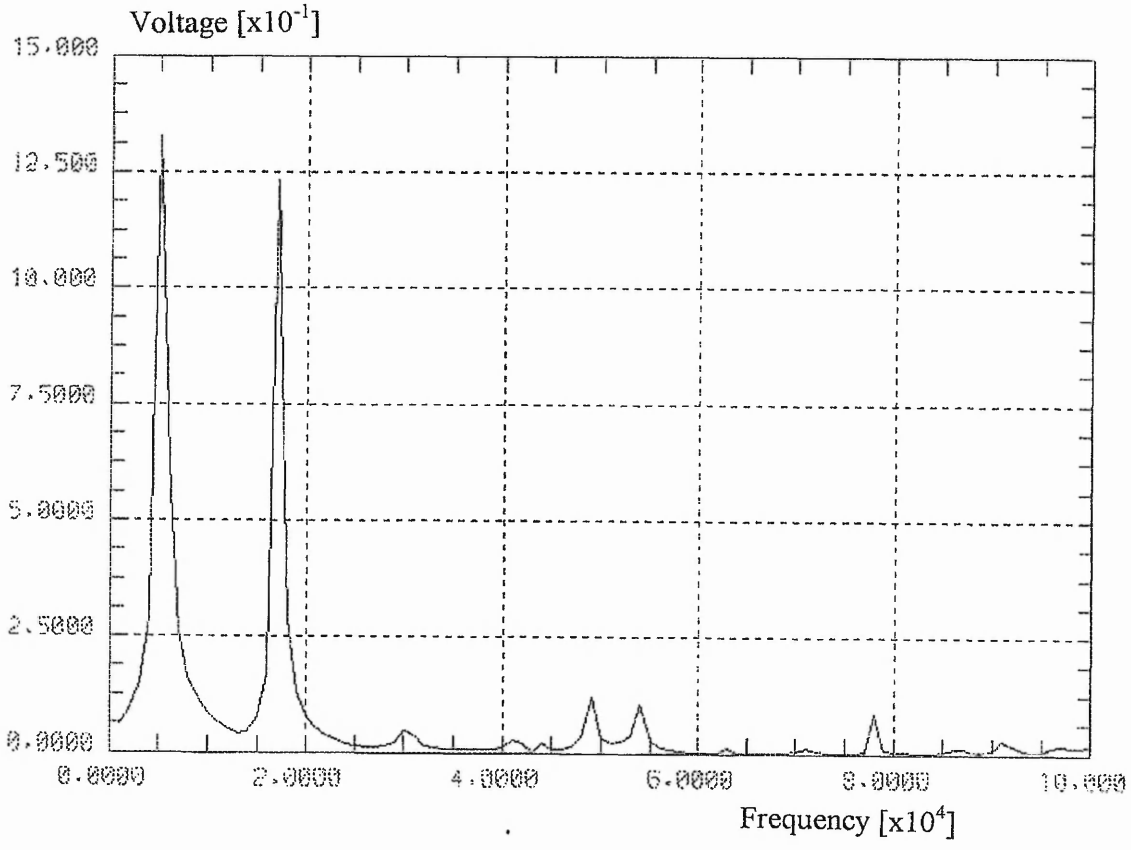

Fig. 3.25 Output voltage against frequency for a grooved back plate, exponential horn design. The groove starts 2.5 mm from the centre of the back plate.

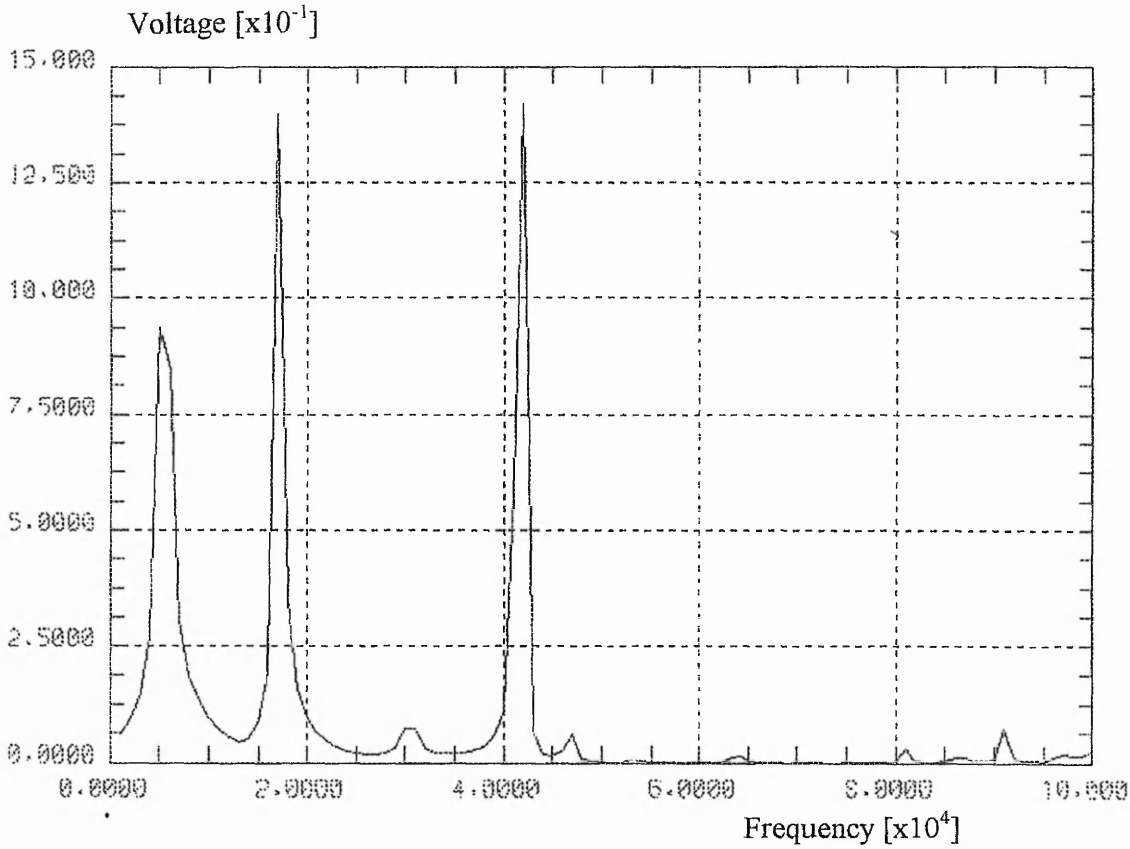

Fig. 3.26 Output voltage against frequency for a grooved back plate, exponential horn design. The groove starts 10 mm from the centre of the back plate.

Above 50 kHz there is little sign of structural resonance. The reason for the second mode amplitude increase is because the groove occurs at a point of maximum flexure for this mode (fig. 3.7).

At the final groove position modelled using FE, the amplitude of all the resonant frequency peaks drops again (table 3.8). This time a multiple resonance effect is seen in fig. 3.27 from 1-55 kHz, with the transducer producing a continuous output voltage.

Having considered the effect of a single element groove, a wider groove was modelled. A groove of double width was modelled by removing two elements from the back plate, starting at a distance of 2.5 mm. The output voltage amplitude of the 5 kHz mode, in table 3.8, has returned to above its original value. The 17 kHz mode amplitude has also increased, while higher frequency mode output voltages are small.

Due to the larger groove at the point of maximum compression (fig. 3.6), the back plate can bend easily, which is why the first two audio frequency modes give a high output voltage. Back plate modes above 20 kHz are excited by a combination of bending in the thickness direction and radial deformation, but do not appear to be excited as effectively as the 5 and 17 kHz modes, with this design.

A three element wide groove (7.5 mm), starting in the same position as the two element groove, does not produce a further increase to the first mode amplitudes (table 3.8). Instead, the output voltage from the audio frequency modes has dropped from the double width groove design and from the original design. As a result of the different output voltage scale, a collection of peaks in the 30-70 kHz frequency range can be seen in fig. 3.28, which, although small in amplitude when compared to the original design (table 3.8), provide a continuous region of output voltage. Larger peaks are seen in fig. 3.28 at 37 and 64 kHz.

This collection of peaks indicates the generation of multimode output that was aimed for. Combining this idea with other optimisation methods would hopefully lead to greater amplitude in this signal.

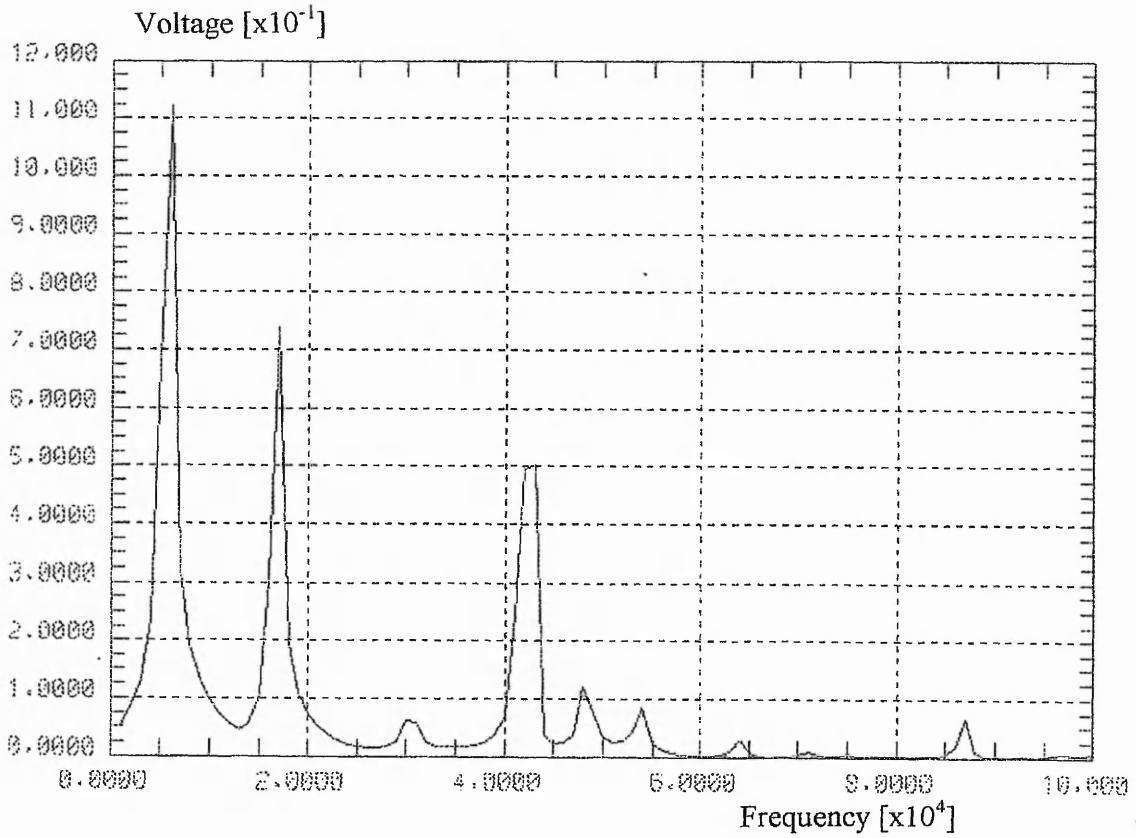

Fig. 3.27 Output voltage against frequency for a grooved back plate, exponential horn design. The groove starts 15 mm from the centre of the back plate.

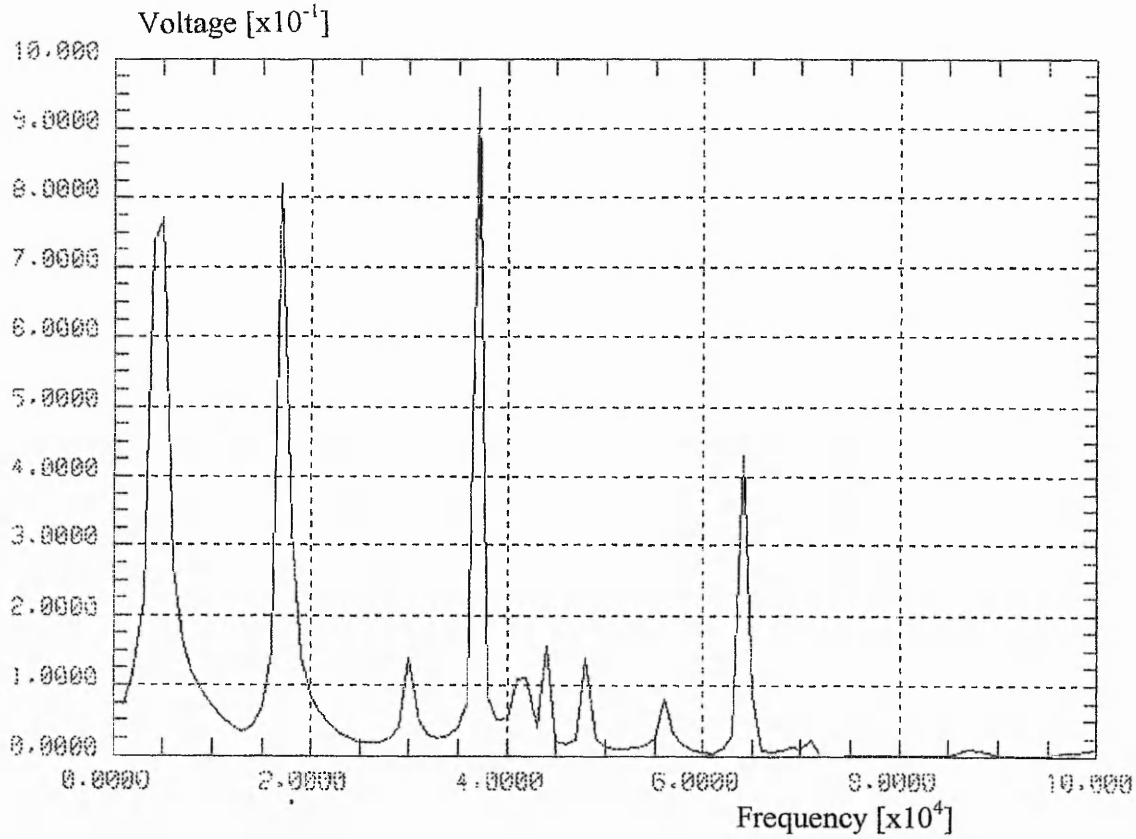

Fig. 3.28 Output voltage against frequency for a grooved back plate, exponential horn design. The groove starts 2.5 mm from the centre of the back plate and is 7.5 mm wide (3 elements).

Further increases to the groove width to four elements (10 mm), show a return to the high amplitude peak in the first mode (fig. 3.29), and very small peaks elsewhere. The slight decrease in the frequency of the 5.5 kHz mode to 4 kHz would suggest that the back plate in behaving as if it were thinner than in the original design. If the circular plate frequency is calculated for a 2.45 mm thick disc (half original thickness, 25 mm radius), using equation 3 in section 3.3.4, the 5.5 kHz mode drops to 2.5 kHz. The fact that the frequency has only dropped by 1.5 kHz in the FE model, indicates the back plate is behaving as a thinner disc than the original back plate dimension, but this effective thickness cannot be predicted by traditional applied mathematics.

Moving the start of the groove further from the centre to 7.5 mm, and using a width of three elements, produces a different effect. In table 3.8, the output voltage at the first resonant frequency is smaller than in the original model and the largest output voltage amplitude occurs at 33 kHz.

These wider groove models have again highlighted the usefulness of FEM for design purposes. Although the designs are very similar, they produce some very different responses from the transducer.

The last combination of grooves modelled had multiple, single width grooves. Each groove was one element wide (2.5 mm) and there was a single groove width between them. The first combination had two grooves, as shown in the example in fig. 3.23. As with the single groove in either of these two positions, the output voltage was only large at the 5 and 17 kHz resonances (fig. 3.30), and there was little output above these frequencies. However, with the two grooves, the 5 kHz mode amplitude was more than double that of the single grooves at 2.5 or 7.5 mm. The amplitude was still less than with the original back plate (table 3.8).

Adding a third groove to the back plate gave an increase to the amplitude of the 5 kHz mode, so that it became 50% larger than the original design (table 3.8). The 17 and 41 kHz modes also showed slight increases in amplitude over their respective amplitudes with the original back plate (table 3.8).

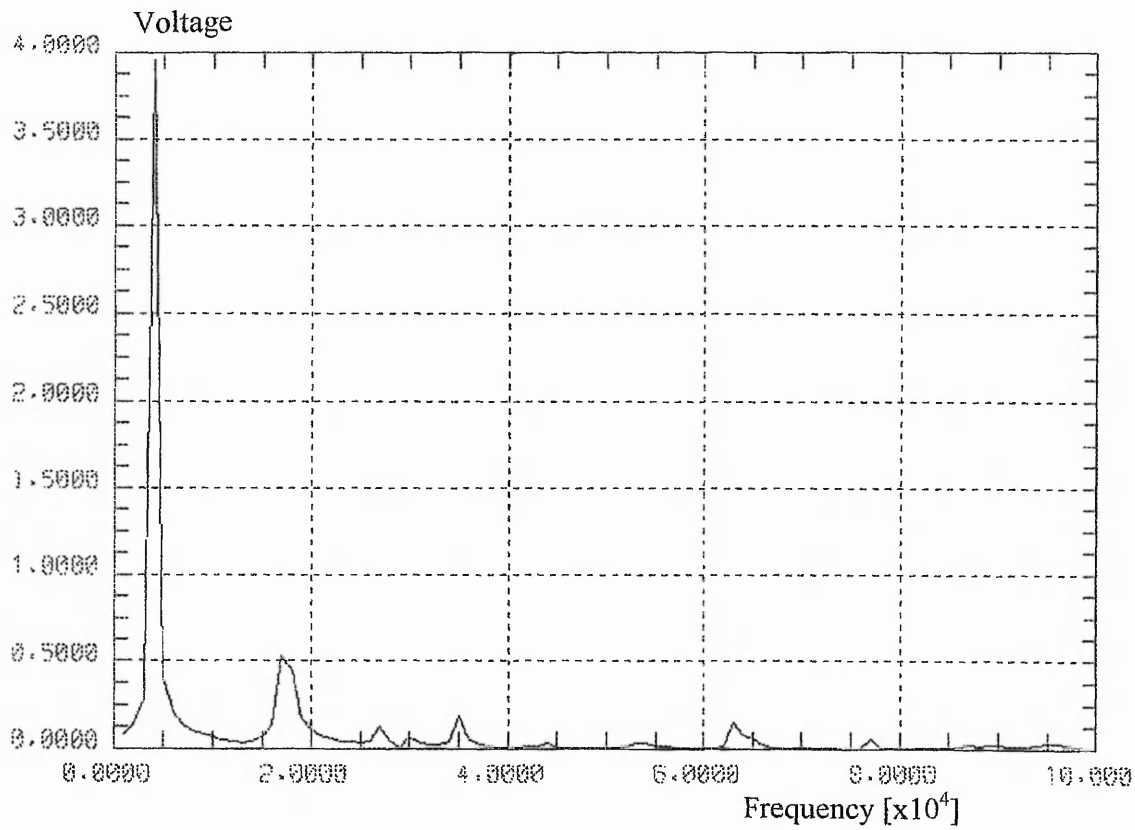

Fig. 3.29 Output voltage against frequency for a grooved back plate, exponential horn design. The groove starts 2.5 mm from the centre of the back plate and is 10 mm wide (4 elements).

Design [distances are centre to start of groove]										
Original	f_r	5.5	17	41	64	86				
	volts	5	1	0.9	<0.1	0.9				
Hole in centre of BP	f_r	6	17	41	64	86				
	volts	0.9	0.9	<0.1	<0.1	<0.1				
Groove at 2.5 mm	f_r	5	17	41	49	55				
	volts	1.3	1.2	<0.1	0.1	0.1				
Groove at 5 mm	f_r	5	17	41	64					
	volts	1.4	0.7	0.2	0.1					
Groove at 7.5 mm	f_r	5	17	41	64	88				
	volts	1.1	0.7	0.6	<0.1	<0.1				
Groove at 10 mm	f_r	5	17	41.5						
	volts	0.9	1.4	1.4						
Groove at 12.5 mm	f_r	5	17	43						
	volts	1.0	2.7	1.2						
Groove at 15 mm	f_r	6	17	41	48	54				
	volts	1.1	0.7	0.5	0.1	0.1				
2xWidth Groove at 2.5 mm	f_r	5	17	41	86					
	volts	6.3	1.5	0.2	0.2					
3xWidth Groove at 2.5 mm	f_r	5	17	30	37	41.5	44	48	56	64
	volts	0.8	0.8	0.1	1.0	0.1	0.2	0.1	0.1	0.4
4xWidth Groove at 2.5 mm	f_r	4	17	35	64					
	volts	3.9	0.5	0.2	1.7					
3xWidth Groove at 7.5 mm	f_r	5	18	33	41.5	64				
	volts	2.9	0.8	11.4	0.2	<0.1				
2 Grooves at 2.5 mm separated by a 2.5 mm gap	f_r	5	17	41	46					
	volts	3.9	0.8	0.3	0.3					
3 Grooves at 2.5 mm separated by a 2.5 mm gap	f_r	5	17	41						
	volts	7.5	1.6	1.2						
2 Grooves at 7.5 mm separated by a 2.5 mm gap	f_r	5	17	40	64					
	volts	1.5	1.4	3.8	<0.1					

Table 3.8 Comparison of transducer resonant frequencies (in kHz) and their respective output voltage amplitudes for the tapered and original transducer designs.

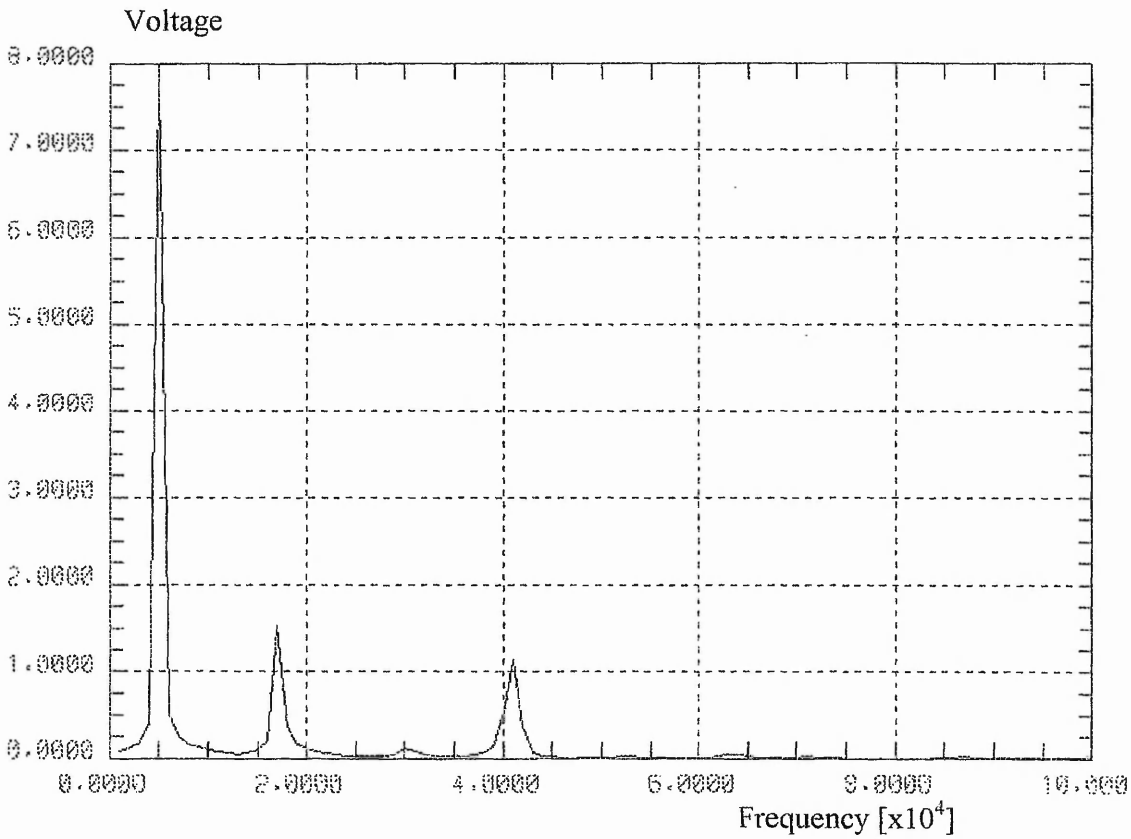

Fig. 3.30 Output voltage against frequency for a grooved back plate, exponential horn design. There are two grooves starting at 2.5 mm from the centre of the back plate, separated by a gap of 2.5 mm (1 element).

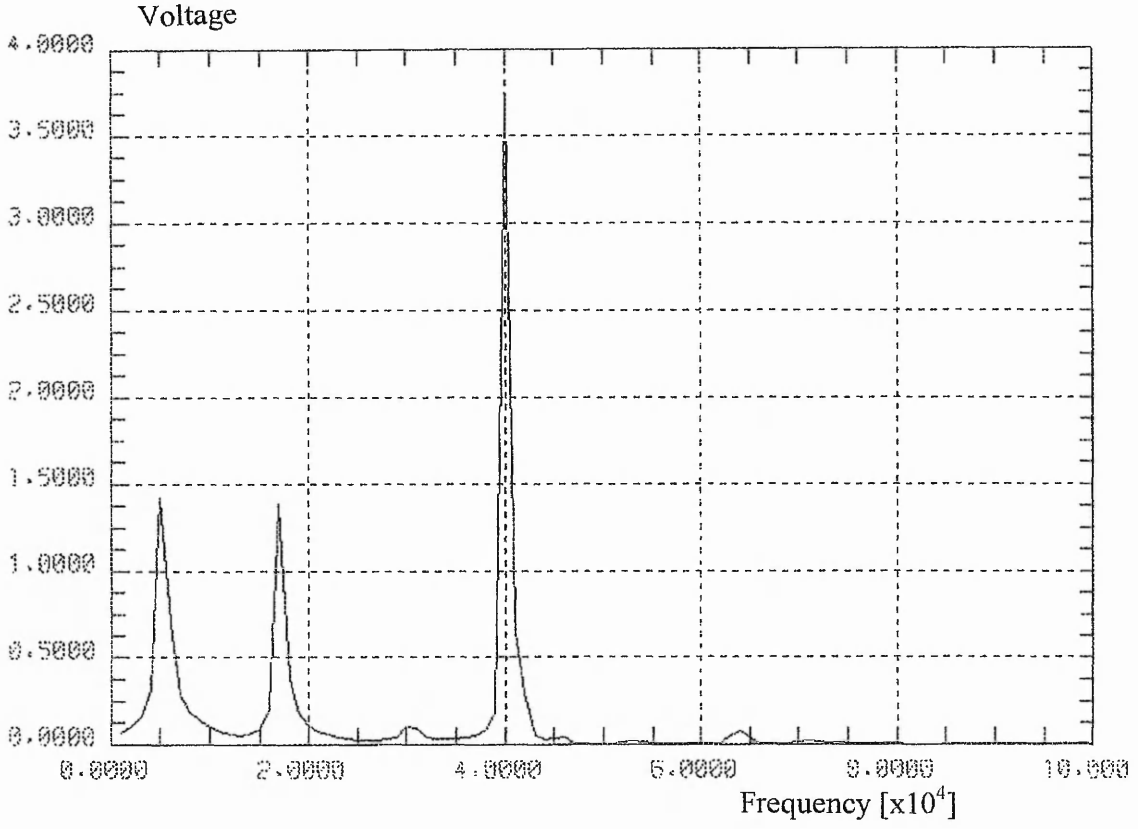

Fig. 3.31 Output voltage against frequency for a grooved back plate, exponential horn design. There are two grooves starting at 7.5 mm from the centre of the back plate, separated by a gap of 2.5 mm (1 element).

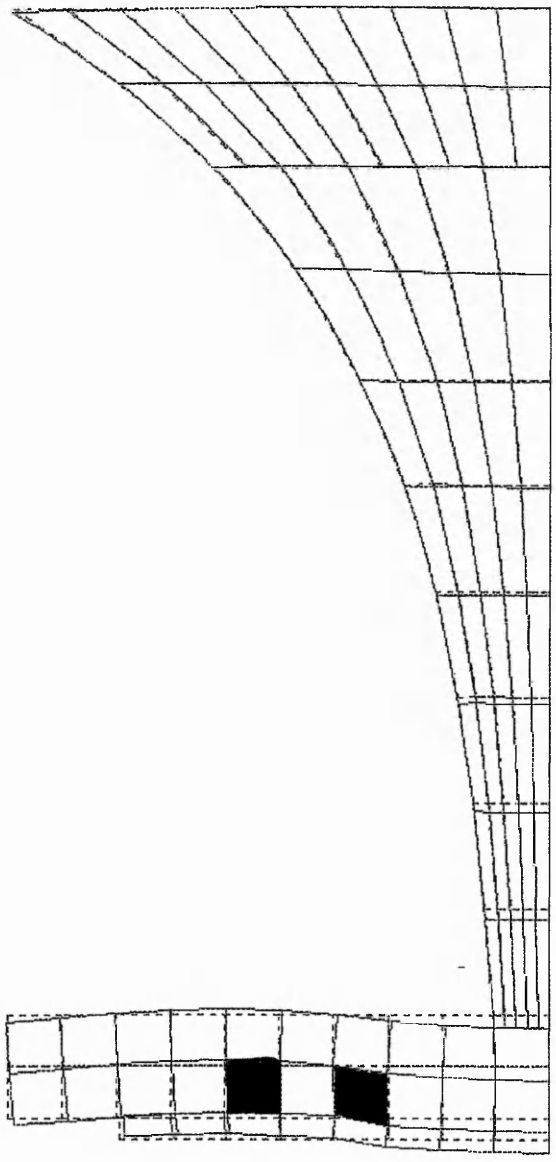

Fig. 3.32 Mode at 40 kHz for a grooved back plate, exponential horn design. There are two grooves starting at 7.5 mm from the centre of the back plate, separated by a gap of 2.5 mm (1 element).

Finally, the outer two of the three grooves were modelled, so that the first of the two grooves started at 7.5 mm from the back plate centre. As with the single groove at a 10 mm distance from the transducer centre, the output voltage at the 40 kHz mode is greatly improved (fig. 3.31). This time the 40 kHz mode is more than 4 times the original amplitude. The first two resonances have equal amplitudes, the second mode also being larger than in the original model. Higher frequency modes have been reduced in amplitude to the extent that they are not identifiable on this scale (fig. 3.31).

3.7.2.1 Effect of using a Grooved Back Plate on the Original Back Plate Vibration Modes

It appears that, even with a single groove, higher order modes can be significantly reduced in amplitude. Using the grooved back plate, no resonances above the 40 kHz mode showed significant amplitudes of output voltage. This means that the groove significantly reduces the radial excitation, thus limiting the number of complex flexural modes that develop as the frequency of excitation increases.

The first two modes involve simple bending of the back plate about the horn throat. These modes are easily excited and therefore, dominate the transducer frequency response, in the 1-100 kHz frequency range investigated. The 41 kHz mode in the original model is still quite simple, and involves the back plate reaching a maximum deformation at a distance of half the back plate radius (fig. 3.8). This is why a transducer with a groove at this distance (12.5 mm from the back plate centre) shows an increase in the amplitude of this mode. Two grooves around this radius give further freedom to this mode, giving the largest amplitude with this design (fig. 3.31).

Compared with the 41 kHz mode of the original axisymmetric model (fig. 3.8), the 40 kHz mode with two grooves (fig. 3.32) shows less deformation at the horn mouth, giving a purely longitudinal displacement at the horn throat. This produces minimum radial deformation in the back plate and, as a result, the piezoelectric disc undergoes thickness displacement.

At the point of the first groove, there is a transition from displacement away from the transducer face to displacement towards the transducer face (fig. 3.32), causing a thickness shearing action. It is probably this movement that causes the greater amplitude output voltage, at this frequency, than in the original design. It is not as significant an increase as in the optimised designs, but the use of a thicker piezoelectric disc is likely to increase the output voltage amplitude.

Only with a three element (7.5 mm) wide groove did the close multimode resonance occur (fig. 3.28). This demonstrates that complicating the shape of the back plate can be used to broaden resonant peaks, which was also confirmed using a tapered back plate in section 3.7.1. However, it is clear that FEM is the best tool to predict the behaviour of such designs as slight variations can produce different, and possibly undesirable, effects on the performance.

As with the process of optimising the back plate and piezoelectric dimensions, discussed in section 3.5, a combination of changes can provide the best performance. Therefore, a combination of tapering and grooves may provide further improvements in performance and a topic for further study.

Full three dimensional modelling would allow asymmetric designs to be investigated that are likely to increase the complexity of vibration and, therefore, provide more mode shapes and potential increase to transducer bandwidth. It is clear that FEM is the fastest way to predict and choose the most appropriate designs.

3.8 PERFORMANCE ADVANTAGES OF USING THE HORN DESIGN OVER A SIMPLE DISC

So far, Chapter Three has considered a transducer design for geotechnical work in the 40 kHz region. Chapter Two considered a higher frequency transducer consisting of a piezoelectric disc mounted onto a thinner, larger diameter plastic disc. That simple design had its main resonant frequency at 176.5 kHz. Although the resonance was governed by the piezoelectric disc, the plastic was shown to affect the performance.

Now, the same piezoelectric disc will be considered mounted to the brass horn and back plate, without the thin plastic disc. In the 1-100 kHz range, the geotechnical transducer resonances were seen to be controlled by the back plate and horn components rather than the piezoelectric itself. When these two components were combined with a suitable geometry piezoelectric element, the transducer gave its optimum performance (section 3.5).

Whilst using acoustic FEM to investigate the variation of piezoelectric to back plate diameter ratio in section 3.4.1, a piezoelectric disc with the same dimensions as the one used for the bi-laminar disc transducer, in Chapter Two, had been modelled. The piezoelectric disc was 5 mm thick and 10 mm in diameter. This could be used to compare the merits of the horn and back plate design against a typical resonant device, like the bi-laminar disc design.

From the FE model of the horn, with a 10 mm diameter and 5 mm thick piezoelectric disc, the output voltage at 5 kHz (fig. 3.33) is low compared to the 41.5 and 86 kHz modes. Although these two higher modes produce a larger output voltage than with the original size piezoelectric (1 mm thick, 38 mm diameter), in section 3.3.2, they are not as high as in the optimised design, in section 3.5. The reason for the high amplitude at 86 kHz is likely to be caused by a piezoelectric disc mode, coupling to a horn section mode. The disc was shown to have a resonance frequency of 94.5 kHz in section 2.2.1, when constrained by a plastic disc. The greater constraining effect of the back plate may lower the frequency of this mode further.

In order to compare the effect of introducing the horn in place of the plastic disc wear plate, the horn model was run in the 50 to 250 kHz frequency range. Because the piezoelectric disc of dimensions 10 mm diameter by 5 mm thick has resonances in this range, it was hoped that the horn would help to amplify these responses.

For this horn transducer a resonant peak is seen in fig. 3.34 at 237 kHz, with an amplitude of 17.5×10^4 volts compared to 1.4 volts for the bi-laminar disc transducer in Chapter Two (fig. 2.24).

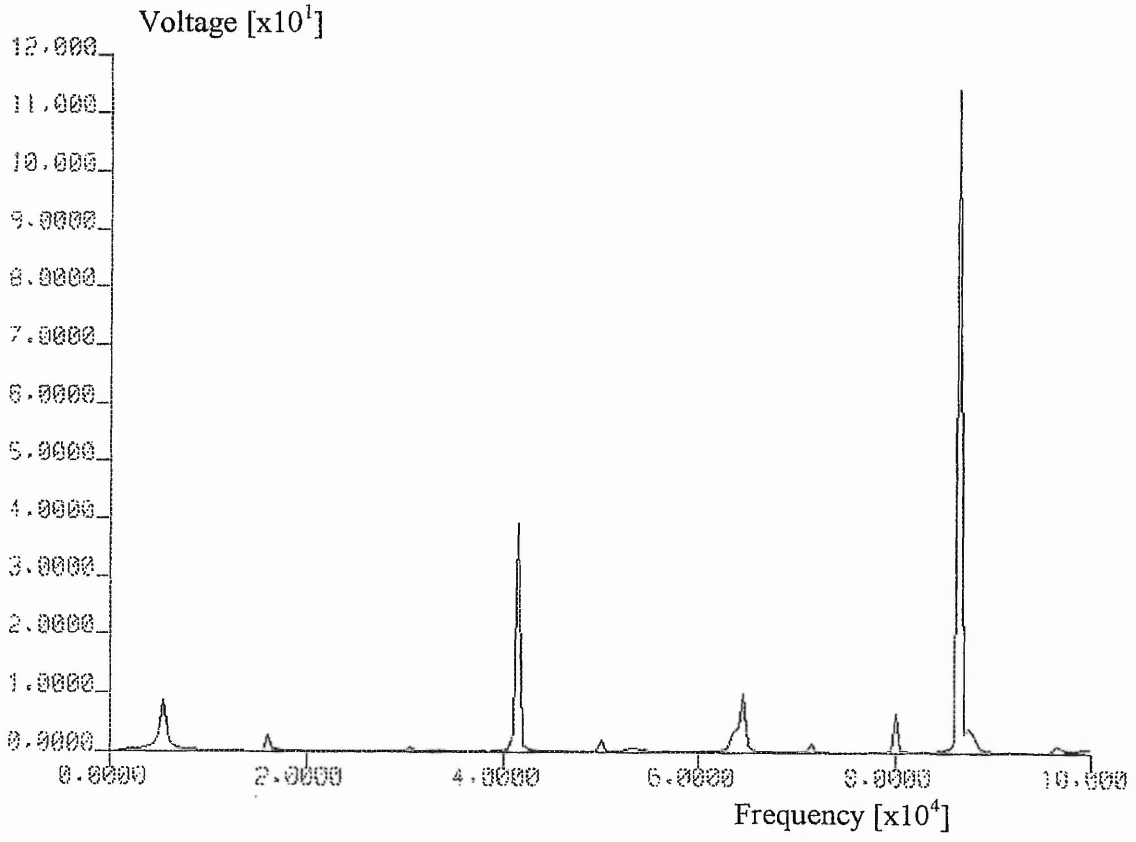

Fig. 3.33 Output voltage against frequency for the original exponential horn design with a 10 mm diameter, 5 mm thick piezoelectric disc. The frequency range is 1-100 kHz.

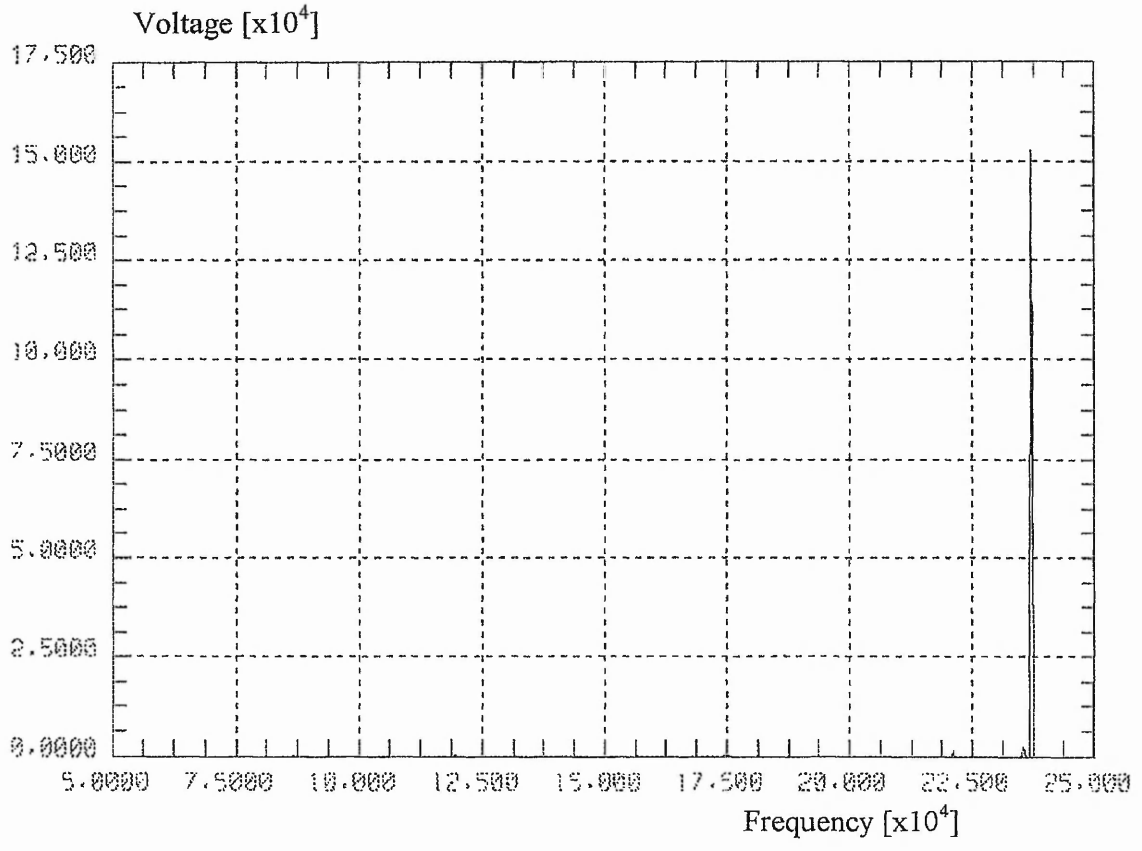

Fig. 3.34 Output voltage against frequency for the original exponential horn design with a 10 mm diameter, 5 mm thick piezoelectric disc. The frequency range is 50-250 kHz.

This is also far higher than at the lower frequency horn resonances. A different voltage scale has been used in fig. 3.35 to study other resonant frequencies.

There is a large resonance at 175 kHz, producing an output voltage of 240 volts, over one hundred times greater than the 1.4 volts of the bi-laminar disc transducer. Other large frequency resonances are 86 kHz, 220 kHz and 250 kHz. The horn and back plate appear to increase the Q value of the peak, which for 175 kHz is 230 compared to 17 in the bi-laminar disc design. The Q value is given by the frequency of the resonance divided by the difference between the frequencies that produce half of the resonance output amplitude. A high Q value thus indicates a large amplitude narrow peak.

The 175 kHz mode shape, seen in fig. 3.36, shows large displacement in the piezoelectric, compared to the horn and back plate. Displacements occur at the disc centre in the thickness direction, causing the top edge to bend towards the centre.

The large displacement at the centre (fig. 3.36) was observed by Ono (fig. 2.3), in larger D/t ratios of piezoelectric discs, as a convex-compression mode. This suggests the back plate increases the effective diameter of the piezoelectric, an effect also caused by the plastic in Chapter Two.

If the piezoelectric disc is seen individually, the deformation resembles the M_{01} mode in fig. 2.5, but the constraining effect of the back plate causes extra deformation at the piezoelectric disc edge leading to a possible M_{21} mode. The piezoelectric disc of the bi-laminar transducer also vibrated in an M_{21} mode at 176.5 kHz, but in a different phase and with more obvious shape to the vibration.

The back plate's influence has increased the effective D/t ratio and is the reason for the resonant frequency being at 175 kHz and not 176.5 kHz, as in the bi-laminar disc transducer.

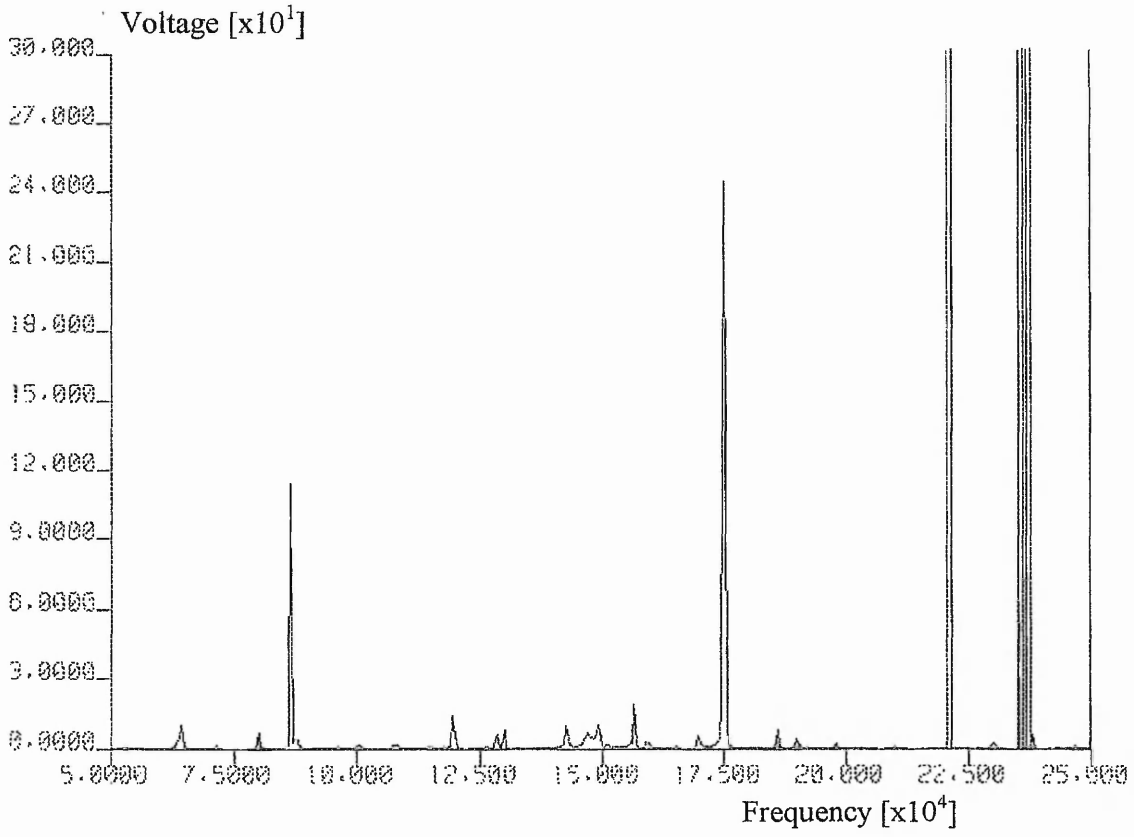

Fig. 3.35 Enlarged scale of output voltage against frequency for the original exponential horn design with a 10 mm diameter, 5 mm thick piezoelectric disc. The frequency range is 50-250 kHz.

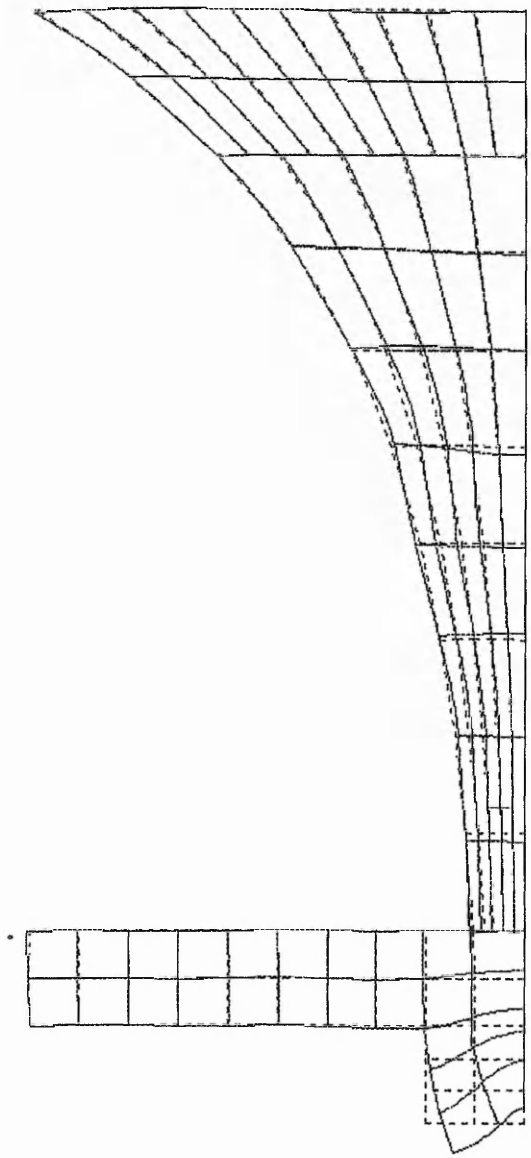

Fig. 3.36 Mode shape at 175 kHz for the original exponential horn and back plate with a 10 mm diameter, 5 mm thick piezoelectric disc. Model is axisymmetric about the right hand vertical axis.

At 237 kHz the back plate is relatively undeformed, compared with the horn mouth (fig. 3.37). This deformation of the transducer face is likely to be damped when mounted to a test specimen. However, when the bi-laminar disc transducer was mounted in section 2.4.2, the transducer face appeared to maintain its freedom to some extent, suggesting that this mode would remain a high output one. At this frequency, the piezoelectric disc is less deformed relative to the horn and back plate.

When the piezoelectric disc was seen in more detail, the disc was displaced in a shearing action in both the thickness and radial directions, giving a possible M_{33} mode notation. It is this shearing action that causes high material stresses that induce the high output voltages, due to the piezoelectric effect. This deformation is seen in fig. 2.30, except in the opposite phase, and also in fig. 2.21. Again, the constraining effect of the back plate has caused the frequency of this mode to drop from 249 kHz, in the acoustic FE model of the bi-laminar disc transducer, to 237 kHz in the horn device.

The exponential horn and back plate give the transducer sharp resonant output voltages with a large amplitude, compared with those observed when the piezoelectric disc is mounted on the thin plastic facing disc. This gives the 175 kHz mode a Q value of approximately 230 compared with 17 in the bi-laminar disc transducer. Although these Q values may change if a higher frequency resolution is used in the FE models, their relative differences will still be apparent.

Even though the plastic disc had a low mass and stiffness it still had an effect on the piezoelectric disc performance, seen in Chapter Two, but this effect was small compared to the heavier and stiffer brass.

With the piezoelectric attached to the brass back plate, the effect was to excite the disc more uniformly, suggested by similarities of the piezoelectric modes with those seen in section 2.2.2, in which a forced sinusoidal analysis was used. This leads to higher Q values in the resonant modes because there is less potential for multiple modes being excited, leading to modal coupling.

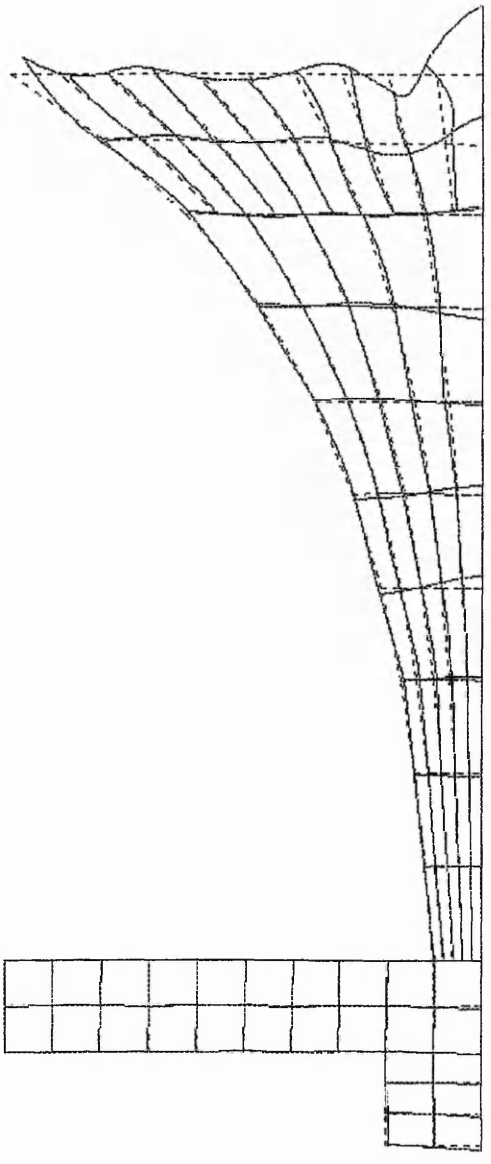

Fig. 3.37 Mode shape at 237 kHz for the original exponential horn and back plate with a 10 mm diameter, 5 mm thick piezoelectric disc. Model is axisymmetric about the right hand vertical axis.

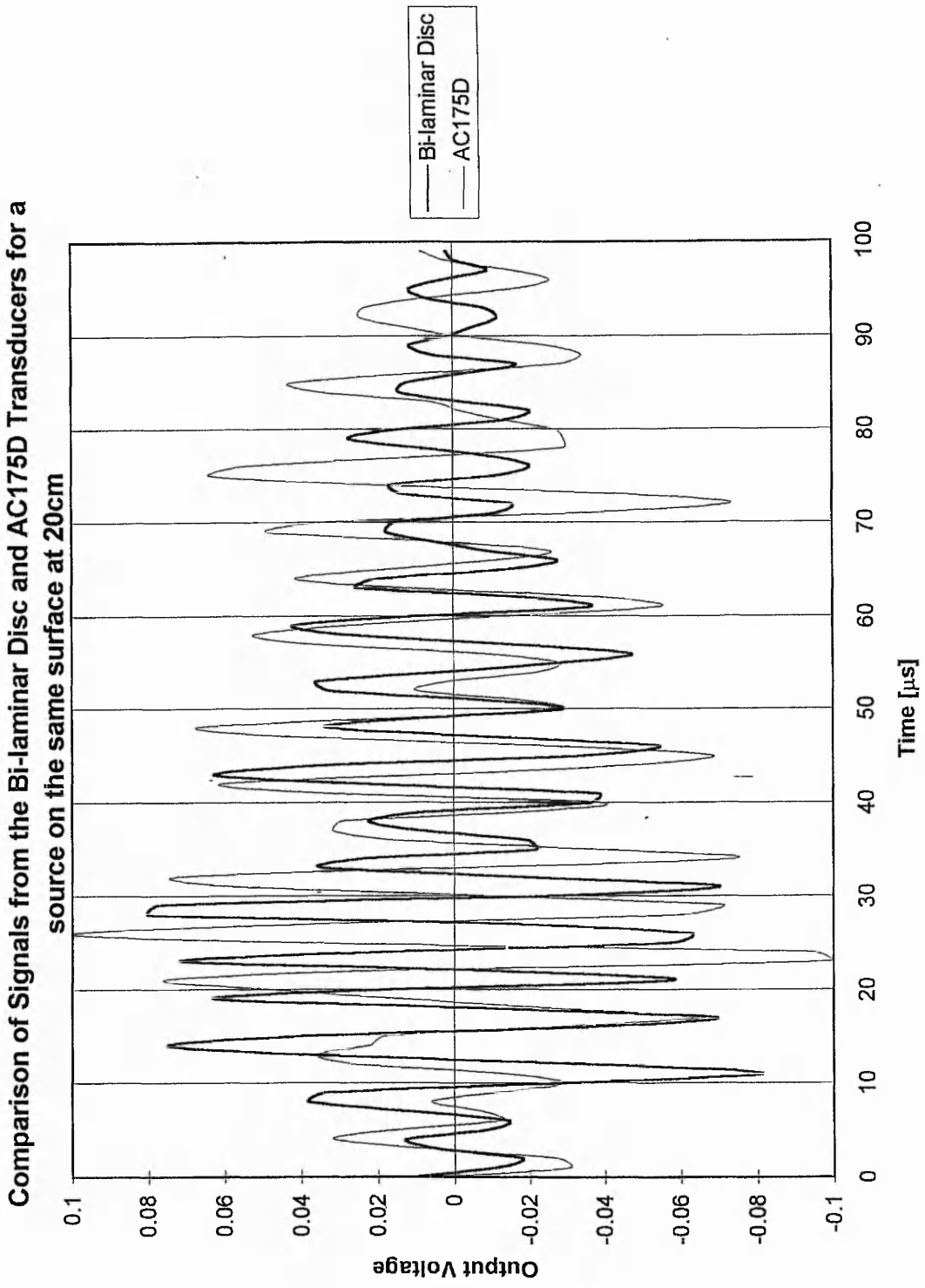

Fig. 3.38 Output voltage against frequency for the bi-laminar disc transducer and a commercial AE175D transducer. The transducers are responding to a simulated AE event on the surface of a 25 mm thick steel plate, at a source-transducer distance of 20 cm. Experimental details are given in section 4.4.1.

The exponential horn appears, therefore, to improve the transducer resonant output, which should improve sensitivity in practical situations. The fact that the transducer is made from brass and a common size piezoelectric disc mean that it is very cheap to build, compared with the complicated 1-3 type composite designs, for example. Given the fact that the bi-laminar disc transducer (Chapter Two) has been tested in practice, and is known to be as sensitive as other, typical, commercial resonant transducers (fig. 3.38), it is fair to predict that the exponential horn and back plate will provide a noticeable improvement to the piezoelectric disc performance. A disadvantage would be the size and mass of such a transducer.

3.9 COMPLETE DESIGN OF A 175 KHZ TRANSDUCER USING MODE COUPLING

In section 3.8, the effect of mounting a piezoelectric disc on an exponential horn and back plate was compared to mounting the same disc on to a plastic disc. FE modelling has suggested that the horn and back plate should give improved sensitivity over the bi-laminar disc transducer, which was discussed in Chapter Two.

This section will now consider the use of mode coupling to design a 175 kHz transducer, for comparison with both the horn design, in section 3.8, and the bi-laminar disc transducer, considered in Chapter Two. The aim would be to couple the longitudinal mode of the brass exponential horn section with the radial mode of the piezoelectric disc. This time, no back plate will be used. If successful, then this design method will be equally applicable at other frequencies.

The equations in section 3.1.1, describing the horn dimensions, were used to design a horn with the first longitudinal mode at 175 kHz. The flare constant β has the same value as the original horn at 47.5 m^{-1}. A 2 mm throat radius was chosen and a set of co-ordinates were produced to describe the shape of the horn. The co-ordinates, produced using a spreadsheet, were used to create nodes in a PAFEC data file. Elements were then constructed and a forced sinusoidal analysis was carried out. The nodes on the

mouth face of the horn were assigned repeated freedoms. These nodes were forced sinusoidally.

This analysis confirmed that a primary mode existed at 175 kHz. Looking at the displaced shape of the mesh in PIGS and viewing an oscillating mesh, confirmed a longitudinal mode was being excited. Comparing the input and output displacements in the PAFEC results file confirmed that the horn was amplifying the input displacement.

Now, a suitable piezoelectric disc could be chosen with a 175 kHz resonance, and be modelled attached to the horn throat. A 1 mm thick piezoelectric disc was chosen to give the same ratio of disc thickness to horn length that the brass back plate used on the original horn. Using a diameter of 14 mm, the resonant frequency of the disc alone was 157 kHz. The first disc resonance was at 100 kHz, but this was a relatively low output, piston-like mode. At 157 kHz the disc vibrates in a radial mode, which results in high transducer sensitivity.

When this disc was modelled on the brass horn, the resonant frequency was 162 kHz. To increase the frequency to nearer 175 kHz, the piezoelectric disc was reduced in diameter to 13.33 mm, thus reducing the D/t ratio. A forced sinusoidal FE analysis predicted the new radial resonance at 188 kHz for the disc alone.

This disc was attached to the horn and again modelled. The predicted resonances were at 114, 171 and 185 kHz (fig. 3.39). The most sensitive was at 171 kHz, because the disc was vibrating in a radial mode while the horn was vibrating in a longitudinal mode (fig. 3.40).

Finally, an acoustic analysis was performed, as this is known to provide an accurate resonant frequency prediction. Unlike in Chapter Two, in which the frequency difference between the forced sinusoidal and acoustic analyses was not greater than 5 kHz (173 and 176.5 kHz), the resonant frequency for the horn and disc was at 158 kHz. This compares to 171 kHz in the forced sinusoidal analysis. Also, the piezoelectric disc at 158 kHz was no longer in a radial mode, but more of a flexural mode.

When the piezoelectric disc was mounted to a thin plastic disc in the bi-laminar design, or to the back plate and horn, the piezoelectric disc was excited uniformly. By mounting the piezoelectric disc directly on to the throat of the horn section, the disc is then excited at a few centre nodes only. The large difference between the acoustic FE and the forced sinusoidal FE resonant frequency predictions must be due to the loading at the transducer face, as this is the only difference between the two methods.

A uniform excitation condition at the transducer face (using repeated freedoms) provides an FE simulation of a theoretical situation, such as that used to calculate the frequency of the longitudinal mode in section 3.1.1. The acoustic FE model provides non-uniform loading across the transducer face and some radiation damping. This appears to affect the excitation of the longitudinal mode in the horn and, hence, the excitation of the piezoelectric disc is altered. As a result, the resonant frequency is affected.

In practical work, in which the horn is mounted to a metal test object, the resonant frequency may increase from 158 kHz to nearer the 171 kHz predicted by the forced sinusoidal analysis. This was shown to be the case for the bi-laminar disc transducer mounted to a steel plate in section 2.3.4, Chapter Two. Therefore, this design may prove to be suitable in practice.

Sections 3.8 and 3.9 and, section 2.2.3 have shown that the same resonant frequency can be achieved by various transducer designs. Ultimately, the excitation of the transducer face is seen to be the crucial factor in the transducer performance.

In simple designs, such as the bi-laminar disc transducer, different boundary conditions on the transducer face do not have as much of an effect on the resonant frequency as in more complex designs, like the coupled horn and piezoelectric design in section 3.9. The horn and back plate design, considered in section 3.8, was able to produce almost the same resonant frequency as the bi-laminar disc design (175 and 176.5 kHz respectively), because it provided the same constraining effect on the piezoelectric disc.

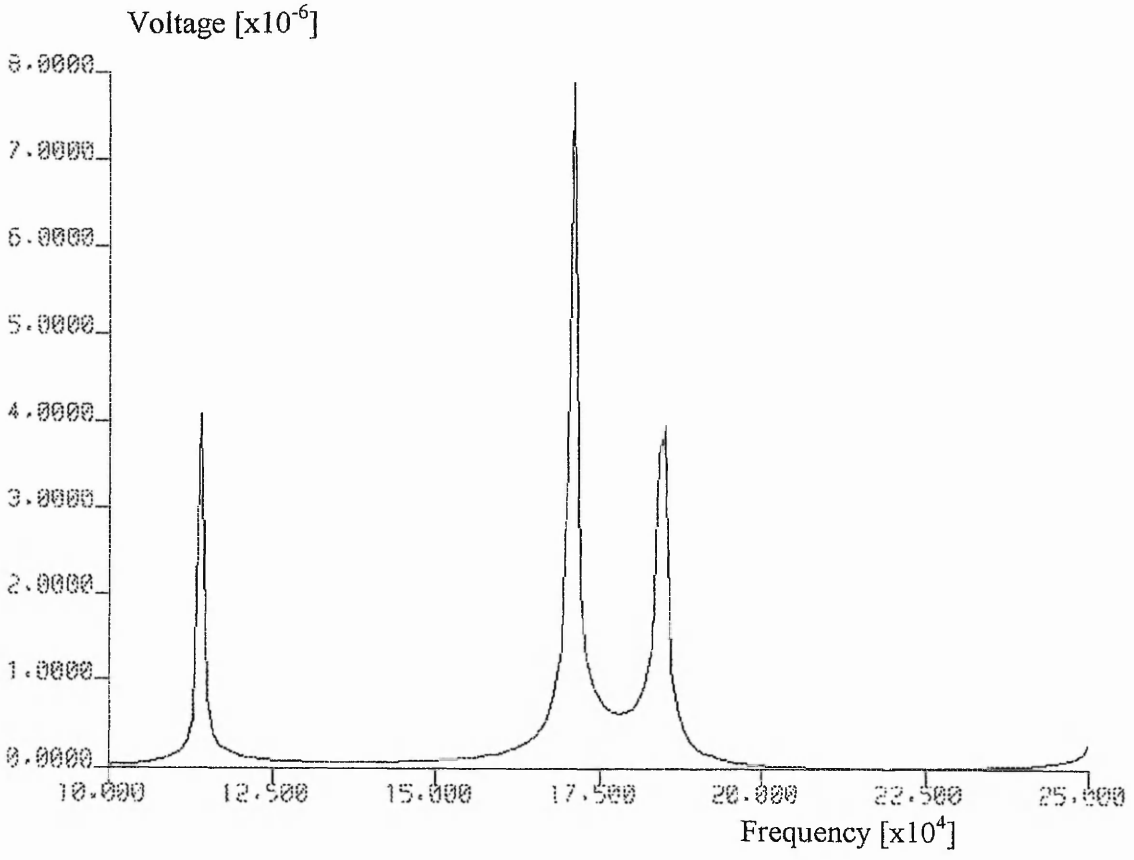

Fig. 3.39 Output voltage against frequency for an exponential horn transducer design with a 13.33 mm diameter piezoelectric disc. The piezoelectric thickness is 1 mm. A forced sinusoidal FE analysis was used.

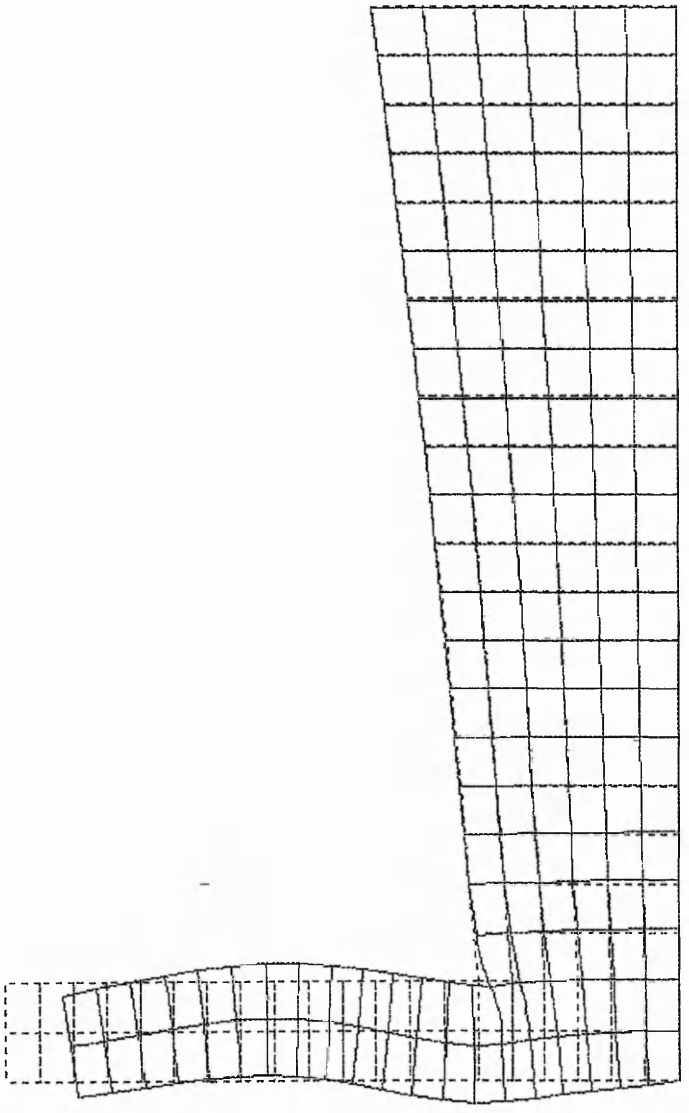

Fig. 3.40 Resonant mode at 171 kHz for an exponential horn transducer design with a 13.33 mm diameter piezoelectric. The piezoelectric thickness is 1 mm. A forced sinusoidal FE analysis was used.

As the excitation of the piezoelectric disc becomes more complex, as in the case of the coupled horn/disc design, so the need for FE modelling increases for predicting the transducer behaviour. Even though theory could be used to calculate the resonant frequencies of the individual components of the transducer, FEM is seen as the best method of predicting their combined performance. The modelling in Chapters Two and Three has shown that there can be variation in the predictions of one FE method and another. Care must therefore be exerted when choosing the appropriate FE model. Although the acoustic FE method using PAFEC-FE Vibroacoustics software has proved the most suitable for this study, it is recommended that a new or complex transducer design is considered using a variety methods initially, in order to establish their appropriateness to the specific application.

3.10 SENSITIVITY COMPARISONS

There are many ways in which to define the transducer sensitivity. With the two main types of modelling used, the acoustic sinusoidal and the forced sinusoidal using repeated freedoms on the transducer face, there are two methods of quantifying the sensitivity. The first is to use the output voltage produced by the piezoelectric element as a comparative measure of sensitivity, because in both types of analysis the input was constant, i.e. either a constant acoustic source, or a constant value input force. A second method might be to measure the output voltage per unit of movement at the centre of the transducer face.

Table 3.9 shows the comparison of transducer sensitivities for the three 175 kHz designs studied. These were; the bi-laminar disc transducer considered in Chapter Two, the 10 mm diameter, 5 mm thick, piezoelectric disc on the original exponential horn and back plate in section 3.8 and, finally, the coupled mode horn and piezoelectric disc design, considered in section 3.9.

Knowing that the bi-laminar disc transducer has similar sensitivity to a standard commercial resonant device (section 3.8, fig. 3.40) means that any predicted improvement to this performance in an FE model, should translate to a real improvement

in practice. From table 3.9, it is clear that the piezoelectric disc on the original horn and back plate offers improved sensitivity over the other designs, as all voltages or sensitivity units are larger by at least an order of magnitude. Only the direct value of output voltage predicted by the forced sinusoidal analysis does not indicate this, but instead, predicts the bi-laminar transducer as having the largest output voltage.

Transducer Design [Resonant frequency acoustic/sinusoidal]	Acoustic FE [volts/source strength]	Acoustic FE [mV/pm]	Forced Sinusoidal FE [volts/unit force]	Forced Sinusoidal FE [mV/pm]
Bi-laminar disc [176.5 / 173 kHz]	1.39	1.19	3.31×10^{-4}	1.21
PZT Disc on Horn [175 / 170 kHz]	1.35×10^{2}	2.01×10^{2}	2.67×10^{-5}	2.61×10^{1}
Coupled mode Horn & PZT Disc [158 / 171 kHz]	3.12×10^{-3}	2.11×10^{-2}	7.81×10^{-6}	8.3

Table 3.9 Transducer sensitivities for three designs using different modelling methods and sensitivity units.

Because the acoustic FE modelling has natural damping provided by the fluid, the output amplitude predictions have finite values and can be used as a guide to the real transducer's output. Given the reliability of the acoustic analysis for other performance predictions (i.e. frequency), it is likely that the disc and horn combination would prove more sensitive for detecting AE and other similar ultrasonic signals. On the other hand, the low sensitivity predictions by the majority of FE analyses in table 3.9 indicate significant improvements in performance are not achieved for the coupled mode transducer. The acoustic FE prediction in this case again provides the best indication of the real performance. The predicted output voltage is 3.12×10^{-3} volts compared with 1.39 volts from the same source strength in the bi-laminar disc transducer, which has a known real life performance.

3.11 SUMMARY OF CHAPTER THREE

Chapter Three has considered the use of an exponential horn with added components to produce a composite transducer design with improved sensitivity over a basic disc design. A transducer tuned for a specific geotechnical application has also been considered. The acoustic FE modelling was shown to be very accurate in predicting the resonant frequencies of such designs and even predicted slight changes to individual components (e.g. the back plate dimensions). This accuracy was demonstrated against both experimental measurements and theoretical calculations. By carrying out systematic modelling of the transducer's individual components, the ideal geometry of the horn and back plate design was chosen, with the model predicting substantial improvement to the transducer sensitivity.

Methods of spreading the resonance by shaping the back plate component of the transducer have been shown to work only when the back plate is of a particular geometry. FE modelling is considered to be an essential tool for these complex designs that no longer fit into any theoretical models.

Finally, the horn design has been utilised in two different transducers to compare its performance against the simpler bi-laminar disc transducer design. These transducers had resonances in the 175 kHz region and their sensitivities showed that the horn and back plate potentially provide the highest sensitivity.

Chapter Four

Transient Analysis of Transducer Response to an Acoustic Emission Event

4.0 INTRODUCTION

Previous chapters have considered the response of a transducer to a steady state sinusoidal input, at a constant frequency. In this chapter, the transducer response to a simulated acoustic emission event will be predicted, using transient FE analysis. Any transient acoustic source in a solid will produce a broadband acoustic waveform that will propagate and excite the transducer, causing it to produce an associated electrical waveform.

FEM and analytical methods have been used recently to study acoustic wave propagation in solids. These studies have not attempted to include the transducer response to the wave propagation. It is often assumed that broadband transducers are being used, which accurately represent the detected waveform at a point. However, many detectors used in practice are resonant in nature and will not recreate the incoming waveform. The waveform will be distorted by amplification of the frequency components at the transducer resonances, while other frequencies may be poorly represented. By using FEM, it may be possible to model not only the wave propagation, but also the response of a resonant device. An understanding of this more complex response, to a multi-frequency source, may give the user of resonant devices a more detailed knowledge, and understanding of what is being detected.

Modal analysis of waveforms, particularly using Lamb wave modes, is an area in which there has been a recent interest with regard to practical work [**26-28**]. The modelling may open up possibilities for simulations of practical systems and further understanding of the propagation and detection process.

4.1 METHODS USED TO SIMULATE AN ACOUSTIC EMISSION EVENT

Better understanding of the different events that cause acoustic emission will help in understanding material degradation mechanisms. Common practical sources are impulsive crack openings, delaminations, fibre breaks, or surface mechanical disturbance, such as an impact. Two common methods of modelling an acoustic emission event were used as input to a solid plate with the simple bi-laminar disc transducer, discussed in Chapter Two, attached to the surface. These inputs to the plate were simple step force-time functions.

The first source considered was a constant force, being instantaneously applied and then removed, on the plate surface, thus causing an artificial acoustic emission. A second source considered was a dipolar step force-time function, applied to a point within the plate, with two forces in opposite directions. This source was chosen to simulate a crack opening in a material. In practice, there are many varieties of AE events. The aim of this study was to see how far the resonant transducer signal could still carry information about the source. Further work will consider different methods of event modelling.

The two source functions were used as input to a finite element model of a plate, with a transducer on one surface, and they are described in section 4.1.2. Similar functions were used within a theoretical computer program, which modelled wave propagation in a plate. This program calculated the displacements under the transducer, at a distance from the source, which were then used as the input to an FE model of the transducer alone. This method is described in section 4.1.1.

4.1.1 AE Source Simulated by a Dynamic Green's Function and Data Preparation

It is possible to simulate the transient response of a plate AE source using a computer program called GPLATE, written by Nelson Hsu [**59**], at the NIST in the USA. This code calculates the Dynamic Green's Function of an infinite plate. The software gives

the displacement against time information, at a point on the surface of a plate. Dimensional information for this model is shown in fig. 4.1.

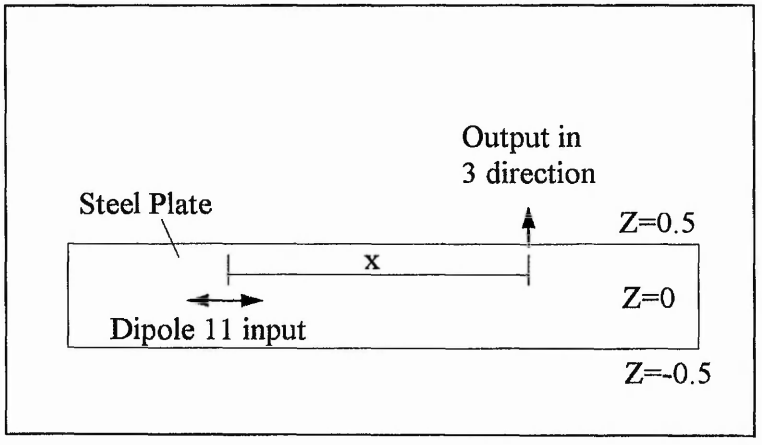

Fig. 4.1 Typical parameters for the GPLATE computer program.

The following input data are provided for the program:

Plate material properties:

HTHICK - plate thickness (mm)

SHSPD - shear wave speed (mm/μs)

PSPD - longitudinal wave speed (mm/μs)

SHMDUL - shear modulus (N/mm^2)

Source data:

x - distance between detector and source (mm)

Z - source position within plate (surface or inside)

INDEX - type of crack (step force or dipole) and detection direction (parallel or normal to plate surface)

Sampling data:

DT - sample interval (μs)

NPT - number of sample points.

The computer calculated the arrival time of the sound waves, generated by an acoustic emission source, for a specific position on the plate. The program causes the contribution of each wave to be summed, to give a displacement, at the specified position, for each time interval. When the maximum number of sampling points has been

reached, the program moves on to the next specified position, and calculates the arrival times at this new distance from the source.

The following input data were used and are typical values for steel:

HTHICK - 25 mm

PSPD - 5.176 mm/μs

SHSPD - 3.262 mm/μs

SHMDUL - 83000 N/mm^2

DT - 0.05 μs

NPT - 500

x - (every 0.5 mm at various distances)

Z - 0.5 (same surface as detector), 0.1,0, -0.1 etc. (positions inside plate) and -0.5 (opposite surface to detector)

INDEX- 113 (dipole force in 11 direction, detection in 3 direction) or 33 (step force in 3 direction, detection in 3 direction).

At each x position, the displacement at the detector, caused by the AE source, was calculated every 0.05 μs. The first time recorded is a few sample points before the first wave arrival, and the last time is 500 x 0.05 μs after this. Therefore, at each position x, there are 500 times and displacements. For the PZT-5A disc, with a 20 mm diameter plastic face, there are $\frac{20mm}{0.5mm} \times 500 = 20000$ data points. Increments in x of 0.5 mm were chosen, in order to provide an accurate representation of the waveform, whilst limiting the data demands.

Unfortunately, the data from the GPLATE program was not in a suitable form to put into a PAFEC data file. Instead of having time and displacement data at each x position, the PAFEC 'Define Response' module requires the data in the form, displacement at x (node) at each time interval. In order to arrange the data, an Excel spreadsheet was used, with two Macros to sort and assign node numbers to the x positions. Also, line continuation characters had to be used, to avoid more than 80 characters per line in a PAFEC data file. Eventually, a Turbo Pascal computer program was written, to deal with the case of extremely large three-dimensional models.

4.1.2 FE Model of AE Source and Transducer Response

Recent work has shown that finite element modelling can be used to effectively simulate wave propagation in plates [**33-36 & 59-61**]. The method has been developed for far field investigations, to assist in the knowledge of AE wave propagation, and can now deal with complex reflections at corners, and other obstacles, encountered in a practical specimen geometry [**35**]. The obvious advantage of FE over other techniques, such as the Green's function methods, is that it can deal with finite test specimen geometry and, hence, more realistic structures.

The disadvantage of the FE technique is that it is computationally demanding, pushing the limits of today's workstations, with hundreds of megabytes of RAM required. Because of these limitations, for the work reported in this thesis, a two-dimensional model was the only viable option.

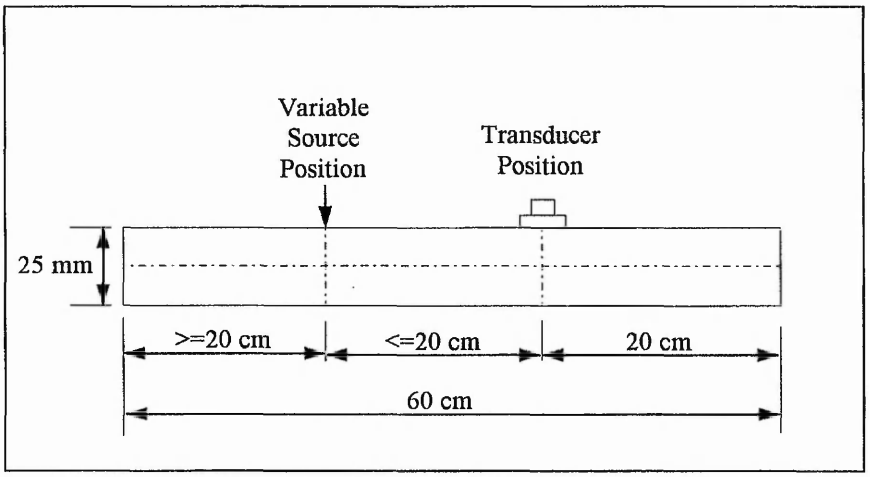

Fig. 4.2 Plate dimensions for the 2D FE model of the plate and transducer combination. The transducer position was constant while the source position varied as described in later sections.

In order to avoid acoustic wave reflections, the modelled plate dimensions were chosen such that any edge reflection would arrive at the transducer after a suitable time delay, allowing the transducer response to the first pulse to be studied. The dimensions of the plate, used for modelling, are shown in fig. 4.2 (not to scale) and are designed to allow study of first arrival signals for source-transducer distances of up to 20 cm. The aim was to model firstly, the effect of a square step up, then step down force (fig. 4.3), applied

normal to the upper and lower surfaces of the plate, and secondly a dipole force, parallel to the plate length. These inputs simulate a calibration signal using a pencil lead break on the surface and a crack opening inside the plate, respectively. To model the dipole, the step function in fig. 4.4 was applied to two superimposed nodes, in opposite directions.

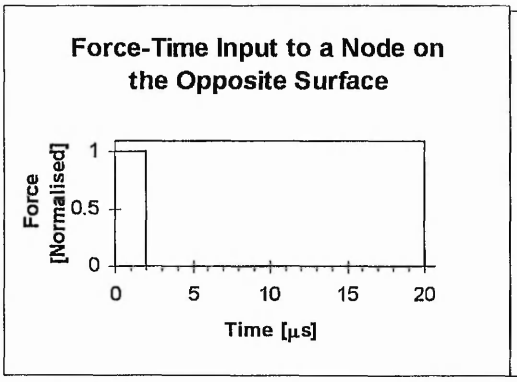

Fig. 4.3 At time zero the force steps up from 0 to 1 and then returns to 0 at 2 μs. The force value is −1 for a source on the same surface.

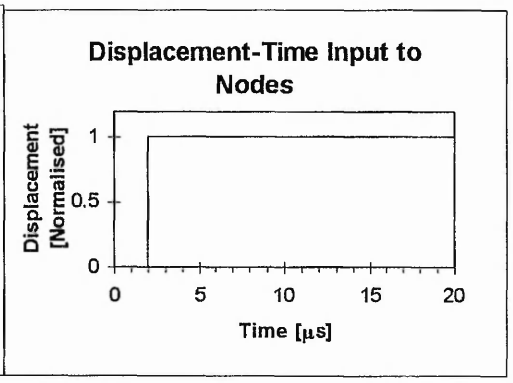

Fig. 4.4 The displacement value is −1 for the superimposed node moved in the opposite direction.

An epicentre source was also modelled, in which the source was under the transducer's central axis. For this, a smaller plate model was used to save on computer resources (fig. 4.5).

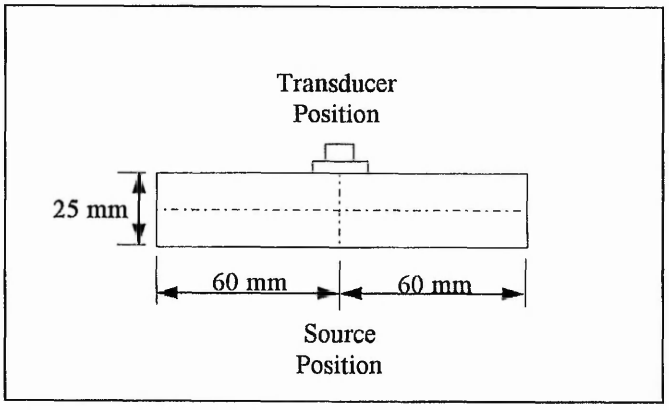

Fig. 4.5 Plate dimensions for the 2D, epicentral FE model (not to scale).

Following other work, using FEM to simulate ultrasonic wave propagation [**33, 34, 60**], four node, plane strain, finite elements were used. A four node element would appear to

be less accurate than the equivalent eight node element, but it gives a uniform distribution of mass in all directions, which is important for these type of problems so that the model provides realistic wave propagation and avoids spurious results [**33**]. With a large number of elements the accuracy will be good.

4.1.3 Transient FE Model Requirements for Spatial and Time Sampling

To further this study, a modified transient code was developed by PAFEC and this was used to perform the analysis of the AE response.

Suitable time intervals and element sizes, suggested for finite element calculations involving wave propagation, are as follows [**33**].

$$\text{Time interval } t = \frac{1}{20 f_{max}} \qquad \text{Element length } l_e = \frac{\lambda_{min}}{20}$$

where f_{max} is the maximum frequency of interest, and λ_{min} is the minimum wavelength involved. An easier way to imagine the element length, is that each element length must be less than the distance travelled by the acoustic wave in each time interval, to calculate accurate nodal displacements. This distance is the product of the sound velocity and the time interval t i.e. distance=ct.

A consideration for the model using the GPLATE data was the mesh density, because the time interval would be 0.05 μs, as pre-determined by the time interval in the GPLATE program. The smallest displacement in each time interval will occur for the material with the lowest sound velocity, (in this case the plastic), and was calculated as follows:

$$3353 \text{ms}^{-1} * 0.05 \mu\text{s} = 0.1676 \text{mm},$$

which means that the plastic elements have to have a spatial resolution of 0.1676 mm or less. This leads to a high mesh density. The piezoelectric elements used on the piezoelectric material can be larger, but the overall number of elements for the transient models is still very high.

The maximum frequency of interest was chosen as 250 kHz, for the FE model of the plate and the transducer. This is quite low, but was used to test the feasibility of higher frequency models. Even in a two dimensional model, a 1 MHz frequency limit for this problem would involve up to half a million elements, which would make calculation impossible.

For 250 kHz, a time interval of 0.2 μs, and an element size of about 1 mm, in the steel plate, are required. This ensures the distance the wave propagates in each time interval, will be accurately modelled. For the plate and transducer positions, shown in fig 4.2, the number of elements required is about 20,000. Each time interval takes about ten minutes of processor time and so, for a 100 μs time window, the calculation would take about three and a half days of continuous processing. It is easy to appreciate that these analyses can become troublesome when run on a networked workstation (even with light usage). A 500 kHz frequency model was attempted, but never ran to completion after going into a second week of calculation.

However, the 250 kHz frequency limit used does give a realistic representation of what would happen, because the 175 kHz resonant transducer would have most of its response, to an incoming acoustic wave, distributed around this resonant frequency. Also, electronic filters are often used in measurement systems, which further limit the bandwidth.

4.1.4 Establishing Suitable Methods for Modelling

Due to the large number of elements needed for transient calculations of AE events, an axisymmetric model would be ideal for computational efficiency. An axisymmetric model was used, for the initial modelling with the GPLATE input data, but this could only simulate an epicentre source which, in practice, rarely occurs. However, it does serve some practical purpose, especially for modelling experimental test conditions. As mentioned in previous chapters, the axisymmetric models are more efficient computationally. Even so, for a transient analysis of the first 50 μs only, the processor time for phase seven (the calculation phase of a PAFEC analysis) was about 8 hours.

As mentioned in section 4.1.1, the increment distance (x), used in the GPLATE program, was 0.5 mm. There are 3 or 4 finite elements over this distance, so the exact displacement at each node is unknown. If x was set to 0.25 mm, this would double the number of output displacement values from the GPLATE program, hence doubling the input data for the FE model. Therefore, nodes adjacent to a calculated x position were given repeated freedoms, which means they moved with the same displacement. Use of repeated freedoms, however, led to the transducer face vibrating as a series of 'steps', each step comprising several elements. This is because nodes, with the same degrees freedom, always move together, as seen in section 2.2.2.

It was decided that a good compromise was to manually assign the calculated displacement at one point to several adjacent nodes. This meant that each node could move individually, after the specified input data had ended. A computer program (in Turbo Pascal) was written, to assign the GPLATE data to a PAFEC data file. Every 0.25 mm on the transducer face, nodes were assigned input displacements, from the GPLATE output data, for each 0.05 μs time increment. Due to the large number of nodes, some nodes were still not directly excited at all and, despite the close distance between the specified nodal inputs, a slight 'ripple' effect (fig. 4.6) was seen at early time. This effect is less extreme, than when input data was specified every 0.5 mm. The effect is soon lost, as the transducer starts to vibrate and, therefore, gives a better simulation, than a model involving repeated freedoms.

To model an AE source from an off-epicentre position, a full 3D model is the ideal option. However, this put huge demands on the hardware. For example the processor time just to create the transducer mesh, in "phase two" of PAFEC, would increase from a few seconds to a few hours.

The file size, for this smaller phase, went from a magnitude of hundreds of kbytes, to hundreds of Mbytes. The GPLATE and 3D FE transducer combination was deemed inappropriate for the software and hardware available and also, too many approximations were needed to combine the two types of data.

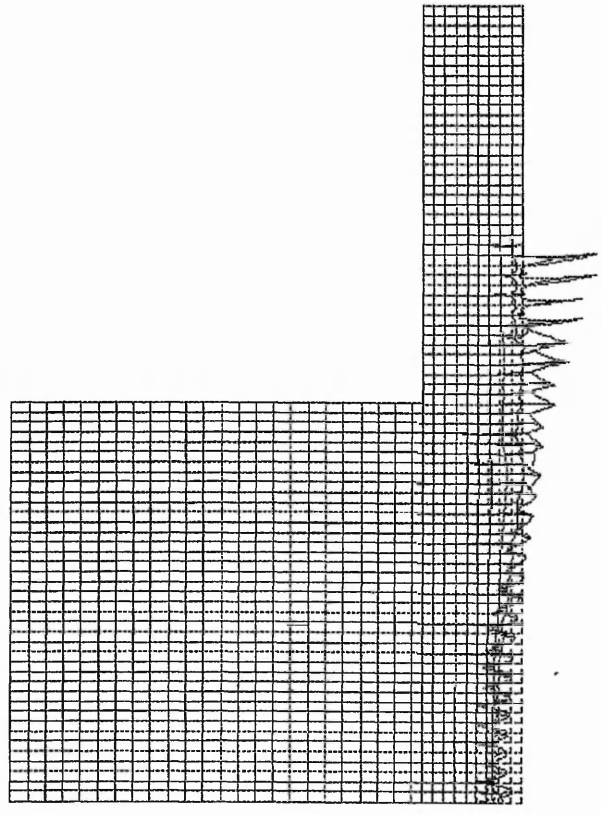

Fig. 4.6 Example of the 'ripple' effect, observed at early-time in a transient model, because not every node is specified as an input using displacement from the GPLATE data.

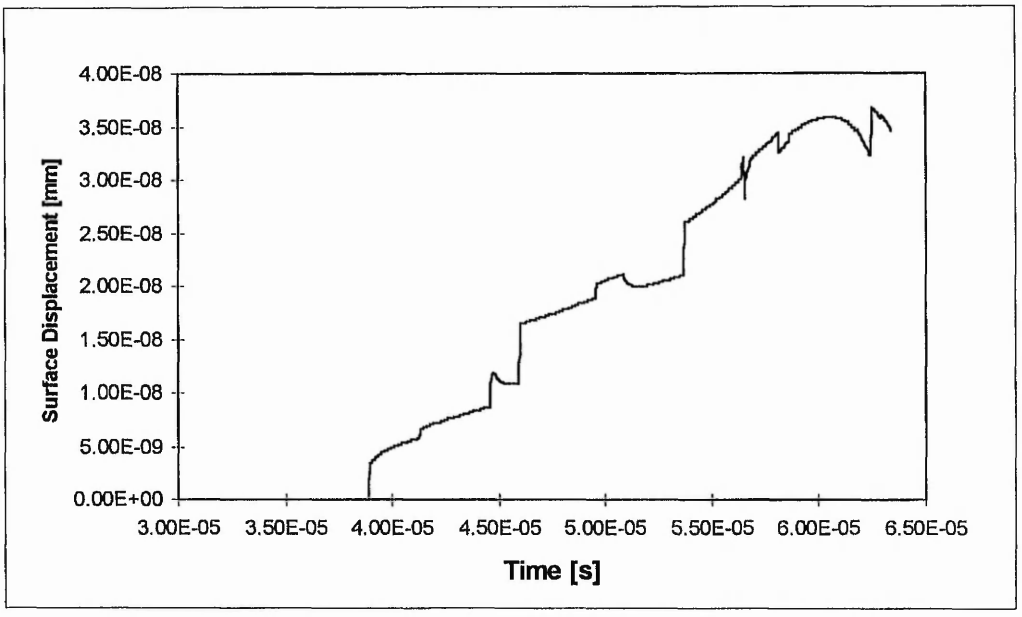

Fig. 4.7 Normal displacement at the plate surface at a propagation distance of 20 cm calculated using the GPLATE program.

To model a source at a distance, an axisymmetric model was eventually used, in which the GPLATE displacement waveform in fig. 4.7, was input at the transducer's centre node only (fig. 4.8).

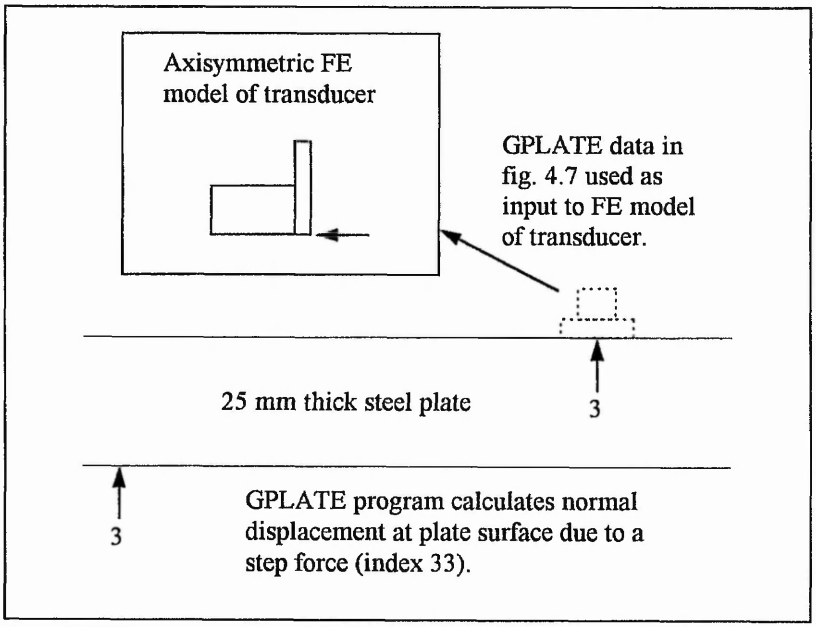

Fig. 4.8 'GP-FE' model combining output data from the GPLATE program by Hsu [**59**], as the input to the centre node in an axisymmetric FE model of the transducer.

This avoided more complex methods required to deal with an asymmetrical source in an axisymmetrical model. Although this involved a considerable approximation of the actual problem, it seemed the most suitable way forward.

The GPLATE computer program calculated the normal surface displacement, at a source-transducer distance of 20 cm, for a normal step force on the plate surface. This requires a 33 index in the GPLATE program.

The following CONTROL options were used for the transient models in the PAFEC data files (appendix V):

```
FRONTAL.TRANSIENT
AXISYMMETRIC (not for 3D model)
PHASE=1
SEMI.USE1
PHASE=2
TOLERANCE=10E-5
PHASE=4
SEMI.USE4
BASE=6000000
PHASE=7
SEMI.USE7
```

The SEMI.USE command specifies object files that contain the new transient code, developed by PAFEC for this work. The TOLERANCE option had to be used to overcome meshing problems with the Pafblocks, caused by the small element size. If this were left as the default of 10E-4, then the mesh would often connect the wrong nodes for the element topology, at the block interfaces. If the tolerance was set too small, at 10E-6, then there were coupling problems, between the piezoelectric and plastic elements.

The advantage of using the FE method, to model the plate and transducer combination, is that the input displacement is calculated at every node on the transducer face, and no approximations (such as the distance increment x) have to be employed, as when using

the GPLATE input data. The obvious disadvantage is that there are many more elements involved in each model, and so the models are very demanding on computer hardware resources. Table 4.1 provides a summary of the various approaches to the transient modelling problem with their individual merits and disadvantages. Naturally the two achievable methods were used as the other two were impractical, due to the reasons already discussed.

Modelling Method	Accuracy of input data to transducer	Transducer Resonance	Relative Computational Demands	Feasibility
3D FE	Most accurate, all nodes on face individually excited	Realistic	Very high	Impractical
3D GPLATE & FE	Too many approximations required to excite all nodes	Realistic	High	Impractical
2D FE	Accurate, all nodes on transducer face excited	Different to 3D	Medium	Achievable
GP-FE/ axisymmetric	Displacement input at one point only	Realistic	Low	Achievable

Table 4.1 Summary of the various merits of the main modelling methods explored, using the transient FE analysis of the transducer response, to an off-epicentre AE event.

4.2 COMPARISON OF TRANSDUCER SIGNALS PRODUCED BY TWO DIFFERENT FE MODELS, FOR AN EPICENTRAL STEP FORCE ON THE OPPOSITE SURFACE OF A PLATE

This section considers the modelling of an epicentral step force, suddenly applied to and then removed from, the steel plate surface opposite the transducer, and on its central axis. Two FE models were employed, using two distinct methods of calculating the displacements at the transducer face. The first method used the GPLATE computer program, by Hsu [**59**], to model wave propagation and define the input displacements to an FE model of the transducer only (as described in section 4.1.1). A 33 index was used in the GPLATE program to specify a normal step force input and normal surface displacement output. The GPLATE program calculated the plate's surface displacement every 0.5 mm. This data was input to nodes every 0.25 mm on the transducer face. This model will be referred to as "GP-FE".

The second model involved applying the step force input, in fig. 4.3, to the node on the opposite surface of the plate, directly below the transducer centre, using an FE model of the complete wave propagation-transducer system. The dimensions of the plate are shown in fig. 4.5. This model shall be referred to as "FE".

Normalised output voltage, produced by the bi-laminar disc transducer, was plotted against time (fig. 4.9). In the FE model of the source and transducer, the unit force is applied at zero time and then drops to zero at 2 μs. In the GPLATE program, the model source is a Heaviside step down function. In order to simulate the 2 μs square pulse of fig. 4.3, the waveform data from the step down was inverted at time zero. Two microseconds later, the original step down data was added. These two signals were then summed together and plotted in fig. 4.9, to give comparable waveforms for 2 μs square wave excitation. Although the FE input is not strictly a square wave input, because the force is already at its maximum at time zero, the resulting displacement at the input node is such that it is equivalent to an instantaneous step up created by a Heaviside function.

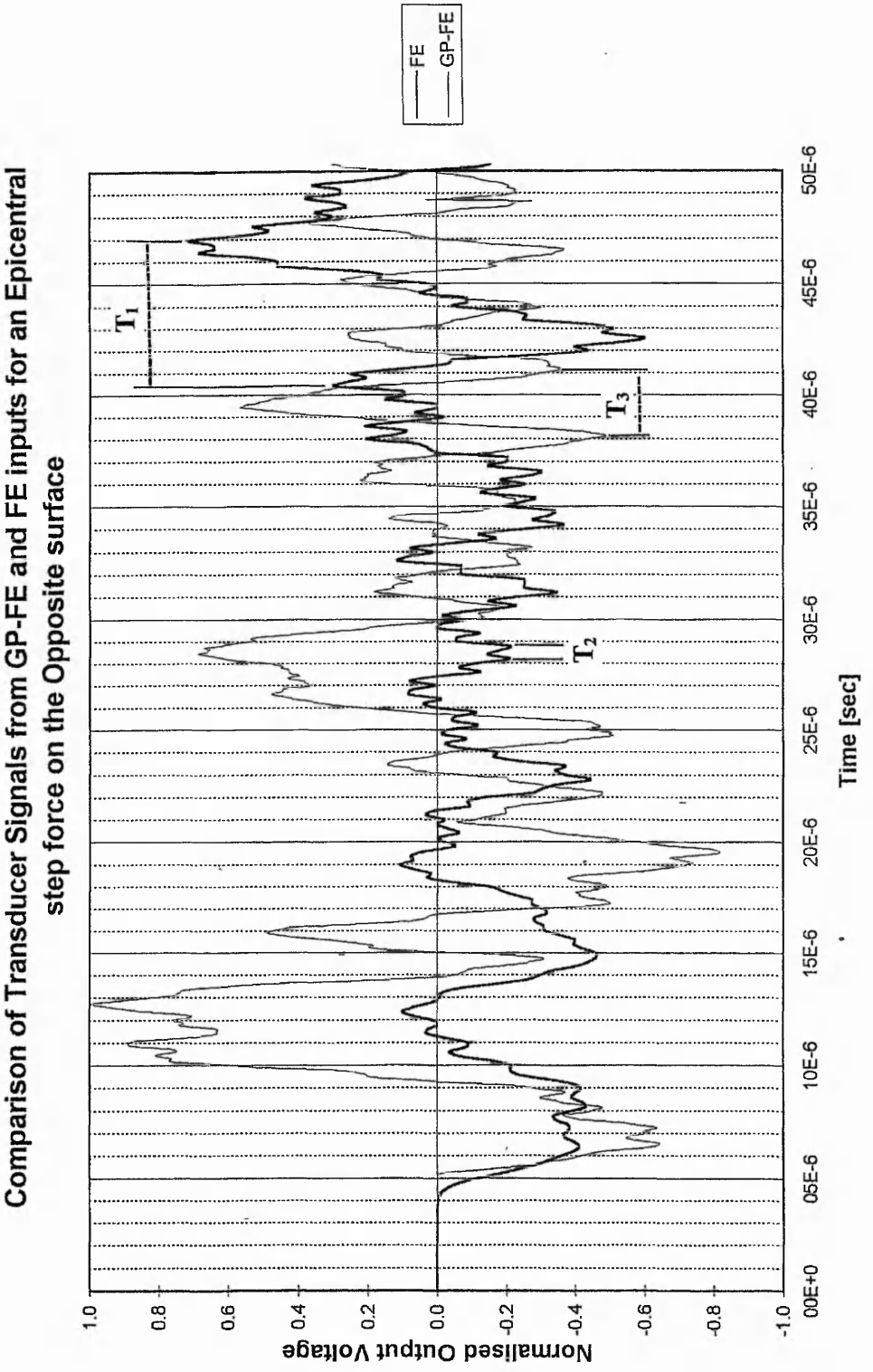

Fig. 4.9 Comparison of transducer signals produced by the GPLATE and FE method (GP-FE), and by the FE only method (FE). The source is a step force (fig. 4.3) on the opposite surface of the plate, and is epicentral.

Both signals show an oscillating waveform. Superimposed on the peaks is a further, smaller amplitude, higher frequency oscillation. After about 17 μs, the two signals start to differ in phase. Between 25 and 30 μs, the FE signal is producing lower amplitude oscillations, in comparison to the GP-FE signal. The two signals then show a similar, low amplitude of output voltage, between 30 and 37 μs, after which time the voltage oscillations increase again.

The theoretical time for a bar longitudinal wave (or P-wave) to travel 25 mm (the plate thickness) is 4.83 μs, at 5176 ms^{-1}. The GP-FE signal (fig. 4.9) shows the output voltage noticeably start to rise at 5.2 μs, but does in fact show the first values for voltage at 4.85 μs. This is the nearest time possible, given the 0.05 μs sampling rate used in the model.

The FE signal starts at 4.2 μs, which is accurate for the bulk longitudinal wave velocity (V_L) of 6006 ms^{-1}. This is calculated using the velocity formula

$$V_L = \left[\frac{E(1-\sigma)}{\rho(1+\sigma)(1-2\sigma)} \right]^{1/2}$$

where E is the Young's modulus, ρ is the density, and σ is the Poisson's ratio.

This bulk velocity is faster than the bar velocity used in the GPLATE program, which was equal to $\sqrt{E/\rho}$. The bar longitudinal velocity should only be used at a large propagation distance, in which the wavelength is much greater than the thickness of the plate. Both models accurately predict the start of the transducer signal, indicating the P-wave arrival.

Fig. 4.9 shows that, following the slightly different start times, the GP-FE signal and the FE signal are initially in phase. The shear wave should arrive at the transducer face at the same time in both models, which is 7.66 μs. This time in fig. 4.9 may correspond to a waveform discontinuity.

The initial first main oscillation occurs at the same times for the two models. The difference between the two signals appears in the amplitudes of the output voltages. The GP-FE signal produces larger output voltages. The FE waveform appears to have an initial negative DC bias. However, this does eventually disappear. Because the model takes account of low frequency plate motion, it is likely that the whole plate has been given a slight shift in displacement from its original position, caused by the imbalance of the input force. This gives the initial signal a DC offset, which gradually reduces at late time.

At just under 30 μs, the GP-FE input signal ends, since output data from the GPLATE program is only calculated for five hundred, 0.05 μs time increments, from the P-wave arrival (500 x 0.05 + 4.83 = 30 μs). The signal settles into a steady oscillation after this time (fig 4.9). The frequency corresponding to period T_3 in fig. 4.9 is approximately 333 kHz, which is high when compared to the transducer's main resonance, at 176.5 kHz. The axisymmetric model of the plain disc, in Chapter Two, does predict the existence of resonances in this frequency region (M_{43} at 317 kHz and M_{44} at 340 kHz).

The FE signal does appear to have a higher frequency content, which becomes more apparent after 25 μs. This is not seen in the GP-FE signal and, is a frequency beyond the minimum specified upper frequency limit of the model (250 kHz). The high frequency content is about 1.5 MHz, with period T_2 in fig. 4.9 and indicates that the resolution in the FE model is capable of modelling frequencies well above the frequency used for calculating the resolution in section 4.1.3. The spatial sampling used was higher than some authors suggest is necessary **[61]** and therefore, the model should be suitable for frequencies of at least 500 kHz. In fig. 4.10 a fast Fourier transform (FFT) of the FE signal, seen in fig. 4.9, shows the largest frequency content at 146 kHz (period T_1 in fig. 4.9), which correspond to the 2D transducer's radial mode at 147 kHz (section 4.6.1). This mode is the main mode of the transducer and is therefore, expected to dominate the frequency response of the resonant device. There are smaller magnitude peaks at 253, 283 and 361 kHz, all of which are resonant frequencies of the 2D transducer. The only higher frequency content is at 1.6 MHz, although it is of a smaller magnitude in comparison with the other frequencies mentioned.

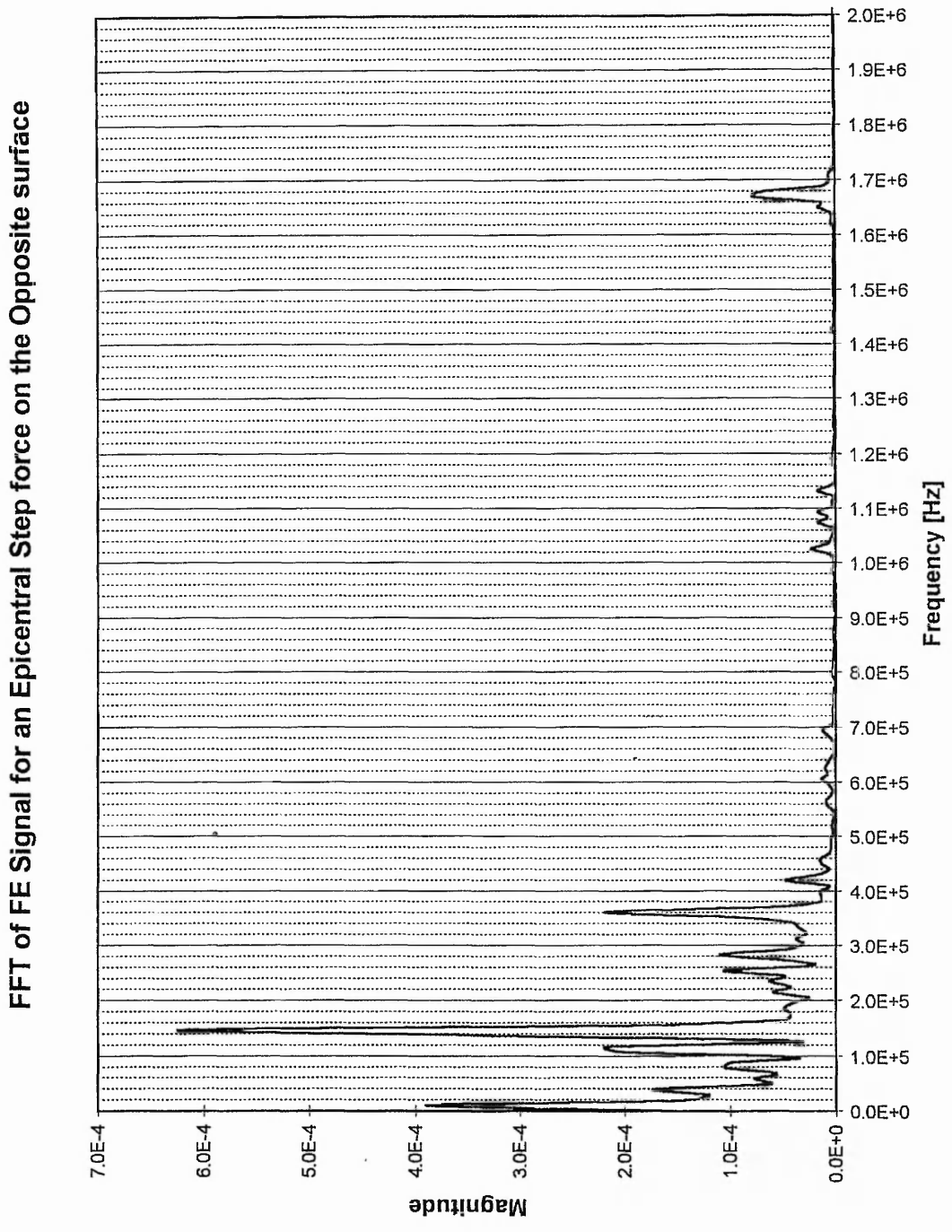

Fig. 4.10 Fast Fourier transform of the FE signal, for an epicentral step force, on the opposite surface of the plate.

As expected, the resonant transducer produces an output voltage signal, which is dominated by frequencies that match the resonant frequencies of the transducer. Because the GP-FE model used a 3D transducer (actually axisymmetric), while the FE model had a 2D transducer, the transducers had different resonant frequencies in each case. In the case of the 2D transducer, the main resonant frequency was at 147 kHz, while in the axisymmetric transducer, the main resonant frequency was 176.5 kHz. The different resonant frequencies of the 2D and axisymmetric FE models leads to the different shape in the output voltage signals once the transducers begin to resonate.

The early time correspondence of the waveforms is as expected and this is before the transducer begins to resonate freely, seen after approximately 30 μs. Therefore, this early time may offer more information about the excitation process.

Both modelling methods have their respective limitations due to the approximations required to make them computationally practical. The GPLATE program, although providing accurate information in the near field, only provides detail about the plate displacement for a limited time period. After this time (in this case approximately 30 μs), the transient has passed and the plate no longer provides input to the transducer vibration. Also, the GPLATE displacement data was not input to every node on the transducer face, due to the huge amount of data this would have needed. As discussed in Chapters Two and Three, the input to the transducer face may have an effect on the transducer modes that are excited.

Finite element modelling has been shown, by others [**33-36**], to be an accurate method of simulating transient wave propagation. The system of plate and transducer had to be modelled in two dimensions to make it computationally practical. Although a full 3D model is the best way to get realistic predictions of the transient wave and transducer response, the 2D FE model does provide a good example of the wave propagation in a large plate in which the third dimension is very large in comparison to the two considered. The inaccuracy lies in the 2D transducer, which will have different resonances to a 3D transducer. However, if the different frequency response of the transducer is borne in mind, then it would be sensible to assume that the FE model of the

whole system provides a more robust method of modelling the AE source and transducer system than combining the GPLATE and FE methods.

The overall advantages of the FE method to perform the modelling of the whole system compared with the GP-FE method are:

1. Accurate control of the source type, strength and direction.
2. Input displacements over the entire transducer face.
3. Post-processing facilities enabling study of the waveform in the plate and the transducer vibration, to help analysis.

4.3 INVESTIGATION INTO TRANSDUCER SIGNAL VARIATION WITH SOURCE LOCATION USING FEM TO MODEL A STEP FORCE ON THE PLATE SURFACES

4.3.1 Comparison of Transducer Waveforms for a Step Force on the Same Surface and Opposite Surface for a Propagation Distance of 20 cm

Work in earlier sections of this chapter suggests full FE modelling of wave propagation and transduction is likely to be more effective than the GP-FE method. Since this approach appears robust, it will now be used exclusively, to compare the output voltage signals produced by a step force on both plate surfaces, at a source-transducer distance of 20 cm. The aim of this section was to study waveforms from the same source, when situated on opposite sides of the plate, at a fixed source-transducer distance. The step force excitation used is shown in fig. 4.3. The wave propagation in the plate was examined using the PIGS post-processing facility, as was the transducer vibration.

The signal produced by the transducer, when the source is on the opposite surface of the plate to the transducer, will be referred to as the "OS" signal. The signal produced by the transducer with the source located on the same surface of the plate as the transducer, will be referred to as the "SS" signal. The dimensions of the model are outlined in fig. 4.2.

The main discussion will now compare the OS and SS signals. Both sources produce an identical transducer output voltage (fig. 4.11) for the first 7 μs after the fastest source wave has propagated to the transducer, which indicates that the symmetric Lamb wave modes, travelling at the P-wave velocity, are causing the first displacement at the transducer face. The two signals appear to have opposite polarity between 60 and 70 μs. After this time, the SS signal shows opposite DC bias and opposite oscillation polarity, until 95 μs. It is expected that after this time source effects will have disappeared, and the OS and SS signals will be in phase, the later signal largely arising due to free transducer vibration.

Using PIGS (the PAFEC interactive graphics system), the deformed structure was analysed at different time intervals (fig. 4.12 to 4.20). The entire plate is not seen in the figures, due to the scale used. Where possible, the source and transducer locations are included in the figures.

Fig. 4.12a shows the plate deformation 4 μs after the start of the force, on the same surface as the transducer. Fig. 4.12b shows a detailed view of the source region. The P-wave has travelled 24.02 mm and is just reaching the opposite surface of the 25 mm thick plate. On all figures, 'P' marks the calculated position of the longitudinal wave front at a radius of 24.02 mm, and 'S' marks the shear wave front at a radius of 13.05 mm, which clearly produces a much larger displacement. Fig. 4.13a and 4.13b show the plate after 20 μs, while fig. 4.14 shows the plate after 40 μs. At these later times, the Lamb wave modes are well established and the 'P' in the figures represents the fastest Lamb waves, travelling at the P-wave velocity. It is clear from fig. 4.13a and 4.14, that these fastest waves cause very little displacement at the plate surfaces, which accounts for the small output voltage at the transducer. Most of the displacement appears to be associated with the asymmetric Lamb waves that arrive later.

Magnification of the plate deformation is seen in fig. 4.13b, with the calculated P-wave front immediately followed by a symmetric Lamb wave mode, marked 'L'.

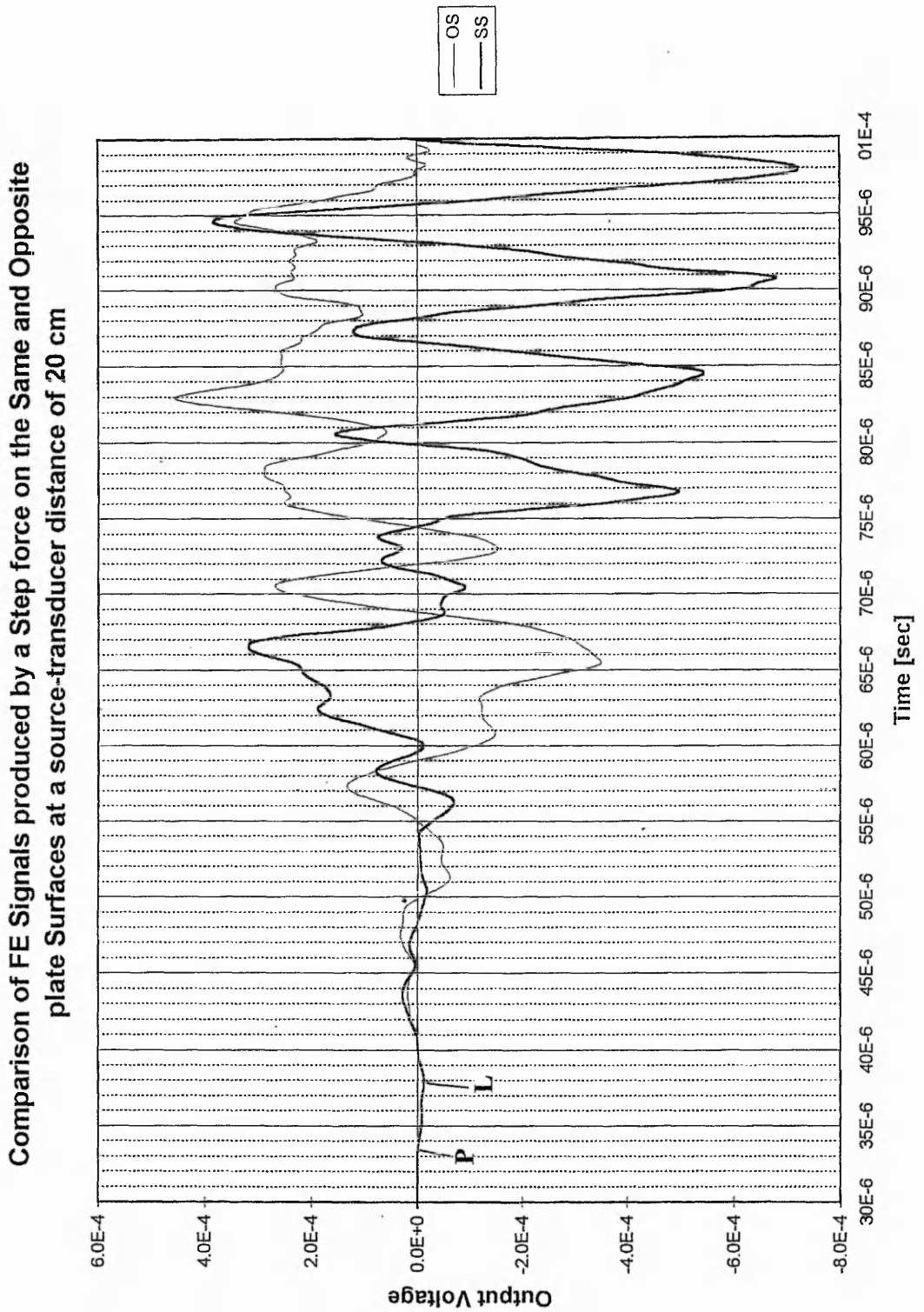

Fig. 4.11 Comparison of the FE signals, for a step force on the same surface (SS) and opposite surface (OS) of the plate, at a source-transducer distance of 20 cm.

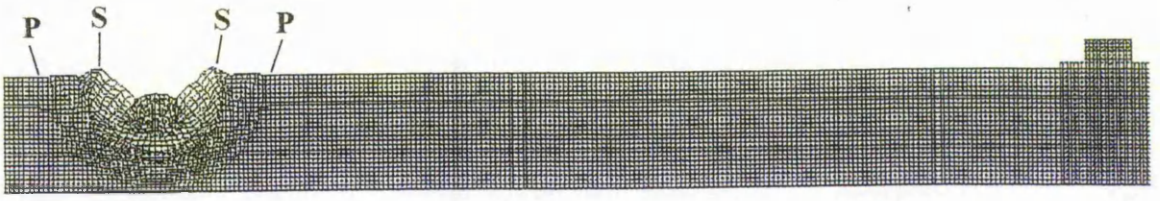

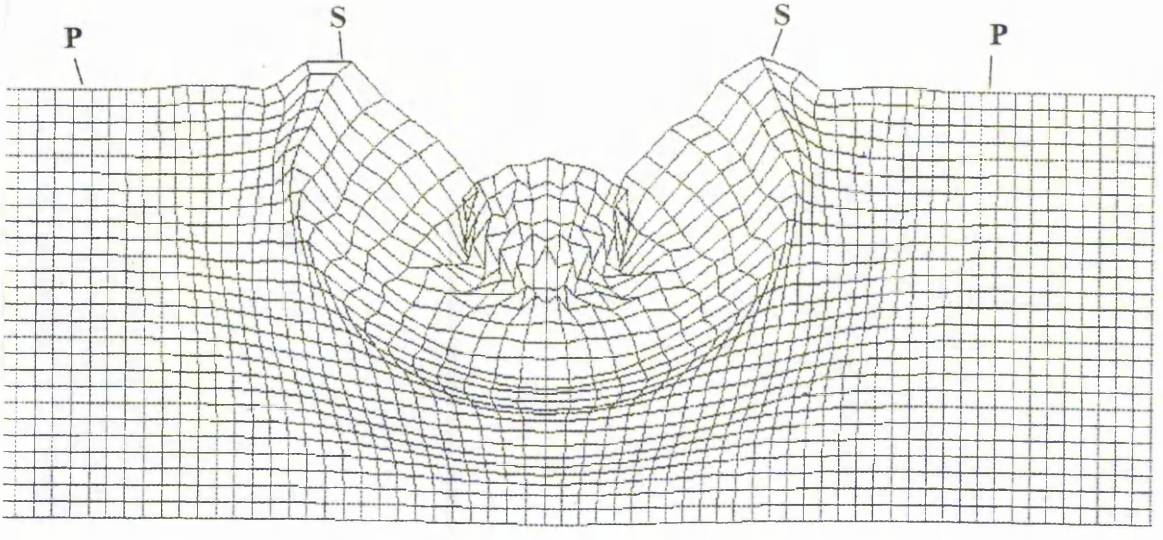

Fig. 4.12a (top) & Fig. 4.12b (magnified)

Deformed plate at 4 μs. The points marked 'P' show the P-wave front, while points marked 'S' show shear wave front. The source is a step force on the same surface of the plate, at a source-transducer distance of 20 cm.

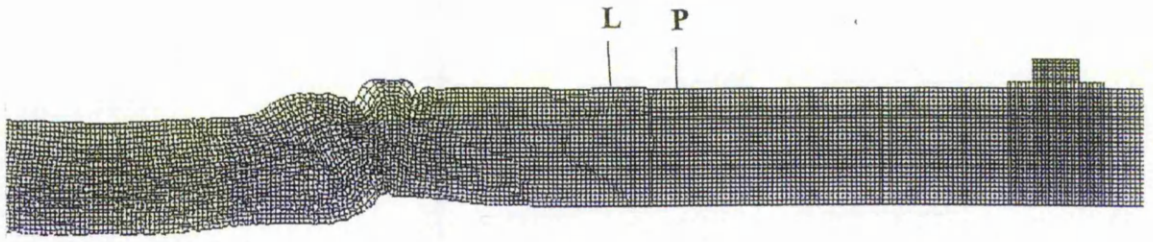

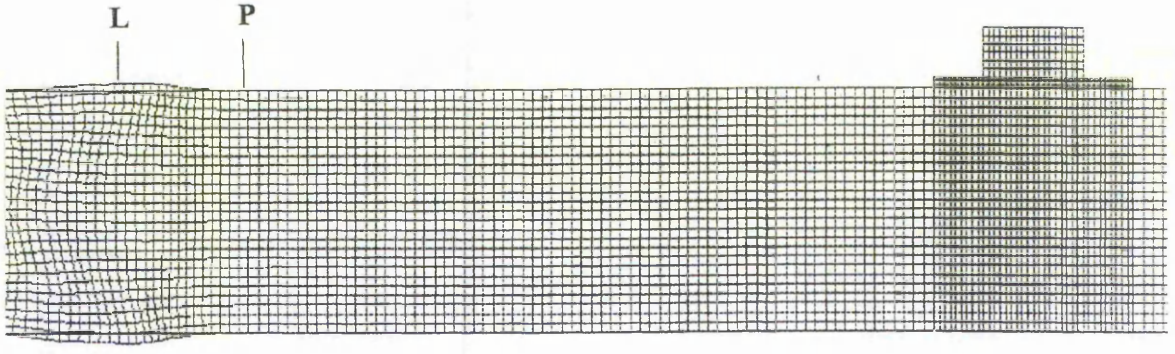

Fig. 4.13a (top) & Fig. 4.13b (magnified) Deformed plate at 20 μs. The points marked 'P' show the P-wave front, while points marked 'L' show the fastest symmetric Lamb wave mode. The source is a step force on the same surface of the plate, at a source-transducer distance of 20 cm.

Fig. 4.14 Deformed plate after 40 μs, for a step force on the same surface of the plate, at a source-transducer distance of 20 cm.

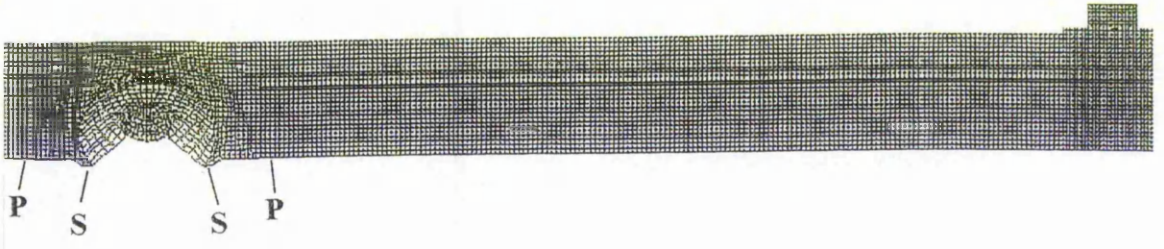

Fig. 4.15 Deformed plate after 4 μs, for a step force on the opposite surface of the plate, at a source-transducer distance of 20 cm.

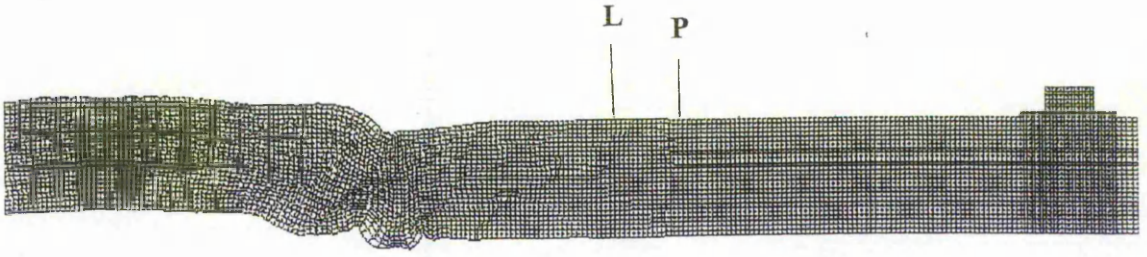

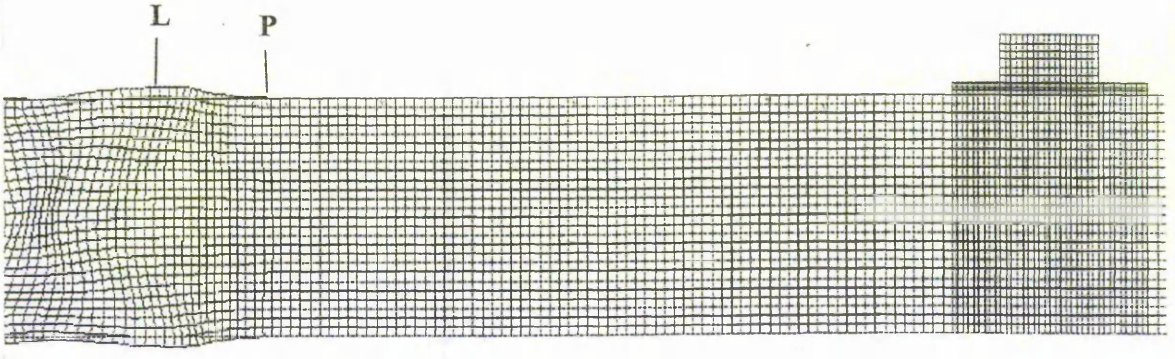

Fig. 4.16a (top) & Fig. 4.16b (magnified) Deformed plate at 20 μs. The points marked 'P' show the P-wave front, while points marked 'L' show the fastest symmetric Lamb wave mode. The source is a step force on the opposite surface of the plate, at a source-transducer distance of 20 cm.

Fig. 4.17 Deformed plate after 40 μs, for a step force on the opposite surface of the plate, at a source-transducer distance of 20 cm.

The arrival of the point 'L' is marked on the waveform in fig. 4.11 and appears responsible for the first peak in the output voltage signal. Due to the symmetry of the surface displacement, the OS signal produces exactly the same output voltage as the SS signal, at this time.

Taking the resonant frequency of the 2D transducer as 147 kHz, the fastest Lamb wave mode is the L_{12} mode. This mode is symmetric, and should arrive at the transducer at approximately 40 μs, which is the case. Looking at the deformed plate with the OS model (fig. 4.15-4.17), it is clear that the transducer excitation is now created by an identical plate displacement but inverted.

The next Lamb wave modes are slower and, at this transducer resonant frequency (147 kHz), are the L_{21} mode and the L_{22} mode, which would arrive at about 65 μs (appendix VI). The transducer signals appear to indicate this, because they become opposite in polarity (fig. 4.11). The increase in the transducer output voltage amplitude indicates that these modes have been strongly excited, which should be the case, due to the asymmetry of the source (i.e. off the central plate axis).

In order to gain a better understanding of signal generation by the transducer, the deformed plate mesh was studied at a time of 55 μs. This time was chosen because the propagating asymmetric Lamb waves would be close enough to the transducer to be seen clearly, just before they strike the transducer. Fig. 4.16 shows the symmetric waves' relatively small influence on the plate deformation at 20 μs and, at 55 μs, they will have already passed under the transducer.

Fig. 4.18 shows the deformed plate and part of the transducer, at 55 μs, caused by a step force, on the same surface of the plate as the transducer. Two parallel horizontal lines represent the undeformed plate surfaces. Using these as a reference, it is possible to establish the type of symmetry for the Lamb wave modes that are propagating in the plate.

Points of interest have been numbered on fig. 4.18. Knowing the size of the elements, the source and the transducer locations and also the time at which this deformation occurs (55 μs), the velocities of the waves at these points were calculated. These velocities were then used to calculate the arrival times of these wave points at the transducer centre and, hence, their arrival times are marked on the signals in fig. 4.19.

Fig. 4.20 shows the case for the source being located on the opposite surface of the plate to the transducer. The same points have been marked for comparison with the SS case. It is clear that the plate deformation is the inverse of the SS case.

Point 1 (fig. 4.18) shows a small displacement that is almost symmetrical about the centre of the plate length and, therefore, the same displacement occurs at the top and bottom surfaces. This is seen in the SS signal (at point 1) as producing an output voltage equal to that seen in the OS signal. When the P-wave velocity waves first arrives, at 33 μs, the two models have exactly the same displacement and output voltage, due to the acoustic wave symmetry (compare fig. 4.13b, 4.16b & 4.19).

Point 2 is showing a much larger displacement that is asymmetric (fig. 4.18). At point 2 on the SS signal (fig. 4.19), the output voltage has increased significantly. Due to the asymmetry, the OS signal is producing the opposite polarity signal at this time (fig. 4.19). Because the source is asymmetrical, it will excite the flexural modes more strongly than the extensional (symmetric) modes. This results in large amplitude output voltages, at times when asymmetric modes are arriving, and small amplitudes, when the symmetric modes are arriving. Point 3 (fig. 4.18 and 4.20) confirms this, as it has a small, symmetric displacement in the plate, and produces a low amplitude output voltage in both signals (fig. 4.19).

The region marked between points 4 and 5 (fig. 4.18 and 4.19), occurs at the start of an extended period of asymmetry, with large surface displacements. This is clearly represented by the large oscillations, seen in the SS signal during this time period, occurring as a result of transducer resonance.

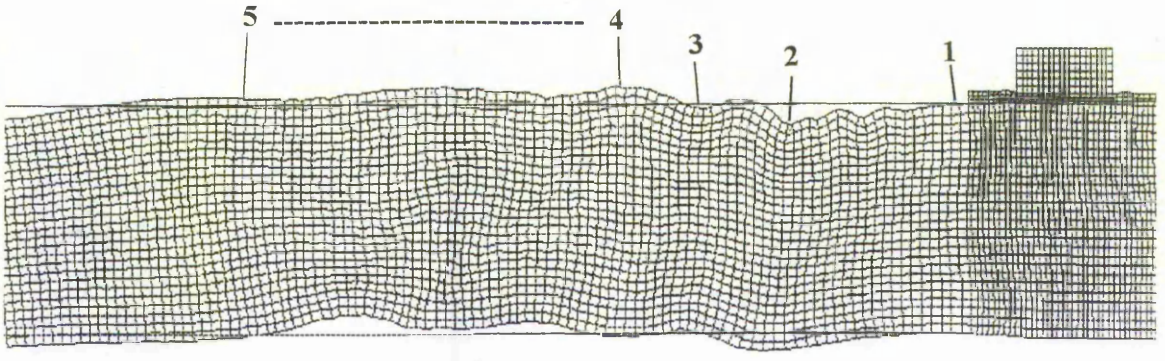

Fig. 4.18 Deformed plate after 55 μs, for a step force on the same surface of the plate, at a source-transducer distance of 20 cm. Reference points are marked 1-5 on waves the plate surfaces. Their calculated arrival times, at the centre of the transducer face, are marked on the transducer signal in fig. 4.19.

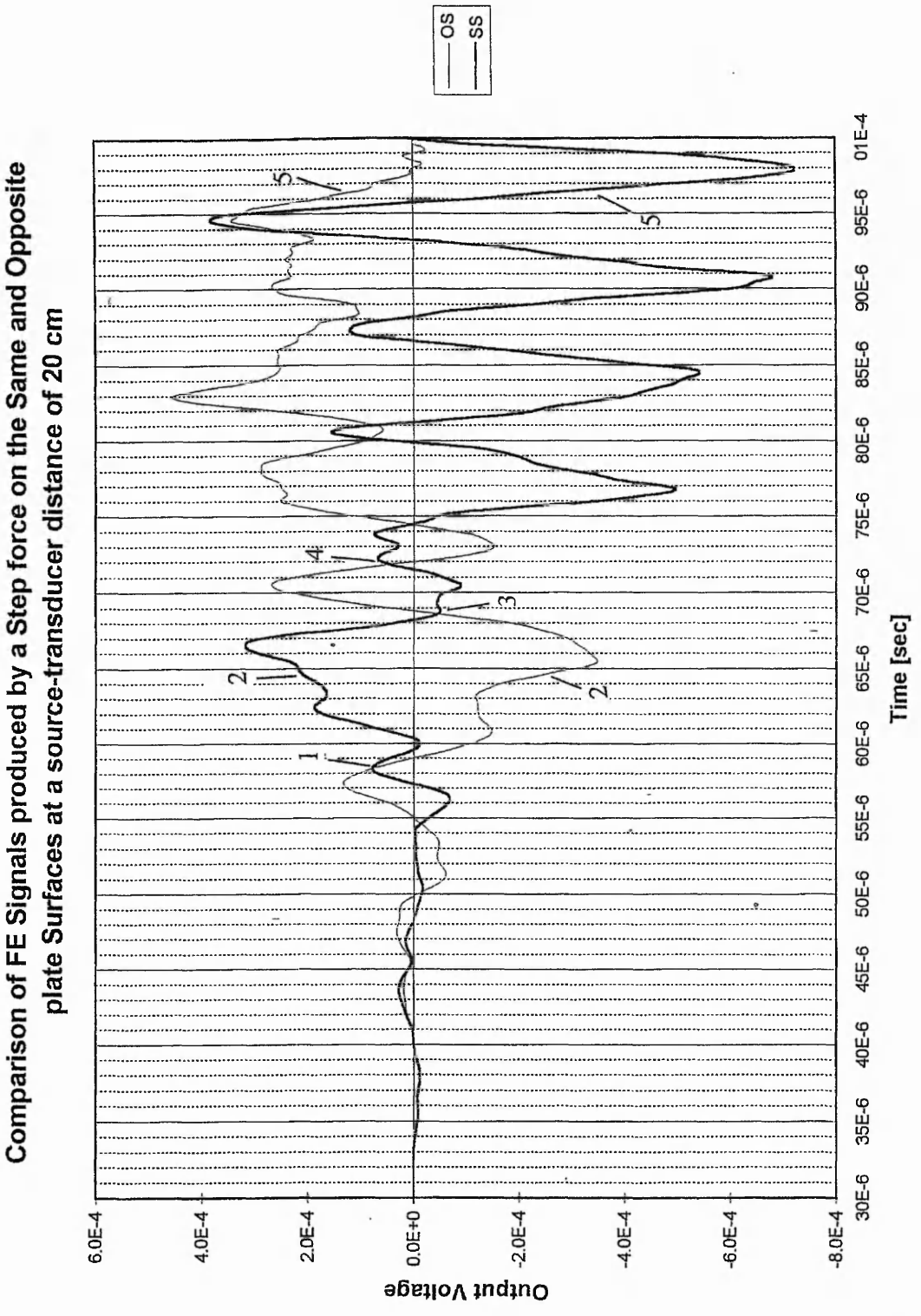

Fig. 4.19 Comparison of the FE signals for a step force, on the same surface (SS), and opposite surface (OS) of the plate, at a source-transducer distance of 20 cm. The numbered points are the arrival times of the marked points in fig. 4.18 and 4.20.

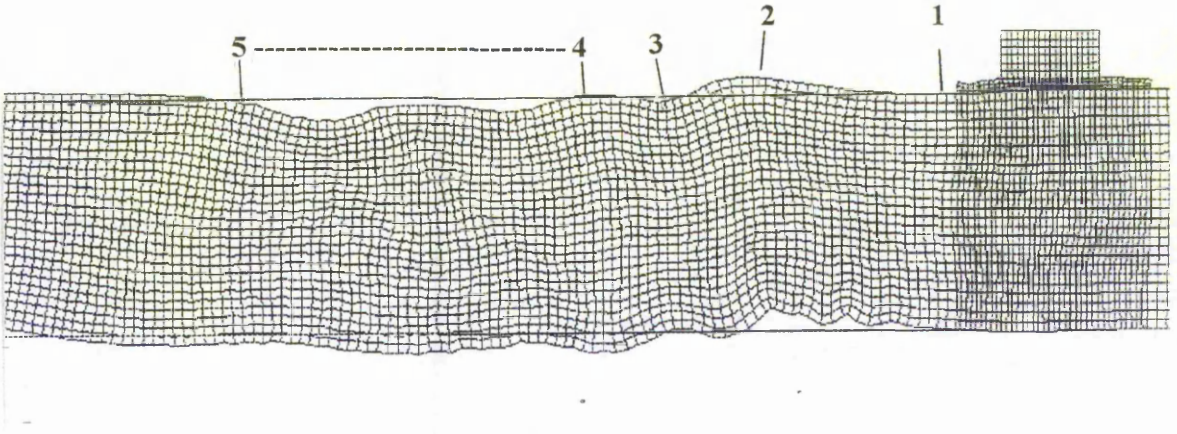

Fig. 4.20 Deformed plate after 55 μs, for a step force on the opposite surface of the plate, at a source-transducer distance of 20 cm. Reference points are marked 1-5 on waves the plate surfaces. Their calculated arrival times, at the centre of the transducer face, are marked on the transducer signal in fig. 4.19.

The asymmetric aspect of the excitation is present as the negative DC offset, seen in the signal. Near the end of region 4-5, the deformation appears more symmetrical, and is seen as the SS and OS signals and waveform surface displacements move into phase, and the DC offset reduces. Despite the overall asymmetry during the region 4-5, the deformation in the plate looks more symmetrical than at point 2 (fig. 4.18). The slowest Lamb wave mode, at 147 kHz, is the symmetric L_{11} mode.

This L_{11} mode should arrive at the transducer after 76 μs. Due to the source asymmetry, due to the source being on the plate surface, this mode would be poorly excited and, this may explain why the signal is still largely influenced by asymmetric vibration, but appears to come into phase at late time (95 μs).

As mentioned for fig. 4.18, point 1 in fig. 4.20 shows almost symmetrical deformation, of low amplitude. At this point, the transducer time waveform (fig. 4.19) shows that the two signals are beginning to separate. This was predicted, and shown to be caused by slower, asymmetric Lamb wave modes arriving, and this is seen by comparing points 1 and 2 (fig. 4.19 and 4.20).

What is interesting, is the fact that the resonant transducer is producing a signal that clearly represents detail about the plate surface. Between points 1 and 2, the OS and SS signals differ, in the size and shape of their waveform features (fig. 4.19). While the SS signal shows a series of small maxima and minima, between 62 and 66 μs, the OS signal has a smoother appearance. This is a direct representation of what is happening on the plate surface. In fig. 4.18, the SS signal is produced by the series of higher frequency oscillations between points 1 and 2. Fig. 4.20 shows that, with the source on the opposite surface, the surface on which the transducer is located is subject to a lower frequency displacement waveform and, hence, produces a lower frequency output voltage.

Point 3 shows more symmetric deformation (fig. 4.20), and so both signals have the same, low amplitude output voltage. The region marked 4-5 is responsible for the period

of positive DC bias in the OS signal (fig. 4.19), and shows the inverse displacement and polarity to the SS case.

As mentioned above, this asymmetric waveform is due to the asymmetric Lamb wave modes that arrive at this time. Finally, the slowest symmetric Lamb wave modes will arrive at approximately 70 μs, travelling at a velocity close to the Rayleigh wave velocity of 2976 ms^{-1}. Both fig. 4.18 and 4.20 show the plate having asymmetric deformation, however, during the region marked 4-5. This is related to the large asymmetry of the input force. But, compared to the asymmetry at point 2, in which the top surface and bottom surface are in opposite strain (tension or compression), the region 4-5 shows the top and bottom surfaces of the plate undergoing the same strain. This suggests that the symmetric mode is superimposed on a more powerful, asymmetric mode.

Taking the dominant frequency of the transducer resonance of 147 kHz, which is within the 250 kHz frequency limit in the FE mesh of the steel plate (using the highest spatial resolution requirements), there are several Lamb wave modes that will propagate in the plate. These are the symmetric L_{12} mode, asymmetric L_{21} and L_{22} modes and, finally, the symmetric L_{11} mode (in order of velocity, see appendix VI). There are several types of asymmetric mode, and these will be more strongly excited, due to the asymmetry of the source. This means they will have a comparatively large amplitude. This is confirmed by the increase in output voltage, in both the SS and OS signals, with the arrival of asymmetric wave components, and the delay in establishing the late-time symmetric oscillations, which clearly show a degree of asymmetric influence (region 4-5 in fig. 4.18 and 4.20).

The results presented in this section have indicated that a narrowband resonant transducer can reproduce transient deformation of the surface on which a source is located, and this is evident in the detail of the waveform produced.

4.3.2 Comparison of Transducer Waveforms for a Step Force on the Same Surface and Opposite Surface for a Propagation Distance of 10 cm

The previous section considered signals produced when the source was located on opposite surfaces of the plate. Around the arrival time of the asymmetric Lamb wave modes, the two signals showed opposite polarity, clearly indicating the fact that they were produced by opposite forces. This section will consider the same situation at a source-transducer distance of 10 cm.

The signals will, again, be referred to as SS and OS, to identify the output voltage produced when the source is on the same surface as the transducer and opposite surface to the transducer, respectively. Fig. 4.21 shows the transducer voltage waveforms for this case.

The output voltage starts at the same time, for both the SS and OS signals, and corresponds to the arrival time of the bulk longitudinal wave.

The fastest Lamb waves will be travelling at this speed. The time for this wave to travel the 10 cm distance, at 6006 ms^{-1}, is 16.65 μs, which is confirmed by the FE model output. The two signals quickly show differences, with the OS output voltage having a larger amplitude than the SS signal between 25 and 30 μs. The fastest Lamb wave mode at 147 kHz (the radial mode) is symmetrical and is the cause of the initial similarity in the two signals. The 147 kHz mode is the main transducer resonant frequency and this frequency will be dominant in the transducer's response. At 147 kHz, the L_{12} mode would arrive at the transducer close to 20 μs. This is when the OS output voltage becomes noticeably larger than the SS output voltage, which could indicate this mode is stronger for the OS model.

Fig. 4.22a shows the deformation in the plate at 10 μs, caused by the source on the opposite surface as the transducer. The calculated P-wave front is followed by the fastest Lamb wave mode, which causes only a small displacement at the plate surface, marked 'L'.

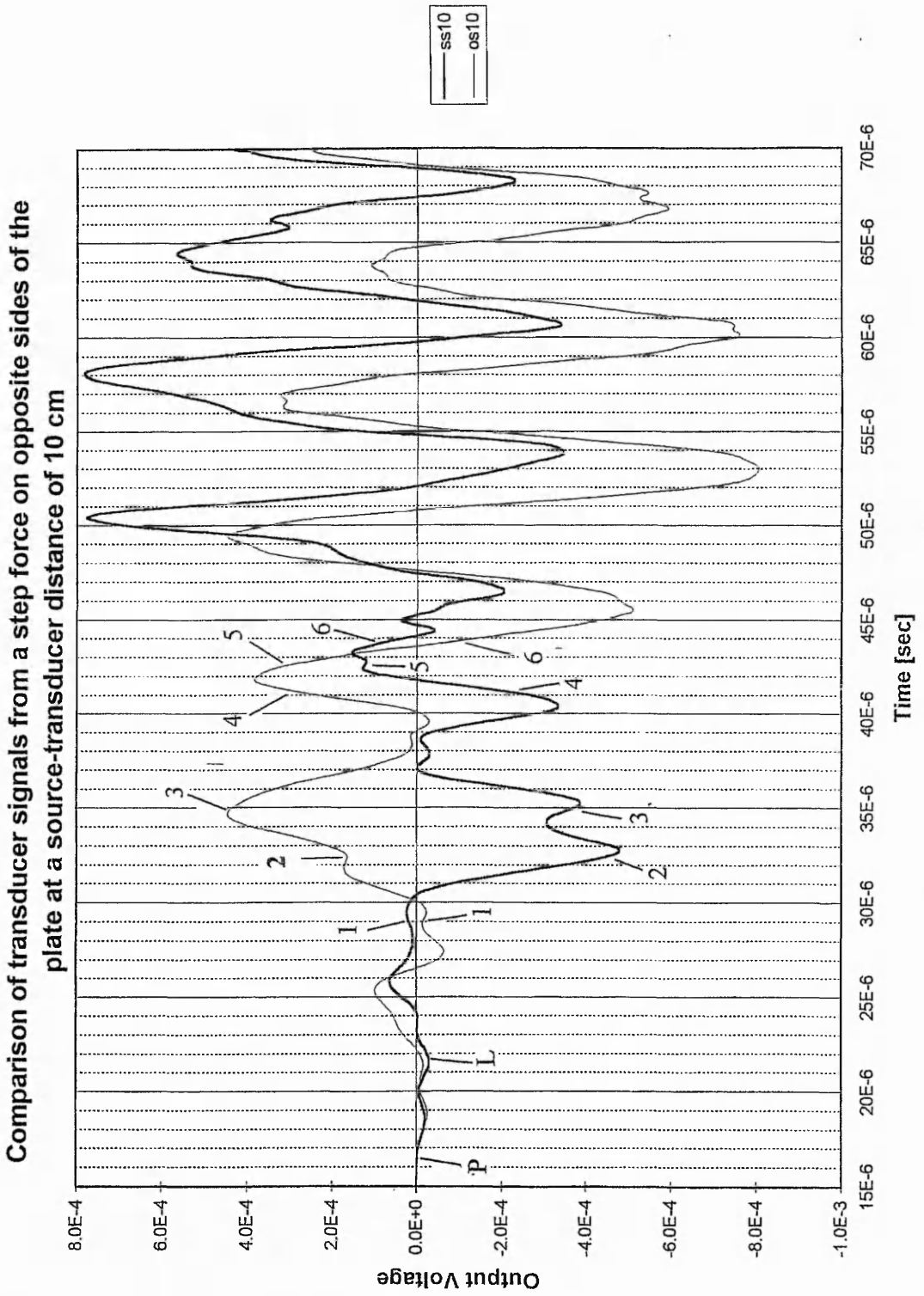

Fig. 4.21 Comparison of transducer signals, for a step force on the same surface (SS), and opposite surface (OS), of the plate, at a source-transducer distance of 10 cm.

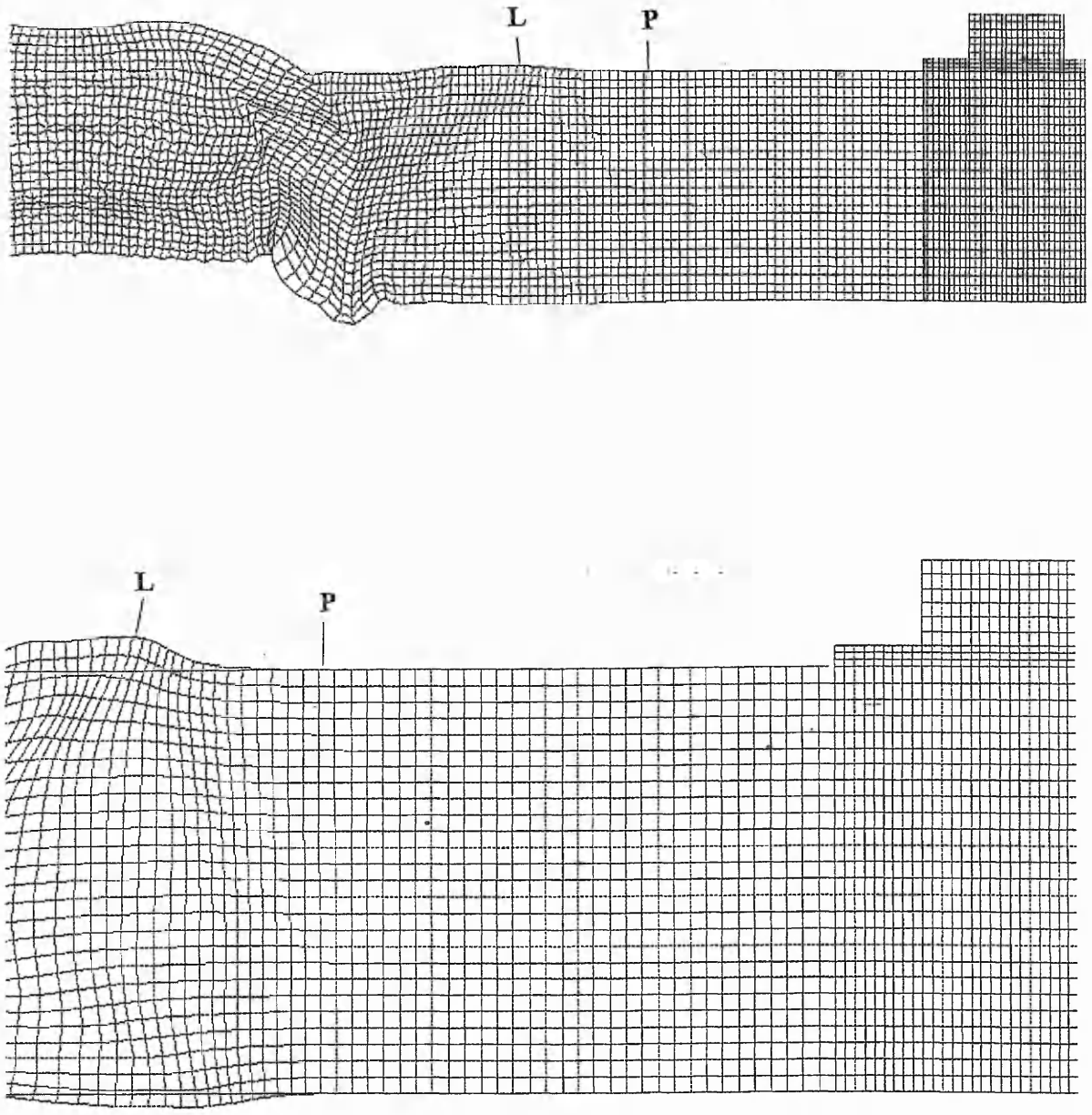

Fig. 4.22a (top) & Fig. 4.22b (magnified)

Deformed plate at 10 μs. The points marked 'P' show the P-wave front, while points marked 'L' show the fastest symmetric Lamb wave mode. The source is a step force on the opposite surface of the plate, at a source-transducer distance of 10 cm.

Large deformation is due to the asymmetric modes that follow later, as was the case in section 4.3.1. A magnified view, of the front end of the acoustic wave (fig. 4.22b), shows the first Lamb wave mode, which is symmetric about the plate length (i.e. the axis parallel to the undisplaced plate surfaces).

This was also the case with the source at 20 cm from the transducer (fig. 4.13b), but at 10 cm this symmetry has not been fully established. The point marked 'L' in fig. 4.22b highlights this slight asymmetry, which is the reason why the two transducer signals separate when this wave arrives (fig. 4.21).

With the source located on the same surface as the transducer, the inverse plate deformation to that seen in fig. 4.22 occurs.

Due to the closer distance between the source and transducer, it appears that the Lamb wave modes do not have time to form properly and, probably due to the asymmetry of the source, the first symmetric mode has a slight asymmetric appearance, represented by the early separation in the signals at the point marked 'L' in fig. 4.21.

The feature of most interest, seen in the comparison of the step force signals produced at 20 cm, in section 4.3.1, is the opposite polarity around the arrival time of the asymmetric Lamb wave modes at 30 to 40 μs (fig. 4.21). In the previous section (4.3.1), the SS signal was positive and the OS signal was negative. The opposite is true for a propagation distance of 10 cm. Taking the frequency of 147 kHz as the primary frequency of interest, there are two asymmetric Lamb wave modes that would be arriving at the transducer between 31 and 33 μs. These are the L_{21} mode and the L_{22} mode. Due to the asymmetric source excitation, these are likely to be strongly excited and, therefore, produce the large output voltages seen around the time of their arrival at the transducer (fig. 4.21).

The wave propagation in the plate was studied at 25 μs, just prior to the large increase in the signal amplitude at 30 μs, to see if the Lamb wave modes could be identified.

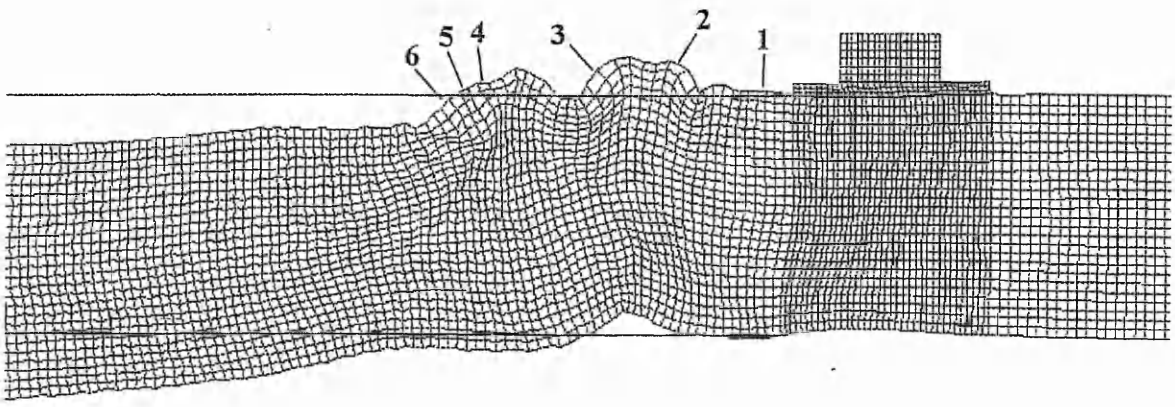

Fig. 4.23 Deformed plate after 25 μs, for a step force on the same surface of the plate, at a source-transducer distance of 10 cm. Reference points are marked 1-6 on waves the plate surfaces. Their calculated arrival times, at the centre of the transducer face, are marked on the transducer signal in fig. 4.21.

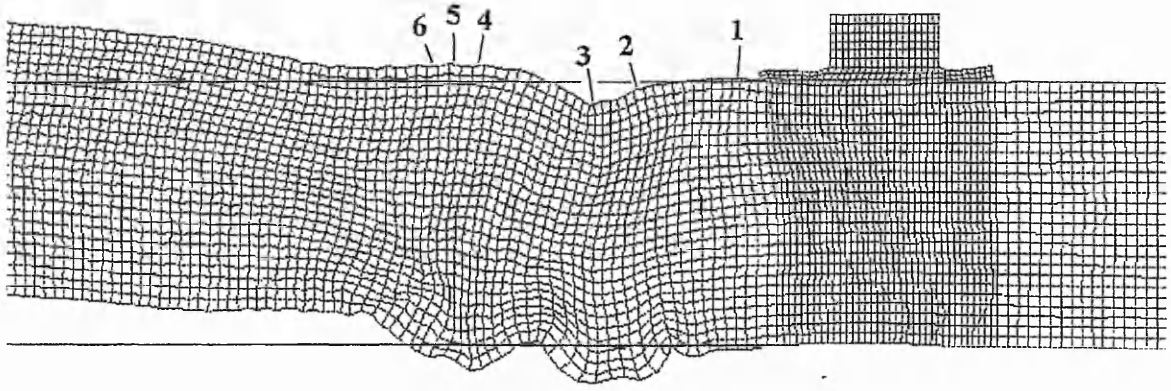

Fig. 4.24 Deformed plate after 25 μs, for a step force on the opposite surface of the plate, at a source-transducer distance of 10 cm. Reference points are marked 1-6 on waves the plate surfaces. Their calculated arrival times, at the centre of the transducer face, are marked on the transducer signal in fig. 4.21.

Points were marked on waves, on the plate surfaces in fig. 4.23 and 4.24. The arrival of these waves, at the centre of the transducer face, was calculated and also indicated in fig. 4.21.

Fig. 4.23 shows the deformation of the plate at a time of 25 μs, when the source is located on the same surface as the transducer. The plate to the right hand side of the transducer is relatively undeformed, although the P-wave has passed under the transducer at this time. At the point marked '1', the deformation about the plate centre is almost symmetrical. This produces very similar amplitudes of output voltage in both signals shown in fig. 4.21. Point 2 (fig. 4.23) shows asymmetric deformation, and this is reflected in the output voltage of the two signals at this point. Fig. 4.24 shows the source on the opposite surface produces the inverse deformation. The different deformation on the plate surfaces, around point 3, results in the different shape signals in fig. 4.21.

Between points 3 and 4, the displacement of the plate surfaces, from their original position, is almost zero at one point. This is represented in the output voltage signals, when both the SS and OS signals produce low amplitudes, around 38 μs. Points 4, 5 and 6 highlight the fact that the transducer waveform responds to very small variations, in the surface displacement.

After point 6, fig. 4.23 and 4.24 show large deformation, low frequency flexure in the plate. This creates the opposite DC offsets, observed in both the SS and OS signals (fig. 4.21).

It appears that the closer source-transducer distance results in more powerful excitation of the asymmetric Lamb wave modes, indicated by the different shapes seen in the output voltage signals between 29 and 39 μs.

However, with the arrival of the symmetrical deformation, around point 4, the two signals move into phase almost immediately, unlike at 20 cm when the two signals remained out of phase for some time. This in-phase oscillation, seen after 40 μs,

indicates the symmetric Lamb wave modes have arrived. Again, the period of these large oscillations is about 7 μs, which would indicate a transducer resonant frequency near to 147 kHz. The slowest Lamb wave mode at this frequency is the L_{11} mode, which is symmetric, and arrives at about 38 μs, which is when the opposite polarity phase ends and, hence, the asymmetric excitation. Although both signals produce positive and negative oscillations at later time, both signals still show opposite DC bias.

This data has again shown the ability of the FE modelling to predict the transducer response to complex Lamb wave mode excitation. This leads to the possibility of source characterisation (on one surface or the other), by means of the polarity, and waveform information, caused by the asymmetric excitation. Clearly the resonant transducer signal carries more information than is apparent at first sight, or generally assumed.

4.3.3 Comparison of Transducer Waveforms for a Step Force on the Same Surface and Opposite Surface for a Propagation Distance of 5 cm

To help provide further confirmation of the results of the modelling, for the case of the surface excitation by a step force, one more source-transducer distance will be considered, using the FE model of the plate and transducer. A step force is considered (fig. 4.3) at a distance of 5 cm in this case, on the same and opposite surfaces of the plate.

Due to the short distance between the source and the transducer, this might be considered as being close to, or within, the near-field and the plate thickness plays a more direct role in the formation of the waveform. For instance, the percentage difference in distance that the wave has to travel, with the source on the same and opposite surface, results (fig. 4.25) in a wave arrival time difference of nearly 1 μs later. Instead of a 5 cm path on the same surface, the wave in the OS model has to travel 5.59 cm. Also, the greater normal component of the P-wave, from the opposite surface, might be expected to cause a larger initial output voltage.

The two signals almost immediately go into a large amplitude oscillation, but just before this there is a period of opposite polarity, between 15 and 20 μs. This opposite polarity was seen for source-transducer distances of 10 and 20 cm. As at 10 cm, the SS signal has a negative output voltage, while the OS signal has a positive output voltage.

Immediately following the P-wave, the fastest symmetric Lamb wave mode will occur (L_{12} at 147 kHz). At 10 cm, there was a degree of asymmetry present (fig. 4.22b), which caused the output voltage signals to separate. At 5 cm, there is even less time for this L_{12} Lamb wave mode to establish itself and, therefore, the two signals separate immediately (see 10 μs in fig. 4.25).

As seen already in previous sections, the L_{21} and the L_{22} asymmetric Lamb wave modes are responsible for the signal shape and, in this case, are due to arrive between 15 and 16.5 μs (using the velocities for a 147 kHz frequency, appendix VI).

Again, the late time oscillations have a peak-to-peak time period of approximately 7 μs, showing more of a pure tone than the SS signal (as was the case for 10, and 20 cm, source-transducer distances). This time period corresponds to a frequency close to the 147 kHz transducer resonance. At this frequency, the last Lamb wave mode to arrive at the transducer is the L_{11} symmetric mode.

The transient elastic pulse was studied for the OS case only (fig. 4.26), as other sections in this chapter have shown the SS waveform to be the exact inverse.

Points of interest were marked on the plate surface in fig. 4.26, with their corresponding arrival times marked on the transducer output voltage signals (fig. 4.25). Rather than the two large rounded displacements on the opposite surface, seen at 10 cm in fig. 4.24, only one such displacement can be seen opposite point 3 in the deformed plate at 5 cm (fig. 4.26). This is why the voltage peak is more uniform in the OS output voltage signal, during the period of opposite polarity, than at 10 or 20 cm.

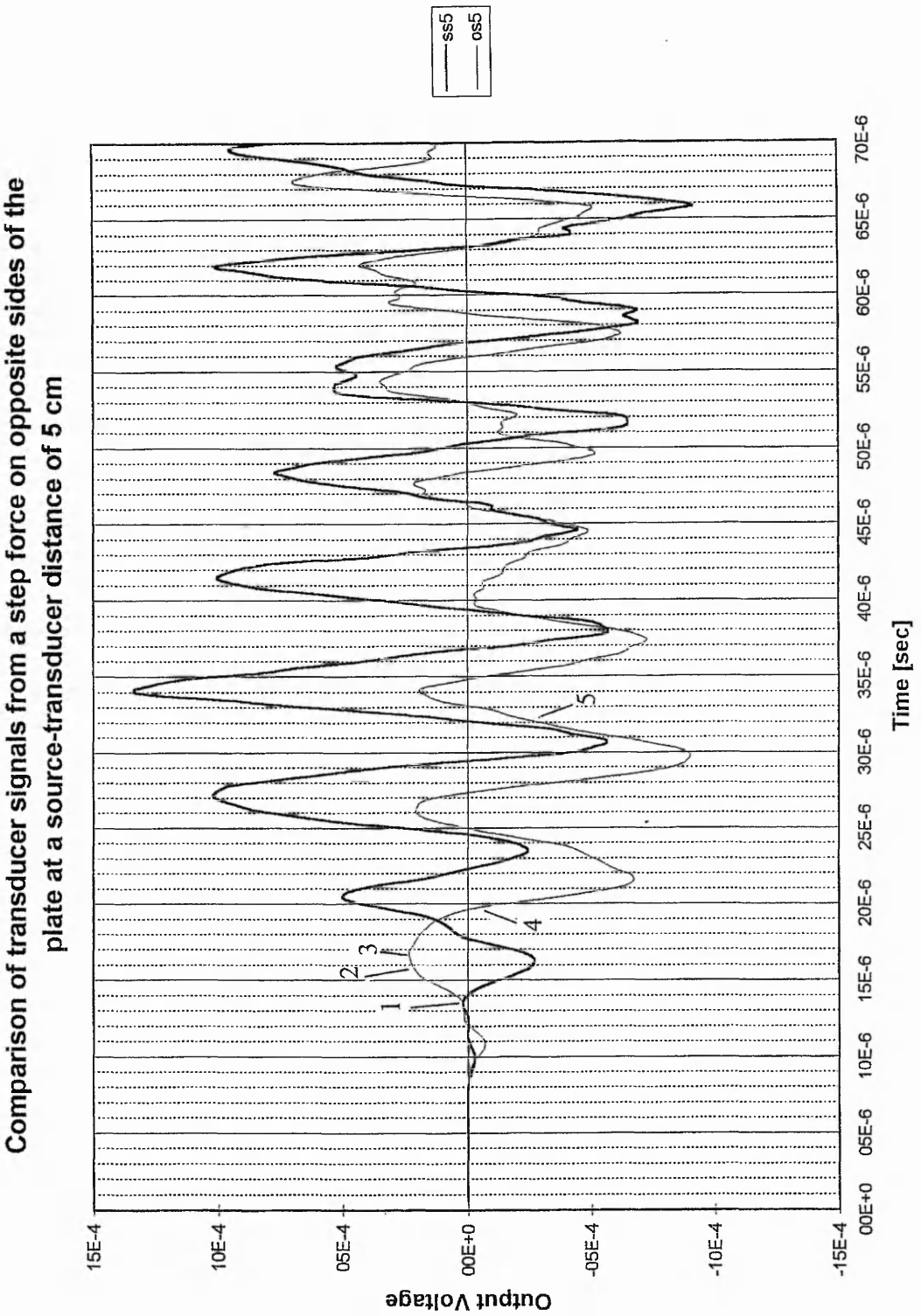

Fig. 4.25 Comparison of transducer signals for a step force on the same surface (SS), and opposite surface (OS), of the plate, at a source-transducer distance of 5 cm.

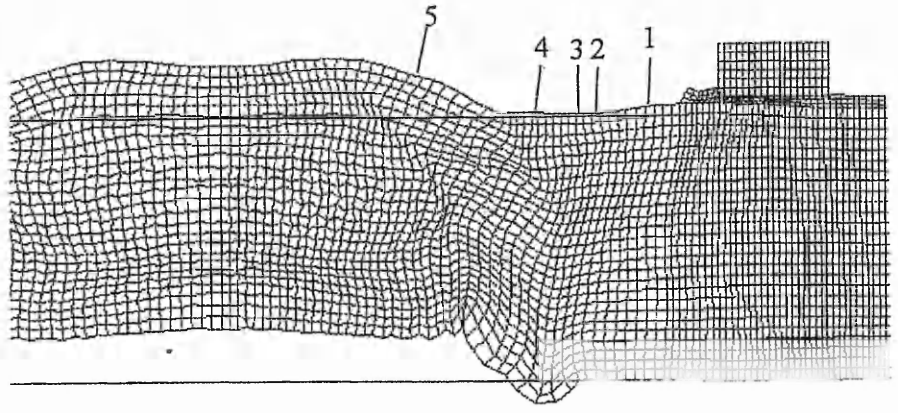

Fig. 4.26 Deformed plate after 10 μs, for a step force on the opposite surface of the plate, at a source-transducer distance of 5 cm. Reference points are marked 1-5 on waves the plate surfaces. Their calculated arrival times, at the centre of the transducer face, are marked on the transducer signal in fig. 4.25.

Between points 3 and 4 on the opposite surface (fig. 4.26), there is a small minimum in the surface displacement. This indicates that the single large wave pulse will separate into the two pulses seen at 10 cm in fig. 4.24. The dispersive nature of the asymmetric (flexural) Lamb wave modes is such that the separation between different frequency components can be seen even over such a small propagation distance.

The L_{11} symmetric Lamb wave mode is due to arrive at about 19 μs, based on a frequency of 147 kHz. At this time, the two signals show the same value of transducer output voltage (fig. 4.25). After this time, both transducer signals develop a DC offset due to the plate deformation between points 4 and 5, in fig. 4.25 and 4.26. This offset gradually reduces at late time.

The FE mesh, in the plate thickness direction, can deal with slightly higher frequencies, than in the plate length direction. This could be the reason for the less uniform vibration in the OS signal, because some higher frequency components are being transmitted in the OS models, at all distances.

The models at 5 cm have shown that the symmetric Lamb wave modes are undetectable in the transducer waveform, due to the large asymmetric disturbance. At greater distances, these modes have time to form properly, as seen at 20 cm.

4.3.4 Comparison of Signals on the Opposite Surface at a Variety of Distances to consider the Effect of Source Distance using a Single Transducer

Sections 4.3.1 to 4.3.3 have considered the comparison of signals from sources on opposite surfaces of the plate, at distances of 5, 10, and 20 cm from the transducer. These revealed that the polarity of the signal at appropriate times could be used to distinguish sources on opposite surfaces, even though the source was the same. It must be stressed that this work involves modelling of the wave propagation and identifies features in the modelled transducer waveforms which provide potential for source identification from resonant transducer signals. Practical application of these principles has still to be demonstrated. For the cases studied, the polarity of the signal during the

arrival of asymmetric Lamb wave components, from a source on one side of the plate, was different at 20 cm, than at 5 and 10 cm. For this reason, some other propagation distances were modelled to gain further information, but for a source on one side only, since a source on the opposite side will produce a response to the bottom surface deformation, which has been clearly demonstrated.

Source-transducer distances of 2, 5, 10, 15, 18, and 20 cm were modelled, with the step force on the opposite surface of the plate to the transducer. Fig. 4.27 shows the OS2 and OS5 signals represent the 2, and 5 cm distances, respectively. Fig. 4.28 shows the OS10 and OS15 signals, while fig. 4.29 displays the OS10 and OS18 signals, the waveform codes representing the respective source-transducer distances. Note that the time axes do not always start at zero to aid presentation of the waveforms.

The reason for the structure of the waveforms, at 5, 10, and 20 cm, has already been discussed in detail, in previous sections, in terms of Lamb wave mode arrivals. The analysis used in this section will address general differences between signals, using the ideas previously discussed.

At 5 cm, it was commented that the round peak, in the 15 μs time region, was due to the fact that the asymmetric Lamb wave modes all arrive in close proximity to one another. At 2 cm, this extended period of single polarity output voltage is such that the first 20 μs of the OS2 signal are negative (fig. 4.27). This is longer than at any other distance, and is again due to the arrival of several mode types, within 5 μs of the initial P-wave arrival at 5.3 μs. At this 2 cm source-transducer distance, fig. 4.27 shows that an output voltage has already been produced, caused by the P-wave arriving at the edge of the transducer nearest to the source. Also, at this close distance, the plate thickness is greater than the horizontal distance (2.5 cm compared with 2 cm), and so plays an important part in the arrival time. A wave produced by a source on the same side at the same lateral distance, would be seen to arrive much earlier because of this. In practical work, the wave transit time would probably be unknown.

The phase difference, for the latter part of the signals, is related to the distance between the two sources, suggesting the transducer is subject to slightly different modal excitation. In the OS2 signal, there are some higher frequency components, up to approximately 500 kHz in frequency (indicated by the oscillation period of 2 μs at some points in the waveform in fig. 4.27). This again shows that the FE mesh used can cope with frequencies higher than 250 kHz used to initially calculate the required spatial resolution. If a resolution of 10 nodes per wavelength is suitable, as suggested by some authors [**61**] and not 20, as used in this study, then the mesh is capable of accurately modelling frequencies of 500 kHz.

Secondly, when receiving a signal from the epicentre (section 4.2), the FE signals do contain higher frequency components at short propagation distances, indicating the spatial resolution used does allow higher frequency representation over a short distance. Longer wave propagation distances and dispersion effects probably result in the loss of these higher frequency components, due to the lower mesh density, which is demonstrated by the lack of high frequency content in the OS5, OS10, etc., signals.

The two important observations about the OS2 and the OS5 signals, are the fact that the polarity of the signals, during the period of the asymmetric Lamb wave arrivals, is opposite and, a higher frequency content is apparent in the OS2 signal during the period of steady oscillation. The OS2 signal has the same, negative polarity, as the OS20 signal. At 5, 10, and 15 cm, the polarity is positive during the same time period (fig. 4.27 & 4.28), which is when the asymmetric modes arrive. The DC bias is less obvious at 2 and 15 cm.

The late time oscillations in fig. 4.27 and 4.28 indicate the arrival of the L_{11} symmetric Lamb wave mode, discussed in previous sections, with the transducer oscillations having a period of about 7 μs. Neither signal in fig. 4.28 has the high frequency content of the OS2 signal.

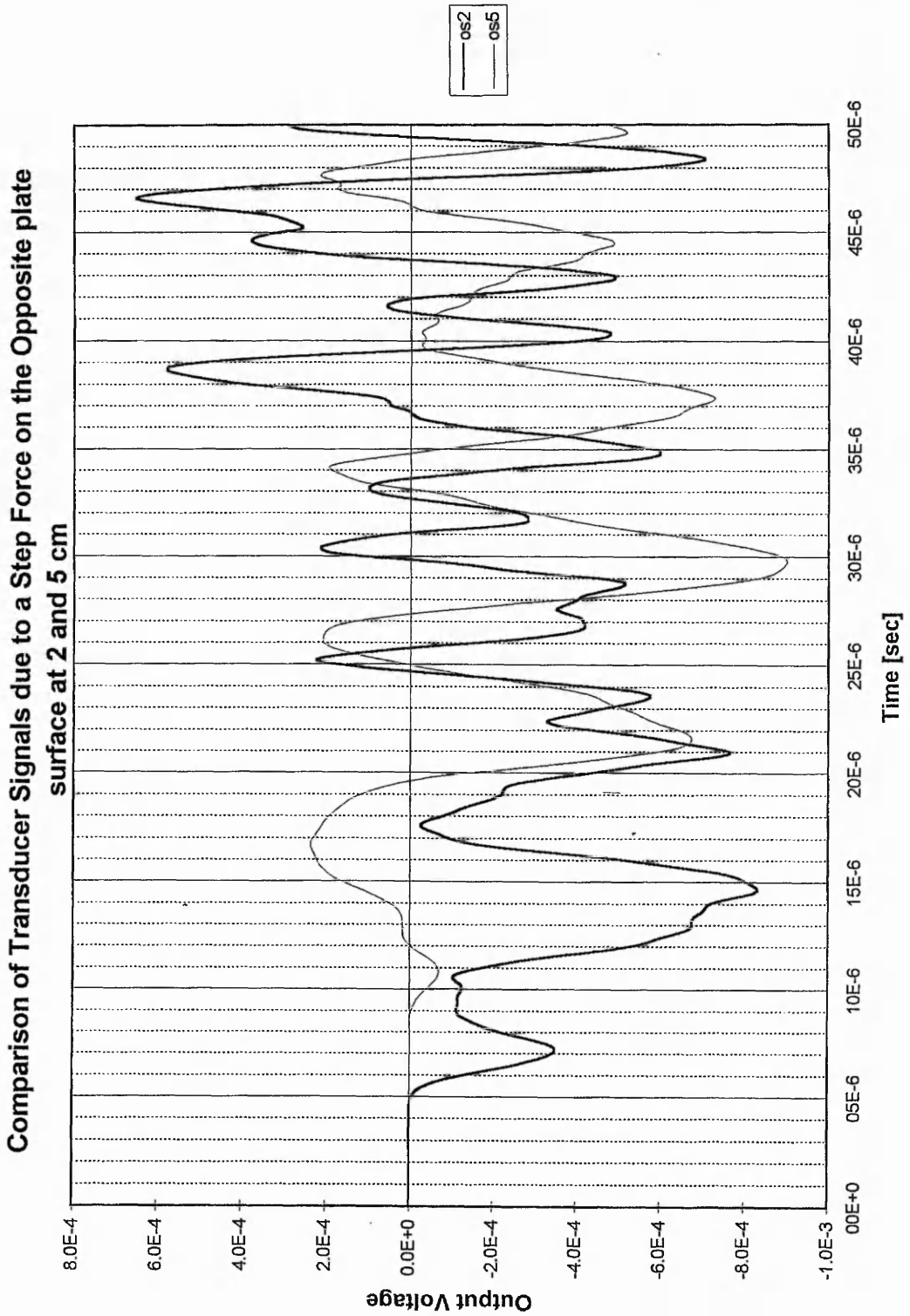

Fig. 4.27 Comparison of transducer signals from the opposite surface, for a step force, at source-transducer distances of 2 and 5 cm.

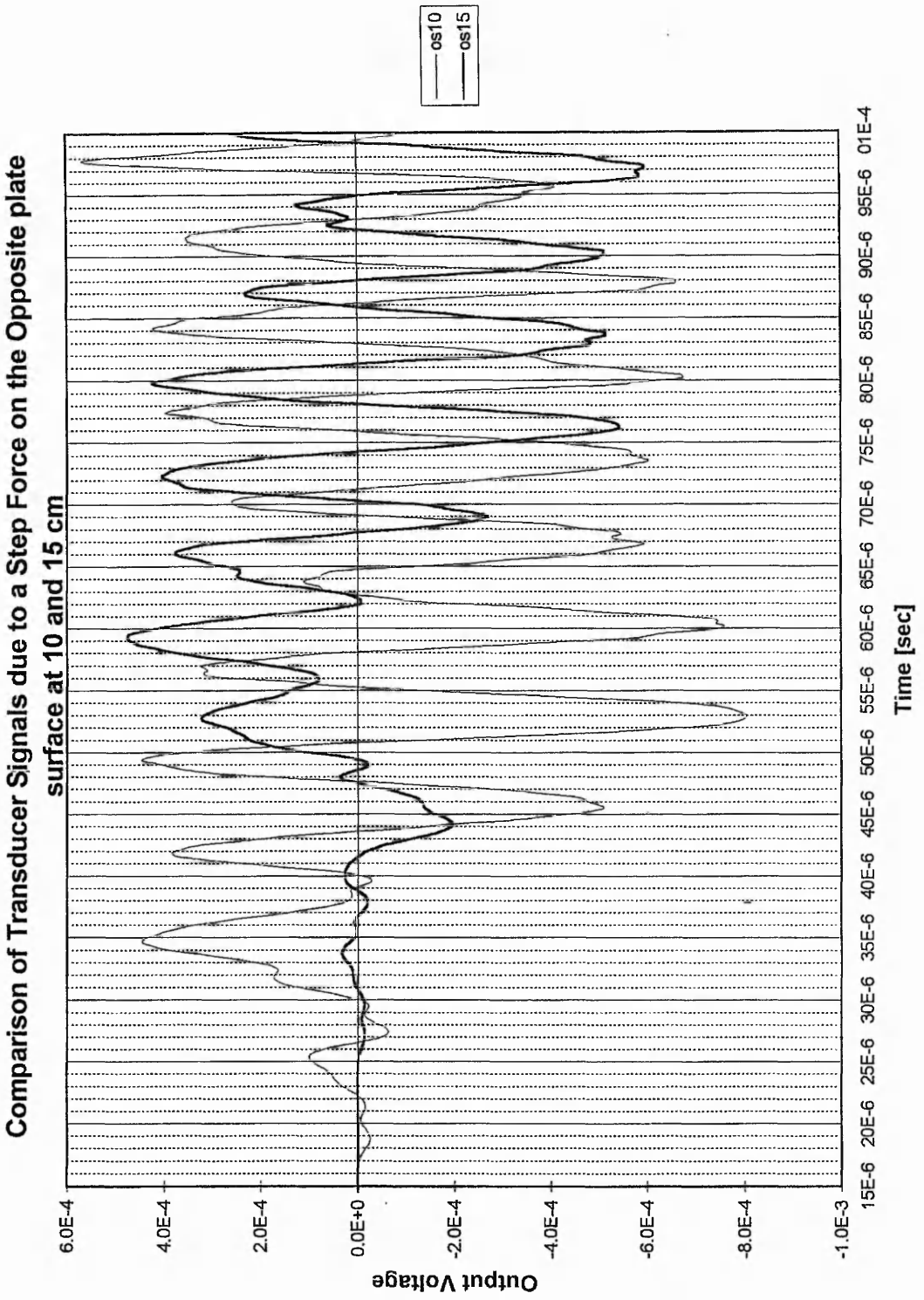

Fig. 4.28 Comparison of transducer signals from the opposite surface, for a step force, at source-transducer distances of 10 and 15 cm.

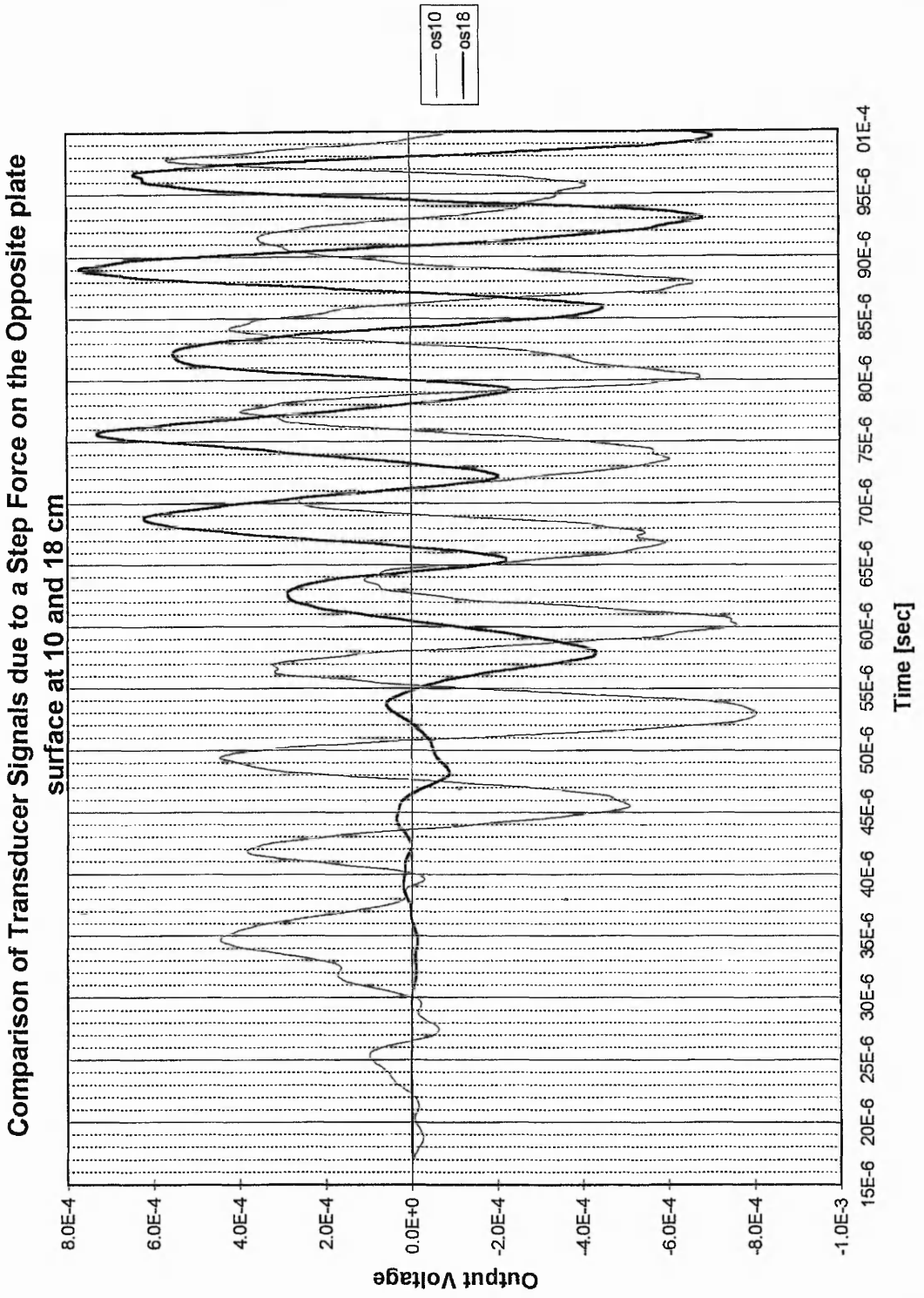

Fig. 4.29 Comparison of transducer signals from the opposite surface, for a step force, at source-transducer distances of 10 and 18 cm.

It has been shown that the shape of the output voltage waveforms is mainly due to a combination of asymmetric Lamb wave modes arriving at the transducer. The arrival of the asymmetric Lamb wave modes was the reason for the different polarity, when the source was located on opposite surfaces of the plate to the transducer. These modes are, therefore, likely to be the reason for the change in polarity with distance (between 2 and 5 cm for example). The group velocity of each Lamb wave mode varies with the frequency at a constant plate thickness. A broadband AE event consists of multiple frequencies and, therefore, excites multiple velocity components of each Lamb wave mode. Arrival times of some of the modes have been calculated, using the group velocities, at the transducer resonant frequency of 147 and the highest resolution frequency limit of 250 kHz (appendix VI).

The deformation on the opposite surface, at 20 cm, 10 cm, and 5 cm, was seen in fig. 4.20, 4.24 and 4.26 respectively. At 5 cm, there is one large wave pulse (around point 3), consisting of all the Lamb wave modes. At 10 cm, two large wave pulses can be seen (around point 3), and at 20 cm, there are several, smaller wave pulses. This indicates the dispersive nature of Lamb wave modes and, therefore, the reason for the significant variation in the shape of the signals' front end. The plate deformation figures have also shown that symmetric, and asymmetric, deformation occurs throughout the excitation period. This is why there are variations in the waveforms at late time, when the mode of vibration is theoretically supposed to be symmetrical, because the symmetrical mode is the slowest to arrive.

Using the waveforms alone to identify the source in a practical situation presents some problems. Detecting the front end of the signal accurately is sometimes difficult in noisy systems, although a resonant device has an inherently good signal-to-noise ratio. Variation of source strength for a real test situation prevents direct comparison of signal amplitudes, which attenuate. Sources in close proximity would give very similar waveforms and would make rapid identification of differences in the signal features difficult. A first stage analysis must provide accurate signal characterisation quickly, to give the analyst advantages. The detailed analysis of the waveforms discussed in this

section is not a very fast method of gaining source information and is recommended as a secondary method of signal analysis.

Analysis of the transducer waveforms might also be carried out when the location of the source is known. The features in the waveform can then be used to gain information about the exact propagation of an AE source. Polarity at the arrival time of the asymmetric Lamb wave modes, along with the DC offset, can be used to indicate which surface the source is on, or very close to and, if source propagation (cracking) is occurring. It must be observed that because the sources in the models considered are acting in opposite directions, simulating the same load condition at each surface, the inverse polarity effect would also be observed if opposite forces were acting on one surface. In practice, this is unlikely to cause a problem because the source orientation is going to be constant, once a crack plane has developed in a material and, therefore, the source orientation will be fixed. With the source orientation fixed, the polarity of the transducer signal during the arrival of the asymmetric Lamb wave modes will then indicate the surface at which the source is located.

4.3.5 Prediction of the Source-Transducer Distance using the Signal Energy

Acoustic emission monitoring often provides a large quantity of data and, therefore, detailed analyses, used in previous sections, would only be appropriate for selected larger amplitude waveforms. The signal predicted from transducer models has been seen to vary in structure, with distance from the source. Parameters that quickly provide information about the source type, or source distance, are always going to be useful. Waveform detection and recording often occurs in time windows, controlled by a computer. When the transducer output voltage passes a specified threshold (to eliminate noise), then a computer records the transducer response over a fixed period of time, usually in the order of hundreds of microseconds.

Practical AE monitoring results in hundreds or thousands of waveforms that have to be sorted out to eliminate 'good' waveforms from 'bad' ones. Good waveforms, which lead to effective material characterisation, are those that are likely to be caused by the AE source of interest (e.g. a crack), while so called bad waveforms may be from other

known sources, such as grip slippage in experimental work or frictional effects on a real structure. Automating such sorting of waveforms is desirable and the following signal analysis is seen as one possible method of automating signal analysis. The previous analysis in section 4.3 has shown that small detail in the waveforms can give important information about the AE source. The FE models do not contain any system noise etc., while in practice, these small differences in the waveform features may be hard to identify, especially quickly. By studying the signal energy in a time window it is hoped that the subtle differences between the waveforms will be more obvious, leading to a possible rapid method of source monitoring or signal elimination.

This section will consider the signal energy in a time window, to see how it varies with the source-transducer distance for a fixed source energy. For voltage against time signals, the parameter $\Sigma V^2 dt$ is used as a proportional measure of the signal energy. V is the output voltage and dt is the sampling time, which in the transient FE models involving the plate, is 0.2 μs. The energy in each time interval will be summed to give the total energy in a time window, in this case 70 μs from the arrival of the P-wave. A 70 μs time window was used to avoid the inclusion of the end reflection from the plate edges. Inclusion of the reflection would complicate the analysis, but would be an area for future investigation.

In any practical use of AE, the magnitude of the AE source will vary. Here the data is normalised, to allow comparison of different event magnitudes, with the type of source being the same. This means that the relationship between the normalised signal energy and the source-transducer distance should be independent of the source strength, giving the parameter more practical use, because one of the AE variables has been eliminated. Fig. 4.30 illustrates the energy parameter $\Sigma V^2 dt$ in different time intervals, normalised to the total energy in a 70 μs time window (e.g. $\frac{\sum_{0}^{20} V^2 dt}{\sum_{0}^{70} V^2 dt}$), plotted against source-transducer distance in cm. A polynomial function (fifth order, exact fit) has been fitted to the points, to illustrate the complex relationship between the energy and the distance.

Time intervals of 0-10, 0-20, 0-30 μs, etc. were used to see how the energy arrival at the transducer was distributed in time.

Clearly, the total signal energy ($\Sigma V^2 dt$) increases with length of the time window. Graph (f) represents the energy distribution for the time interval 0-60 μs. It is clear that the percentage of the signal energy, arriving at the transducer for each 10 μs time increment, varies at each specific distance. The energy difference between time increments, at one distance, is greater at early time, for short distances, i.e. 2 and 5 cm, and greater at late time, for long distances, i.e. 15 and 18 cm. Distances of 10 and 20 cm appear to show more uniform energy increase between each time increment.

Taking the first propagation distance of 2 cm, the first two time intervals show large increases in the signal energy, with nearly 40% of the total energy arriving in the first 20 μs after the P-wave arrival time (curve b). This is because all of the Lamb wave modes arrive in this initial time period, which shows the largest increase in signal amplitude (fig. 4.27), and causes large amplitude oscillations in the output voltage. As time increases at this distance, the energy is increasingly dispersed, giving more equal energy increases between each time increment (b-c, c-d, etc.).

The 5 cm source-transducer distance shows the time between 10-20 μs having a large percentage increase (24%) in the signal energy. This is consistent with the knowledge that the asymmetric Lamb waves arrive during this time period, which is when the output voltage amplitude increases most dramatically (fig. 4.27). The largest increase in signal energy (29%) comes in the time interval 20-30 μs. This is when the symmetric Lamb wave modes are arriving at the transducer, combined with the flexural plate displacement, resulting in a DC bias to the output voltage as it goes into large amplitude oscillation. As at 2 cm, the increments in the transducer signal energy decrease with time.

At 10 cm, the increased time separation between the different Lamb wave modes, due to their different velocities, becomes apparent.

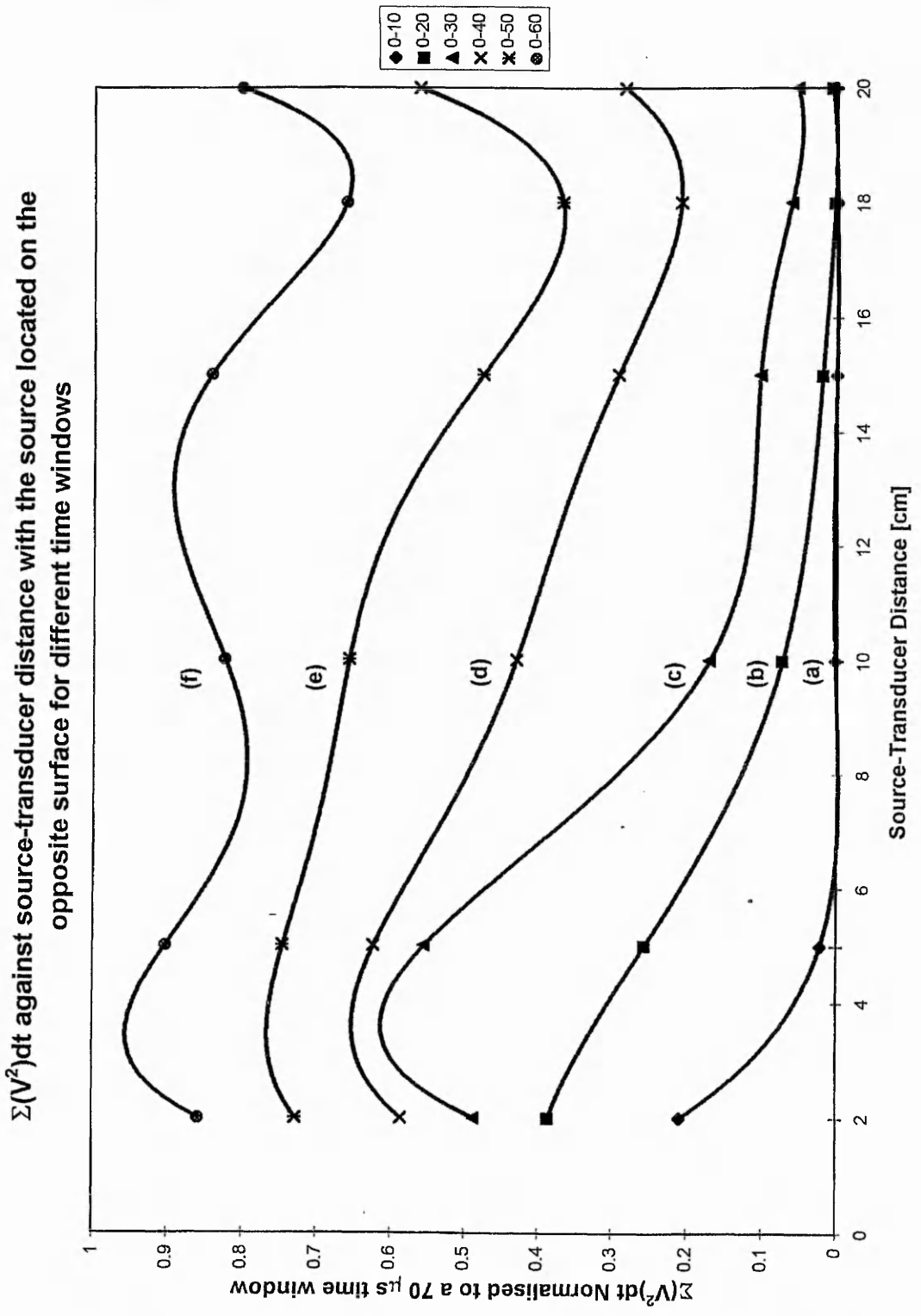

Fig. 4.30 Signal energy $\Sigma(V^2)dt$ against source-transducer distance, for a step force, on the opposite surface of the plate. The signal energy, in each time interval, is normalised to the signal energy in a 0-70 μs time window.

The first 30 μs, after the arrival of the longitudinal wave, shows a lower value of the signal energy (17% at curve c), when compared to that at 2 and 5 cm propagation distances (48% and 55%, curve c in fig. 4.30). It is the 30-40 μs interval that shows the largest increase (26%) in signal energy (curve c-d). This is when the large amplitude output voltage oscillations are reaching their maximum amplitudes, after the slower, symmetric Lamb wave modes have arrived at the transducer, and the transducer waveform DC offset is evident due to plate flexure. The 40-50 μs interval has a similar (22%), large increase in the signal energy, which is followed by a smaller increase in the final 50-60 μs window.

With a source-transducer distance of 15 cm, the time interval that has the largest increase in signal energy (37%) is the 50-60 μs interval. The next largest increase (19%) is in the 30-40 μs time interval. Between 30 and 40 μs after the P-wave arrives, the OS15 signal (fig. 4.28) has an extended period of positive output voltage, caused by the asymmetric Lamb wave modes. During the time period 50-60 μs after the P-wave arrival, the OS15 signal has large amplitude oscillations due to the transducer beginning to vibrate at its resonant frequency.

The signal energy at 18 cm shows uniform energy increase, with a large increase (29%) in the 50-60 μs interval. This is when the large amplitude transducer oscillation occurs. It is noticeable that the signal energy, in each time interval, is lower than at any other distance, including 20 cm.

At 20 cm, the signal energy in each time interval increases from that seen at 18 cm, after the 0-30 μs time interval. The three time intervals 30-40, 40-50, and 50-60 μs, show a similar increase in the signal energy, with the 40-50 μs interval being the largest (28%). At this time, the OS20 signal has settled into large amplitude oscillations. The next time interval contains larger amplitude peaks, but the DC offset is reducing, giving a smaller energy increment.

From this data some conclusions can be drawn. Early parts of the time window (e.g. 0-10 μs) indicate the percentage of energy at the front end of the waveform, which is large in signals from a source close to the transducer.

This normalised signal energy obeys the inverse square law as the source-transducer distance is increased (curve a). A large increase in energy between time intervals, indicates that large amplitude oscillations have been established, which is known to occur when the slowest symmetric Lamb wave modes arrive and the transducer vibrates at its main resonant frequency. Each curve in fig. 4.30 reaches a minimum at a distance of 18 cm. This feature caused by the energy dispersion would probably reoccur at other distances and could, therefore, be used to help locate the source.

The distribution of the signal energy is a possible way to gain some information on source distance. More accurate location might be gained from a detailed study of individual signals or by decreasing the time interval from 10 μs to 5 μs, for instance. Decreasing the time interval might help to identify the exact time interval in which the largest increases in normalised signal energy occur and, therefore, the times of the asymmetric mode arrival and the end of the transient (when free vibration starts) could be found. In practice, there are often large quantities of data associated with AE events, and this type of rapid location might provide a good estimate as to source position, without the need for more quantitative methods.

The normalised signal energy information is summarised in table 4.2, which shows the time interval with the largest energy increase. Table 4.2 shows that each distance has a unique time interval with the largest energy increment, which could provide an immediate indication of the source location to within 2 cm. Further indicators of the propagation distance are taken from the actual transducer signals that provide further detail. Modelling of shorter distance intervals (e.g. every 5 mm) and reduction of the time intervals would allow the method to predict the location more accurately and possibly exactly.

Practical difficulties could occur if the front end of the signal were lost because it did not pass the specified amplitude threshold. This would change the time interval in which the largest energy increase occurs thus changing the diagnosis. Improvements in the FE modelling might allow more detailed knowledge of the maximum signal amplitude to be gained, which could be combined with some form of experimental calibration method to avoid system noise, prior to the actual AE monitoring.

The FE model has no bandpass applied, other than the upper frequency limits imposed by the resolution of the model (over 500 kHz). It must be borne in mind that if a bandpass was imposed on a system in practice, then this would alter the energy distribution in the time window. The effect would be to remove the large signal energy arising from the low frequency DC offset and other low frequency signal components. Maximum signal energy may then shift to another time window as a result, e.g. to when the asymmetric Lamb waves arrive. It is recommended that bandpass restrictions should be incorporated into future FE models to predict the effect on the normalised signal energy distribution. Such modelling would help to choose suitable practical electronics.

	Source-Transducer Distance					
Signal feature	2 cm	5 cm	10 cm	15 cm	18 cm	20 cm
Interval with largest increase in normalised signal energy	0-10 μs	20-30 μs	30-40 μs	50-60 μs	60-70 μs	40-50 μs
Polarity during arrival of asymmetric modes	- ve	+ ve	+ ve	+ ve/- ve	- ve	- ve
Polarity of DC bias	none	- ve	- ve	- ve	+ ve	+ ve

Table 4.2 Summary of waveform indicators related to the source-transducer distance. The source is a step force on the opposite surface of the plate.

Resonant devices have the advantage that they are generally more sensitive than broadband designs and have a good signal-to-noise ratio. Increasing their bandwidth may reduce this advantage, but give more source information. This energy analysis method should be equally suitable for broadband transducers.

4.4 USE OF TRANSIENT EXPERIMENTAL TRANSDUCER WAVEFORMS TO ASSESS THE TRANSIENT FE MODELLING

4.4.1 Experimental Method used for Comparison and Validation

In Chapters Two and Three, models of the bi-laminar disc transducer, and brass exponential horn transducer were investigated respectively, both showing good agreement between FE and selected experimental data. Finite element methods have also proven their usefulness in many of the papers, reviewed in Chapter One. Transient analysis applied to acoustic wave propagation, is a more recent area for the use of finite element analysis, with other workers having studied aspects of modelling for this type of work (section 4.1). It was deemed appropriate that some experimental comparison between the transient FE models and experimental data should be used.

Fig. 4.31 shows the experimental system. The voltage source was a 50 Hz, 20 volts square wave produced by an HP 33120A arbitrary waveform generator, driving a 'pinducer' piezoelectric transducer. This type of sensor provides a simulated broadband source with a constant amplitude. The pinducer was held against a steel plate (1m x 1m x 25 mm) by a magnetic clamp (fig. 4.31). The transducer being tested was coupled to the plate with 'SoundClear' ultrasonic coupling gel. A square wave input to the pinducer would provide a close simulation of the step input used in the FE model.

The receiving transducer was the purpose built transducer used in Chapter Two, consisting of a PZT-5A disc mounted on "printed-circuit" board, in an aluminium case. The transducer signal passed through a 40 dB AECL 2100/PA preamplifier/filter module with a 115-550 kHz bandpass and a further AECL 20 dB amplifier.

A DAS-50 (A to D) board was used to collect the data, which was processed with Viewdac data acquisition software on a PC. The sample rate of the DAS-50 board was 1 MHz.

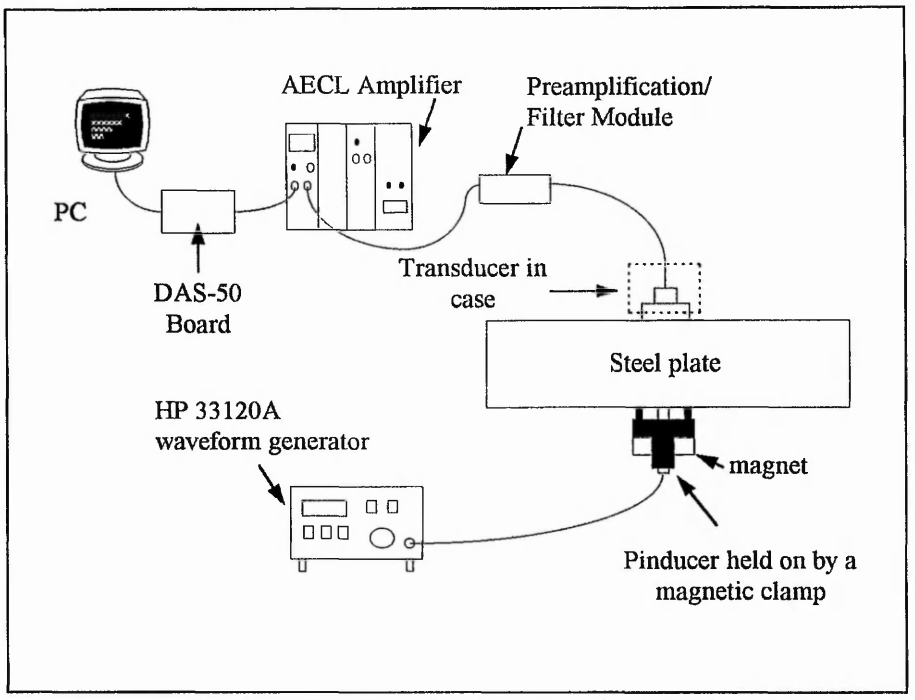

Fig. 4.31 Experimental arrangement for detecting the transducer response to a square wave input, via a pinducer. The pinducer is acting as an epicentre source, on the opposite surface of the plate.

The source pinducer was placed in the centre of the plate, and the receiving transducer was positioned at 5, 10 and 20 cm intervals, on the same side and on the opposite side of the plate. Twenty waveforms were recorded, each 400 μs in length. This process was repeated three times at each distance, giving a total of 60 waveforms. The waveforms were compared using Viewdac signal processing software. The responses were very consistent and so typical waveforms have been picked at random from the data sets, for more detailed analysis.

4.4.2 Comparison of FE and Experimental AE Signals due to a Source on the Opposite Side at Different Distances

Using the data obtained by the method described in section 4.4.1, a comparison was made between the experimental waveforms and the voltage-time signals predicted by the transient FEM. Four typical waveforms from the experimental data, at each distance, were imported into Microsoft Excel for comparison with the FE data. For the experimental data, it is difficult to identify the P-wave arrival, due to electronic noise and imprecise triggering. To overcome this problem the time axis for the experimental data was varied, so that the two signals could be matched up. The two closest matching experimental results are presented in fig. 4.32.

The first comparison was between data for the source and transducer located on the opposite side of the plate. Fig. 4.32 shows the comparison when the source-transducer distance is 20 cm, plotting normalised output voltage against time. The comparison between all of the signals is general and detailed features of the signals are not compared. The period of the square wave (0.02 s), used in the experiment, is long enough that the transducer will be responding to a single step up, or down in voltage, and not the square function seen in fig. 4.3.

Also, the 2D FE model has different transducer resonances to the real 3D transducer, while the GP-FE model only has a single input point at the transducer centre. Agreement is not expected, but comparison between the FE models and experiment should demonstrate that the front end of the signal varies with the propagation distance before the transducer settles into free vibration in its lowest radial mode. The GP-FE signal should, therefore, show agreement with experimental signals in the frequency of the resonant oscillations, but it will also have some higher frequency content not seen in the experiment. It should be noted that the FE models have no lower bandwidth limitations, below the upper cut off frequency associated with the mesh density.

Looking at the FE and experimental signals first (fig. 4.32), both FE and experimental waveforms produce their largest amplitude voltage peaks close to 65 μs. Then the

experimental signals show a decrease in amplitude. After 75 μs the FE signal has a DC bias, which is not apparent in the experimental signals due to the restricted bandwidth. The difference in amplitude between the maxima and minima in the FE signal suggest that the FE output voltage is decreasing as in the experimental signals, but this is obscured by the DC offset.

In Chapter Two, FEM predicted the bi-laminar disc transducer, used in the experiment, to have a resonant frequency of 176.5 kHz, due to a radial vibration mode. The 2D transducer, used in the transient FEM, has an equivalent radial mode shape at 147 kHz (fig. 4.48), and the period of the large amplitude oscillations suggests that the 2D and 3D transducers settle into their strongest resonant mode, once the transient Lamb wave modes have passed under the transducer.

The FE modelling and the experimental signal (OS5) were also compared with the source on the opposite surface, at a source-transducer distance of 5 cm. The same method was used, as described in section 4.4.1. Again, two typical waveforms were chosen, and are shown in fig. 4.33.

Looking at the overall shape of the two signals at 5 cm (fig. 4.33), the FE signal can be seen to follow the rapid increase in the output voltage amplitude in the experimental signals, between 10 and 25 μs.

Both the FE and experimental signals then settle into their respective resonant modes, which have frequencies of 147 and 176 kHz respectively. At 5 cm, early representation of the modelled waveform appears better, and does suggest that some increase in the electronic bandwidth, to detect the Lamb wave pulse (see for instance fig. 4.26), would be effective. The difference between the front end of the signals at 5 cm and 20 cm is clear when comparing both FE and experimental signals.

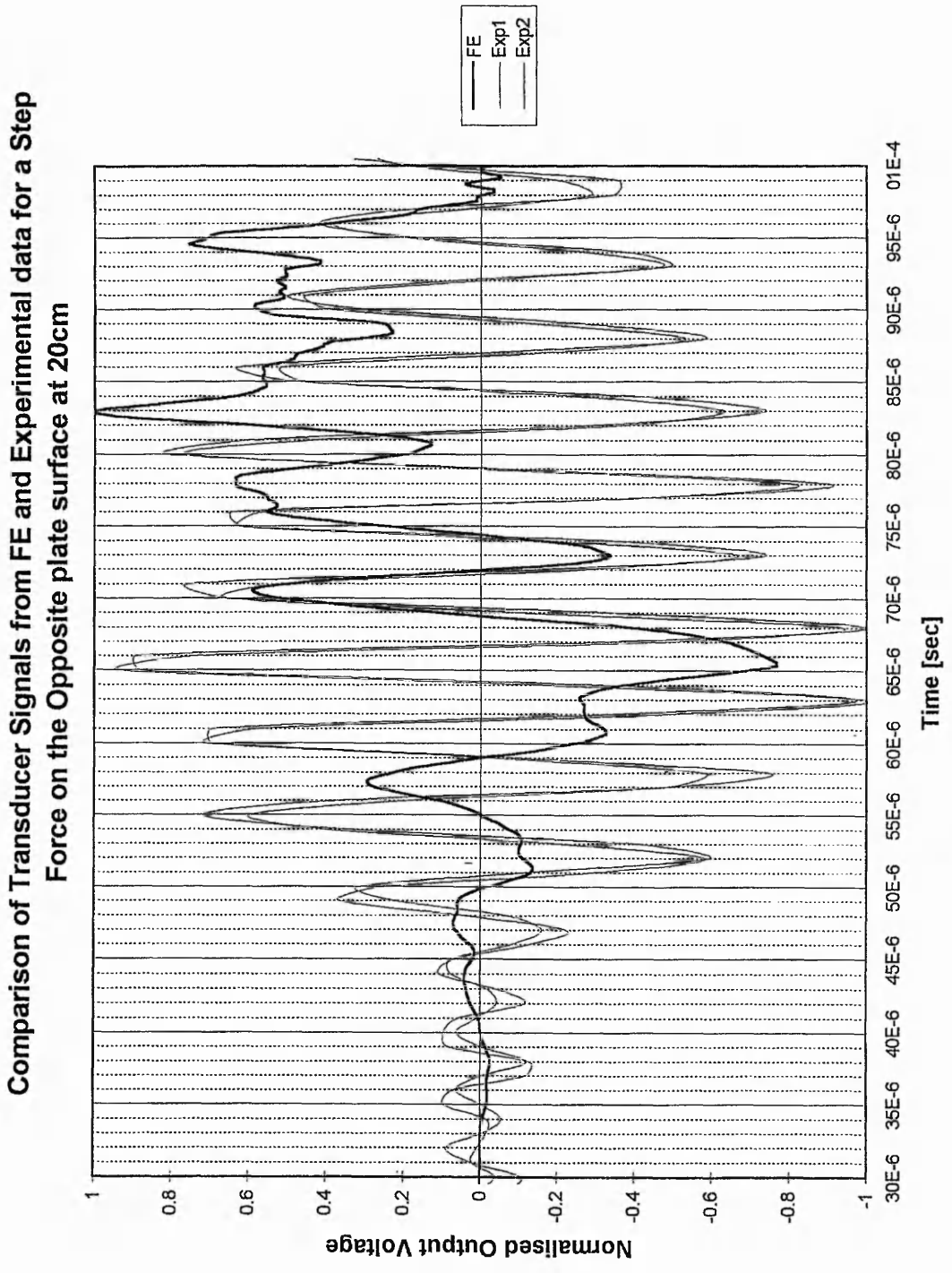

Fig. 4.32 Comparison of transducer signals from FE and experimental data, for a step force, on the opposite surface of the plate, at a source-transducer distance of 20 cm.

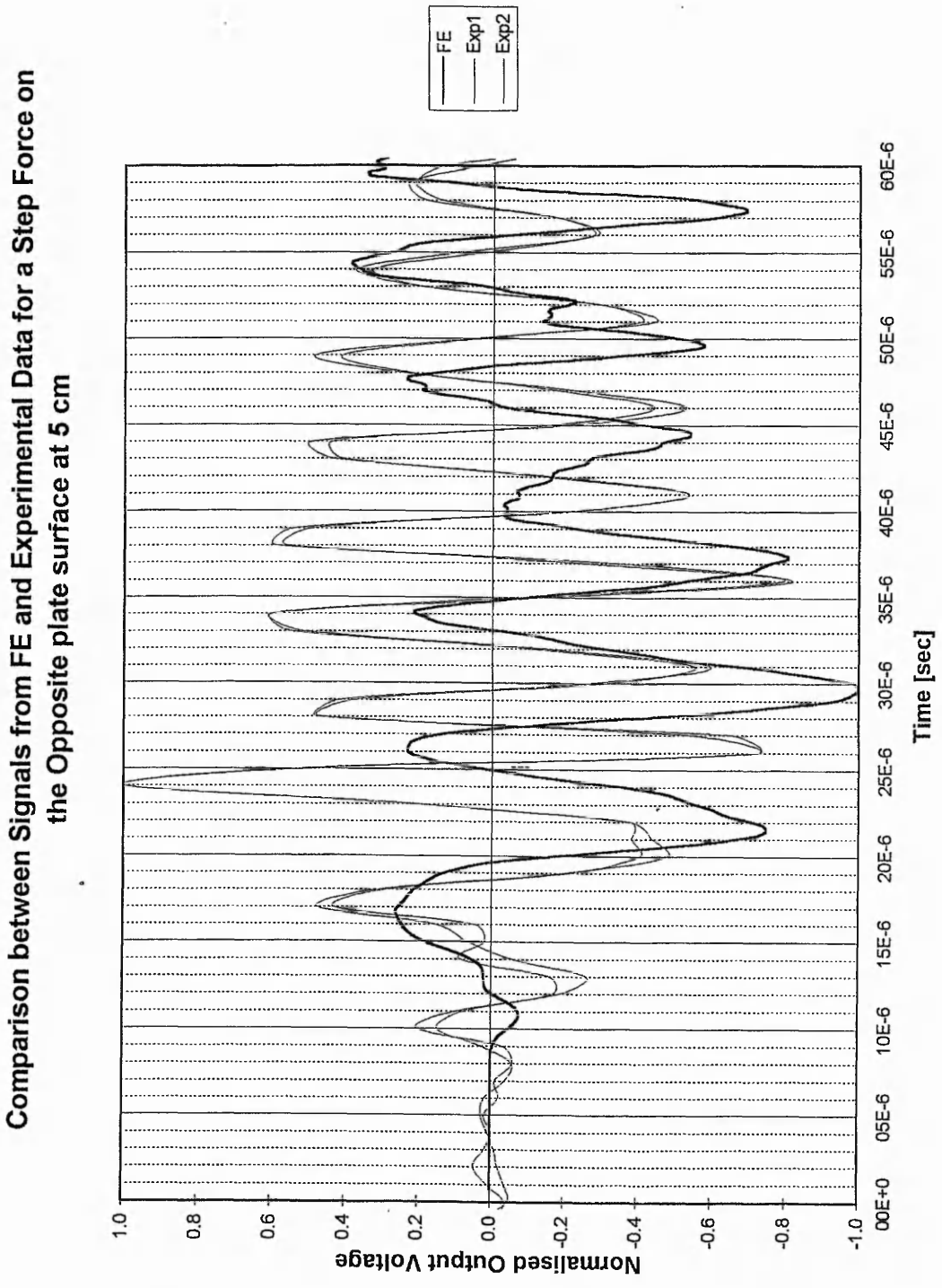

Fig. 4.33 Comparison of transducer signals from FE and experimental data, for a step force, on the opposite surface of the plate, at a source-transducer distance of 5 cm.

These results do show some similarities between experimental waveforms and those predicted by FEM, involving the plate and transducer. The aim to demonstrate that the signal front end contains information about the source location has been demonstrated, along with the fact that the resonant device then settles into its main resonant frequency. To be able to compare the FE and experimental signals in detail, improvements to both methods would have to be achieved, which is beyond the scope of this work.

The FE model would need to use a full 3D transducer model to give the same resonant frequency. From the signals studied, it is clear that the experimental data would improve by increasing electronic bandwidth, at frequencies below the main transducer resonance, so that details could be detected in the waveform, and compared to those in the FE models. Problems associated with electronic noise and stable triggering would remain, and increased bandwidth would require careful experimental procedures to eliminate environmental interference.

4.4.3 Comparison of GP-FE and Experimental Signals from a Source on the Opposite Side at 20 cm

As the previous section has considered the similarities between the FE signal and an experimental one, this section will consider the GP-FE signal, and compare it to signals produced by the experimental method, described in section 4.4.1. Again, the source-transducer distance is 20 cm, and the source is a step force on the opposite surface to the transducer.

The two typical experimental signals, used in the previous comparison, are shown (fig. 4.34) with the GP-FE signal. As mentioned in section 4.4.2, the exact arrival time of the P-wave is impossible to identify in the experimental signals, due to the electronic noise on the signals. As a consequence, the first large negative peak in both signals was used to align the signals. The same time scale is used as in the previous section, to compare the FE and experiment. Other starting points for the experimental signals were investigated, but the one used was the most suitable.

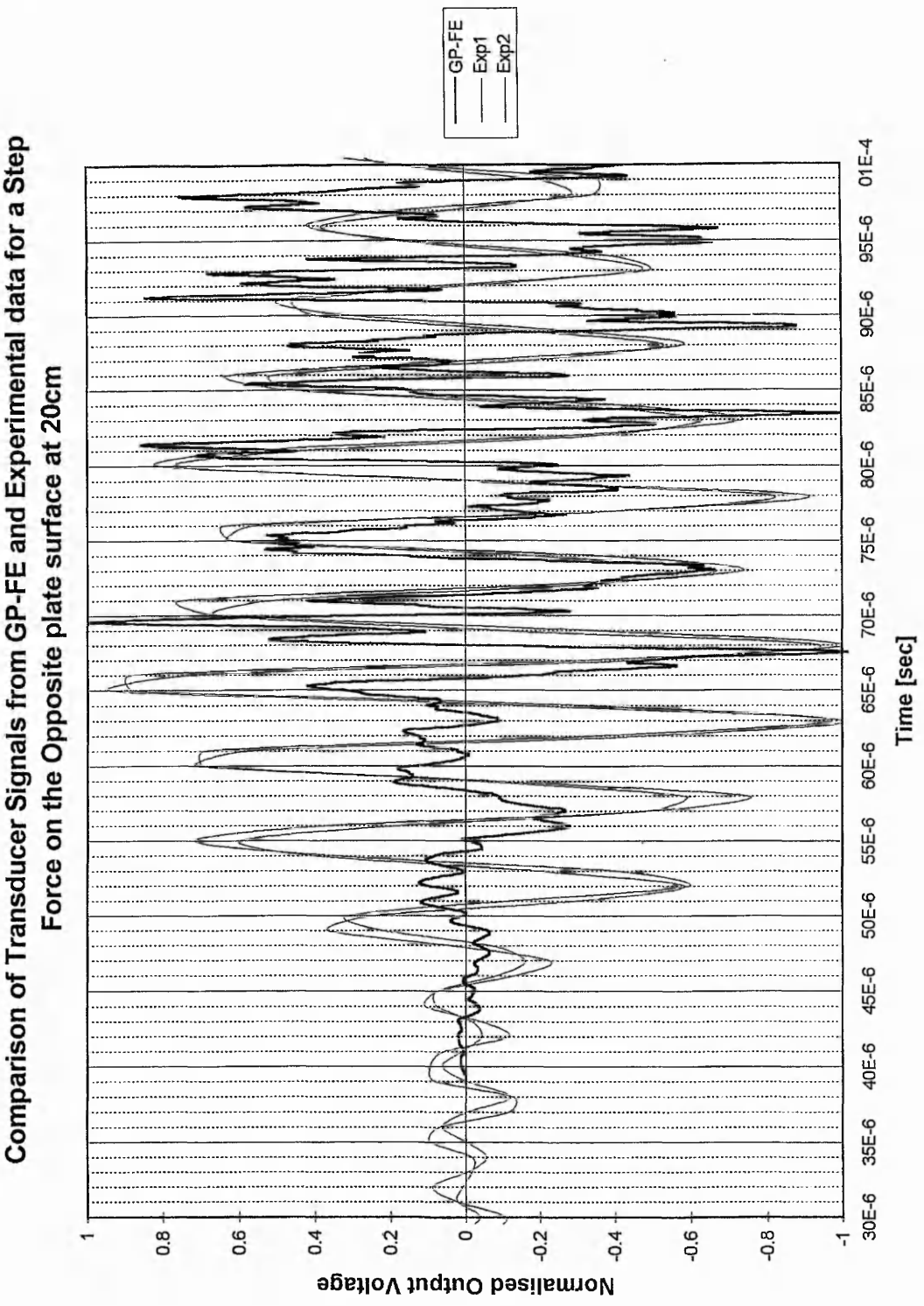

Fig. 4.34 Comparison of transducer signals from GP-FE and experimental data, for a step force, on the opposite surface of the plate, at a source-transducer distance of 20 cm.

The GP-FE signal gives a better match to the experimental signals, because the period of the oscillations is very similar. This is because the axisymmetric model of the transducer is known to give a very accurate prediction of the experimental transducer response, as discussed in Chapter Two. There is a difference in the detail in the two signals, because the GP-FE model had a much higher sampling rate than in the experiment (0.05 μs compared with 1 μs).

The modelling process has been shown to be capable of predicting the general transducer response to a typical acoustic emission waveform. The differences between the FE and GP-FE signals are based on the differences between the transducer resonant frequencies, and have been discussed in section 4.2. Both methods of modelling the AE event and transducer vibration may be useful, given the approximations used, which were necessary due to the computational restrictions, discussed in section 4.1.

4.5 USE OF FEM TO MODEL CRACK OPENING AND INVESTIGATE EFFECT OF VARIATION OF SOURCE DEPTH AT A SOURCE-TRANSDUCER DISTANCE OF 20 cm

4.5.1 Comparison of FE generated transducer waveforms due to a Surface Step Force and a Dipole Force 0.5 mm below the Same Surface for a propagation distance of 20 cm

The preceding sections of this chapter have considered sources on the surface of a plate. Now the case of a source within a plate will be considered. An internal source could result from a crack opening and a dipole force is considered to be a good simulation of such a source.

The FE model simulated transient wave propagation between the plate and transducer, with a full prediction of transducer output. The plate used was the 25 mm thick steel plate, shown in fig. 4.2. The source-transducer distance was 20 cm. In order to simulate the dipole source, two coincident nodes were moved horizontally in opposite directions,

at a time of 2 μs, and left in their new position (fig. 4.4). This produces a Heaviside function dipole displacement.

This source acting parallel to the plate surface, at a depth of 0.5 mm, was compared to the step force on the same surface, at the same lateral distance, to see if there were any recognisable features in the transducer signals. Because the source is very near to the surface, relative to the plate thickness, the two signals should show similarities due to their similar locations. The different source orientation is a factor that should, on the other hand, cause differences in the transducer waveforms.

In order to achieve a direct comparison of the dipole (DP) signal and the step force (SS) signal, the time axis for the DP signal was adjusted so that the event occurred at time zero, as for the step force.

Considering the early part of the signal, the difference between the two source signals becomes quickly apparent. While the SS signal becomes positive at 40 μs, the DP signal remains negative for an extra 2 μs, until 42 μs. This extended period of output voltage is explained by considering the propagating Lamb wave modes. Taking the transducer resonant frequency of 147 kHz, the largest resonance within the frequency limits of the FE model, the first Lamb wave mode to arrive at the transducer, is the L_{12} mode. This is a symmetrical mode, and the dipole force, acting parallel to the plate surface, will excite the extensional modes more effectively than a single force acting normal to the plate surface, which will be more effective in exciting the asymmetric, flexural modes.

The post processing facility of PIGS was used to study the wave propagation in the plate, at several times. In fig. 4.36, the source deformation is pictured in detail. Because the source is near to the surface, much of the displacement occurs at this surface. The SS model produced strong, asymmetric Lamb wave modes (fig. 4.18), due to the source being located in a position that was asymmetrical about the plate centre.

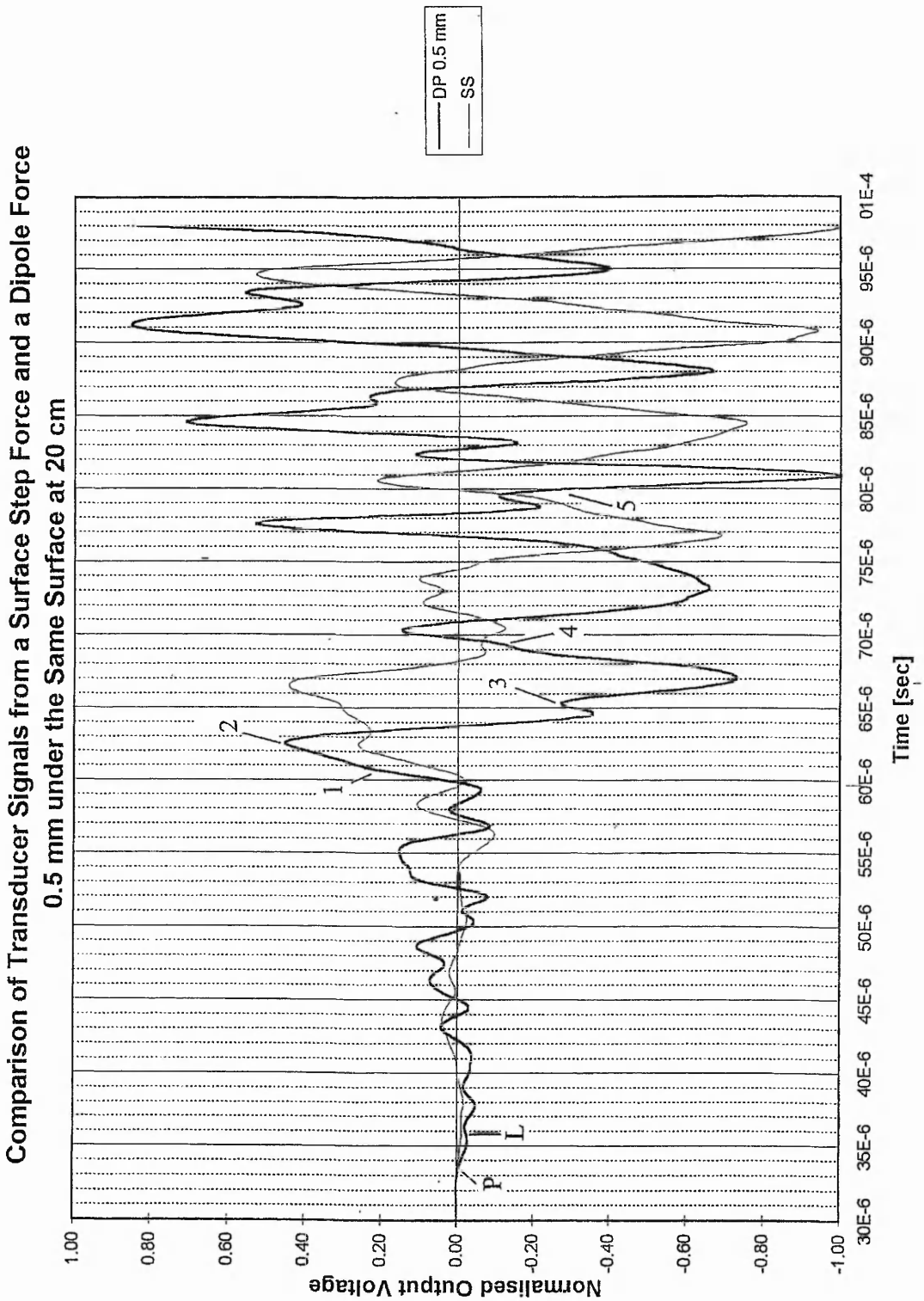

Fig. 4.35 Comparison of FE transducer signals, for a dipole force, 0.5 mm under the same surface, and a step force, on the same surface (SS), both at a source-transducer distance of 20 cm.

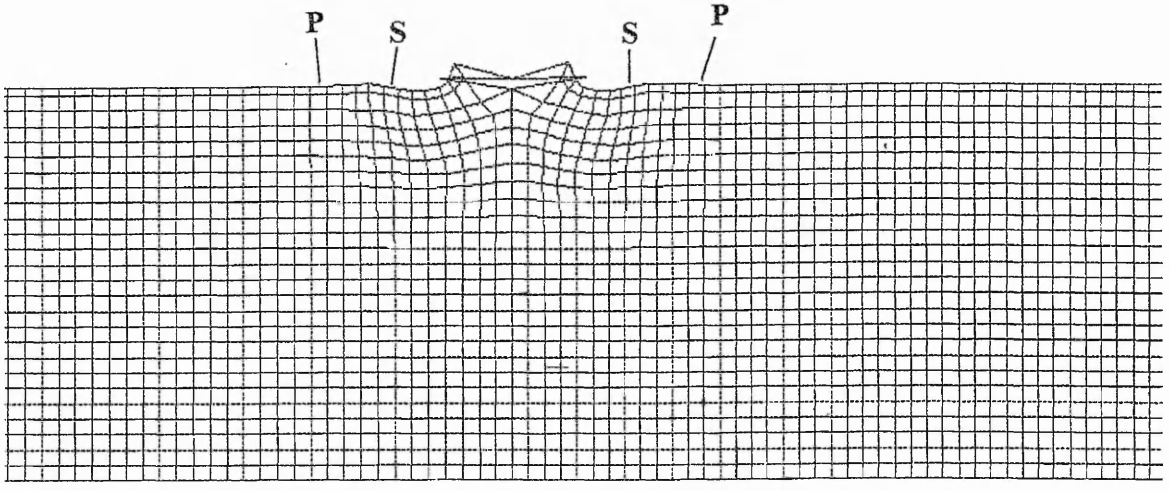

Fig. 4.36 Deformed plate at 2 μs after the crack opens. The points marked 'P' show the P-wave front, while the points marked 'S' show the shear wave front. The source is a dipole force, 0.5 mm under the plate surface, at a source-transducer distance of 20 cm

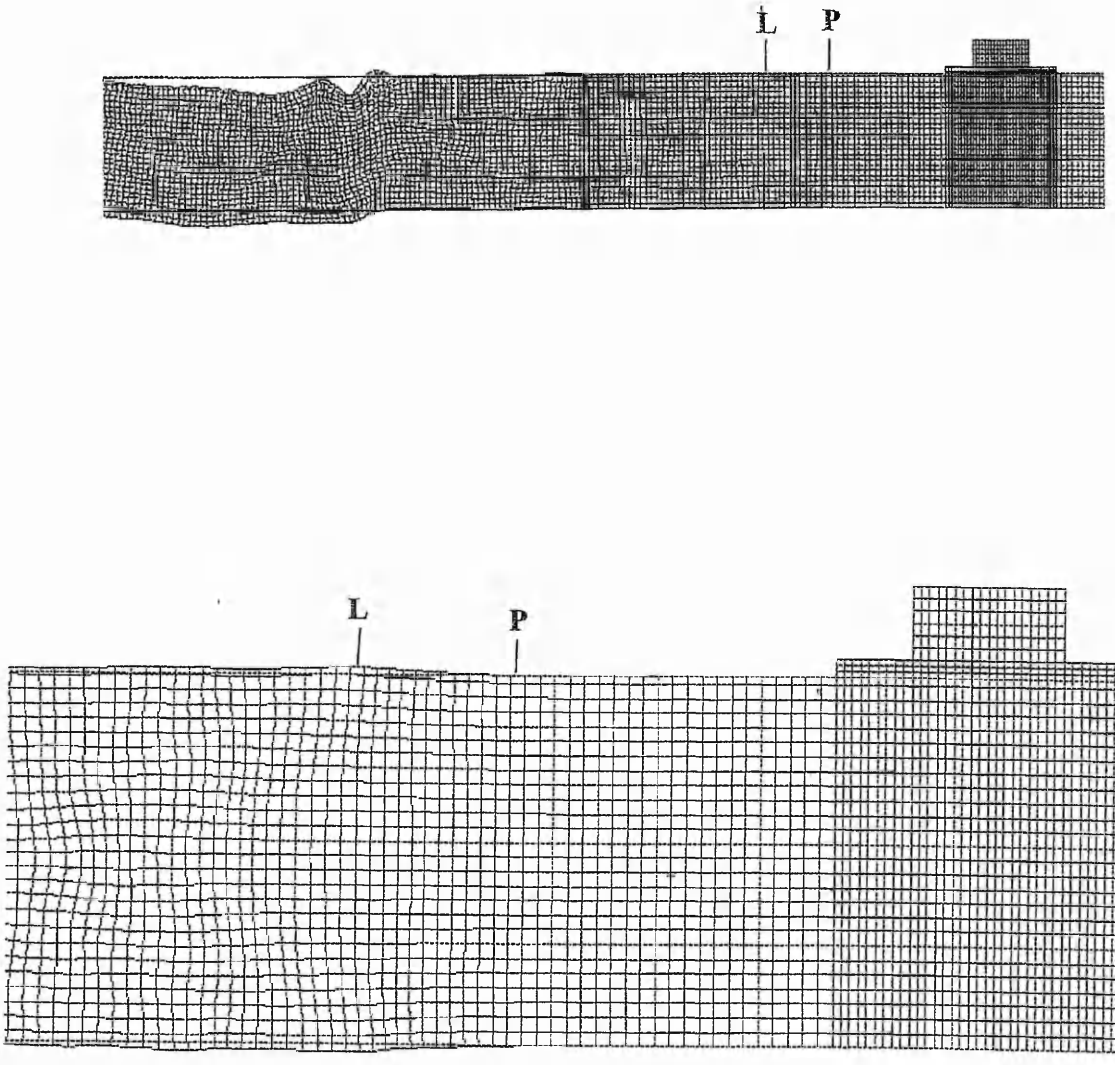

Fig. 4.37a (top) & Fig. 4.37b (magnified) Deformed plate at 28 μs. The points marked 'P' represent the P-wave front, while points marked 'L' show the fastest symmetric Lamb wave mode.

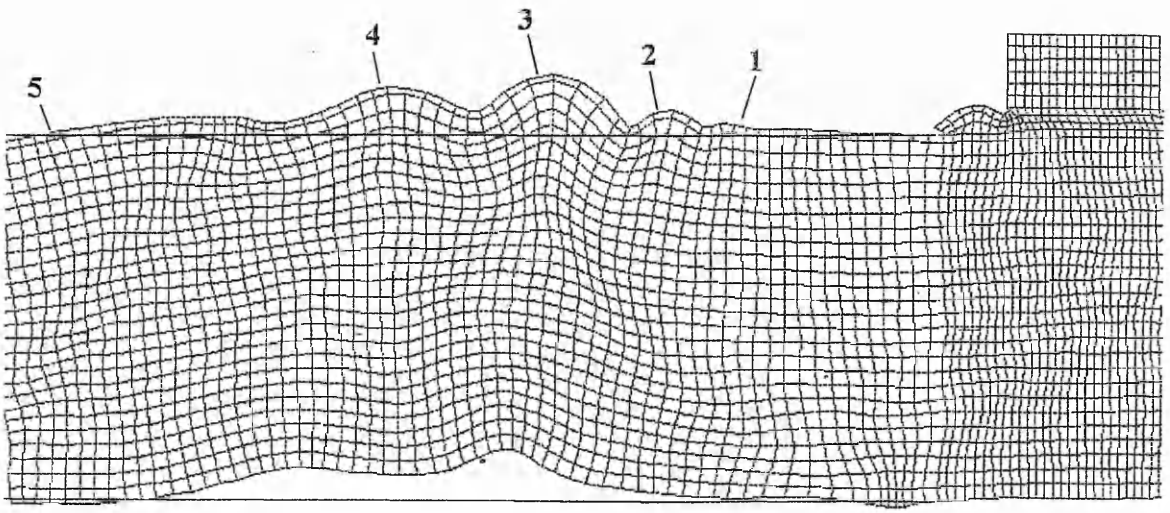

Fig. 4.38 Deformed plate at 53 μs. The points marked '1-5' represent symmetric and asymmetric deformation about the plate centre. Their calculated arrival times, at the centre of the transducer face, are marked on the transducer signal in fig. 4.35.

Similar modes are seen in fig. 4.37a, at 28 μs, just before the Lamb waves travelling at the P-wave velocity arrive at the transducer. These flexural modes indicate the source is close to the surface.

Compared to the following flexural displacement, the initial extensional wave causes very small surface deformation. Fig. 4.37b shows a magnified view of the front end of the elastic wave, in which the first symmetric Lamb wave mode can be seen (marked L).

The calculated arrival time of this wave at the centre of the transducer face, is marked on the output voltage signal (fig. 4.35), and it corresponds to the predicted arrival of the L_{12} symmetric mode (appendix VI).

At 53 μs, the plate deformation can be seen in fig. 4.38. This shows the larger amplitude, flexural modes as they approach the transducer. The transducer can be seen to be responding to the earlier excitation from the symmetric Lamb modes. Points have been marked on the plate surface and the arrival times of these points, at the centre of the transducer face, are marked on fig. 4.35.

The first point of interest is marked '1'. This is when the large, asymmetric deformation of the plate starts. The transducer waveform represents this increase in surface displacement, with an increase in the output voltage amplitude. It is interesting to note the similarity between the SS signal and the DP signal, from 55 to 65 μs, in fig. 4.35. Point 2 (fig. 4.38) produces a peak in the output voltage, which is also seen in the SS signal. Due to the similarity with the SS signal, it would appear that this mode is indicative of the source location (i.e. near to or at, the top surface of the plate).

At point 3 in fig. 4.35, the DP signal shows the opposite polarity to the SS signal. This effect was seen in section 4.3.1, when comparing the SS and OS signals. The deformation at point 3 is large, and asymmetric about the plate length. At point 4, it is clear that there is a DC bias to the DP signal. It has occurred slightly earlier than in the SS signal, but is of the same polarity. This polarity is another indicator of the source location. In fig. 4.38, the deformation at point 5 shows a reduction in the plate

displacement, which is repeated in the DC bias reducing in the output voltage signal (fig. 4.35).

Due to the asymmetry of the dipole source about the plate centre, the asymmetric Lamb wave modes are going to be excited more strongly than the symmetric modes. This is why there is an increase in the output voltage amplitude during the period of their arrival (around 65 μs, appendix VI).

After 70 μs, the transducer signal begins to swing from a negative DC bias to a positive one. Overall, the signal is more symmetrical, about the zero voltage axis than either of the two surface signals (SS or OS). The period of oscillation of the signal is approximately 7 μs, corresponding to the 147 kHz radial mode of the transducer, this resonance generating the large amplitude of output voltage. There are also some smaller peaks, at a higher frequency, indicating other modes of vibration are being excited, but to a lesser extent.

At 147 kHz, the L_{11} Lamb wave mode will arrive at 76 μs. This is close to the point marked 5, at which the deformation about the plate centre begins to look more symmetrical. After this time, the transducer output voltage increases and larger amplitude oscillations begin, as the transducer begins to demonstrate free resonant behaviour. The L_{11} mode is symmetrical and the dipole signal appears more symmetrical about the zero voltage axis (after 75 μs), than the SS, or OS signals. This would indicate the dipole source excites the symmetrical modes more effectively than the surface sources, due to its orientation.

Concluding, the FE model has predicted several differences in the DP and SS signals, generated by resonant sensors, that would indicate the fact that they were caused by different sources. The initial excitation of the transducer, caused by the fastest symmetrical Lamb wave modes arriving, results in a larger output voltage, over a longer period of time, in the DP signal than in the SS signal. The sharp peak starting at 60 μs also indicates source differences, as does the opposite polarity at 67 μs. The earlier start

time of the large amplitude oscillations in the DP signal and more symmetric behaviour after 75 μs are further differences that could distinguish between the two source types.

Similarities seen at other times indicate the fact that both sources come from the same location (relative to the plate dimensions). The same start time for the two signals indicate the same propagation distance, as does the same time to the first large positive output voltage, at 62.5 μs and the next large peaks at 67 μs (although these have opposite polarity). Also, the increase in the signal amplitude at these times indicates the flexural modes have been strongly excited, due to the source's asymmetrical location.

4.5.2 Comparison of FE generated transducer waveforms due to a Surface Step Force and a Dipole Force 12.5 mm below the Same Surface (plate centre) for a propagation distance of 20 cm

A dipole source acting along the plate length, parallel to the surface, at the centre of the plate thickness (12.5 mm below the top surface), is compared to the same surface signal (SS). This dipole source is used to simulate a crack opening within the material. Due to the central location of the dipole, it should generate higher amplitude output voltages for the symmetric Lamb wave modes and lower amplitude output voltages for asymmetric Lamb wave modes than, for instance, the dipole situated 0.5 mm under the plate surface.

Fig. 4.39 shows the first increase in the output voltage from the DP signal is seen at 33 μs, which matches the expected arrival time for the fastest Lamb waves (33.3 μs). The dipole generated output voltage, in this initial period, is negative and of a larger amplitude on the normalised scale, than the surface source (SS) signal. The fact that the dipole source in the plate centre produces a larger amplitude output voltage than the surface dipole source (fig. 4.35), during the entire period up to the known arrival time of the asymmetric modes (around 65 μs), indicates that the source location has increased the excitation of the extensional modes.

For 147 kHz, the fastest Lamb wave mode is the L_{12} mode that will arrive at approximately 40 μs, after the AE event occurs. The L_{12} mode is symmetrical, and so

the symmetrical nature of the source will excite this mode of vibration of the plate more strongly.

In fact, all of the fastest Lamb wave modes in the frequency range of the FE model (up to 250 kHz), are symmetrical modes. Compared to the DP signal for the source at a depth of 0.5 mm, between 34 and 50 μs, the signal amplitude is much greater from the source at the plate centre. This indicates that all of the fast, symmetric Lamb wave modes have been strongly excited, which is largely due to the source location at the plate centre and, to a lesser extent, the source orientation.

PIGS was used to analyse the plate deformation at various time intervals. Fig. 4.40 shows the source epicentre, 2 μs after the dipole crack opens. There is no surface deformation yet, unlike the case for the dipole at 0.5 mm under the same surface, since the waves have not reached the plate surface (fig. 4.40). The points 'P' and 'S' indicate the calculated wave fronts of the longitudinal and shear waves respectively within the plate. At this early time the plate, or Lamb wave modes, are not yet established.

Fig. 4.41a shows the plate deformation at 18 μs. As with the other transient models, the symmetric modes travelling at the P-wave velocity cause displacements that cannot be seen on this scale. Unlike the other models, however, the large deformation that follows later is not flexural, but extensional in nature. This highlights the fact that the source location is symmetrical within the plate. In fig. 4.41b, the wave front can be seen magnified. The calculated P-wave front appears to cause little displacement at the plate surface, while the first symmetric Lamb wave can be clearly seen.

For the increased wave propagation time of 53 μs, several reference points have been marked (fig. 4.42). The corresponding arrival times of these points, at the centre of the transducer face, are marked on the dipole signal in fig. 4.39. The output voltage at point 1 shows an increase in amplitude, from the front end of the signal, and is due to the symmetric displacement at this point, seen in fig. 4.42. This increase in the output voltage amplitude is earlier than in the SS signal.

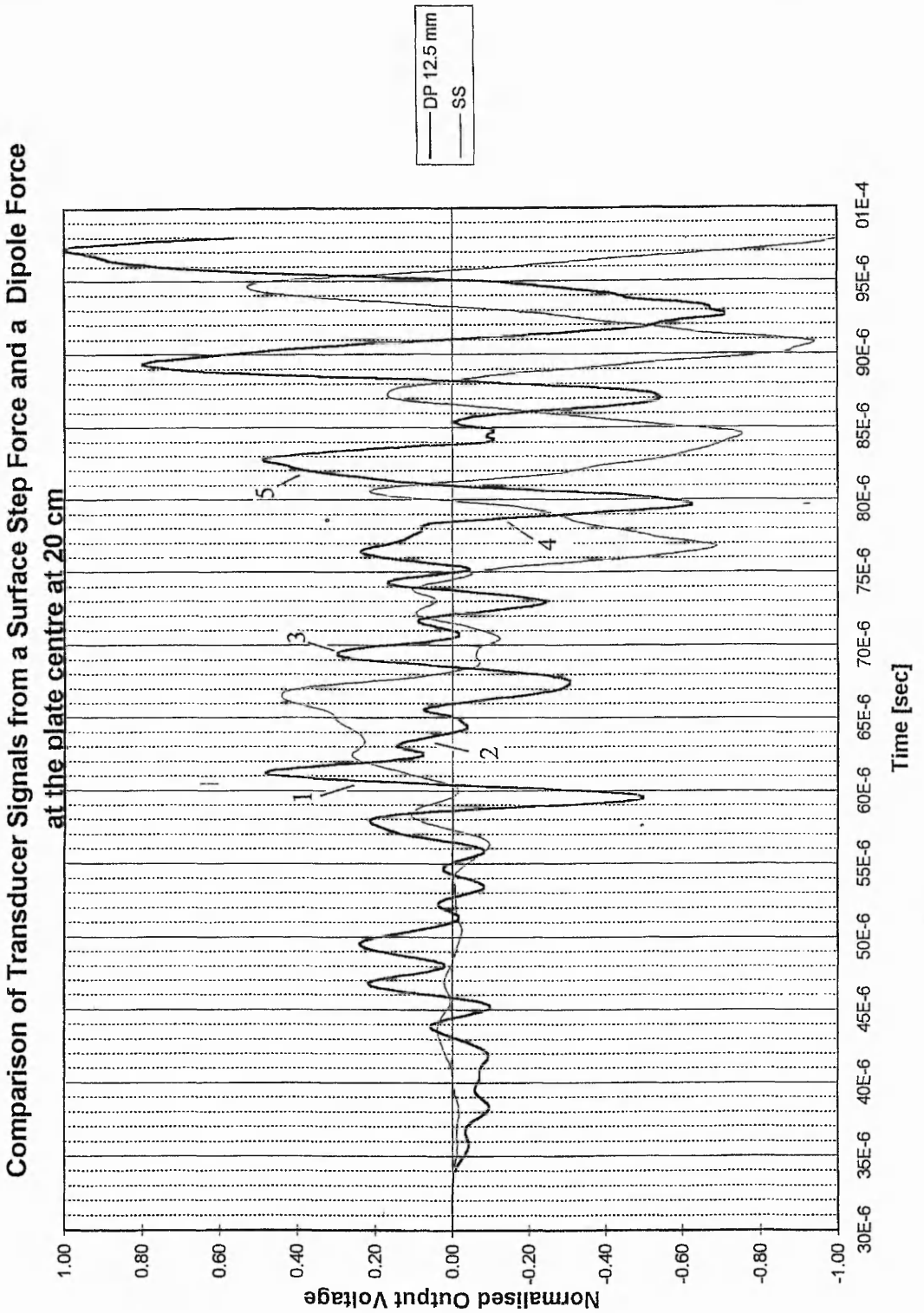

Fig. 4.39 Comparison of FE transducer signals, for a dipole force, at the plate centre (12.5 mm under the same surface), and a step force, on the same surface (SS), both at a source-transducer distance of 20 cm.

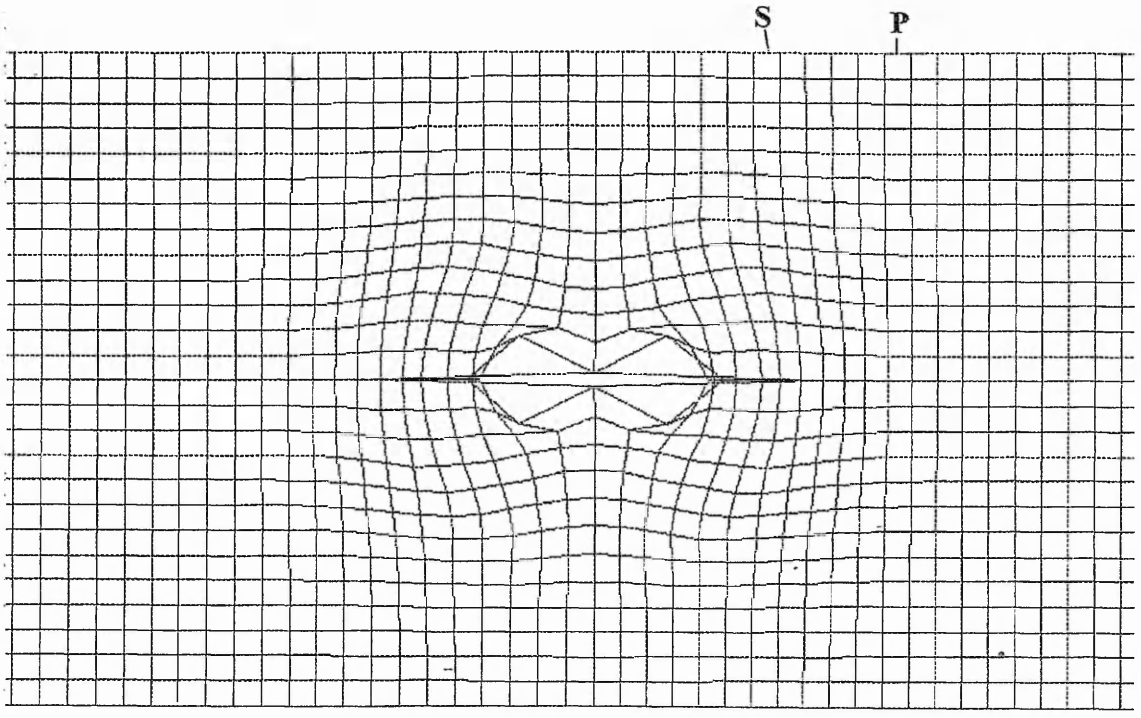

Fig. 4.40 Deformed plate at 2 μs after the crack opens. The points marked 'P' show the P-wave front, while the points marked 'S' show the shear wave front. The source is a dipole force, at the plate centre, at a source-transducer distance of 20 cm

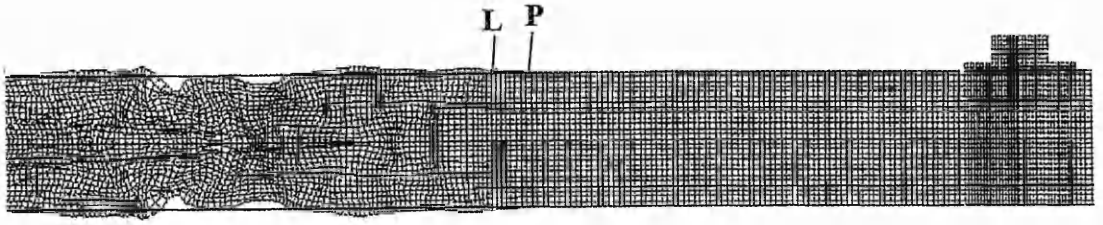

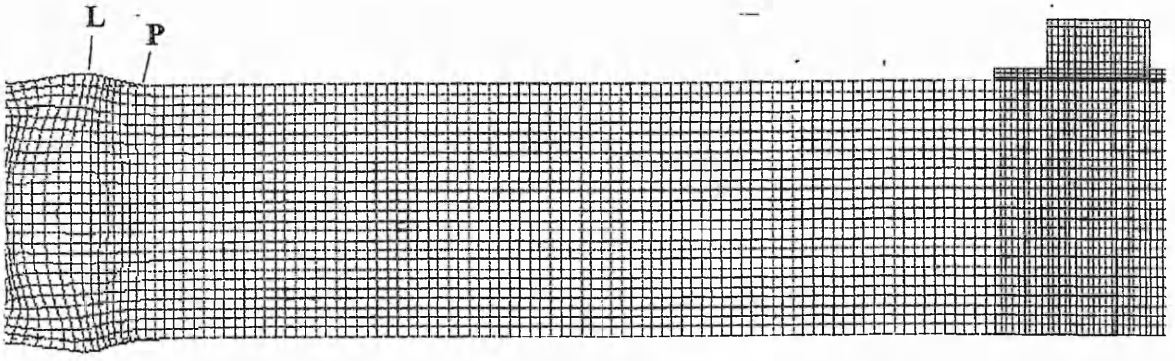

Fig. 4.41a (top) & Fig. 4.41b (magnified)

Deformed plate at 18 μs. The points marked 'P' represent the P-wave front, while points marked 'L' show the fastest symmetric Lamb wave mode. The source is a dipole force, at the plate centre, at a source-transducer distance of 20 cm

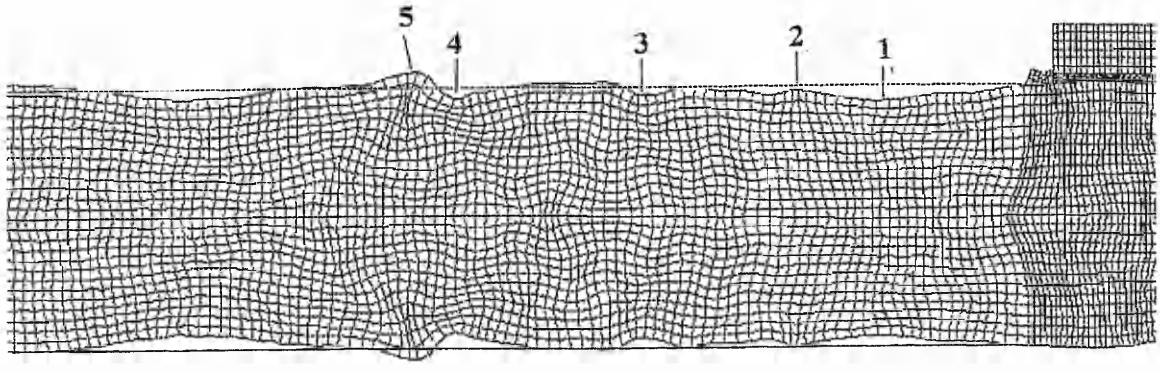

Fig. 4.42 Deformed plate at 53 μs. The points marked '1-5' represent symmetric and asymmetric deformation about the plate centre. Their calculated arrival times, at the centre of the transducer face, are marked on the transducer signal in fig. 4.39.

In the SS signal, the increase in signal amplitude was a result of the transducer responding to asymmetric Lamb wave modes arriving. These flexural modes are poorly excited in the dipole model, while the symmetric modes, which arrive first, are strongly excited.

Point 2 (fig. 4.39) indicates the time when the output voltage drops, which is when the asymmetric Lamb modes are arriving.

The first large increase in output voltage occurred at this time in the SS model. The amplitude of the DP signal remains low, reflecting the smaller surface displacement in the plate, until a large increase after 76 μs.

This time corresponds to the arrival of the slowest symmetrical Lamb wave modes, which will be strongly excited due to the symmetry of the source type and location (giving the transducer a strong excitation). The plate deformation around points 4 and 5 corresponds to this symmetrical excitation. The time period of the large amplitude oscillations (e.g. taking the peak-to-peak time interval between 80 and 87 μs) indicates, as in the surface source (SS) models, the transducer is vibrating in its radial mode, around 147 kHz.

At later times, the dipole signal is more symmetrical about the zero voltage axis, than either of the surface source signals. This lack of bias on the signal is another indication of the source symmetry and, therefore, is a feature that could help to identify the position of a source within a plate.

To conclude, it has been demonstrated that FEM can be used to accurately model complex wave propagation problems, associated with acoustic emission detection in plates and also, the resonant transducer response to these waveforms. The different sources modelled are typical AE sources and therefore, the transducer output voltage waveforms are representative of transducer signals that might be expected. The shape of the waveforms has been shown to give some indication of the orientation, and location of the source. Using the advantages of the PIGS post processing software, AE events, in a

25 mm steel plate, have been shown to excite a variety of complex, transient Lamb wave modes. Depending on the source symmetry, the symmetric or asymmetric modes will be excited to varying degrees. Knowing the dominant frequencies of the resonant transducer leads to some identification of these mode types. The predicted arrival times of the symmetric and asymmetric Lamb wave modes are shown to correspond to particular deformation in the plate and also, features in the output voltage signals.

These signal features contain the information about the source and its location. The signal front end appears to carry detail about the source type and orientation, while the fastest asymmetric Lamb modes, arriving around 55-63 μs, contain location detail. This is suggested by the similarity between the surface dipole and the SS signals at this time. The signal shape between 64-70 μs appears to be largely influenced by source type or orientation rather than location. This is suggested because the two dipole signals are very similar in shape at this time, both differing from the SS signal.

FEM opens the door to detailed signal analysis which, with improvements for more realism (e.g. bandpass filters), will hopefully lead to improved understanding for NDE.

This work has shown that users of resonant transducers, contrary to the accepted view, may gain much information from a single waveform. The advantages of the resonant transducer are its high sensitivity and better signal-to-noise ratio. However, modelling and experimentation do suggest the need for wider electronic bandwidth. The limited frequency response, imposed by a resonant transducer, has been shown to be an advantage in many applications, particularly in source location using Lamb wave modes [**31**]. Examples in this section have demonstrated the ability to, perhaps, predict the source depth, by means of the waveform symmetry. It is clear that the power of FEM allows the user to enter a new era of AE detection and understanding.

4.5.3 Effect of Source Depth on the Signal Energy in a Time window

In AE experimentation, there are often many AE events occurring in a short period of time. The software, used to capture the events, may record the transducer output

voltage in time windows, specified by the user. A parameter that can be measured within a time window might provide an advantage, when attempting to track the type of AE events.

To this end, the dipole source was modelled at a variety of depths, through the 25 mm plate thickness, at a source-transducer distance of 20 cm. The signal energy, evaluated in a variety of time intervals, has been normalised to the total signal energy in the time window and has been plotted against source depth within the plate (fig. 4.43). The time window used was 70 μs, measured from the start of the modelled output voltage signal. Time increments of 10 μs were used, with the calculated P-wave arrival at time zero.

As seen in the previous sections (4.2 to 4.5), the initial part of the signal corresponds to the arrival of the symmetric Lamb wave modes. It was seen to have a larger amplitude of output voltage with the same source in the plate centre, than when it was near to the surface.

Curve (a) in fig. 4.43, shows the signal energy against source depth, for the first 30 μs of the signal. Because the sources in the centre of the plate excite the fast, symmetrical Lamb wave modes strongest, they provide the most output voltage in this time interval and hence, the largest normalised signal energy. The integral of the first 20 μs is not shown, because the signal energy was extremely small, in comparison with the total energy in the 70 μs time window (about 1%).

In systems in which there is continuous monitoring of events, exact P-wave detection is difficult, due to noise in the system. However, the trend in the 0-30 μs interval would provide an indication as to the depth of the source, assuming all other source characteristics were constant. The very front of the signal contains the least energy and, therefore, if it is lost the effect on the overall energy distribution will be minimal. The 30 μs length of this first window is long enough to be indicative of the energy distribution, even in a noisy system in which the front end is lost. Assuming that the following asymmetric modes trigger the signal capture in a practical system, the first 30 μs could correspond to the pretrigger points defined by the user.

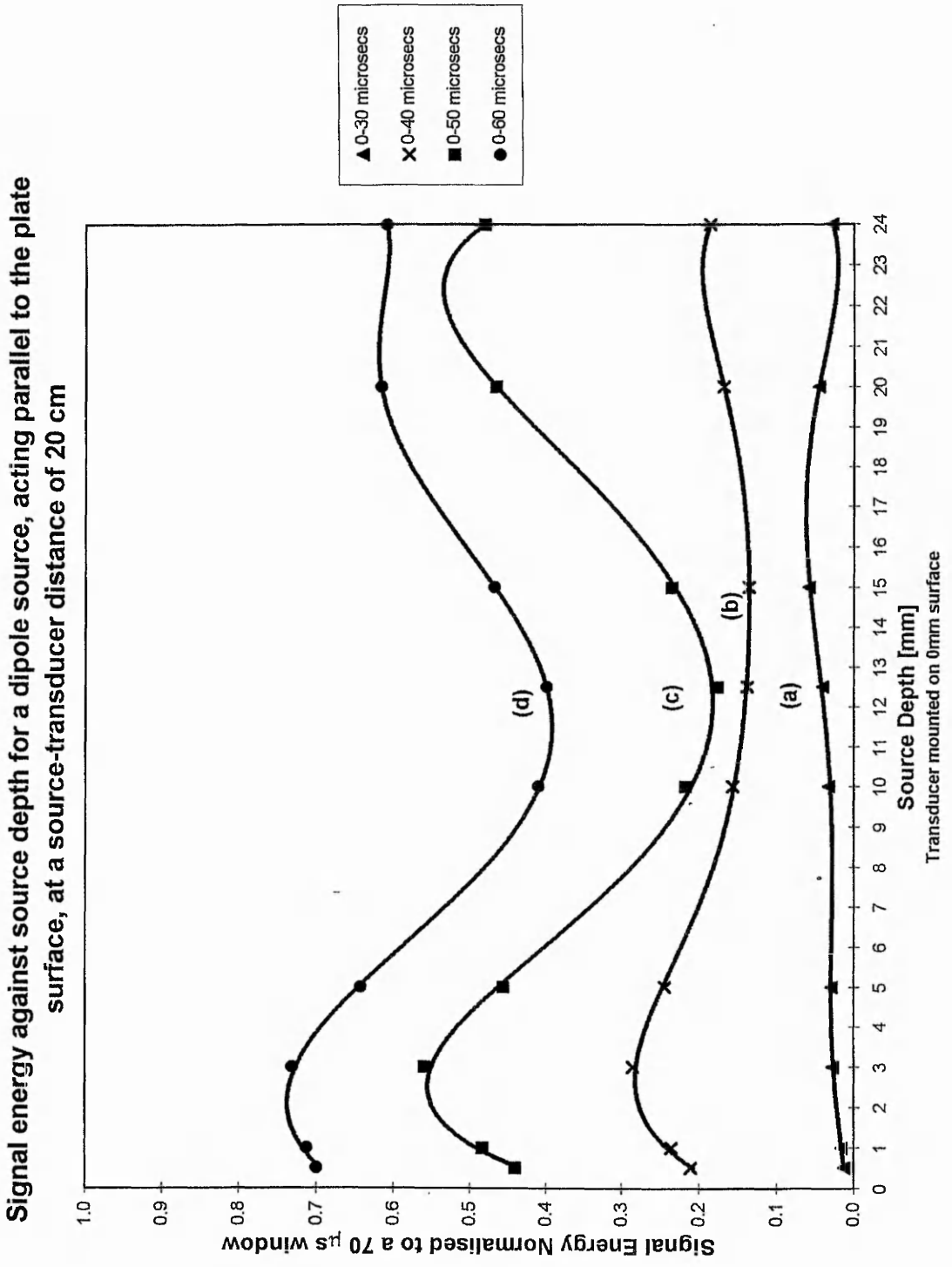

Fig. 4.43 Signal energy $\Sigma(V^2)dt$ against source-transducer distance, for a dipole force inside the plate. The signal energy, in each time interval, is normalised to the signal energy in a 0-70 μs time window.

The next window (30-40 μs), incorporates the period in which the asymmetric Lamb waves arrive at the transducer, at this source-transducer distance of 20 cm. This data shows a minimum energy for a dipole source at the centre of the plate, as a percentage of the energy in the 70 μs time window.

Sources near to the opposite surface provide larger normalised signal energy increases (17%), than sources in the centre (10%), but these energy increases are still not as large as from sources near the same surface as the transducer (20%).

This period of the signal, 30-40 μs after the calculated P-wave arrival time, is easily detected, due to the large amplitudes in the output voltage, and so this time window information would provide a useful guide to the source depth in a practical system. It is, however, difficult to predict the exact source depth with this time interval, especially near to the surface, as the normalised signal energy relationship with the source depth is very complex. For example, if the signal energy, in this 0-40 μs time interval (curve b), was above 20% of the total energy in the 70 μs window, then the source is likely to be within 5 mm of the surface. It is not, however, possible to specify whether the source is at a depth of 2 or 4 mm because curve (b) provides two solutions. However, this uncertainty might be resolved if, for instance, data is being detected from a known crack. Clearly, statistical methods would be applicable in this type of situation.

The 40-50 μs time interval (curve b-c) shows large increases in the signal energy as the source drops below both surfaces (>23%), with the smallest increase at the plate centre (<5%). This time period for the output voltage involves detection of both asymmetric and symmetric modes. The signal from the source at a depth of 0.5 mm (fig. 4.35), has a large amplitude, low frequency peak in the output voltage in this interval, while the mid-plate source has low amplitude, high frequency peaks (fig. 4.39). This 40-50 μs time interval provides a clear indication of the influence of the source location on the shape of the waveform produced and hence, the signal energy. The fact that the normalised signal energy (curve c) is almost symmetrical about the plate centre, means that it is even more difficult to identify a near-surface source, than in other time intervals. For example, if the normalised signal energy is 0.5 for the 0-50 μs interval (curve c) then the source

could be at any of four depths (1, 4, 21 or 24 mm approx.). However, a source at the plate centre does give a unique solution using the curve (c).

In the final time interval of 50-60 μs, normalised to the total time window of 70 μs, curve (d) follows the same pattern as curve (c) in the 40-50 μs interval. This time, the fact that the near surface sources produce a higher normalised signal energy, than the sources near to the opposite surface, is clearer. Both near-surface sources produce more normalised signal energy than a source positioned at the centre. This may not be the case if the sources were different magnitudes in practice, but for the model this is true.

Other methods of presenting the signal energy data were investigated, but these also showed unhelpful relationships. The most useful relationship appeared to be the normalised signal energy increase in the first three time intervals (0-10, 0-20 and 0-30 μs). The energy in these three intervals was plotted for each depth. At any depth, the increase from the 0-10 to the 0-30 intervals followed a quadratic curve. The coefficients of these curves are seen in fig. 4.44 against the source depth. Sources at the centre give opposite coefficients (high/low relationship) to sources near to a surface. The difference between the high and low coefficients is greater for sources near the opposite surface than near the same surface. This is another indicator of the effect of source depth.

The FE models all used the same amplitude source acting in the same direction. Practical variables include different source types (dipole, shear etc.), source orientation, source depth, source strength and source distance. The modelling allowed the only variable to be the source depth and has shown that some understanding of its effect on the transducer signal can be obtained. This highlights the use of such tools for research purposes and potential for further development.

Once a crack has started, in a material such as steel, the source distance is fixed (relative to the transducer position), the source type is fixed (depending on the material loading) and the orientation is constant (given an established crack plane and uniform material). This leaves the source strength and depth as the main variables.

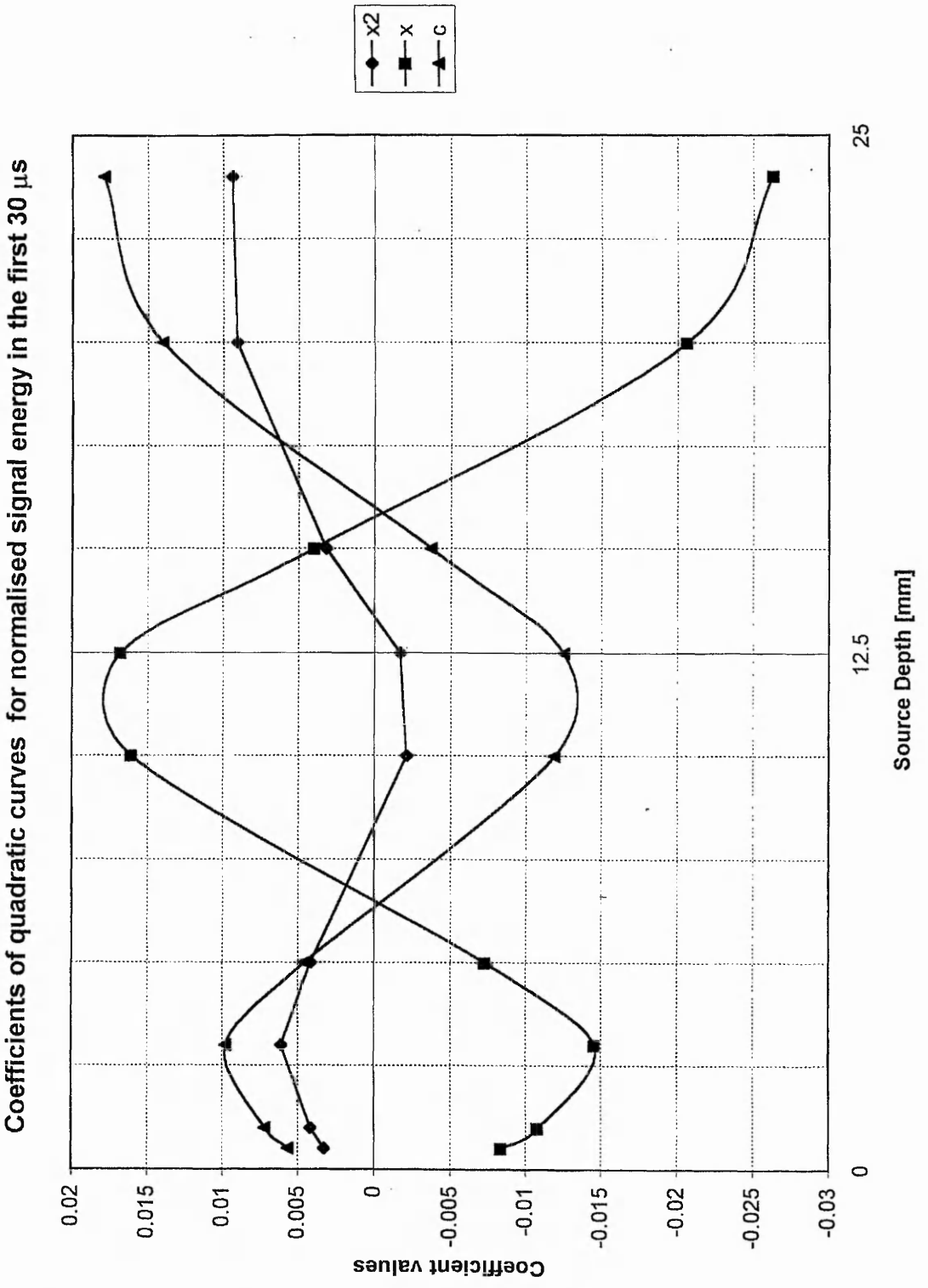

Fig. 4.44 The x^2 and x coefficients and the constant of the quadratic curves that fit the normalised signal energy against source depth points, for the time intervals 0-10, 10-20 and 20-30 µs.

By normalising the signal energy in each time interval to the total signal energy in the time window, the relative distributions of signal energy from a number of signals can be compared to those predicted by the idealised FE model. It is also true that the initial crack depth may be known via other NDE methods.

It is clear that comparing the normalised signal energy distribution, within a time window (in this case 70 μs) for each AE event, can give some indication of the depth of an acoustic emission source. This type of monitoring would have most practical use at one specific distance. If a defect is located using a rapid nondestructive evaluation technique, then a transducer could be positioned suitably in order to monitor it more closely.

With further development, the analysis seen in fig. 4.43 could be used to help determine if the crack was travelling through the plate thickness and, provide useful information for fracture mechanics calculations.

The final determination, as to which surface a source is nearest, would come from a polarity check of the actual output voltage signal. During the arrival of the first asymmetric Lamb wave modes, 30-35 μs after the calculated P-wave arrival time, the polarity of the signal will be the same as that produced by a step force on the nearest surface i.e. SS or OS signal (section 4.3.1). After this short time the polarity reverses, as seen in fig. 4.35 (section 4.5.1). However, signals at the same depth from opposite surfaces, will produce opposite polarity signals after the asymmetric Lamb mode arrivals.

Using this type of technique for monitoring damage in, for instance, composite materials would be much more difficult due to the more complex material behaviour. In such a case the technique of analysing the normalised signal energy may have some use for identifying the damage modes. Surgeon and Wevers [**27**] have recently discussed modal techniques for analysis of composites. Two typical damage mechanisms in a fibre/resin matrix are matrix cracking, causing excitation of the extensional modes and delamination growth, causing flexural excitation. The extensional excitation would produce a normalised energy distribution different to that of the flexural excitation. Therefore, the normalised energy distribution could have some potential for analysing a variety of AE

data and, if coupled with other NDE methods may provide quantitative on-line default monitoring.

4.6 ANALYSIS OF TRANSIENT TRANSDUCER VIBRATION IN RESPONSE TO AN AE SIGNAL AND USE OF FEM TO IMPROVE THE TRANSDUCER SENSITIVITY

4.6.1 Analysis of transient transducer vibration in response to an AE source

A 2D (two dimensional) FE model was used in the transient analyses, involving the plate and the transducer combination. The resonant frequencies of the 2D bi-laminar disc transducer model are different to the 3D axisymmetric model, because the transducer is only able to move in two directions and not three. This was seen in the different frequency contents of the transducer signals in section 4.2. The GP-FE model signal had a main peak at 176 kHz, matching the acoustic axisymmetric FE model prediction. The 2D FE model signal had a peak in the frequency amplitude at 146 kHz, indicating this is the main resonant frequency of the 2D transducer.

To confirm this, the 2D transducer resonances were predicted using a forced sinusoidal analysis, using repeated freedoms on the transducer face, as used in section 2.2.2. Although the acoustic analysis is the preferred method (Chapter Two), the forced sinusoidal analysis is computationally faster and was considered accurate enough for comparison to the known 3D axisymmetric results.

Fig. 4.45 shows the resonance spectrum for the 2D transducer predicted using the forced sinusoidal analysis, with repeated freedoms on the face nodes. There are only peaks at 133 and 146 kHz, with the peak at 133 kHz being much larger in amplitude. The 133 kHz frequency does not produce a peak in an FFT of any of the 2D transducer transient model signals and, therefore, the repeated freedom boundary condition is unrealistic. As a comparison, the transducer face was forced sinusoidally at the centre node only. Fig. 4.46 shows the transducer resonance spectrum due to this excitation has a single peak at 147 kHz, in the 50-250 kHz range modelled.

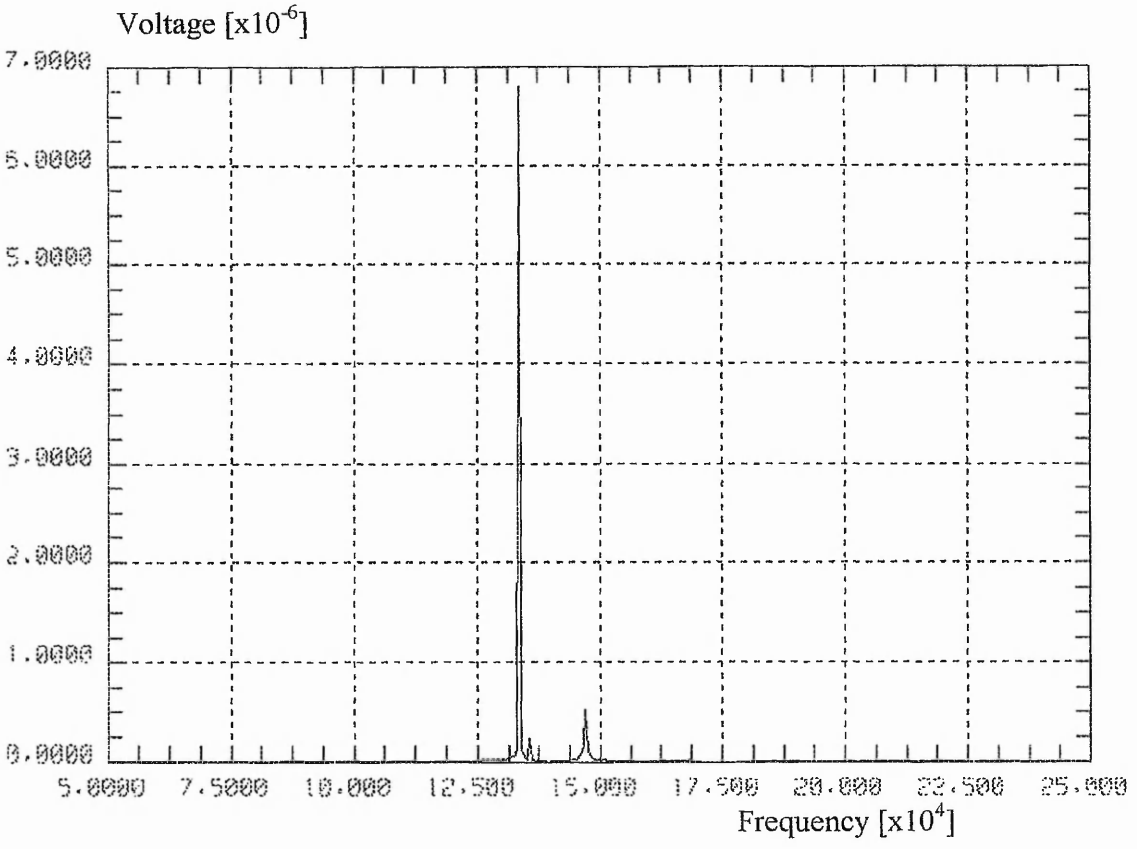

Fig. 4.45 The 2D transducer spectrum showing the resonance at 133 kHz, predicted by a forced sinusoidal FE analysis. The nodes on the transducer face were given repeated freedoms.

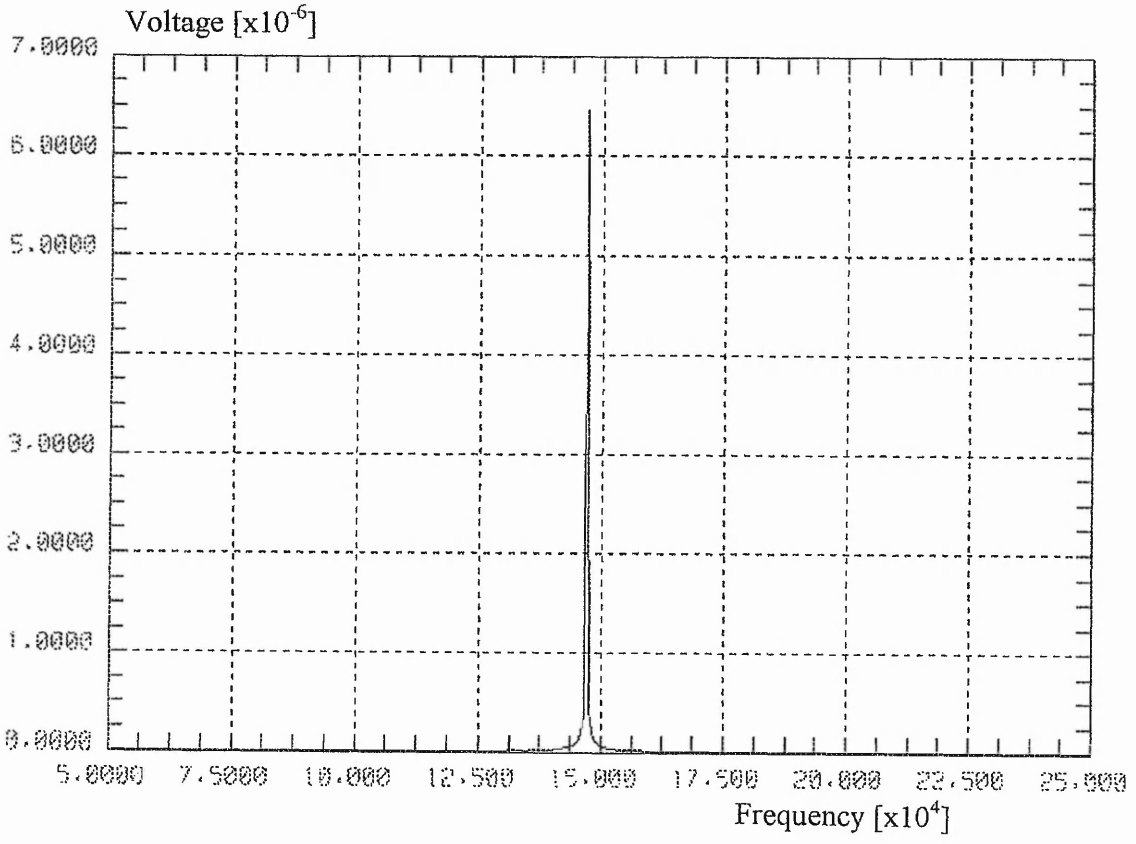

Fig. 4.46 The 2D transducer spectrum showing the resonance at 147 kHz, predicted by a forced sinusoidal FE analysis. Only the centre node on the transducer face was excited.

Although these sinusoidal models have confirmed that the 2D transducer has a resonance matching the dominant frequency amplitude in the transient models, they also indicate that the simplified boundary conditions employed are far from adequate for predicting the complex frequency response of the transducer, seen in any FFT of a transient signal. It is interesting to note that the FFT of the transducer response to an epicentral source, in fig. 4.10, clearly has the largest amplitude peak at 146 kHz, showing that the centre node excitation is dominating the transducer vibration. The FFT of the transducer responding to an off-epicentre source in fig. 4.47, shows large peaks at several frequencies (including 146 kHz), indicating that many modes are being excited.

This helps to confirm that the acoustic FE model, involving the fluid region, is the best form of sinusoidal modelling because it excites the full range of transducer resonances, which are seen when a transducer is excited by a broadband AE source.

Now, a more detailed consideration of the transducer vibration, at various time intervals, will be undertaken. The aim of this section is to compare the vibration of the transducer, due to transient excitation, with the transducer's resonant modes seen in Chapter Two, to see which modes are being excited and to what degree. The 2D transducer mode at 147 kHz can be seen in fig. 4.48. The piezoelectric mode is equivalent to the M_{21} mode of the axisymmetric model in fig. 2.29, except in opposite phase (the axisymmetric model only showed half of the transducer seen in the 2D model).

The transducer will be analysed for the case of the transducer excited by a 2 μs square wave input force (fig. 4.3), normal to the opposite plate surface, at a source-transducer distance of 20 cm, as detailed in section 4.3. To analyse the transducer vibration in detail, the transducer deformation at various times was viewed individually in PIGS, without the presence of the plate. Fig. 4.49 shows the deformed transducer at 40 μs, when the transducer is responding to the fastest symmetric Lamb wave modes, first arriving at 33.3 μs. The plastic facing is being displaced horizontally, parallel to the plate surface and, therefore, is only producing a small, normal displacement component, to be transferred into the piezoelectric element.

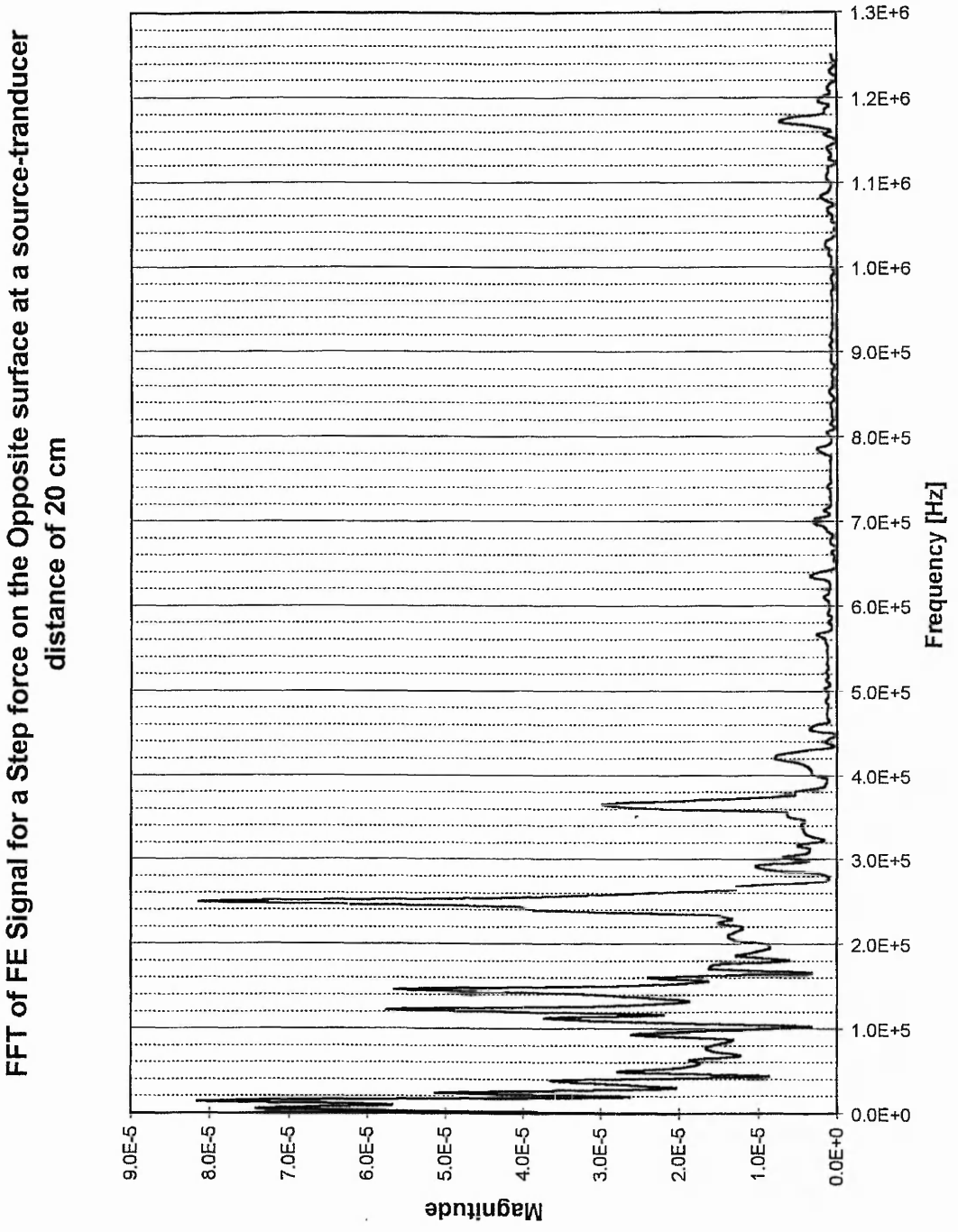

Fig. 4.47 Fast Fourier Transform of the transducer signal, for a step force on the opposite surface of the plate, at a source-transducer distance of 20 cm.

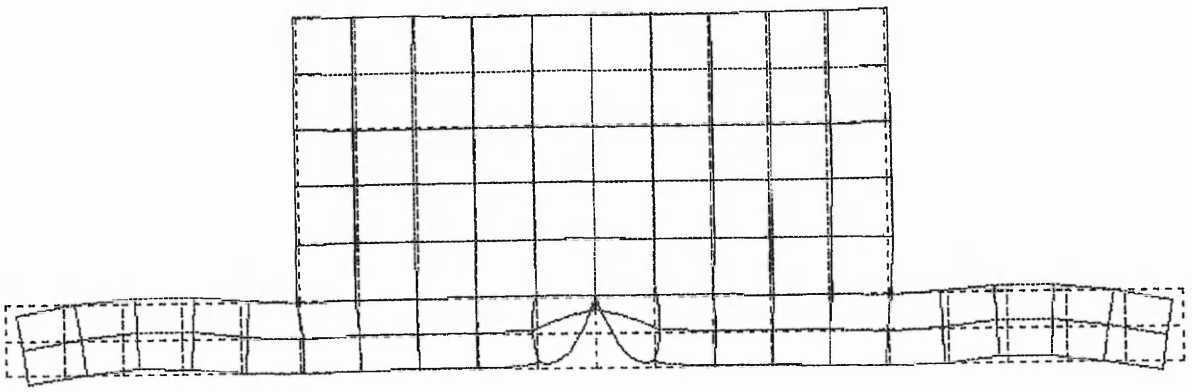

Fig. 4.48 Deformed shape of the 2D transducer mode at 147 kHz, predicted by a forced sinusoidal FE analysis. Only the centre node on the transducer face was excited.

All of the displacement in fig. 4.49 appears to be in the plastic facing and so the piezoelectric was viewed individually, to see how it was vibrating. In practice, a thin layer of couplant is often used to couple the transducer to a test object. It is likely that the couplant would behave in a similar way to the plastic disc, reducing the transition of energy into the piezoelectric.

In fig. 4.50, the piezoelectric at 40 μs can be seen on a larger scale. The normal displacement at the transducer face is 3 orders of magnitude greater than in the piezoelectric. Fig. 4.50 shows that the whole of the piezoelectric is already displaced by the Lamb waves travelling at the P-wave velocity, which first arrived at 33.3 μs.

The same piezoelectric displacement is seen when the transducer responds to a source on the same surface of the plate, which is why the SS and OS signals give the same output voltage at this time, in fig. 4.11. The fastest Lamb wave modes arriving are symmetrical, which cause an equal displacement to the top and bottom surfaces of the plate and, therefore, produce the same transducer vibration in the SS and OS models.

Viewing the transducer and piezoelectric deformation at 60 μs, it was hard to determine which modes of vibration were being excited, as was the case at 40 μs. The broadband source means that several mode shapes will be excited at once, making it impossible to see what is happening from the deformed piezoelectric alone. The transducer deformation, as seen in fig. 4.49, gives more general understanding of the excitation process. It is clear from the frequency content of the signals that the main resonances are dominating the transducer response as expected.

In fig. 4.51 the transducer displacement in the OS model can be seen at 65 μs. The plastic facing can be seen with a large area of compression under the piezoelectric. This large vertical displacement, normal to the plate surface, is clearly responsible for the increased voltage in this time region, and is a result of the large displacement at the plate surface, due to the flexural vibration in the plate (seen in fig. 4.20, section 4.3.1). The plastic is still being displaced parallel to the plate surface, but this time the displacement is almost symmetrical about the transducer's central vertical axis.

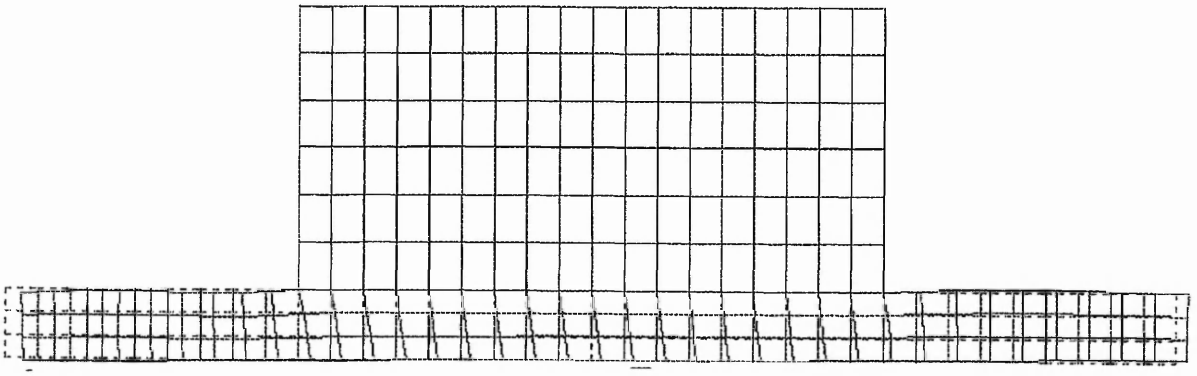

Fig. 4.49 Deformed transducer structure at 40 μs, for a step force, on the opposite surface of the plate, at a source-transducer distance of 20 cm. The piezoelectric deformation is shown alone in fig. 4.50. The dashed lines represents the undeformed structure.

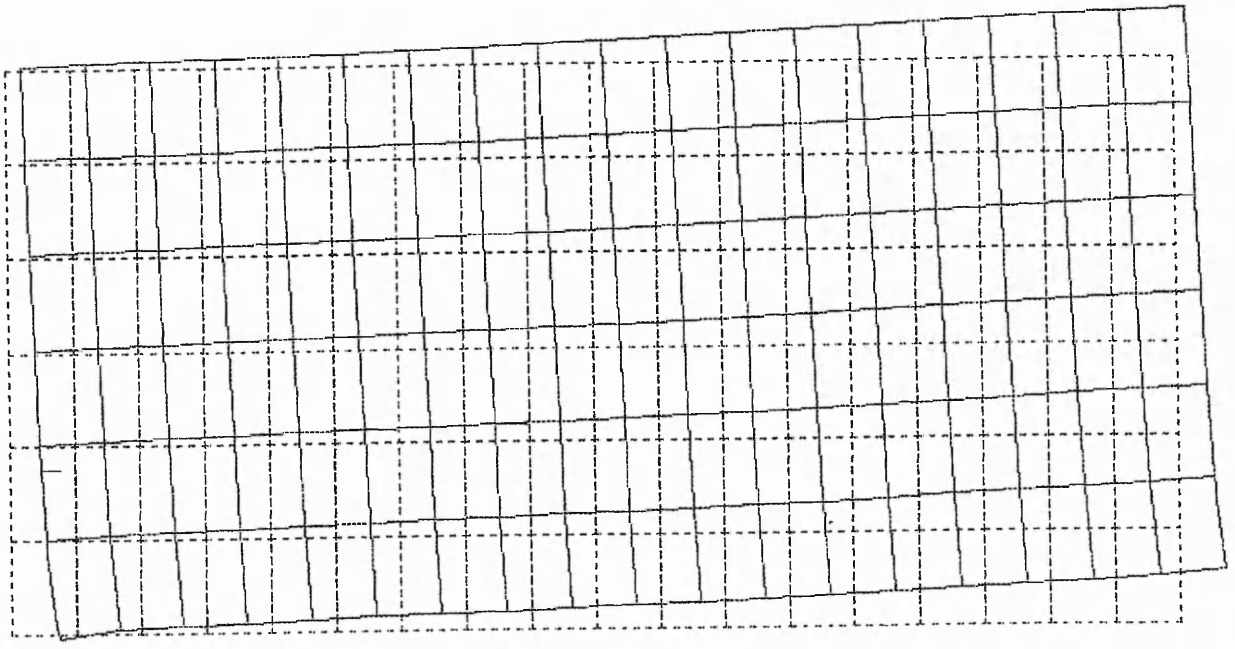

Fig. 4.50 Deformed piezoelectric structure at 40 μs, for a step force, on the opposite surface of the plate, at a source-transducer distance of 20 cm. The piezoelectric is orientated as in fig. 4.49. A larger scale is used to highlight the deformation, which cannot be seen in fig. 4.49. The dashed lines represents the undeformed structure.

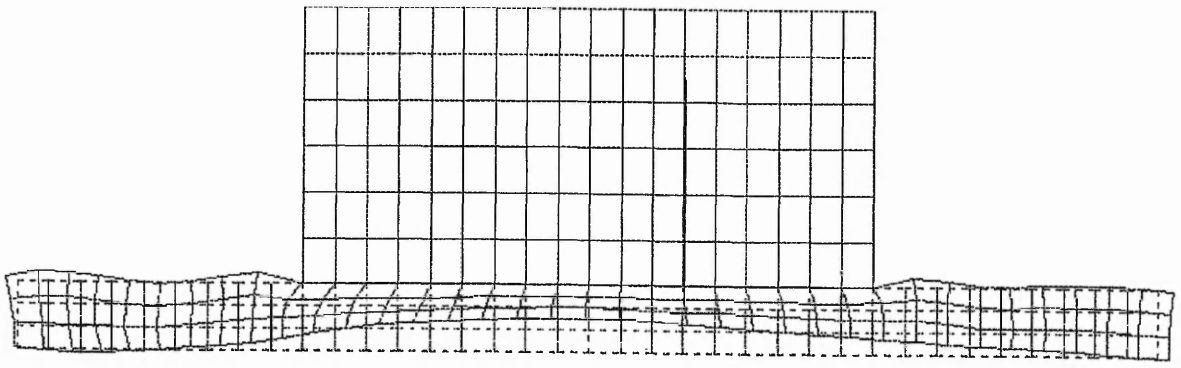

Fig. 4.51 Deformed transducer structure at 65 μs, for a step force, on the opposite surface of the plate, at a source-transducer distance of 20 cm. The dashed lines represents the undeformed structure.

At 40 μs, the displacement was all to the right in fig. 4.49, in the direction the plate wave was travelling, reducing the potential excitation of the piezoelectric element. Now, at 65 μs, the output voltage is much larger in amplitude and indicates that the piezoelectric is being excited more effectively. Possibly the radial-like motion in the transducer face, seen in fig. 4.51, is exciting the main resonant frequency, also suggested by the fact that the large amplitude oscillations begin just after this time in fig. 4.11.

Study of the transducer deformation has shown that it is difficult to excite the transducer into any one mode of vibration with an acoustic emission event. Instead, a combination of modes is excited, producing complex vibration.

This leads to an equally complex waveform produced by the transducer, which could hide some of the features of the input to the transducer face.

Also, it means that the transducer is unlikely to give maximum theoretical sensitivity, because the most powerful modes of vibration cannot be uniquely excited. The energy input to the transducer would be most effective at a single resonant frequency. Because a range of frequencies is excited, energy is shared as several different modes try to establish themselves. When the transducer excitation is such that the main resonance can be effectively excited, as appears to be the case in fig. 4.51 at 65 μs, then the main mode of vibration can dominate the response and produce a larger output signal. Energy partitioning between the various modes reduces the potential sensitivity of the transducer at a specific frequency. New designs, like the 1-3 type discussed in Chapter One, try to avoid mode coupling in the transducer so that more input energy is converted into the main resonant mode. As mentioned already, any device using a layer of couplant may not provide efficient energy transfer into the piezoelectric. A subject of further work would be to consider transducer face compliance and its effect on the transducer response.

4.6.2 Comparison between Signals from a Step Force on the Opposite Surface at 20 cm using the Original Bi-laminar Disc Transducer and a Modified Transducer.

Section 4.6.1 has shown that the AE waveform, from the FE model of a step force on the opposite plate surface with 20 cm propagation, does not just excite the main resonant mode of the transducer, but a number of different modes. A resonant transducer will provide maximum sensitivity at a particular resonant frequency and so the ability to fully excite individual resonant modes is important, for achieving maximum AE detection. This section considers how the sensitivity of the transducer may be improved.

Using the PIGS post-processing facility in PAFEC, the transducer vibration was studied in section 4.6.1. One general observation, was that the plastic protective facing showed greater displacement than the piezoelectric element. This suggested that the plastic was acting as a compliant layer, lowering the displacement at the piezoelectric and, thus, the potential sensitivity of the transducer. A stiffer plastic disc was modelled to see if a larger amplitude voltage signal could be achieved.

In PAFEC, the data file containing the material properties was changed to simulate a stiffer facing material. The Young's modulus (E) was increased, and so was the density (ρ), to try and simulate a realistic material (gains in one property are rarely large without other properties being affected). Higher density would also improve the acoustic impedance match between the plastic and steel. These material properties were given the values seen in table 4.4.

Property [Units]	Original Transducer Face	Modified Transducer Face
E [N/m^2]	8.66×10^9	50×10^9
ρ [kg/m^3]	1037	3000

Table 4.4 Original and Modified Transducer Face Material Properties.

The modified transducer was modelled, attached to the steel plate shown in fig. 4.2, with a step force input, seen in fig. 4.3, applied to a node on the opposite surface, at a 20 cm

propagation distance. The output voltage was compared to that from the OS signal with the original transducer (fig. 4.52).

The stiffer facing material in the modified design gives an improved sensitivity, with maximum voltage amplitudes approximately three times greater than with the original plastic face. Using the modified face properties in the multilayer transduction theory by Hill et al. [**50**] in Chapter Two, a similar increase in amplitude (2.95 times) is predicted for the resonant mode in the 100-200 kHz range. This confirming the improved sensitivity predicted by the transient FE model.

The arrival time of the P-wave is clearly the same, indicated by the fact that both transducer signals have their first output voltage (fig. 4.52) at this time (33.3 μs).

Immediately, the MT (modified transducer) signal shows an increase in the output voltage amplitude and, hence, shows an increase in the transducer sensitivity, due to the new facing disc (the output voltage scale is the same for both signals). The improved transducer shows the features in the output voltage signal more clearly.

The period of the transducer oscillation is again approximately 7 μs, corresponding to a frequency of about 146 kHz, indicating that the transducer resonance is still governed by the piezoelectric disc, rather than the facing disc. The period is not exactly 7 μs and varies with each oscillation indicating several modes are being excited and a pure radial mode has still not been achieved.

Despite the increased sensitivity, the transducer vibration in fig. 4.53 looks very similar to the unmodified design in fig. 4.49. At 40 μs, the only obvious difference between the modified transducer and the original transducer, is that there is more displacement, at the bottom left hand corner, in the piezoelectric in the MT (fig. 4.54). At 60 μs, the two designs show very similar displacement patterns and this is reflected in the fact that they both produce a similar output voltage amplitude, at this time.

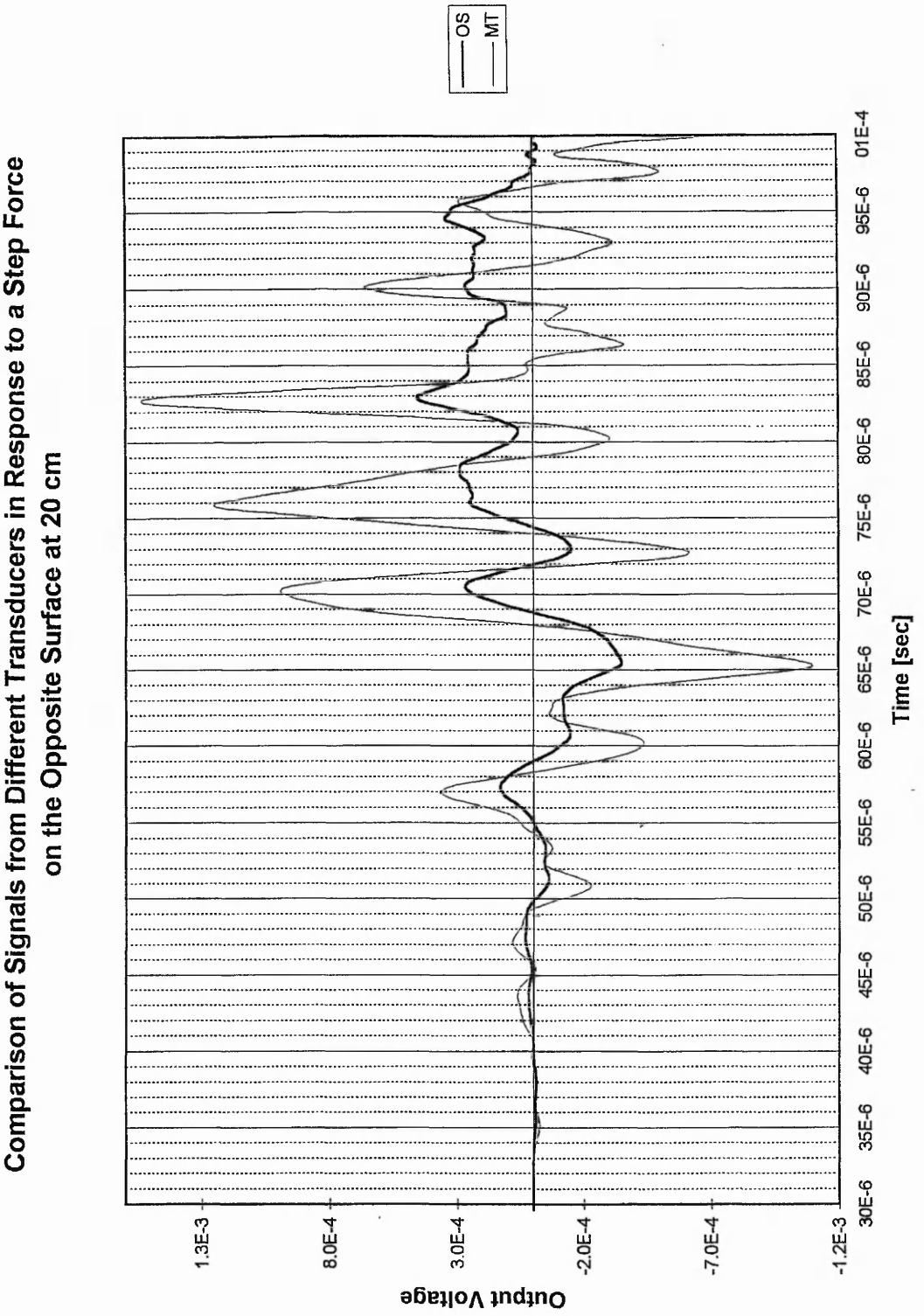

Fig. 4.52 Comparison of transducer signals from the original bi-laminar disc transducer (OS), and a modified transducer (MT), for a step force, on the opposite surface of the plate, at a source-transducer distance of 20 cm.

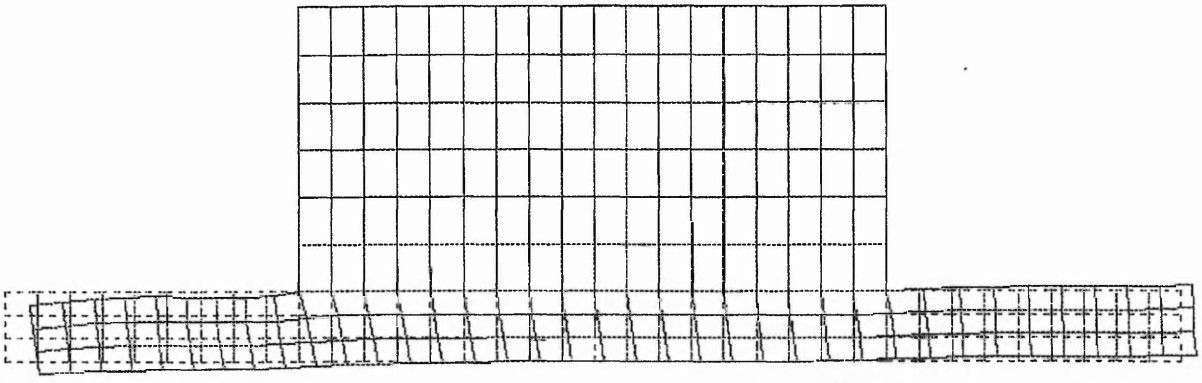

Fig. 4.53 Deformed modified transducer structure at 40 μs. The source is a step force, on the opposite surface of the plate, at a source-transducer distance of 20 cm. The dashed lines represents the undeformed structure.

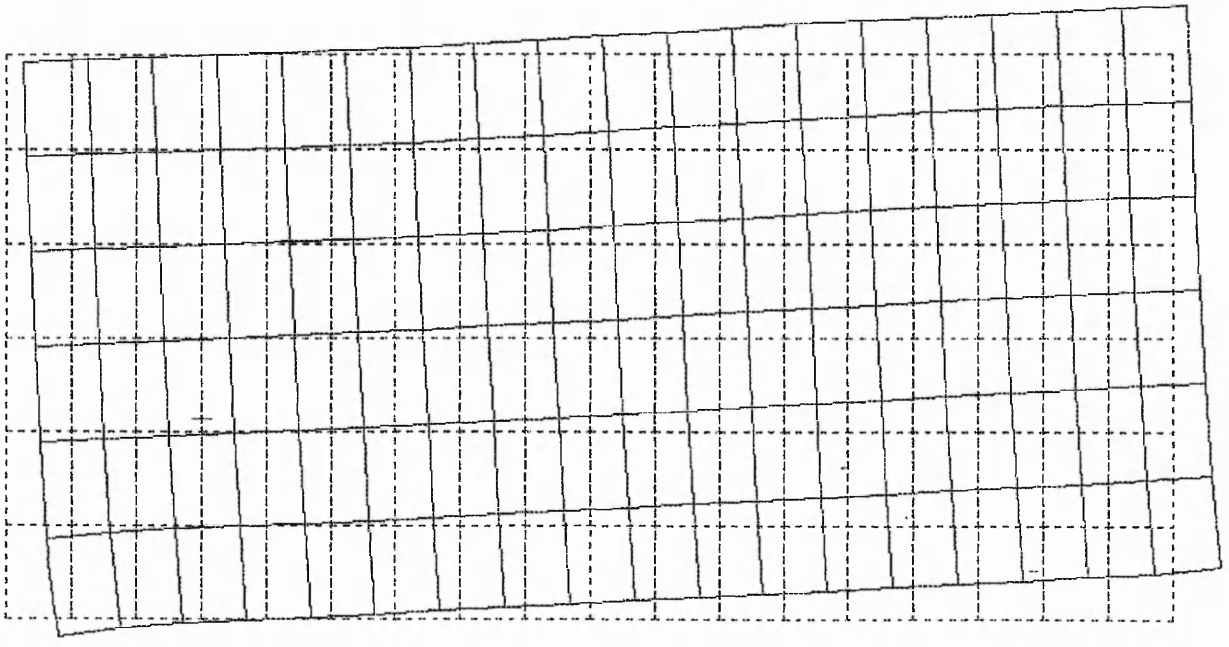

Fig. 4.54 Deformed piezoelectric structure at 40 μs for the modified transducer. The input is a step force, on the same surface of the plate, at a source-transducer distance of 20 cm. The dashed lines represents the undeformed structure.

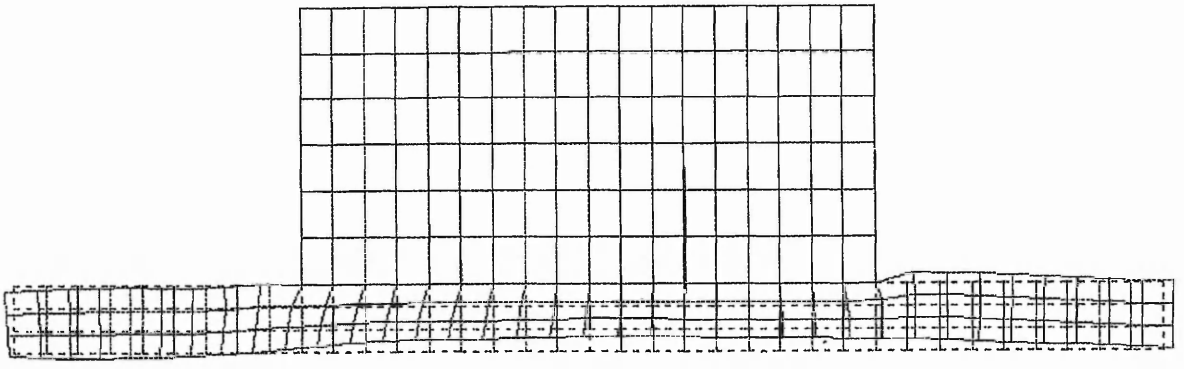

Fig. 4.55 Deformed transducer structure at 65 μs for the modified transducer. The input is a step force, on the same surface of the plate, at a source-transducer distance of 20 cm. The dashed lines represents the undeformed structure.

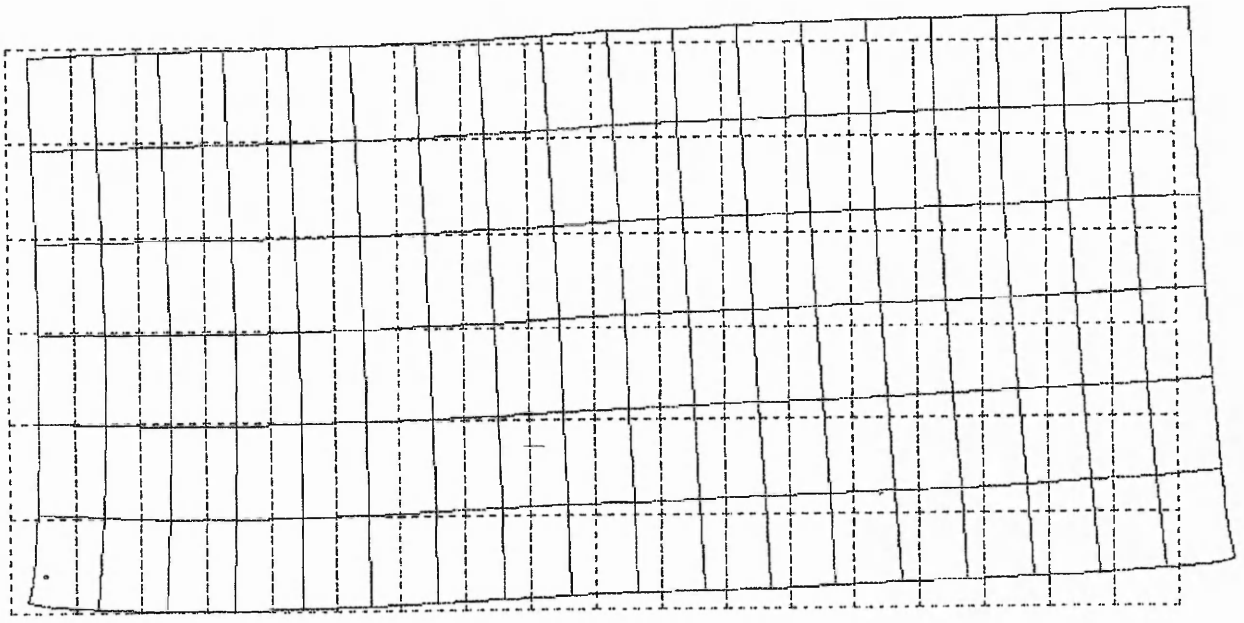

Fig. 4.56 Deformed piezoelectric structure at 65 μs for the modified transducer. The input is a step force, on the same surface of the plate, at a source-transducer distance of 20 cm. The dashed lines represents the undeformed structure.

Due to the stiffer plastic, relatively less normal deformation is seen in the transducer face (fig. 4.55) at 65 μs, when the face is compressed. There is symmetrical radial deformation in the plastic at this time that leads to improved excitation of the main radial mode, seen in the increased signal amplitude (fig. 4.52). Again, the bottom left hand corner is displaced more in the MT piezoelectric (fig. 4.56), thus resulting in a higher output voltage at this time. This suggests the lower compliance of the MT plastic has a greater constraining effect on the piezoelectric vibration. The vibration modes of the transducer are still hard to define, because multiple modes are still being excited. However, more effective energy transfer is occurring, resulting in a much larger amplitude of signal.

By changing two major material properties, the Young's modulus and the density, several acoustic and dynamic properties are altered as a result and are seen in table 4.5.

Property	Original Transducer	Modified Transducer	PZT-5A	Steel
c [ms-1]	3353	4737	4350	6006
Z [kg m-2 s-1]	3.48×10^6	14.21×10^6	3.35×10^7	4.68×10^7
D [Nm]	1.44	8.3	-	-
G [Nm-2]	3.33×10^9	19.23×10^9	-	-
Theoretical output wave amplitude [per unit input]	2.56×10^{-4} at 132.5 kHz	7.56×10^{-4} at 167 kHz	-	-

Table 4.5 Comparison of plastic facing disc properties for the original transducer and the modified transducer designs.

These include the wave velocity that increases from 3353 ms^{-1} to 4737 ms^{-1}, thus giving a much improved acoustic impedance (Z) match with the piezoelectric and steel. The flexural rigidity of the plastic is also increased, reducing the bending at the edges of the plastic and improving the energy input to the piezoelectric. One other property that has been affected is the shear modulus G that has increased in the MT plastic to nearly 6 times the value in the original plastic. This reduces the shearing action seen in the plastic

in fig. 4.45 and, reduces the dissipative effect of the plastic wear face on the incoming wave energy.

The modelled change in the material properties of the transducer face, presented in this section, highlights the usefulness of FEM. Using the modelling alone, a variety of transducer construction materials can be modelled and the best ones selected, before any building of transducers is carried out.

The large changes to several of the facing disc properties come as a result of changing the material density and Young's modulus. These changes to the properties, seen in table 4.5, result in great improvements to the sensitivity of such a simple design as the bi-laminar disc transducer. The choices of every transducer component with regard to both material properties and, as seen in Chapters Two and Three, the component geometry is seen to be critical to the overall transducer performance. FEM provides a valuable design tool to explore the choice of components. The transient modelling provides another method of predicting the performance of a transducer to a realistic broadband ultrasonic source, and might be used to compliment initial design work using sinusoidal models.

4.7 EXPERIMENTAL DATA FROM A PRACTICAL APPLICATION & ITS COMPARISON WITH TRANSIENT FEM

The use of FEM to model transient AE problems is an area in which there is great potential for increasing the understanding of AE detection in practical situations. Hamstad and others have used FEM to quantify various AE parameters. This thesis has shown further potential in the area of transduction modelling, another important factor in the understanding of transient waveforms.

Comparison between FE and experimental data has shown some agreement in section 4.4, with differences in transducer resonant frequency and bandwidth being identified as the major contributors to the waveforms produced. The FE modelling in section 4.5.1 considered the response of a resonant device to the AE waveform from a surface crack

in a 25 mm thick steel plate. Recently, Hamstad [**28**] has presented work regarding such an event in a steel bridge plate of similar dimensions. It was felt that a brief comparison between these practical waveforms and the FEM waveforms would be of interest to observe the differences in the features.

The study by Hamstad has shown that it is important to position the sensors correctly in order to detect the most suitable signals in practical work. Ductile bridge steels were shown to give small amplitude acoustic emissions, making it harder to isolate them from any noise in the system. This experimental study also commented that the choice of useful AE waveforms, from the vast quantity of waveforms obtained, was done by the human eye. Automating such a process and the integrating of model waveforms is another way in which FEM might be of use. Perhaps techniques such as analysing the partitioning of signal energy in a time window, considered in section 4.5.3, will also prove useful in practical situations.

Hamstad's work used both resonant and broadband sensors to detect the acoustic emissions from a crack growing in steel samples of nominally 25 mm thickness (the same used in the Chapter 4 models). The resonant device was given a narrow 100-300 kHz bandpass, while the broadband sensor was given a 50-1500 kHz bandpass. Fig. 4.57 shows broadband (labelled wideband) and resonant transducer signals from two classes of crack AE. The small signal-to-noise ratio is immediately apparent in the signals. Taking the waveforms W1 and R5 (fig. 4.57a), the waveforms have a similar shape but the resonant sensor ringing effect is apparent after 160 μs, when the amplitude is failing to return to its pre-excitation value, unlike the W1 signal. The ringing in the resonant device was seen to occur in the FE model at the main resonant frequency of the transducer. In this study, the period of the ringing indicates a resonant frequency of approximately 143 kHz, similar to the 2D transducer in the FE models.

Differences between the broadband and resonant sensors are more obvious in fig. 4.57b, with the broadband signals showing lower frequency components.

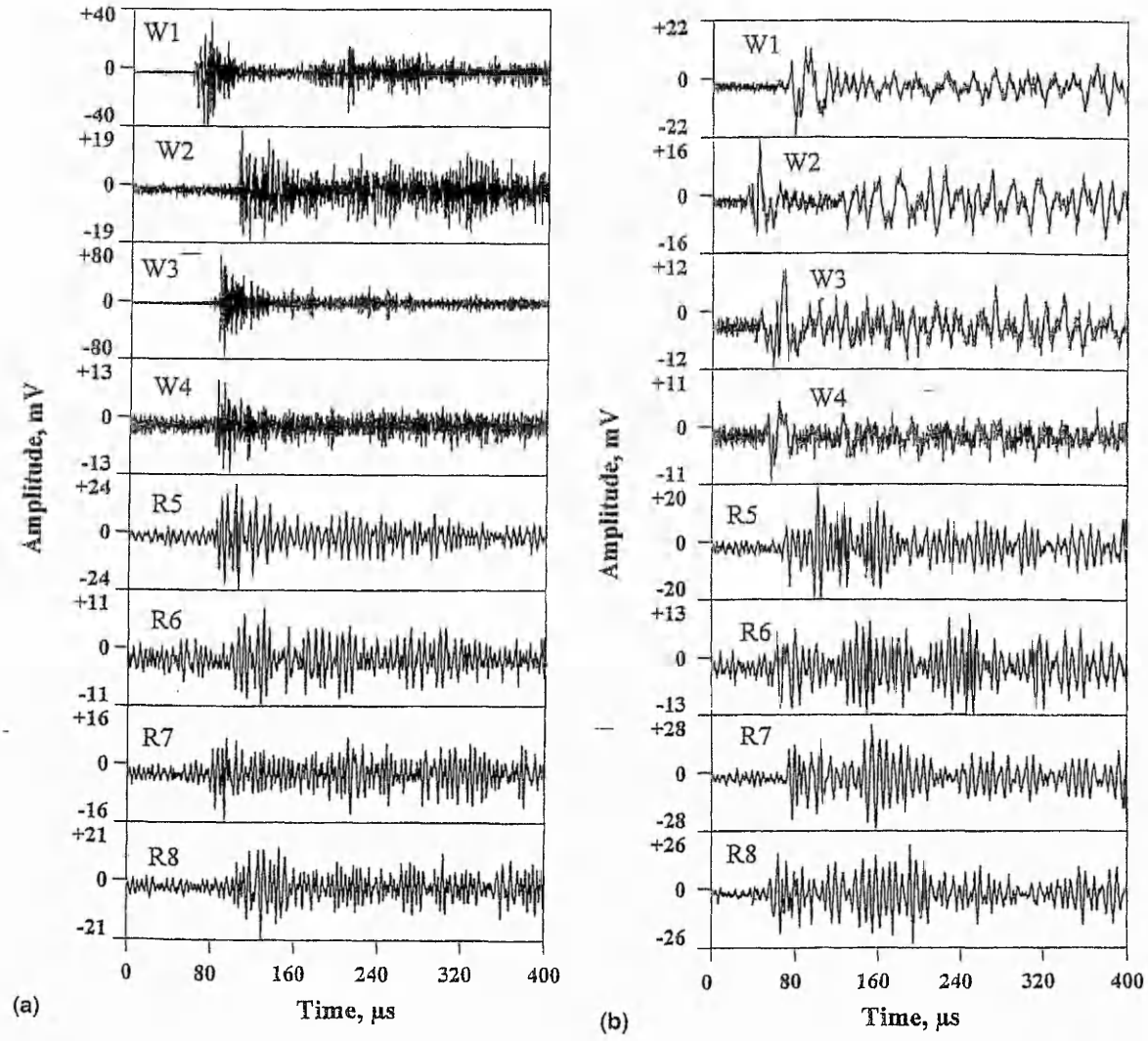

Fig. 4.57a (left) & Fig. 4.57b (right) Typical waveforms for two classes of crack acoustic emission signals. Broadband and resonant sensors are labelled W and R respectively. The waveforms are taken from an experimental study by Hamstad et al [**28**].

The resonant signals are again dominated by the transducer's resonant frequency (approx. 143 kHz), while the broadband signals show longer periods of oscillations with the higher frequencies superimposed on top. This pattern was seen in the FE models because of their unlimited lower bandpass. Measuring the periods in the broadband signals, approximate frequency components are 50, 60, 70 and 95 kHz, all of which are below the 100 kHz limit of the resonant device.

In the finite element models, considered in sections 4.3 and 4.5, the signals produced by the resonant sensor in response to simulated AE sources were dominated by the resonant frequency of the transducer. However, the models are not restricted by any bandpass (other than that imposed by the model resolution (>500 kHz)) and, therefore, the signals also demonstrate lower and higher frequency content, away from the main resonant frequency.

In fig. 4.57b, signal W1 shows the large amplitude features around 80 μs that bear resemblance to the signal features of fig. 4.41 between 55 and 70 μs. No direct comparison is being attempted because of the differences in the experimental and FE systems. However, the apparent lack of features in the experimental resonant waveforms is due to the lack of bandwidth and is not due to the device itself. In fact, the broadband sensors, labelled W in fig. 4.57b, still illustrate some resonant characteristics because it is impossible to get a purely flat response from a transducer.

The transient FE models suggest that increased experimental bandwidth is required, even when using resonant devices in order that the maximum AE detail is presented. Detection of the DC offset, seen in some of the FE models, would require very low frequencies to be present, possibly down to audio frequencies. The fact that even the latest experimental work still raises the same questions of sensor choice, location and signal-to-noise ratio shows that FEM research, such as presented in this thesis, may help to find answers in the future.

CONCLUSIONS

The motivation behind the work in this thesis was to gain a better understanding of the behaviour of resonant ultrasonic transducers, in order that their response to transient broadband excitation, such as acoustic emission events and other ultrasonic waveforms used in nondestructive evaluation of materials, might be better understood. The post processing facilities of the PAFEC-FE vibroacoustics software were used to successfully categorise the resonant behaviour of several transducer designs. Understanding the complexities of ultrasonic transduction suggests design changes that could improve the transducer performance. The FE software was further used to model the entire wave propagation problem associated with acoustic emission detection in plate like structures, providing improved understanding of the transient response of a resonant transducer.

Chapter One reviewed a variety of ultrasonic transducers and their many applications. Although broadband devices are popular, resonant transducers have been chosen by other workers for several applications involving the generation and detection of Lamb wave modes. These dispersive ultrasonic waves propagate in plate like structures and are seen as a useful NDE tool.

New 1-3 composite transducer designs provide improved sensitivity over conventional piezoelectric devices. However, their complicated manufacture leads to high costs. Metal-ceramic composites have been suggested as an alternative method of improving the performance of a standard piezoelectric disc. FEM is increasingly employed as a design tool for these numerous composite transducers.

Chapter Two established that acoustic FEM was the most realistic method of predicting resonant frequencies of practical transducers. The method involved modelling an acoustic wave emitted from a point source in a fluid, at a fixed distance. A 175 kHz bilaminar disc transducer was modelled and close agreement with experimental results led to the use of this method for the majority of the work in this thesis.

Several methods of comparing the sensitivity of different resonant transducer designs were attempted. Relative output voltages from a constant acoustic source, received through water, were found to be one suitable method. Alternatives considered the voltage produced by a displacement at the transducer face (V/m). The electrode detects an average voltage produced across its area when the piezoelectric material is subjected to deformation. This leads to the sensitivity varying across the transducer face depending on the method of excitation, making it hard to specify the overall sensitivity of the transducer. The use of various excitation methods and boundary conditions in different FE models has shown how the resonant modes are very susceptible to small changes in the mode of excitation. Again, the acoustic FE method appeared to offer the best solution.

Effects of mounting transducers to metal plates were studied, simulating the real life situation where a transducer is mounted to a structural member, in a bridge for example. The most appropriate method of modelling such mounting again involved detecting an acoustic source passing through water, then the plate and the transducer. Such mounting was found to cause a slight shift in the transducer frequency response increasing the main resonance from 176.5 kHz to 187 kHz by FEM and experimental measurement. This knowledge allows these effects to be considered at the design stage. Applying multilayer transduction theory [**50**] to the problem was appropriate for predicting the frequency shifts of certain resonant modes, while enforced harmonic displacement FEM and radiation loading theory [**49**] were found to be inappropriate (both predicting frequency shifts of approximately 40 kHz).

In **Chapter Three** a metal-ceramic composite design was considered involving an exponential horn design. Studies of this theoretical design have led to improved understanding as to how sensitivity improvements can be achieved. Optimising transducer design was considered to be an area in which FEM could give an advantage over conventional methods of designing ultrasonic transducers. A 40 kHz transducer, intended for geotechnical AE work, was modelled and the design was optimised to give maximum sensitivity at its 40 kHz resonant frequency. The brass exponential horn section had a length of 47.55 mm with a 5.15 mm diameter throat and a mouth diameter

of 49.30 mm. The optimum brass back plate diameter was found to be 25 mm for a 4.9 mm thick back plate. For the optimum transducer resonance performance at 40 kHz, the 5 mm thick piezoelectric disc element should have a diameter of 3.75 mm. The FE model predicted an output voltage for the optimised design of over 500 times the original design output voltage, for the 40 kHz mode of interest. Such a large increase prediction was seen to be a success with regard to the use of FEM to carefully modify a given design. However, the large increase was also an indicator that further damping (other than that provided by the fluid region) needs to be applied to the FE modelling before the output amplitude predictions can be used in confidence.

This work highlighted the benefits of FEM, allowing methodical testing of design variations before manufacture. Again, the acoustic FE method was shown to provide realistic frequency predictions when compared with experiment.

To obtain a full understanding of the process of transient wave detection, the full AE event was modelled in a 25 mm thick steel plate in **Chapter Four**. This work highlighted several important issues regarding the response of resonant transducers and the capabilities of FEM in understanding this process. Two distinct methods of modelling an acoustic emission source were used as input to a simple resonant transducer. One method involved using displacement-time data, produced by the "GPLATE" computer program (due to Hsu [**59**]), as the input to numerous points on the transducer face. This method used a time resolution of 0.05 μs and was suitable for modelling the response for frequencies up to 1 MHz. The second method involved the use of FEM to model transient wave propagation and transducer response combined. This method used a 2D FE model because a 3D model was not practical due to computational requirements. The temporal and spatial resolution used in this model was suitable for frequencies up to 250 kHz.

The advantage of using input data produced by another method (e.g. the GPLATE program) meant that input data could be compared from a variety of excitation sources. For example, the wave propagation through a large structure could be modelled using a specialist workstation and software only available at research establishments. The output

from this analysis could then be used by others, on their own available systems, as input to smaller models of various transducers to find the most suitable design, whilst avoiding having to re-run the lengthy wave propagation problem (typically several days).

Using FEM to model the whole problem of source excitation, wave propagation and transduction, in one model, was found to be a more robust method. Use of FEM for transient problems allows complex geometry and the effect of a variety of sources to be explored. Computer programs such as the GPLATE program are more limited in their application when propagation occurs into the far field. Even when working in the near field, coupling the theoretical output to the FE transducer model become problematic.

With regard to modelling the resonant devices, full wave propagation transient modelling has shown that it is possible to distinguish between different source positions within the thickness of a 25 mm thick steel plate, from detail on the transducer signal. This emphasises the continuing usefulness of resonant transducers to experimental AE studies, due to their sensitivity advantages over broadband devices. The front end of the transducer signal was shown to closely represent the input at the transducer face, before transducer resonance sets in. Lamb wave modes dominated the transducer excitation and were seen to vary in influence, depending on the source location within the depth of the plate. Asymmetric modes (L_{21}, L_{22}) dominated with a source near to or at the plate surface, whilst symmetric modes (L_{12}, L_{11}) dominated with a source located at the plate centre (for the square step up then step down force and the dipole force sources used in this thesis).

With the aim of automating AE signal identification in the future, the distribution of normalised signal energy in a time window was investigated and found to be of potential use. The same source was seen to give a unique distribution of energy at each propagation distance from the transducer. Similarly, the energy distribution from a source at a fixed distance (20 cm from the transducer) was seen to vary with depth. Both methods provide further information to the user of acoustic emission and are methods that could be implemented in future for specific structural defect monitoring tasks.

The use of transient FEM is still in its early days. Improvements to the modelling will eventually lead to an exact prediction of the transducer response to various types of AE source. Even with the approximations employed in Chapter Four, similarities between FEM and experimental results were seen.

Improvements to the computer model would include improved time and spatial resolution (smaller time increments and element lengths), allowing for increased bandwidth. The models would also benefit from the inclusion of more realistic damping to the responses of materials and piezoelectrics. Improvements in the models would increase the realism of the FE output and provide greater confidence to potential users.

Comparing the FE results with data from a practical AE application suggested that further information might be obtained from a resonant device by increasing the bandpass to include frequencies down to perhaps 50 kHz. Low frequency flexure of the plate, seen in Chapter Four, suggests an attempt to include frequencies as low as 20 kHz should be made when carrying out experimental work. However, the effect of environmental noise would then become an issue.

The modelling of transient excitation, wave propagation and transducer response has only become feasible recently, due to the availability of increased computer power. The nature of modern computing and the rapid developments that occur, means that, even the workstation used for this study has now been superseded by improved hardware.

Bandpass filtering of the transducer signal predicted by the FE model, would allow a more realistic comparison to experimentally obtained data. A 50-250 kHz frequency range is suggested for further modelling with experimentation using the same bandwidth.

Finite element and boundary element methods are being continuously developed. New energy absorbing elements are now being used in specialist applications to model more realistic boundary effects and would provide a natural damping to the models.

With this in mind the future development of this work looks bright as it opens the door for much greater understanding of the complexities of ultrasound wave propagation and ultrasound transducer vibrational response. As the knowledge of the source/detector relationships are improved, catalogues of NDE problems could be developed, including information on their acoustic source and cause. This would allow improvements to automatic and real time monitoring of defects, but particularly to source identification. Computers could compare appropriate actual AE event data with simulated AE events from possible regions of concern, such as material joints, welds, etc. Quantitative AE would allow maintenance engineers to take suitable decisions regarding the requirement for any further structural inspection and decide on the need for possible repair/replacement procedures.

The work in this thesis has hopefully increased the understanding of FE modelling and its application to AE and ultrasonic NDE. Even a small company can now afford to use the methods outlined, to design transducers that are tailor made for specific applications. AE transducers (for instance) could be manufactured and distributed with a known response to a specific type of source, allowing the user a greater understanding of what is being detected without having to carry out numerous tests. Alternatively, the transient methods could help to position transducers more efficiently on a large structure for maximum effectiveness.

The possibilities for computer modelling of physical phenomena will be of great use in the future and studies such as this can only cover a limited range of the potential uses of this method. If the work in this thesis can help to further understanding of the propagation and detection of transient ultrasonic waves, then it has served its purpose well.

RECOMMENDATIONS FOR FURTHER WORK

A number of topics for further work arise from the work described in this thesis:

1. The optimised 40 kHz exponential horn transducer design, in section 3.5, should be built and evaluated experimentally. This will provide information related to the true behaviour and provide insight into factory which should be addressed when doing further FE modelling.

2. To establish the most realistic sensitivity measure from the modelling, experimental comparisons between different sensors should be made. Specifically, the sensitivity of the optimised exponential horn transducer (section 3.5) should be compared to the original design of exponential horn transducer (section 3.3) and experiment. These results will allow damping to be integrated into the modelling process.

3. As the computer hardware and software develops, the sophistication of the FE models can be improved. Short term improvements might involve increasing the temporal and spatial resolution to allow modelling up to higher frequencies (say up to 1 or 2 MHz). Post processing of the transducer waveform to restrict the bandwidth of the signal will allow closer comparison to be made with experimentally obtained AE waveforms (e.g. 50-250 kHz would be a typical bandpass for a 150 kHz transducer). Long term aims would be to develop a 3D model for the plate and transducer.

   Other suggested improvements to the FE model are to incorporate the transducer casing to take account of this when the stress wave passes beneath the transducer. The revised model might also use boundary elements on the plate surfaces that absorb energy, to simulate losses after reflections at boundaries.

4. The work in Chapter Four suggests that increasing the usual transducer bandpass used in practical work, when using resonant transducers, might provide more detail

on the nature of the AE source. Therefore, it is suggested that a variety of bandpasses are used in experimental work for comparison with the FE models.

5. Normalised signal energy distributions within a time window should be investigated experimentally. This may lead to further insights regarding the best time interval to be used within the capture window (10 μs has been studied in Chapter Four). Consideration also needs to be given to the effect upon the methodology if the signal front end cannot be found (the case when the signal to noise ratio is low).

REFERENCES

CHAPTER ONE

1 Ono K., Ohtsu M.
Analysis of Piezoelectric Disks and Cylinders Using Finite Element Method.
Progress in Acoustic Emission IV, Japanese Society for Non-Destructive Inspection. (1986).

2 Miller R., McIntire P.
Nondestructive Testing Handbook 2nd Edition - Volume 5 Acoustic Emission Section 15, pp. 515-530. American Society of Nondestructive Testing. (1987).

3 Birks A., Green R. McIntire P.
Nondestructive Testing Handbook 2nd Edition - Volume 7 Ultrasonic Testing.
Section 4, pp. 66-99. American Society of Nondestructive Testing. (1987).

4 Mattiat Oskar E.
Ultrasonic Transducer Materials.
Plenum Press. (1971).

5 Miller R., McIntire P.
Nondestructive Testing Handbook 2nd Edition - Volume 5 Acoustic Emission.
Section 5, pp. 123-133. American Society of Nondestructive Testing. (1987).

6 Mason.
Physical Acoustics.
Vol. 1A. Academic Press. (1964).

7 Macey P.C. (PAFEC Limited).
Analysis of Transducers Using Piezoelectric Finite Elements and Acoustic Boundary Elements.
Proceedings of the Institute of Acoustics, Vol. 12 (4), pp. 66-75. (1990).

8 Hamonic B., Decarpigny J.N.
Power Sonic and Ultrasonic Transducers Design.
Springer-Verlag. (1988).

9 Smith W.A., Shaulov A.A.
Composite Piezoelectrics: Basic Research to a Practical Device.
Ferroelectrics, Vol. 87, pp. 309-320. (1988).

10 Durris L. et al.
Airborne Ultrasonic Transducer.
ULTRASONICS, Vol.34, No.2-5, pp. 153-158. (1996).

11 Brush Clevite Company Limited. (1966).
A Data Book for Designers - Piezoelectricity.

12 Hayward G., Gachagan A.
An Evaluation of 1-3 Connectivity Composite Transducers for Air-coupled Ultrasonics Applications.
Journal of the Acoustic Society of America, Vol. 99 (4), Pt. 1, pp. 2148-2157. (1996).

13 Hossack J.A., Bedi R.L.
Design of Composite Piezoelectric Transducers.
Key Engineering Materials, Vols. 92-93, pp. 301-322. (1994). Trans Tech Publications.

14 Hossack J.A., Hayward G.
Finite-Element Analysis of 1-3 Composite Transducers.
IEEE Transactions on Ultrasonics, Ferroelectrics and Frequency Control, Vol. 38 (6), pp. 618-629. (1991).

15 Hayward G., Bennett J.
Assessing the Influence of Pillar Aspect Ratio on the Behaviour of 1-3 Connectivity Composite Transducers.
IEEE Transactions on Ultrasonics, Ferroelectrics and Frequency Control, Vol. 43 (1), pp. 98-108. Jan. (1996).

16 Mitra R., Saksena T.K.
Study on the vibrational characteristics of ultrasonic transducers using tapered piezoelectric ceramic elements.
Journal of the Acoustic Society of America, Vol. 101 (4), Pt. 1, pp. 323-329. Jan. (1997).

17 Onitsuka K., Dogan A. et al.
Metal-Ceramic Composite Transducer, The 'Moonie'.
Journal of Intelligent Material Systems and Structures, Vol. 6 (4), pp. 447-455. (1995).

18 Dogan A., Uchino K., Newnham R.E.
Composite Piezoelectric Transducer with Truncated conical Endcaps "Cymbal".
IEEE Transactions on Ultrasonics, Ferroelectrics and Frequency Control, Vol. 44 (3), pp. 597-605. (1997).

19 Bray D.E., Stanley R.K.
Nondestructive Evaluation.
McGraw-Hill Book Company. (1989).

20 Lemon D.K.
A Review of Advanced Acoustic Emission Sensors.
Battelle Pacific Northwest Laboratories. (1981).

21 Fortunko C.M., Boltz E.S.
Comparison of Absolute Sensitivity Limits of Various Ultrasonic and Vibration Transducers.
Materials Science Forum, Vol. 210-213, pp. 471-478. (1996).

22 Proctor T.M.
Journal of the Acoustic Society of America, Suppl. 1, 68, S568. (1980).

23 Koberna M.
Broadband Acoustic Emission Sensor with a Conical Active Element in Practice.
Journal of Acoustic Emission, Vol. 11 (2), pp. 61-63. (1993).

24 Proctor Thomas M.
A High Fidelity Piezoelectric Tangential Displacement Transducer for Acoustic Emission.
Journal of Acoustic Emission, Vol. 7 (1), pp. 41-47. (1988).

25 Ohara Y., Shiwa M., Yanagida H., Kishi T.
Design and Characterisation for Wide-Band AE Transducer by 1-3 Piezoelectric Composite.
Journal of the Ceramic Society of Japan,Vol. 103, pp. 655-660. (1995).

26 Gorman Michael R.
Some Connections Between AE Testing Large Structures and Small Samples.
Nondestructive Evaluation & Testing. (1997).

27 Surgeon M., Wevers M.
Modal analysis of acoustic emission signals from CFRP laminates.
NDT&E International, Vol. 32, pp. 311-322. (1999).

28 Hamstad M.A., McColskey J.D.
Detectablity of Slow Crack Growth in Bridge Steels by Acoustic Emission
Materials Evaluation Vol. 57 (32), pp. 1165-1174. Nov. (1999).

29 Cawley P.
The Rapid Non-Destructive Inspection of Large Composite Structures.
Composites, Vol. 1 (5), pp. 351-357. (1994).

30 Castaings M., Cawley P.
The Generation, Propagation, and Detection of Lamb Waves in Plates using Air-coupled Ultrasonic Transducers.
Journal of the Acoustic Society of America, Vol. 100 (5), pp. 3070-77. (1996).

31 Maji A.K., Satpathi D., Kratochvil T.
Acoustic Emission Source Location Using Lamb Wave Modes.
Journal of Engineering Mechanics. pp. 154-161. Feb. (1997).

32 Moulin E., Assaad J., Delebarre C.
Piezoelectric transducer embedded in a compositeplate: Application to Lamb wave generation.
Journal of Applied Physics. Vol. 82 (5), pp. 2049-2055. Sep. (1997).

33 Moser F., Jacobs L.J.
Application of Finite Element methods to study transient wave propagation in elastic waveguides.
Review of Progress in Quantitative NDE, Vol. 17, pp. 161-167. (1998).

34 Moser F., Jacobs L., Qu J.
Modelling Elastic Wave Propagation in Waveguides with the Finite Element Method.
NDT&E Interantional, Vol. 32, pp. 225-234. (1999).

35 Hamstad M.A., Guo D., Mal A.
Acoustic Emission Wavefield Calculations in a Plate.
Progress in Acoustic Emission IX. pp. IV19-29. (1998).

36 Hamstad M.A., Gary J., O'Gallagher A.
Wideband Acoustic Emission Displacement Signals as a Function of Source Rise Time.
Progress in Acoustic Emission IX. pp. IV48-56. (1998).

37 PAFEC-FE Level 8.1.
Acoustics User Manual.
PAFEC Limited.

38 Macey P.C.
Finite Element/Boundary Element Modelling Techniques Applied to Ring Transducers with Viscoelastic Coating.
Ferroelectrics Vol. 187, pp. 201-211. (1996).

39 Guo N., Cawley P.
The Finite Element Analysis of the Vibration Characteristics of Piezoelectric Discs.
Journal of Sound & Vibration, Vol. 159, pp. 115-138. (1992).

40 Guo N., Cawley P.
Transient Response of Piezoelectric Discs to Applied Voltage Pulses.
Ultrasonics, Vol. 29, pp. 208-217. May (1991).

41 Allik H., Hughes Thomas J.R.
Finite Element Method for Piezoelectric Vibration.
International Journal for Numerical Methods in Engineering, Vol. 2, pp. 115-157. (1970).

42 Brissaud M.
Three Dimensional Model for the Mode Analysis of a Loaded Piezoelectric Plate.
INSA, France. (1994)

43 PAFEC-FE Level 8.5.
Theory.
PAFEC Limited.

44 Henshell R.D., Macey P.C.
A Major Structural Analysis System with a Full Acoustic Capability.
Proceedings of StruCoMe 88. PAFEC Ltd.

45 PAFEC.
Data Preparation Manuals.
PAFEC Ltd.

46 PAFEC.
Interactive Graphics System (PIGS) User Manuals.
PAFEC Ltd.

CHAPTER TWO

47 Redwood M.
Coupling between Two Modes of Vibration in a Piezoelectric Resonator.
Journal of the Acoustic Society of America, Vol. 38 (4), pp. 576-582. (1965).

48 IEEE 177. (1966).
Standard Definitions and Methods of Measurement for Piezoelectric Vibrators.

49 Kinsler, Frey.
Fundamentals of Acoustics.
Second Edition, John Wiley & Sons. (1962).

50 Hill R., El-Dardiry S.
Variables in the Use and Design of Acoustic Emission Transducers
Ultrasonics, 9-16. January (1981).

CHAPTER THREE

51 Nicholson N.C., McDicken W.N.
A Comparison of Coupling Horns for Waveguides used in Medical Ultrasonics.
Ultrasonics, Vol. 34, pp. 747-755. (1996).

52 Mason W.P., Wick R.F.
A Barium Titanate Transducer Capable of Large Motion at an Ultrasonic Frequency.
Journal of the Acoustical Society of America, Vol. 23 (2), pp. 209-214. (1951).

53 Lin Shuyu.
Study on the Longitudinal-Torsional Composite Mode Exponential Ultrasonic Horns.
Ultrasonics Vol. 34, pp. 757-762. (1996).

54 Lin Shuyu.
Study on the Longitudinal-Torsional Composite Vibration of a Sectional Exponential Horn.
Journal of the Acoustical Society of America, Vol. 102 (3), pp. 1388-1393. (1997).

55 Hoffmann E, Jatho M.
The Acoustic Trachea of Tettigoniids as an Exponential Horn-theoretical calculations and bioacoustical measurements.
Journal of the Acoustical Society of America, Vol. 98 (4), pp.1845-51. (1995).

56 Timoshenko S., Young D.H., Weaver W.
Vibration Problems in Engineering 4th ed.
John Wiley & Sons, Inc. (1974).

57 Meirovitch L.
Principles and Techniques of Vibrations
Prentice-Hall, Inc. New Jersey (1997).

58 Morse, Ingard.
Theoretical Acoustics
McGraw-Hill, Inc. (1968).

CHAPTER FOUR

59 Hsu N.
Dynamic Green's Functions of an Infinite Plate - a computer program.
U.S. Department of Commerce, Malcom Baldrige. (1985).

60 Jaleel K.M.A., Kishore N.N., Sundararajan V.
Finite-Element Simulation of Elastic Wave Propagation in Orthotropic Composite Materials.
Materials Evaluation, pp. 830-838. July (1993).

61 Alleyne D., Cawley P.
A two-dimensional Fourier transform method for measurement of propagating multimode signals.
Journal of the Acoustical Society of America, Vol. 89 (3), pp. 1159-68. (1991).

ADDITIONAL PAPERS

62 Eisner Edward.
Design of Sonic Amplitude Transformers for High Magnification.
Journal of the Acoustical Society of America, Vol. 35 (9), pp. 1367-1377. (1963).

63 Neppiras E.A.
Very High Energy Ultrasonics.
British Journal of Applied Physics, Vol. 11, pp. 143-150. (1960).

64 Eisner E., Seager J.S
A Longitudinally Resonant Stub for Vibration of Large Amplitude.
Ultrasonics, Vol. 3, pp. 88-98. (1965).

65 Ono K., Ohtsu M.
The Generalised Theory and Source Representations of Acoustic Emission.
Journal of Acoustic Emission, Vol. 5 (4), pp. 124-133. (1986).

66 Lamb H., Southwell R.V.
On the Free Transverse Vibrations of a Uniform Circular Disc Clamped at its Centre; and on the Effects of Rotation.
(1921).

67 Pao Y., Gajewski R., Ceranoglu A.N.
Acoustic emission and transient waves in an elastic plate.
Journal of the Acoustical Society of America, Vol. 65 (1), pp. 96-105. Jan. (1979).

68 Hill R., Forsyth S., Macey P.C.
Modelling Acoustic Emission Transducers using Finite Element Methods.
Progress in Acoustic Emission IX. pp. IV86-95. (1998).

69 Hill R., Okoroafor E.U., Priston A.-M.
Acoustic emission and wave propagation model and issues of damage induction in composites.
Ultrasonics, Vol.34, pp. 321-325. (1996).

70 Weaver L., Pao Y.
Spectra of transient waves in elastic plates.
Journal of the Acoustical Society of America, Vol. 72 (6), pp. 1933-1941. Dec. (1982).

BIBLIOGRAPHY

71 PHILLIPS Application Book, pp 43-45.
Piezoelectric Ceramics.
Electronics Components and Materials Division. (1968).

72 Beranek Leo L.
Acoustics.
McGraw-Hill Electrical & Electronic Engineering Series. (1954).

73 Bray Don E., Stanley Roderick K.
Nondestructive Evaluation - A Tool in Design, Manufacturing, and Service.
Revised Edition, CRC Press. (1997).

74 Wert C.A., Thompson R.M.
Physics of Solids.
Second Edition, McGraw-Hill Series in Materials Science and Engineering. (1964).

75 Christman J. Richard.
Fundamentals of Solid State Physics.
John Wiley & Sons, Inc. (1988).

76 Geradin M., Rixen D.
Mechanical Vibrations - Theory and Application to Structural Dynamics.
Second Edition, Wiley. (1997).

77 Wait R., Mitchell A.R.
Finite Element Analysis and Applications.
John Wiley & Sons, Inc. (1985).

78 DeVries P.L.
A first course in Computational Physics.
John Wiley & Sons, Inc. (1994).

79 MacKeown P.K., Newman D.J.
Computational Techniques in Physics.
Adam Hilger, Bristol. (1987).

80 Akin J.Ed.
Finite Element Analysis for Undergraduates.
Academic Press. (1986).

81 Georgi H.
The Physics of Waves.
Prentice-Hall, Inc. New Jersey. (1993).

APPENDIX I

EXAMPLE OF A PAFEC-FE DATA FILE USED FOR AN ACOUSTIC SINUSOIDAL ANALYSIS OF THE BI-LAMINAR DISC TRANSDUCER

```
C
C   DATA FILE PRODUCED BY PIGS
C
C
TITLE AXIS-SYM. PROBLEM WITH PIEZO-EL. TRANSDUCER PZT_5A
CONTROL
SKIP.COLLAPSE
FRONTAL.SINUSOIDAL.SOLUTION
AXISYMMETRIC
HARMONIC.NUMBER=0
PHASE=7
BASE=10000000
ADD.PROG:
    CALL R09890(74,3,1)
    CALL R09890(83,1,1)
END.OF.ADD.PROG
CONTROL.END
C
C
C   *** THE NODES MODULE IS PRINTED
C   *** USING GLOBAL CARTESIAN AXES
C
NODES
Z=          0.0000000
 NODE        X                Y
    1       0.0000000        0.0000000
    2       0.0000000        0.50099992E-02
    3       0.0000000        0.10000000E-01
    4      -0.12199999E-02     0.0000000
    5      -0.12199999E-02     0.50099992E-02
    6      -0.12199999E-02     0.10000000E-01
    7      -0.12199999E-02     0.0000000
    8      -0.12199999E-02     0.50099992E-02
    9      -0.62299994E-02     0.0000000
   10      -0.62299994E-02      0.50099992E-02
   11       0.0000000         0.0000000
   12       0.0000000         0.10000000E-01
   13       0.38268337E-02      0.92387940E-02
   14       0.70710672E-02      0.70710672E-02
   15       0.92387940E-02      0.38268337E-02
   16       0.10000000E-01      0.0000000
   17       0.10000000E-01      0.0000000
   18       0.99969865E-02      0.24541226E-03
   19       0.99879529E-02      0.49067669E-03
```

```
   20        0.99729039E-02        0.73564560E-03
(etc.)
ELEMENTS
GROU=1
 NUMB  ELEM  PROP  TOPO
    1 42130    14    17    19    18
    2 42130    14    19    21    20
    3 42130    14    21    23    22
    4 42130    14    23    25    24
    5 42130    14    25    27    26
    6 42130    14    27    29    28
    7 42130    14    29    31    30
    8 42130    14    31    33    32
    9 42130    14    33    35    34
   10 42130    14    35    37    36
(etc. for flexible membrane )
   33 35425    11     4    83   106   108    82    97    98   107
   34 35425    11    83    85   108   110    84    98    99   109
   35 35425    11    85    87   110   112    86    99   100   111
   36 35425    11    87    89   112   114    88   100   101   113
   37 35425    11    89    91   114   116    90   101   102   115
   38 35425    11    91    93   116   118    92   102   103   117
   39 35425    11    93    95   118   120    94   103   104   119
   40 35425    11    95     5   120   122    96   104   105   121
   41 35425    11   106   108     9   133   107   123   124   132
   42 35425    11   108   110   133   135   109   124   125   134
   43 35425    11   110   112   135   137   111   125   126   136
   44 35425    11   112   114   137   139   113   126   127   138
   45 35425    11   114   116   139   141   115   127   128   140
(etc. for piezoelectric elements)
  559 29210    13  1266  1268  1289  1267  1279  1278
  560 29210    13  1268  1291  1289  1280  1290  1279
  561 29210    13  1268  1270  1291  1269  1281  1280
  562 29210    13  1270  1293  1291  1282  1292  1281
  563 29210    13  1270  1272  1293  1271  1283  1282
  564 29210    13  1272  1295  1293  1284  1294  1283
  565 29210    13  1272  1274  1295  1273  1285  1284
(etc. for fluid finite elements)
  593 23610    13  1406 1405 1404 1403 1402 1401 1400
*              1399 1398 1397 1396 1395 1394 1393 1392 1391 1390
*              1389 1388 1387 1386 1385 1384 1383 1382 1381 1380
*              1379 1378 1377 1376 1375 1374 1373 1372 1371 1370
*              1369 1368 1367 1366 1365 1364 1363 1362 1361 1360
*              1359 1358 1357 1356 1355 1354 1353 1352 1351 1350
*              1349 1348 1347 1346 1345 1344 1343 1342
(element 593 is the boundary element)
C
C ------------------------------------------------------------
C
```

```
 PLATES.AND.SHELLS
  PLATE  MATE  THICK  RAD1
  14     14    0.001  0.15
  12     12    0.001
C
C
C --- defined for light flex. membrane
```

(this was necessary for acoustic analyses on early versions of PAFEC)

```
C    ------------------------------
 MATERIAL
  MATE  E     NU  RO
  14    209E0 0.3 7800E-9
C
C
C --- defined for water
C    -----------------
 MATERIAL
  MATE  RO    BULK
  13    1000  2.05E9
C
C
C --- define for plastic (EPOXID FIBRE FR4  BS4584 SECTION 102.5)
C                  m=3.072E-3 Kg; T=5.01E-3 m; r=10.02E-3 m
C                  c=2889 m/s; ro=1037 Kg/m; NU=0.3; E=8.66E9 N/m
C    ---------------------------------------------------------------
 MATERIAL
  MATE  E     NU   RO
  12    8.66E9 0.30 1037
C
C --- define piezoelectric material properties
C -------------------------------------------------------
C
 LAMINATES
  NUMBER  ORTHO  AXIS  PIEZO
  11      11     11    11
C
C ORTHOTROPIC PARAMETER
C   VERNITRON --> PAFEC
C --------------------------
C       S11  --> Sxx & Syy
C       S33  --> Szz
C       S12  --> Sxy
C       S13  --> Syz & SZX
C       S66  --> SHXY
C       S44  --> SHYZ & SHZX
C
```

```
 ORTHOTROPIC.MATERIAL
  NUMBER  SXX       SYY
*         SZZ       SXY
*         SYZ       SZX
*         SHXY      SHYZ
*         SHZX      RO
  11      16.4E-12   16.4E-12
*         18.8E-12  -5.74E-12
*        -7.22E-12  -7.22E-12
*         44.3E-12   47.5E-12
*         47.5E-12   7700
C
PIEZOELECTRIC
NUMBER  TYPE  EPZZ  EPXX  EZX  EZZ  EXXZ
11      2     7.346E-9  8.107E-9  -4.779E-11  1.398E-10  1.089E-10
C
C
C ---------------------------------------------------
C
 AXES
  AXIS  RELAXISNO  ANG2
  11    1          -90
C
C ---------------------------------------------------
C
 RESTRAINTS
  NODE  PLANE  AXIS  DIRE
  1     3      1     3
  1     4      1     2
  4     5      1     4   (earthed electrode)
C
C ---------------------------------------------
C
 REPEATED.FREEDOM
  N1  PLANE  AXIS  DIRE
  9   5      1     4
C --- electrode
C
C -----------------------------------------
C
 ACOUSTICS
  SOLUTION  ELEMENT
  4         593
C
 SYMMETRY
  ELEMENT  AXIS  ANTI
  593      1     1
C
C
```

```
 MODES.AND.FREQUENCIES
  MODES   AUTO
  0      0
C
C
 RESPONSE
 TYPE
 0
C
 MASTERS
  NODE   DIRE
   9      14
   4      14
   6      12
   1      1
   17     1
   11     1
   12     1
   14     1
   16     1
C
C
 POINT.FOR.PRESSURE
  NUMBER   TYPE   NODES
  593      4     1 2
C
C
 FREQUENCIES.FOR.ANALYSIS
  TYPE   START   FINISH   STEP
  1      50000   250000   500
C
C
 SINUSOIDAL
  NODE   DIRE
  1      1
C
C --- 0 DEGREE ----
C
 SOURCES                          (acoustic source)
  WAVE    X   Y   Z   TABLE
  1      .1   0   0   1
  1     -.1   0   0   2
 TABLES
  TABLE   BASIS   VALUE
  1       0       100     0
  1       1E10    100     0
  2       0       -100    0
  2       1E10    -100    0
C
```

```
C
 FULL.DYNAMIC.OUTPUT
   TYPE  START  FINISH  STEP
   4     1      401     1
C
C
END.OF.DATA
```

APPENDIX II

EXPERIMENTAL SET UP FOR MEASURING THE TRANSDUCER RESONANT FREQUENCIES USING THE Π NETWORK DESCRIBED IN IEEE 177

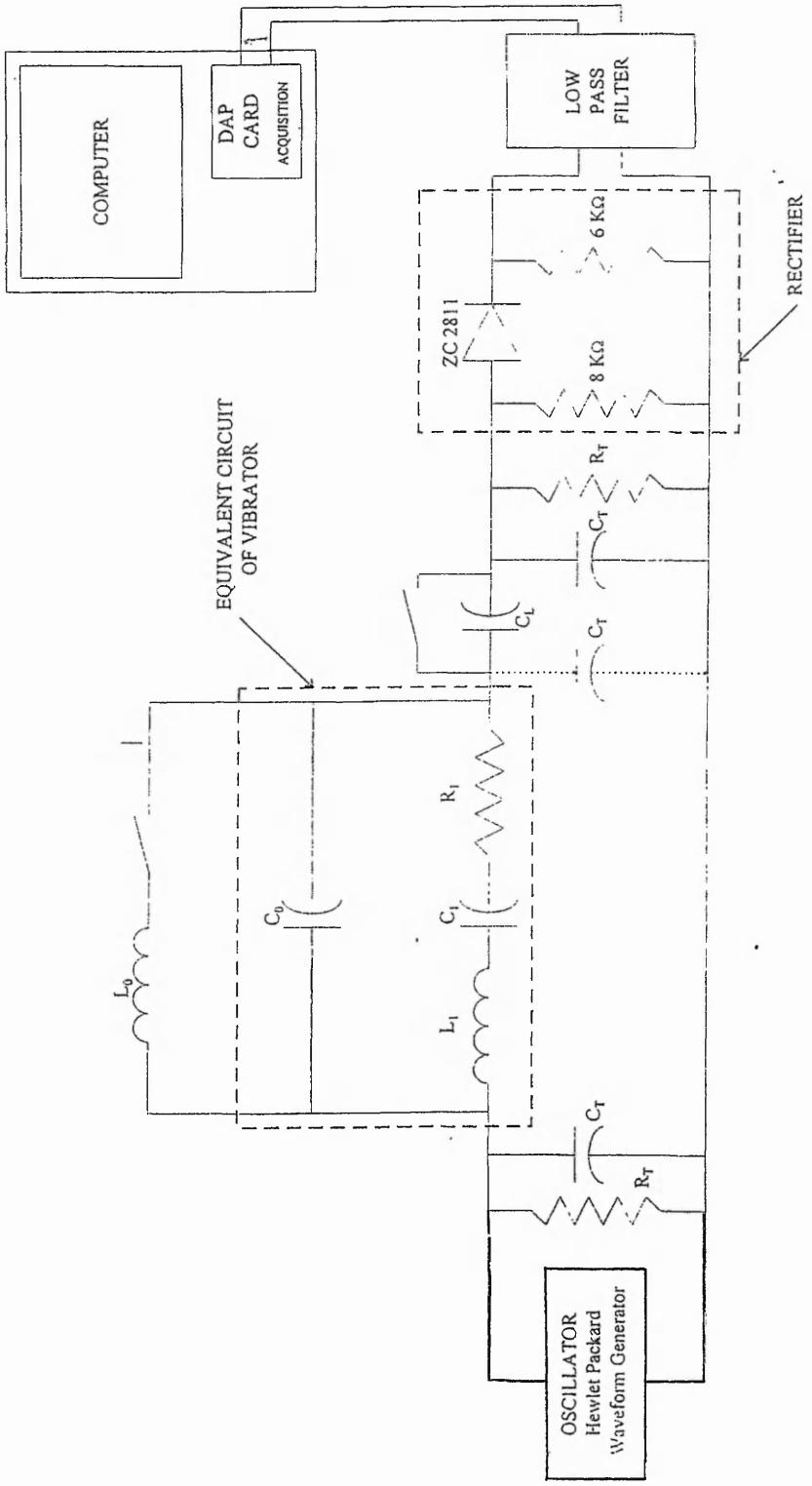

APPENDIX III

EQUATIONS FOR THE MULTILAYER TRANSMISSION THEORY PRESENTED BY HILL & EL-DARDIRY [50]

$$\begin{aligned}\frac{A_1}{A_5} &= \frac{1}{2}\,(F_1 \cos k_2 l_2 \cos k_3 l_3 \cos k_4 l_4 \\ &\quad - F_2 \sin k_2 l_2 \sin k_3 l_3 \cos k_4 l_4 \\ &\quad - F_3 \cos k_2 l_2 \sin k_3 l_3 \sin k_4 l_4 \\ &\quad - F_4 \sin k_2 l_2 \cos k_3 l_3 \sin k_4 l_4) \\ &\quad + j\,(F_5 \cos k_2 l_2 \sin k_3 l_3 \cos k_4 l_4 \\ &\quad + F_6 \cos k_2 l_2 \cos k_3 l_3 \sin k_4 l_4 \\ &\quad + F_7 \sin k_2 l_2 \cos k_3 l_3 \cos k_4 l_4 \\ &\quad - F_8 \sin k_2 l_2 \sin k_3 l_3 \sin k_4 l_4) \end{aligned} \qquad (1)$$

where

$$\begin{aligned} F_1 &= 1 + \frac{Z_1}{Z_5} & , F_2 &= \frac{Z_2}{Z_3} + \frac{Z_1 Z_3}{Z_2 Z_5} \\ F_3 &= \frac{Z_3}{Z_4} + \frac{Z_1 Z_4}{Z_3 Z_5} & , F_4 &= \frac{Z_2}{Z_4} + \frac{Z_1 Z_4}{Z_2 Z_5} \\ F_5 &= \frac{Z_1}{Z_3} + \frac{Z_3}{Z_5} & , F_6 &= \frac{Z_1}{Z_4} + \frac{Z_4}{Z_5} \\ F_7 &= \frac{Z_1}{Z_2} + \frac{Z_2}{Z_5} & , F_8 &= \frac{Z_1 Z_3}{Z_2 Z_4} + \frac{Z_2 Z_4}{Z_3 Z_5} \end{aligned} \qquad (2)$$

The sound pressure transmission coefficient is given by

$$\alpha_{p5} = \left| \frac{A_5}{A_1} \right|$$

APPENDIX IV

EXAMPLE OF A PAFEC-FE DATA FILE USED FOR THE 3D MODEL OF THE BRASS EXPONENTIAL HORN TRANSDUCER

```
C
C   DATA FILE PRODUCED BY PIGS
C
TITLE 3D_MODEL OF BRASS HORN TRANSDUCER
CONTROL
SKIP.COLLAPSE
FRONTAL.SINUSOIDAL.SOLUTION
PHASE=4
USE.R25544
BASE=4000000
PHASE=7
USE.S50100
BASE=10000000
ADD.PROG:
    CALL R09890(74,3,1)
    CALL R09890(83,1,1)
END.OF.ADD.PROG
CONTROL.END
C
C
C   *** THE NODES MODULE IS PRINTED
C   *** USING GLOBAL CARTESIAN AXES
C
NODES
 NODE        X                Y                Z
    1   0.00000000       0.00000000       0.00000000
    2   -0.49000006E-02  0.00000000       0.00000000
    3   -0.49000006E-02  0.25000000E-01   0.00000000
    4   0.00000000       0.25000000E-01   0.00000000
    5   0.00000000       0.25750002E-02   0.00000000
    6   0.47549998E-01   0.00000000       0.00000000
    7   0.47549998E-01   0.24649999E-01   0.00000000
    8   0.50000005E-02   0.00000000       0.00000000
    9   0.10000001E-01   0.00000000       0.00000000
   10   0.15000000E-01   0.00000000       0.00000000
...etc
C
ELEMENTS
 NUMB  GROU  ELEM  PROP  TOPO
   18    1 37110   11    5   61   80   63  496  497  498  499   84
*                  82   85   86  500  501  502  503  504  505
*                 506  507
   20    1 37110   11   80   63   64   62  498  499  584  585   86
*                  88   90   91  502  503  586  587  507  588
```

```
*                589  590
...etc
C
AXES
   AXIS   RELAX   TYPE  NODE     ANG1          ANG2          ANG3
13     1      1      2  0.0000000E+00 -0.9000000E+02  0.0000000E+00
C
C
COUPLING
COUP.REG  TYPE  SURF  N1   PLANE   AXIS
  1      1    0  2     1      1
C
C ---BRASS HORN----
C
MATERIAL
MATE     E      NU     RO
 11    10.4E10  0.37    8500
C
C
C ---WATER----
C
MATERIAL
MATE    RO    BULK
 12    1000    2.05E9
C
C ---PIEZOELECTRIC----
C
LAMINATES
NUMBER   ORTHO   AXIS   PIEZO
 14      14      13      14
C
C
C ORTHOTROPIC PARAMETER
C   VERNITRON --> PAFEC
C --------------------------
C       S11   --> Sxx & Syy
C       S33   --> Szz
C       S12   --> Sxy
C       S13   --> Syz & SZX
C       S66   --> SHXY
C       S44   --> SHYZ & SHZX
C
 ORTHOTROPIC.MATERIAL
  NUMBER  SXX        SYY
*         SZZ        SXY
*         SYZ        SZX
*         SHXY       SHYZ
*         SHZX       RO
  14      16.4E-12   16.4E-12
```

```
*          18.8E-12   -5.74E-12
*         -7.22E-12   -7.22E-12
*          44.3E-12    47.5E-12
*          47.5E-12    7700
C
PIEZOELECTRIC
NUMBER   TYPE   EPZZ   EPXX   EZX   EZZ   EXXZ
14       2      7.346E-9  8.107E-9  -4.779E-11  1.398E-10  1.089E-10
C
C
RESTRAINTS
   NODE   PLANE   AXIS   DIRE
   1940      1       1     4
C -- earthed electrode on brass face
C ------------------------------------------------
C
 REPEATED.FREEDOM
   N1   PLANE   AXIS   DIRE
  1944   1       1      4
C --- electrode
C
C
 ACOUSTICS
   SOLUTION   ELEMENT
   4          73
C
C
 SYMMETRY
   ELEMENT   AXIS   ANTI
   73        11     1
C
 MODES.AND.FREQUENCIES
   MODES   AUTO
   0       0
C
C
 RESPONSE
 TYPE
 0
C
C
 MASTERS
   NODE   DIRE
    2       12
    1944    14
    1940    4
    6       12
    8       123
    40      1
```

```
   167    1
   170    12
   300    1
   425    123
   1062   1
C
C  POINT.FOR.PRESSURE
C   NUMBER   TYPE   NODES
C     73      4      6 344
C
C
FREQUENCIES.FOR.ANALYSIS
   TYPE   START   FINISH   STEP
   1      1000    100000    500
C
C
 SINUSOIDAL
   NODE   DIRE
   6      1
C
C --- 0 DEGREE -----
C
C
 SOURCES
  WAVE  X  Y  Z  TABLE
   1   1.47549998E-01  0  0  1
   1  -1.47549998E-01  0  0  2
C
C
 TABLES
   TABLE   BASIS   VALUE
   1       0       100   0
   1       1E10    100   0
   2       0      -100   0
   2       1E10   -100   0
C
C
 FULL.DYNAMIC.OUTPUT
   TYPE   START   FINISH   STEP
   4      1       199      1
C
C
END.OF.DATA
```

APPENDIX V

EXAMPLE OF A PAFEC-FE DATA FILE USED FOR A TRANSIENT ANALYSIS WITH INPUT DATA FROM THE GPLATE PROGRAM

```
TITLE TRANSIENT PROBLEM WITH TRANSDUCER PZT_5A
C source at Z=-0.5 x=0.001-10mm index=33
C double mesh density for plastic, multi node input
CONTROL
SKIP.COLLAPSE
FRONTAL.TRANSIENT
AXISYMMETRIC
PHASE=1
SEMI.USE1
PHASE=2
TOLERANCE=10E-5
PHASE=4
TOLERANCE=10E-5
SEMI.USE4
PHASE=7
SEMI.USE7
BASE=2000000
HARMONIC.NUMBER=0
TRACE.LEVEL=3
TIME.STAGES
CONTROL.END
NODES
Z=0
NODE X  Y
1  0 0
2  0 10E-3
3  -1.22E-3 10E-3
4  -1.22E-3 5.01E-3
5  -1.22E-3 0
6  -6.22E-3 0
7  -6.22E-3 5.01E-3
8  -1.345E-3 5.01E-3
9  -1.345E-3 0
C
C
PAFBLOCKS
TYPE=1
GROU=1
ELEM=35425
PROP=11
BLOC N1 N2  TOPO
1    1  2 9 8 6 7
3    5  6 9 5 8 4
PAFBLOCKS
```

```
BLOC=2
TYPE=1
GROU=2
ELEM=36610
PROP=12
N1 N2  TOPO
3  4   1 2 5 3
MESH
REFE  SPAC
 1    40
 2    23
 3    80
 4    9
 5    1
 6    40
C
C
 PLATES.AND.SHELLS
   PLATE   MATE   THICK   RAD1
   12      12     0.001
C
C
C --- define for plastic (EPOXID FIBRE FR4  BS4584 SECTION 102.5)
C                    m=3.072E-3 Kg; T=5.01E-3 m; r=10.02E-3 m
C                    c=2889 m/s; ro=1037 Kg/m; NU=0.3; E=8.66E9 N/m
C    ---------------------------------------------------------------
 MATERIAL
   MATE  E      NU   RO
   12    8.66E9 0.30 1037
C
C ------------------------------------------------------
AXES
AXIS NODE  ANG2
 11  1    -90
C
 LAMINATES
   NUMBER   ORTHO   AXIS   PIEZO
   11       11      11     11
C
C ORTHOTROPIC PARAMETER
C   VERNITRON --> PAFEC
C ---------------------------
C       S11  --> Sxx & Syy
C       S33  --> Szz
C       S12  --> Sxy
C       S13  --> Syz & SZX
C       S66  --> SHXY
C       S44  --> SHYZ & SHZX
C
```

```
C
 ORTHOTROPIC.MATERIAL
  NUMBER  SXX       SYY
*         SZZ       SXY
*         SYZ       SZX
*         SHXY      SHYZ
*         SHZX      RO
  11      16.4E-12  16.4E-12
*         18.8E-12  -5.74E-12
*        -7.22E-12  -7.22E-12
*         44.3E-12  47.5E-12
*         47.5E-12  7700
C
PIEZOELECTRIC
NUMBER  TYPE  EPZZ  EPXX  EZX  EZZ  EXXZ
11      2     7.346E-9  8.107E-9  -4.779E-11  1.398E-10  1.089E-10
C
C
 RESTRAINTS
  NODE  PLANE  AXIS  DIRE
  1     3      1     3
  1     4      1     2
  4     5      1     4  (earthed electrode)
C
C ---------------------------------------------
C
 REPEATED.FREEDOM
  N1  PLANE  AXIS  DIRE
  6   5      1     4
C --- electrode
C
C ---------------------------------------------
C
 MODES.AND.FREQUENCIES
  MODES  AUTO
  0      0
C
RESPONSE
TYPE  TIME  FINISH  LIST
 2    0.05E-6  50E-6  6 4  1 1 6 1
C
FULL.DYNAMICS.OUTPUT
TYPE  LIST
 1    5E-6 10E-6 15E-6 20E-6 25E-6 30E-6 35E-6 50E-6
C
DEFINE.RESPONSE      (Input data from GPLATE program)
TIME LIST
4.850E-6,1,1,1,-4.00E-13,1,2896,2,-3.10E-16,1,2896,1,-4.00E-13
* 1,2900,2,-1.40E-14,1,2900,1,-3.40E-13,1,2904,2,-1.40E-14,1,2904,1,-3.40E-13
```

```
* 1,2908,2,-2.10E-14,1,2908,1,-1.70E-13,1,2912,2,-2.10E-14,1,2912,1,-1.70E-13
* 1,2916,2,-1.20E-14,1,2916,1,1.25E-13,1,2920,2,-1.20E-14,1,2920,1,1.25E-13
* 1,2924,2,1.72E-14,1,2924,1,5.24E-13,1,2928,2,1.72E-14,1,2928,1,5.24E-13
* 1,2932,2,0,1,2932,1,0,1,2936,2,0,1,2936,1,0
* 1,2940,2,0,1,2940,1,0,1,2944,2,0,1,2944,1,0
* 1,2948,2,0,1,2948,1,0,1,2952,2,0,1,2952,1,0
* 1,2956,2,0,1,2956,1,0,1,2960,2,0,1,2960,1,0
* 1,2964,2,0,1,2964,1,0,1,2968,2,0,1,2968,1,0
* 1,2972,2,0,1,2972,1,0,1,2976,2,0,1,2976,1,0
* 1,2980,2,0,1,2980,1,0,1,2984,2,0,1,2984,1,0
* 1,2988,2,0,1,2988,1,0,1,2992,2,0,1,2992,1,0
* 1,2996,2,0,1,2996,1,0,1,3000,2,0,1,3000,1,0
* 1,3004,2,0,1,3004,1,0,1,3008,2,0,1,3008,1,0
* 1,3012,2,0,1,3012,1,0,1,3016,2,0,1,3016,1,0
* 1,3020,2,0,1,3020,1,0,1,3024,2,0,1,3024,1,0
* 1,3028,2,0,1,3028,1,0,1,3032,2,0,1,3032,1,0
* 1,3036,2,0,1,3036,1,0,1,3040,2,0,1,3040,1,0
* 1,3044,2,0,1,3044,1,0,1,3048,2,0,1,3048,1,0
* 1,2,2,0,1,2,1,0,1,2,2,0,1,2,1,0
4.900E-6,1,1,1,-1.40E-12,1,2896,2,-1.10E-15,1,2896,1,-1.40E-12
* 1,2900,2,-5.30E-14,1,2900,1,-1.40E-12,1,2904,2,-5.30E-14,1,2904,1,-1.40E-12
* 1,2908,2,-9.90E-14,1,2908,1,-1.20E-12,1,2912,2,-9.90E-14,1,2912,1,-1.20E-12
* 1,2916,2,-1.30E-13,1,2916,1,-8.70E-13,1,2920,2,-1.30E-13,1,2920,1,-8.70E-13
* 1,2924,2,-1.30E-13,1,2924,1,-4.40E-13,1,2928,2,-1.30E-13,1,2928,1,-4.40E-13
* 1,2932,2,-1.10E-13,1,2932,1,9.18E-14,1,2936,2,-1.10E-13,1,2936,1,9.18E-14
* 1,2940,2,-5.10E-14,1,2940,1,7.21E-13,1,2944,2,-5.10E-14,1,2944,1,7.21E-13
* 1,2948,2,4.75E-14,1,2948,1,1.43E-12,1,2952,2,4.75E-14,1,2952,1,1.43E-12
* 1,2956,2,1.89E-13,1,2956,1,2.21E-12,1,2960,2,1.89E-13,1,2960,1,2.21E-12
* 1,2964,2,0,1,2964,1,0,1,2968,2,0,1,2968,1,0
* 1,2972,2,0,1,2972,1,0,1,2976,2,0,1,2976,1,0
* 1,2980,2,0,1,2980,1,0,1,2984,2,0,1,2984,1,0
* 1,2988,2,0,1,2988,1,0,1,2992,2,0,1,2992,1,0
* 1,2996,2,0,1,2996,1,0,1,3000,2,0,1,3000,1,0
* 1,3004,2,0,1,3004,1,0,1,3008,2,0,1,3008,1,0
* 1,3012,2,0,1,3012,1,0,1,3016,2,0,1,3016,1,0
* 1,3020,2,0,1,3020,1,0,1,3024,2,0,1,3024,1,0
* 1,3028,2,0,1,3028,1,0,1,3032,2,0,1,3032,1,0
* 1,3036,2,0,1,3036,1,0,1,3040,2,0,1,3040,1,0
* 1,3044,2,0,1,3044,1,0,1,3048,2,0,1,3048,1,0
* 1,2,2,0,1,2,1,0,1,2,2,0,1,2,1,0
(etc.)
END.OF.DATA
```

APPENDIX VI

APPROXIMATE ARRIVAL TIMES AT THE TRANSDUCER FOR LAMB WAVE MODES IN STEEL [19]

Frequency	Mode	Group Vel [ms^{-1}]	Arrival Time at 20cm [μs]	Arrival Time at 10cm [μs]	Arrival Time at 5cm [μs]
147 kHz	L_{12}	4977	40.18	20.09	10.05
	L_{21}	3172	63.04	31.52	15.76
	L_{22}	3086	64.80	32.40	16.20
	L_{11}	2632	75.98	37.99	19.00
250 kHz	L_{13}	4402	45.43	22.72	11.36
	L_{23}	3862	51.79	25.89	12.95
	L_{21}	3115	64.21	32.10	16.05
	L_{11}	3977	50.29	25.14	12.57
	L_{21}	2690	74.36	37.18	18.59
	L_{12}	2460	81.31	40.65	20.33

PULICATIONS, CONFERENCES & MEETINGS

Modelling Acoustic Emission Transducers Using Finite Element Methods (Oral Presentation)
5th Acoustic Emission World Meeting, Big Island, Hawaii. August 1998.

Modelling Acoustic Emission Transducers Using Finite Element Methods (Proceedings published in Progress in Acoustic Emission IX, p. IV-86. August 1998.

Ultrasonic & Acoustic Transducer Group (UATG) Meetings attended:
New Transducer Technology.
PAFEC Ltd, Strelley Hall, Nottingham, August 1996.

Piezoelectric Ceramics for Transducer Applications.
UMIST, Manchester, May 1998.

Progress in Acoustic Emission IX

Transitions in AE for the 21st Century

Proceedings of
International Acoustic Emission Conference

Incorporating

14th International Acoustic Emission Symposium
and
5th Acoustic Emission World Meeting

Big Island, Hawaii, USA
August 9 – 14, 1998

Conference Organized by
M.A. Hamstad, Teruo Kishi and Kanji Ono

Proceedings Compiled by
Kanji Ono

Published by
Acoustic Emission Working Group
and
Acoustic Emission Group

14th International Acoustic Emission Symposium
&
5th Acoustic Emission World Meeting

Transitions in AE for the 21st Century

An HISTORIC first: a united meeting of the two major and oldest technical groups from different countries dedicated to acoustic emission research and applications.

Sponsored by:

Japanese Society for Non-Destructive Inspection (JSNDI)
Ad Hoc Committee on Acoustic Emission (formerly Committee 006)
&
Acoustic Emission Working Group (AEWG) - USA

Conference Organized by:

Conference Co-Chairs

Marvin A. Hamstad
NIST and University of Denver (AEWG)

Teruo Kishi
University of Tokyo and National Institute for Advanced Interdisciplinary Research (JSNDI)

Kanji Ono
University of California at Los Angeles (AEWG)

Conference Planning and Logistics Manager

Karyn S. Downs (AEWG)
Lockheed Martin Astronautics

Dates & Venue:

August 9 - 14, 1998

The Royal Waikoloan Hotel
Kamuela, Hawaii, USA

MODELLING ACOUSTIC EMISSION TRANSDUCERS USING FINITE ELEMENT METHODS.

ROGER HILL, SIMON FORSYTH
Centre for Research in Materials
The Nottingham Trent University
Nottingham NG11 8NS, UK

PATRICK MACEY
PAFEC Ltd,
Strelley Hall, Nottingham NG8 6PE, UK

ABSTRACT

The propagation and detection of acoustic emission from a transient source to a piezoelectric detector involves a number of factors such as source characteristics, propagation and reflection of source waves and the detail of the mechanisms of piezoelectric detection.

This paper reports on finite element modelling of different transducer designs, to get a better definition of mode of excitation, resonant frequency and sensitivity.

KEYWORDS

Finite elements, modelling, AE transducers, vibroacoustic models.

INTRODUCTION

Acoustic Emission (AE) is detected using piezoelectric transducers. A variety of broadband designs have been produced over the last two decades [1,2] which have been combined with different signal processing techniques to yield information concerning Acoustic Emission and material condition.

However, the most often used have been relatively undamped, simple piezoelectric transducers which provide very high sensitivity to Acoustic Emission. Designs exist which might be termed broadband, multimode, or narrow band. Complete narrow measurement bandwidth is usually achieved by the use of narrow band AE preamplifiers centred on the lowest main resonant frequency of a particular transducer.

When detecting Acoustic Emission, the ability to characterise AE is affected by complex wave paths from an Acoustic Emission source to the transducer and the complex response of resonant transducers to this complex excitation.

Transducer design seems to be largely undiscussed except for cases where the design has a few simple principles applied to remove resonance [1,2]. In the case where complex resonance occurs, the response is difficult to predict and seemingly design is based on the principle of

continuing to use well tried approaches. Experience with resonant sensors over the years has shown them to be very effective detectors of Acoustic Emission and no serious attempts has been made to move our work in materials characterisation to the use of broadband sensors.

Design of resonant sensors, being so much of a black art, has prompted us to do work using finite element modelling, in an attempt to provide more effective design criteria for resonant sensors, without the need for an extensive build and test programme.

Our work has considered design and sensitivity issue for transducer in the frequency ranges from 10kHz up to 500kHz, which is the effective frequency range for the vast array of Acoustic Emission applications.

BROADBAND AND NARROWBAND SENSORS

The earliest designs of Acoustic Emission sensor were based on simple geometry piezoelectric material. These devices were related to other devices such as accelerometers, designed to work at audio frequencies. Accelerometers have wide bandwidth but insufficient sensitivity for AE detection. However, an advantage of accelerometers is that they are effective at translating a surface acceleration on a structure to a proportional voltage. Since vibration might be made at kHz frequencies, the surface of the solid, across the face of the transducer, is moving in phase, with the acoustic wavelength in the solid being several metres.

Traditional ultrasound transducers use in NDE use heavily damped piezoelectrics at high ultrasonic (MHz) frequencies. Since the piezoelectric material, at these frequencies, is in the form of a thin plate, again the design is relatively easy to deal with, with resonance controlled by the thickness of the plate.

Novel AE sensors, due to workers such as Proctor [1,2] dealt with the need for broad, flat bandwidth. The sensor typically has a conical design and is backed by a large mass, which suppresses resonances. The ability of these devices to reproduce standard transient waveforms is well established.

In the case of Acoustic Emission, resonant transducers are used to provide maximum sensitivity and this remains one of the prime requirements and advantages of AE. However the presence of this undamped, behaviour is to introduce complex, multimode vibration characteristics. Any variability in vibration characteristics may be controlled by using narrow frequency banding.

The frequencies used for AE, being in the 100s of kHz range, means that any piezoelectic dimension is likely to be similar in all directions and often transverse rather than thickness modes of vibration control the low frequency resonance. A further difficulty with such devices is the complex mode of excitation. Perhaps the simplest source would be one directly below the transducer where a transient source would generate shear and longitudinal wave components. It is clear that for the use of AE testing on relatively thin plates, with a typical source off axis, these waves will reflect and become complex. The wave propagation to a transducer on the surface of plate, where the source is along the plate by several plate thicknesses, can be studied effectively using the programme due to Hsu [3] . An example of this complex form of transducer excitation is shown in figure 1. Clearly with this complex excitation combined with complex undamped behaviour provided by the transducer, means that developing of a clear knowledge of

the relationship beween AE source characteristics in a material, and resonant transducer output, remains a topic of continuing interest and challenge.

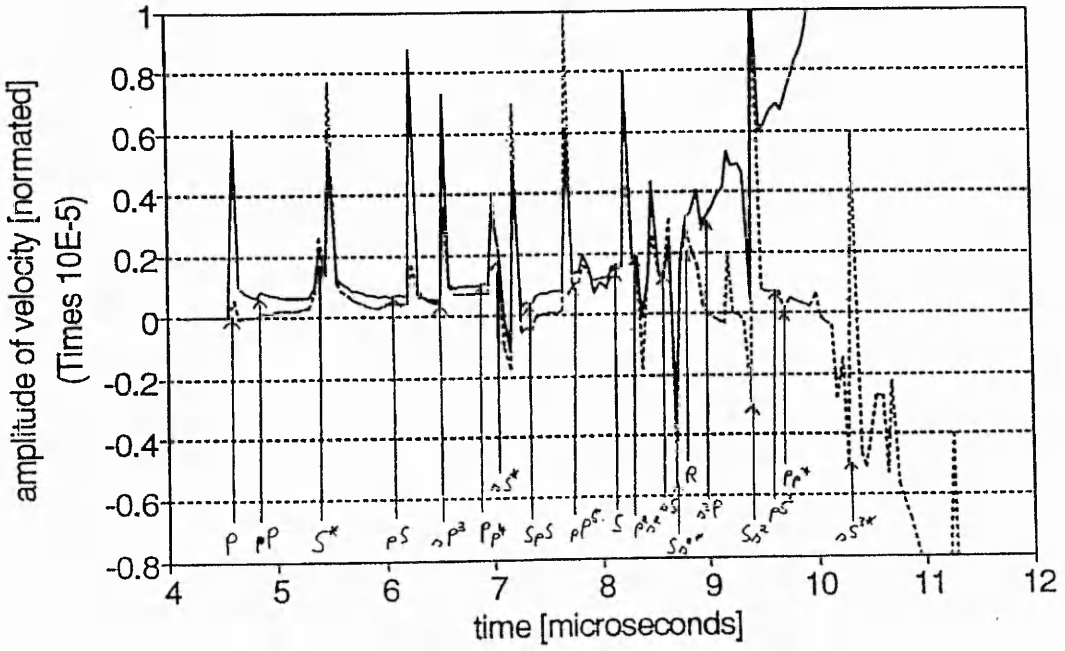

Figure 1 : Velocity waveform exciting an AE transducer, where detection is at a point and 4 plate thicknesses from a central dipole source. Solid line - vertical detection. Dotted line - horizontal detection.

MODELLING AND THE EXPERIMENTAL SYSTEM - DISC PIEZOELECTRIC TRANSDUCER

Modelling of piezoelectric transducers is useful in that the model leads to better understanding of the behaviour of a particular design and what design criteria are needed to achieve a specified performance.

Modelling was carried out using the vibroacoustics portion of PACEF finite element software. Models were constructed using the "PAFEC Interactive Graphics Sytem" (PIGS), which is a sophisticated menu driven CAD package. Elements used were, fluid elements, solid elements and piezoelectric elements. A simple model considered is that of an axi-symmetric piezoelectric disk mounted on a plastic face plate and excited by a point source acoustic signal in water (usually 0.1m from the transducer). Using this model, it is possible to derive the resonant frequency response of such a device in terms of the amplitude of the voltage from the piezoelectric material.

The basic model consisted of a 5.01mm radius, 5.01mm thick piezoelectric disc mounted on a 1.22mm plastic base plate of diameter 20mm (figure 2). The resonant frequency, by modelling, was predicted as 176.5kHz. Electrical admittance measurements were made on a piezoelectic transducer using a standard test circuit. The resonant frequency determined

piezoelectic transducer using a standard test circuit. The resonant frequency determined experimentally, occurred at 176.5kHz.(see figure 3). Modelling allowed the effect of diameter to thickness ratio on resonant frequency, to be determined and this is plotted in figure 4.

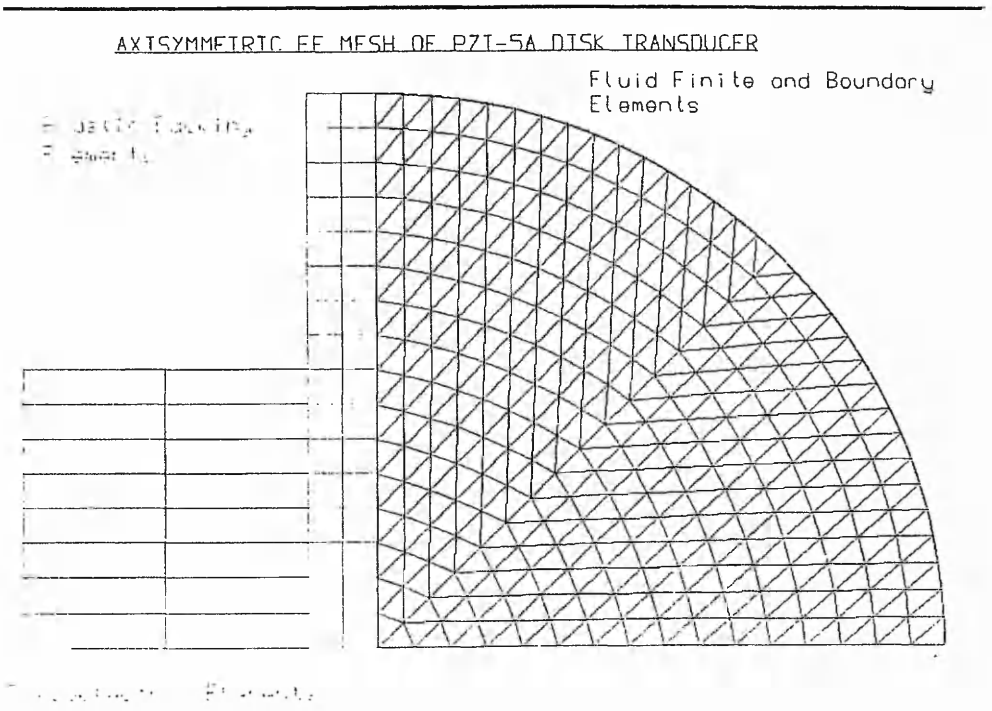

Figure 2 Finite element model of an axi-symmetric piezoelectric disc mounted on a plastic disc and excited by an acoustic sinusoidal source in a semi-infinite body of water.

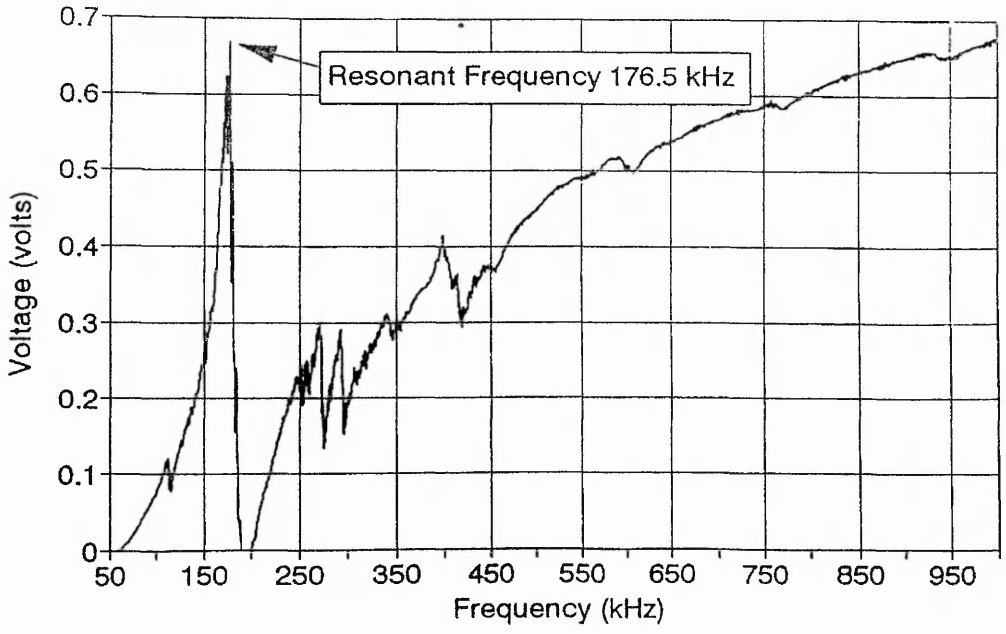

Figure 3 Electrically determined frequency response of 5mm radius, 5mm thickness piezoelectric mounted on a 20mm diameter plastic base plate

This work confirmed the validity of modelling using the PAFEC acoustic / piezoelectric software. The modelling used water as a medium for the acoustic excitation. The water provided an acoustic load to the transducer and allowed far field, point source harmonic excitation of the transducer. Water loading was used to avoid problems associated with the response of a solid.

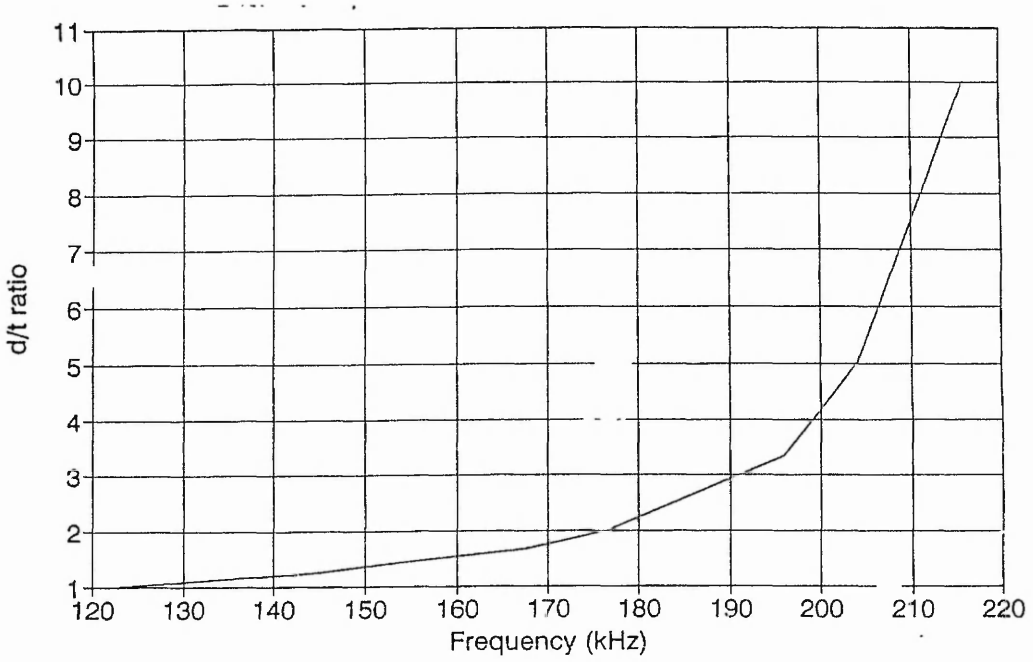

Figure 4 : Effect of changes in diameter to thickness ratio on the main transducer radial resonance.

medium and the mode conversion of waves incident on the front face of the transducer. The agreement between experiment and theory suggests this is a valid approach.

Since an acoustic emission transducer operates on a solid, modelling experiments were carried out with the transducer attached to a finite solid plate of varying thickness and 50mm diameter. The plate was excited directly by a harmonic array of forces at the outer nodes of the plate. This type of modelling was found to add plate structural resonances to the response but provide no useful information on the response of the transducer to Acoustic Emission type excitation. A summary of main resonant frequencies in the 100-200kHz range are given in table 1.

Table 1 : Finite element modelling , steel disc attached to transducer.

Steel	Resonant frequency (kHz)	Other resonances
None	140	225
25mm thick x 50mm diam.	140	-
15mm thick x 50mm diam.	135.5	246.5
10mm thick x 50mm diam.	134, 136, 148	-

Electrical measurements with the transducer attached to a finite large plate of 23mm thickness indicated a rise in resonant frequency to 184kHz with the general shape of the curve conforming to that shown in figure 3 . The differences between the resonant frequencies determined by these two methods is worthy of comment.

When the plate, which is modelled as attached to the transducer, is excited by a harmonic force on the outer surface, then this generates displacements associated with a plane acoustic wave. The effect of this appears to be to excite the system in an unnatural way generating structural resonances not apparent when using the transducers. Since no transverse deformation is present in the excitation then any modes associated with transverse motion of the piezoelectric do not appear (at 176.5kHz).

Excitation by a point acoustic source provides excitation by a wavefront with some curvature which set up the radial mode seen in the response, using both modelling and experiment.

Constraining the bottom surface of the transducer by mounting it on a steel plate produces a transducer with a resonance of 187kHz and correspondingly, a transducer with a smaller effective thickness, due to the constraint around the bottom edge. Figure 4 indicates an effective thickness reduction from 5mm to 4mm. For a system operating with an electronic bandwidth of say 100kHz, then this change in not manifest in normal Acoustic Emission measurements.

ACOUSTIC EMISSION TRANSDUCER SENSITIVITY

In designing transducers, it is normal to define a quantity called sensitivity based on the relationship between an output quantity (voltage amplitude) and an input quantity (surface displacement, velocity or acceleration). A vibration measuring accelerometer can be simply represented as a mass moving on a piezoelectric, sandwiched between the mass and the transducer metal base. The sensitivity of such a system can be stated in terms of output voltage per unit of acceleration. This system is engineered so that measurements are made well below the primary resonance, which typically may be 20 to 30 kHz. There are clearly, similarities between acoustic emission transducers and accelerometers.

This work has attempted to consider sensitivity of the measurement transducer. The full problem of acoustic emission and sensitivity is to consider wave propagating from a known source and determine the transducer output in terms of some variable such as voltage amplitude, spectrum or some other AE parameter. However, AE is affected by the variability of the excitation as the source moves with respect to the transducer.

A simple way to define sensitivity would be to input a known amplitude into the transducer and consider the voltage output. It is much easier to achieve such a situation using modelling, using some specific validation of the model and them assuming general validity for other situations. Such a situation is reported in figure 5.

A transducer, again consisting of a piezoelectric disc (10mm diameter x 5 mm thick) is considered, mounted on a plastic facing disk. In this case, the transducer is excited by constant harmonic displacement amplitude normal to the face of the transducer at all nodes. The frequency response of this system is given in figure 5. This corresponds to the first case in table 1. The

largest resonances are at 140 and 225.5 kHz with others at 117 kHz and 212 kHz. The bandwidth considered takes account of normal AE frequencies.

A transducer, excited in such a way, by an acoustic plane wave, with a known particle displacement, would excite these resonances. If the AE were a broad bandwidth transient over the frequency range of interest, then the transient signal would be a typical decaying sine wave, with frequency components corresponding to the frequencies in the spectrum of figure 5.

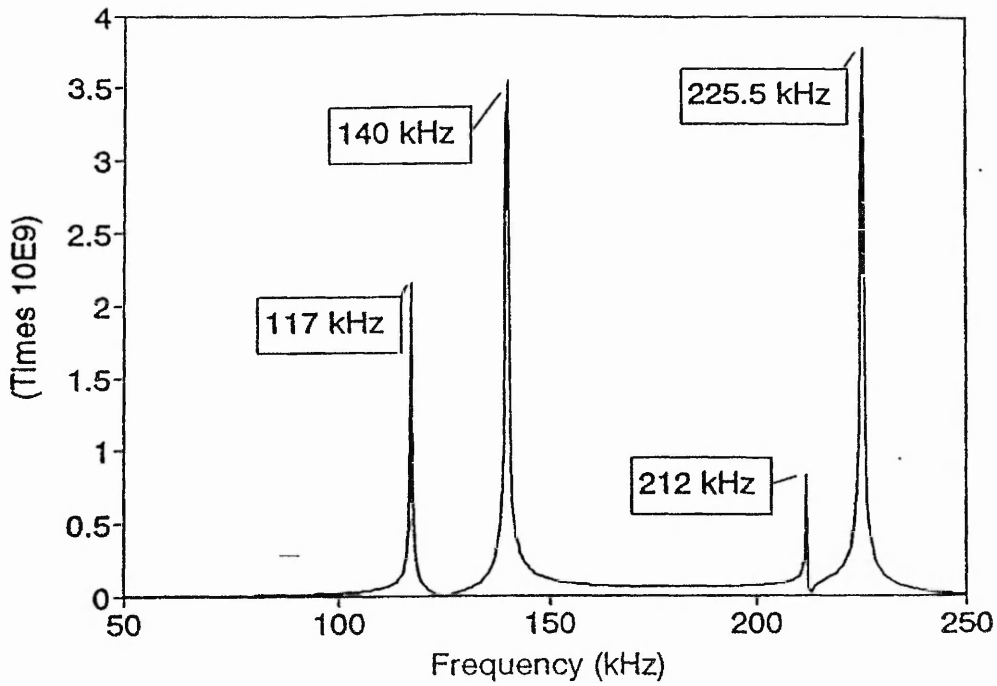

Figure 5 : Finite element model of resonances - piezoelectric disc (10 mm diameter x 5 mm thick) mounted on plastic facing disc. Harmonic excitation at FE nodes normal to the transducer face.

The sensitivity of the transducer would be defined as the integrated voltage across the spectrum divided by the harmonic input displacement. Clearly, from a pure transducer perspective, this is a good definition. The resonances at 140kHz and 225.5kHz appear to be associated with quarter wavelength resonance in the transducer and piezoelectric respectively, although, clearly the actual vibrational response requires the more complex analysis provide by finite element analysis. The complexity of response of such a system has been reported by one of the authors before [4]

However, the complexity of the situation is illustrated when the transducer is excited by a harmonic source on the surface of a plate. The transducer is modelled attached to a 15mm thick steel plate.(figure 6) The transducer quarter wavelength resonance is maintained but other resonances are suppressed.

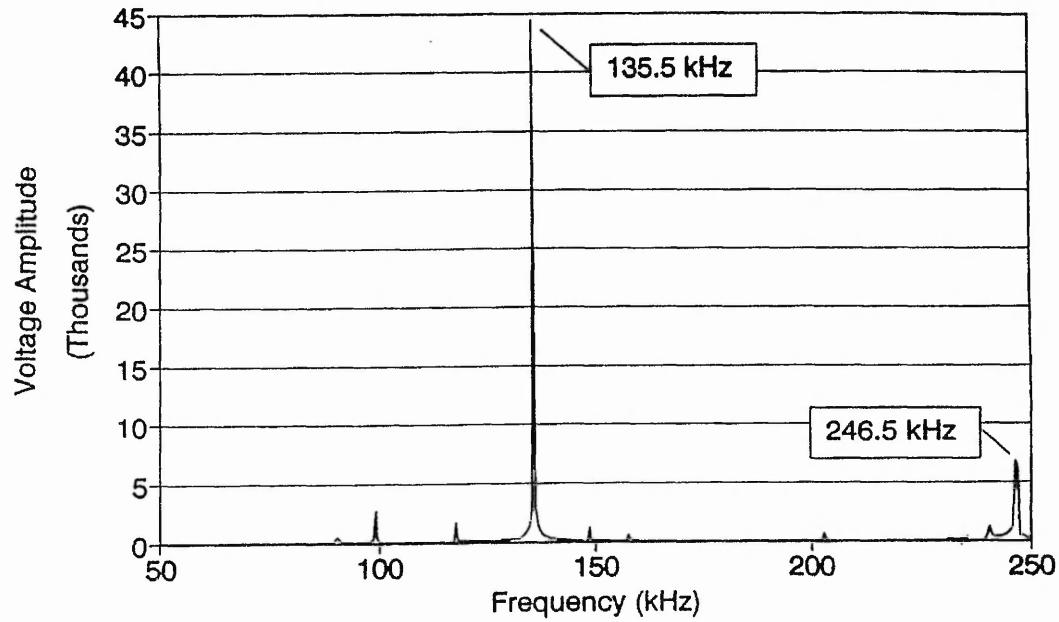

Figure 6 : Finite element model of resonances - piezoelectric disc (10 mm diameter x 5 mm thick) mounted on plastic facing disc and a 15mm diameter steel plate. Harmonic excitation at FE nodes normal to the transducer face and on the outer surface of the steel plate.

In reality, acoustic emission excitation of transducers is both complex and variable and the continued need for resonant devices to utilise the sensitivity of the measurement system based on piezoelectric provides continuing challenges.

LOW FREQUENCY TRANSDUCERS

Our work on geotechnical applications of acoustic emission, and the need for sensors below 50 kHz prompted interest in devices more akin to accelerometers, but used in resonant mode. Sensors at 10-50 kHz would need the use of more massive piezoelectric materials, which focused our attention on the use of metallic structures with smaller piezoelectrics. One such design is the brass horn sensor.

A relatively large design has initially been manufactured as shown in figure 7. The electrically determine resonances are shown in figure 8. This design can be reduced in dimensions to raise resonant frequency values.

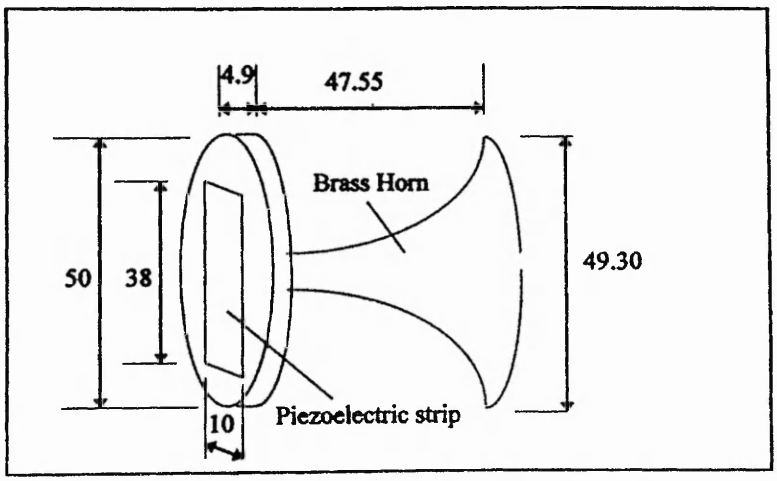

Figure 7 : Low frequency AE sensor using a brass horn.

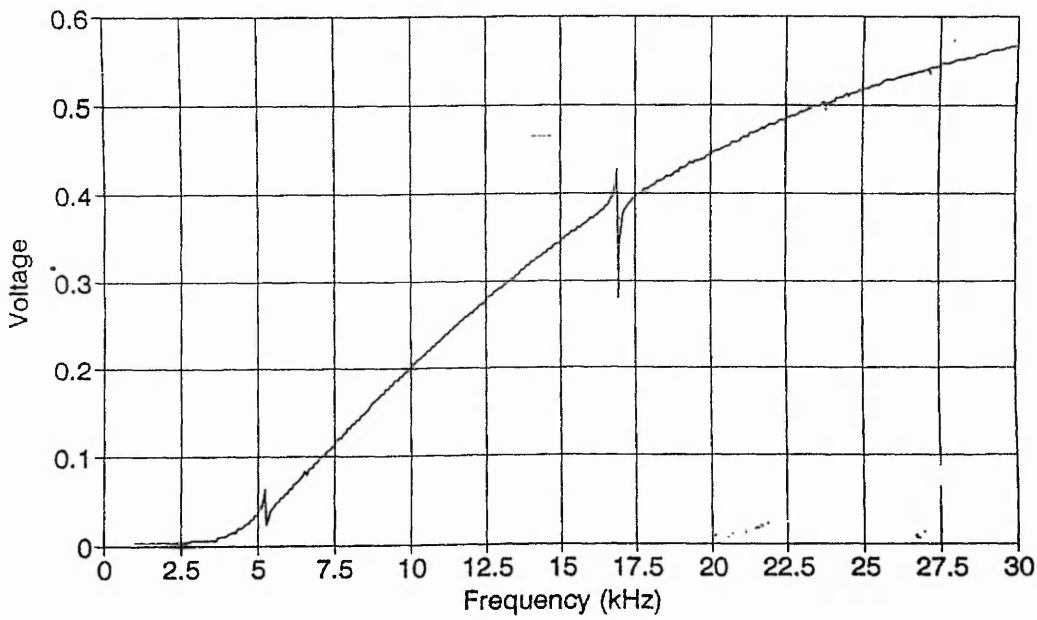

Figure 8 : Electrically determined resonance of brass horn transducer

CONCLUSIONS

Experience has been gained using PAFEC vibroacoustic software applied to ultrasonic / AE transducer designs. Resonant devices show complex behaviour but with maximum sensitivity suitable for AE work. For specific cases, experiment and modelling agree, but excitation

conditions using FE modelling need to be used with care to properly reflect actual response. In this regard, modelling using water borne acoustic waves has proved suitable.

Sensitivity definitions still remains a complex issue and work is continuing on how to achieve design improvements.

ACKNOWLEDGEMENTS

The authors acknowledge the program used to simulate wave propagation in a plate, kindly provided by Dr. Nelson Hsu. Thanks are due to Olaf Teichert for producing the velocity waveform on a plate.

REFERENCES

[1] Proctor T.M. Jr, J.Acoust. Em., Vol. 1, No. 3, 1982, pp 173 - 178
[2] Proctor T.M. Jr., J.Acoust. Em., Vol. 7, No. 1, 1988, pp 41- 47
[3] Hsu N.N., Report NBSIR 85-3234, 1985
[4] Hill R., El-Dardiry S.M.A., J.Acoust. Soc. Am., Vol. 67, No. 2, 1980, pp673-682

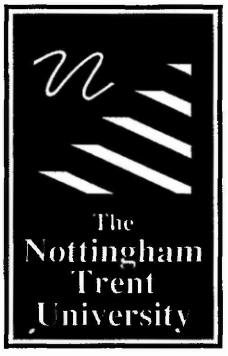

Libraries &
Learning
Resources

The Boots Library: 0115 848 6343
Clifton Campus Library: 0115 848 6612
Brackenhurst Library: 01636 817049